THE UNIVERSITY
of ADELAIDE

Experimental and Numerical Investigation of a Carbon Nanotube Acoustic Absorber

Md. Ayub

School of Mechanical Engineering
The University of Adelaide
South Australia 5005
Australia

A thesis submitted in fulfilment of the requirements for the degree of Ph. D. in Engineering on the 14th of October 2015.

Ph. D. Thesis

Submitted version
14th of October 2015

Acoustics, Vibrations and Control Group
School of Mechanical Engineering
The University of Adelaide
South Australia 5005
Australia

Typeset by the author using LaTeX.
Printed in Australia.

Summary

The interest in applications of nanomaterials for acoustic absorption purposes is growing rapidly with advances in nanotechnology. A need also exists for a simulation framework that is applicable for modelling acoustic absorption in nanomaterials in order to develop an understanding of nanoscopic acoustic absorption mechanisms. The current study investigates the acoustic absorption characteristics of a carbon nanotube (CNT) acoustic absorber to develop an understanding of the absorption behaviour and mechanisms of the CNTs. This task involves undertaking an exploratory study of the absorption characteristics of a CNT forest and modelling the absorption effects of the CNT at the nanoscale. The absorption characteristics of the CNTs were explored by studying the normal incidence absorption coefficient of 3 mm- and 6 mm-long vertically aligned CNT arrays measured experimentally using the two-microphone impedance tube method, while the modelling of the absorption effects was performed using a non-continuum particle-based method. The experimental investigation showed promising results for the acoustic absorption capability of CNT acoustic absorbers and suggests that the absorption performance could be enhanced with longer CNTs and a lower spatial density of the nanotube arrays. The study of absorption using a theoretical model based on classical absorption mechanisms indicated that the absorption behaviour of nanomaterials is likely to deviate from continuum behaviour emphasising the necessity of acoustic modelling at the nanoscale using non-continuum methods. An examination of the physical phenomena that are likely to be relevant for simulating acoustic wave propagation in the presence of CNTs revealed that the modelling of such a system would be a multi-physics problem involving heat transfer and dynamic interaction of particle vibrations. A study of various particle approaches of non-continuum methods indicated that molecular dynamics (MD) is the method best suited to simulate and study the acoustic absorption of CNTs at the nanoscale. A survey of previous molecular simulations demonstrated that the MD simulations carried out thus far have not simultaneously accounted for all relevant

aspects of the multi-physics problem required for modelling the acoustic absorption effects of CNTs. Hence, three independent validation studies were performed using MD simulations for modelling a subset of the relevant phenomena, namely fluid/structure interactions, bi-directional heat transfer, and acoustic wave propagation. Each of these MD simulations were performed for a model incorporating Lennard-Jones (LJ) potentials for the non-bonded interactions of gas and CNT atoms and the REBO potential for the CNT, and the results validated against the reference case studies.

A molecular system was then designed to study acoustic wave propagation in a simple monatomic gas in a domain containing a 50 nm-long CNT opposite to the sound source and parallel to the direction of the acoustic wave propagation. The simulation domain was modelled using argon gas as the wave propagation medium, a piston made of solid argon layers as a sound source, and a specular wall as the termination wall. MD simulations were also performed without the CNT present for comparison. The characteristics of the acoustic field were studied by evaluating the behaviour of various acoustic parameters and comparing the change in behaviour with frequency. The attenuation of the acoustic wave was estimated using thermodynamic exergy concepts and compared against standing wave theory and predictions from continuum mechanics. Similarly, the acoustic field characteristics and attenuation due to the CNT were studied using MD simulations incorporating the CNT. A standing wave model, developed for the domain with the CNT present, was used to predict the attenuation by the CNT and verified against estimates from exergy concepts. Comparison of the simulation results for acoustic wave propagation with and without the CNT present demonstrated that acoustic absorption effects in the presence of CNTs can be simulated using the developed MD simulation setup although the degree of absorption was not sufficient for the CNTs simulated to investigate absorption mechanisms. The modelled MD system can also be used to study deviations from continuum theory in the characteristics of high frequency sound. The study suggests that the investigation of absorption mechanisms in nanomaterials can be conducted using the developed platform for MD simulations, however further investigations are required to capture the loss mechanisms involved in the molecular interactions between the acoustic wave and the CNT. Additionally, to permit simulations in the audible frequency range, it is necessary to speed up the computational process by modifying the system model such as by employing a hybrid model with molecular dynamics coupled to a continuum domain.

Declarations

Originality

This work contains no material which has been accepted for the award of any other degree of diploma in any university or other tertiary institution. To the best of my knowledge and belief, this work contains no material previously published or written by another person, except where due reference has been made in the text.

Permissions

I give consent to this copy of my thesis, when deposited in the University Library, being made available for loan and photocopying, subject to the provisions of the Copyright Act 1968.

I also give permission for the digital version of my thesis to be made available on the web, via the University's digital research repository, the Library catalogue, the Australasian Digital Theses Program (ADTP) and also through web search engines, unless permission has been granted by the University to restrict access for a period of time.

Md. Ayub

Acknowledgements

I would like to express my sincere gratitude to all the people that have made a contribution to the work presented in this thesis. Without their generous supports I would have not been able to finish this thesis. I would like to thank my supervisors Associate Professor Anthony Zander, Professor Benjamin Cazzolato, Associate Professor Carl Howard, and Dr David Huang, who in spite of their tremendous work pressure always extended their helping hand whenever I wanted. I am indebted to my supervisors for proof-reading this thesis during their busy schedules and their insightful comments which helped me to improve the overall quality of the work presented in this thesis. I am grateful to my principal supervisor Associate Professor Anthony Zander for providing me the opportunity to work in the beautiful work environment of AVC (Acoustics, Vibration and Control) group, in the school of mechanical engineering at the University of Adelaide. I would also like to acknowledge Anthony for assigning me this challenging project that helped me to learn a completely different side of acoustics engineering especially acoustic modelling using molecular simulation methods. I am indebted to Anthony for his generous financial support through a short-term scholarship and tuition fee waiver during my difficult times when my postgraduate scholarships were expired. I would like to acknowledge the efforts of the people from mechanical workshop who fabricated my experimental rig (impedance tube) and the people from electronics workshop Mr Philip Schmidt, Mr Derek Franklin, Mr Silvio De leso, and Ms Lydia Zhang, who helped me with my experimental work. A special thanks to Dr Erwin Gamboa for providing me the access to Materials lab for using fume hood.

This research was supported under Australian Research Council's Discovery Projects funding scheme (project number DP130102832). I would like to thank Prof. Vesselin Shanov, Dr Noe Alvarez and Prof. Mark Schulz of Nanoworld Laboratories (University of Cincinnati, USA), Professor Stephen Hawkins and Dr Chi Huynh from CSIRO (Commonwealth Scientific and In-

dustrial Research Organisation, Australia) for providing the carbon nanotube samples. I would also like to acknowledge the financial support provided by the University of Adelaide through an International Postgraduate Research Scholarship (IPRS) and an Australian Postgraduate Award (APA).

I am also thankful to my colleagues Jesse Coombs, Alireza Ahmadi, Chenxi Li, Cristobal Gonzalez, Maung Myo and Hywel Bennett for their help and support. I would like to acknowledge Jesse's contribution for helping me to learn the computation issues. The assistance of Mr Hywel Bennett with the experiments is also greatly appreciated. I would also like to acknowledge eResearch SA for computational support and technical help provided by their support team.

A huge thanks to my Bangladeshi friends and brothers Rahul bhai, Tapu Bhai, Milton Bhai, Mahid Bhai, Numan Bhai, Rumman, Manab, Rabiul Bhai, Kingshuk, Hassan, Javed, Suvro, Suzon, Sayem, Rifa, Mashuq, and Nafees for sharing many happy moments, for their company to make my life enjoyable, and tolerating my frustrations while writing my thesis. I am really grateful to you guys for your help, support and encouragement. I would like to express my sincere thanks to Zahid Bhai and Salma Vabhi for their support during my stay in their house.

Finally, my sincere gratitude and thanks to my parents, family members, and friends back in Bangladesh for their sacrifice and endless support during my stay in Australia. I am indebted to my best friend Mohibul Alam for his financial support and other responsibilities he took for my family over the years during my postgraduate studies.

Contents

List of Figures

List of Tables

List of Abbreviations

- AG: Air Gap
- ASTM: American Society for Testing and Materials
- CNT: Carbon Nanotube
- CVD: Chemical Vapour Deposition
- BGK: Bhatnagar-Gross-Krook
- BNT: Boron Nitride Nanotube
- CFD: Computational Fluid Dynamics
- DCV-GCMD: Dual control volume-grand canonical MD
- DPD: Dissipative Particle Dynamics
- DSMC: Direct Simulation Monte Carlo
- DWCNT: Double walled carbon nanotube
- EMD: Equilibrium Molecular Dynamics
- GCMC: Grand Canonical Monte Carlo
- LAMMPS: Large-scale Atomic/Molecular Massively Parallel Simulator
- LBM: Lattice Boltzmann Method
- MD: Molecular Dynamics
- MWCNT: Multiple walled carbon nanotube.
- NEMD: Non-Equilibrium Molecular Dynamics
- PBC: Periodic Boundary Condition

- PCA: Principal Component Analysis
- PU: Polyurethane
- REBO: Reactive Empirical Bond Order
- RW: Rigid Wall
- SCCM: Standard Cubic Centimetres per Minute
- SEM: Scanning Electronic Microscopy
- SPC: Simple Point Charge
- SRD: Stochastic Rotational Dynamics
- ST: Substrate
- SWCNT: Single walled carbon nanotube
- TBC: Thermal Boundary Conductance
- TBR: Thermal Boundary Resistance
- TEM: Transmission Electron Microscopy
- TNA: Titania Nanotube
- VMD: Visual Molecular Dynamics
- WCA: Weeks-Chandler-Andersen

1 Introduction

1.1 Motivation

Advances in nanotechnology have provided acoustic researchers with a number of new materials comprising nanofibres or nanopores that can potentially be implemented as acoustic porous absorbers. The molecular behaviour of these new nanoscopic materials may have a significant influence on their sound absorption; in addition, their properties could play an important role in reducing the absorber thickness compared with currently available materials. However, the absorption mechanisms of nanoscopic fibres are not fully understood and the application of numerical and analytical modelling methods to this problem is still at an early stage. While the various mechanisms of sound absorption are currently well understood for conventional porous acoustic materials having particle diameters or pores at the microscale (down to 1 μm), the relative influence of the various mechanisms are expected to change for materials with pores or fibres at the smaller nanoscale (down to 1 nm), while other mechanisms and non-linear effects may also have a significant influence. In order to investigate the absorption mechanisms for nanoscale materials, the flow and acoustic propagation within and around nanotube acoustic absorber will need to be modelled using analytical or numerical approaches appropriate to the nanoscale. The current research aims to implement an accurate simulation method to model the acoustic absorption mechanisms of carbon nanotubes (CNTs).

1.2 Noise Control using Nanomaterials

Noise is a common problem in almost every engineering application incorporating a mechanical device or fluid motion that can act as a noise generating source, such as home appliances, engine vibration, buildings, vehicles, and aircraft (Crocker and Arenas 2007; Arenas and Crocker 2010). An effective technique for limiting noise to an acceptable level is to block the sound trans-

mission path and absorb the sound energy using acoustic porous absorbers. Passive noise control using porous materials is common and is popular because of its easy application and economic viability (Crocker and Arenas 2007; Arenas and Crocker 2010). Porous materials can also be used as structural materials; and simultaneously, can provide the necessary aesthetics for the designed device. There are, however, growing health concerns associated with material handling of conventional porous materials such as fibreglass and wool (fibre shedding), foam (toxic fumes released when burnt) and minerals (aspiration of particles). The large material thicknesses necessary for applications requiring low-frequency absorption make current porous materials an incomplete solution for noise control engineering. The use of porous materials for sound absorption in light-weight applications such as aircraft and automotive vehicles has also been reported as inappropriate (Arenas and Crocker 2010), when all the engineering design criteria are taken into consideration.

Numerous research studies have been conducted to introduce new materials and methods for noise control engineering (Hong et al. 2007; Robinson 2008; Leroy et al. 2008). Most have either been concerned with material handling and global resource factors, and therefore endeavour to introduce natural and recyclable materials (Hosseini Fouladi et al. 2011; Nick et al. 2002; Asdrubali 2006), or suitability for structural applications (light-weight, mechanically strong, wide band absorption, etc.). Thus they have attempted to develop novel acoustic absorbers using advanced materials which can also be used as structural materials (Robinson 2008). Careful consideration of the health hazards associated with CNTs and taking preventive measures during the manufacture of the advanced material can address health and environmental concerns. Thus, if the same material used for structural construction (for aircraft, vehicles, appliances, mufflers, buildings etc.) can also simultaneously act as an acoustic absorber, it will reduce the requirement of additional material, and hence the space and cost (Robinson 2008; Leroy et al. 2008). It is anticipated that developing a carbon nanotube (as shown in Figure 1.1) acoustic absorber could fulfil that vision, as it has already been widely considered as an ideal form of fibre with extraordinary mechanical and thermal properties perfectly suited for structural applications (Endo et al. 2008). Currently, three different kinds of nanotube are available that can form nanoscopic fibres: carbon nanotube (CNT) (Iijima 1991; Koziol et al. 2007), boron nitride nanotube (BNT) (Cohen and Zettl 2010) and titania nanotube (TNA) (Peng et al. 2005).

Following the discovery of the carbon nanotube (CNT) structure by Iijima (1991), CNTs have been used in a number of bulk applications such as

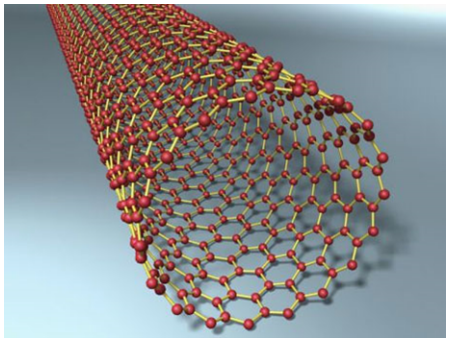

(a) Artist's impression of a CNT (Jha 2009).

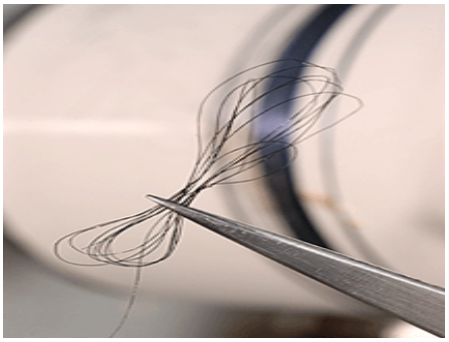

(b) CNT yarn (Toon 2004).

Figure 1.1: Images of carbon nanotubes (CNTs).

mechanical stabilisers in batteries and for electrostatic discharge in plastics (Endo et al. 2008). Consequently, numerous potential applications for CNTs have been suggested in electronics, energy, mechanical and field emission applications (Endo et al. 2008; Ajayan et al. 2006). Some development has already commenced by commercial manufacturers such as Intel, IBM, AMD, UMC, TSMC and NASA (Endo et al. 2008). However, CNTs have not been widely used as sound absorbers, although applications of CNTs in noise control engineering have been suggested (Ajayan et al. 2006). For instance, a light-weight CNT foam was fabricated utilising the extraordinarily strong inter-tube interactions between carbon nanotubes, which could be used as a shock-absorbing and acoustic-damping material (Ajayan et al. 2006). Recent developments in nanotechnology are also providing the opportunity to construct uniform CNT structures aligned in the same direction as the tubes (i.e. vertical or horizontal), which allows the creation of structures with various desired orientations of the fibres (CSIRO 2005; Yang et al. 1999; Huang et al. 2000). These developments in nanotechnology offer exciting possibilities for acoustic absorbing materials that are more compact and effective than conventional porous absorber materials.

Carbon nanotubes can be produced that have an average diameter in the range of 3 to 50 nm and an average length of 10 µm to hundreds of micrometres (Seetharamappa et al. 2006). Having fibres at the nanoscale will also provide the ability to produce absorbers with nanopores (Ajayan et al. 2006). In general, for absorber materials, the smaller the diameter of the fibre, the greater the acoustic absorption, as the reduction of the fibre diameter results in more fibres to achieve the same volume density for the same thickness, which creates a more tortuous path and higher airflow resistance

(Sun et al. 1993; Lee and Sinnott 2003; Nor et al. 2010). Moreover, thin fibres can move more easily than thick fibres in the presence of sound waves, which induces vibrations in air and increases airflow resistance by means of friction through the vibration of the air particles (Nor et al. 2010). Hence, absorbers with thin fibres can provide enhanced acoustic absorption at low frequency for a given absorber thickness.

The particular arrangement of the fibres in the constructed material will allow flexibility in choosing the desired absorption characteristics. In addition, the most important physical property of a porous material is the flow resistivity, which has significant control over the absorption performance of an acoustic absorber. However, flow resistivity is considerably affected by the porosity of the material, and thus the pore size of the material. Hence, small pores that are sufficiently large to allow the propagation of sound waves may have a substantial impact on the absorption characteristics of the material. Moreover, open cell structures (or pores) within a porous material can play a role in guiding the propagation of sound waves and causing effective acoustic absorption. Advanced technology for nano structures will facilitate the tailoring of open cell structures in an array of CNT (Ajayan et al. 2006; Cho et al. 2014a; Cho et al. 2014b). Figure 1.2 shows the vertical arrangement of a CNT array and an open cell structure of a CNT foam from Ajayan et al. (2006). The open pores of the cell structures together with the

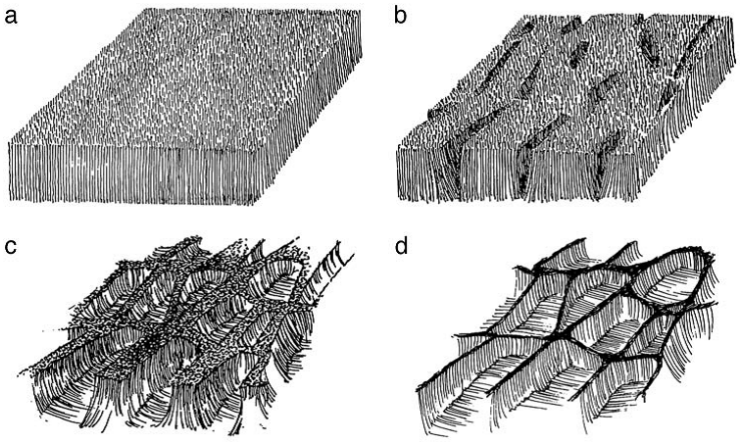

Figure 1.2: Schematic illustrating the formation of cellular structures in carbon nanotube films in four stages of processing. (a) Film composed of vertically aligned carbon nanotubes. (b) Formation of cracks during evaporation of liquid from the nanotube film. (c) Shrinkage of the array and bending of nanotubes resulting in formation of open cellular structures. (d) Final cellular structure. Images from Ajayan et al. (2006).

individual nanopores of the tubes could have a significant influence on the enhancement of acoustic absorption of a CNT absorber. However, very limited measurements of the acoustic properties of nano-materials such as CNTs have been reported. The investigation of the vibro-acoustic absorption mechanisms of CNT arrays will guide the development of effective acoustic absorbers that makes use of various arrangements of carbon nanotubes including cellular structures. For instance, some recent improvements in the fabrication of CNT absorbers with various CNT forest densities can be seen from Figure 1.3 (Cho et al. 2014a; Cho et al. 2014b). These results suggest that advances in CNT fabrication will allow the structure and arrangement of CNTs to be optimised for absorption applications.

Finally, investigation of the absorption characteristics of carbon nanotubes will potentially lead to the creation of advanced acoustic absorbers, which could be implemented to reduce noise emissions and to keep the noise levels within a human tolerable limit. Therefore, in a broad sense, this research will contribute to the general health and well-being of mankind, because noise-induced hearing loss, annoyance, sleep disturbance, and activity interference are considered to affect more people than any other illness or accident, according to the World Health Organization (WHO 2010; WHO-Europe 2011).

1.3 Overview of the Research

A fundamental understanding of the physical mechanisms associated with the use of nanotubes acting as acoustic absorbers and their potential benefits has not as yet been developed. Development of this understanding will advance the knowledge base of the discipline, and will also allow a number of novel arrangements for acoustic absorbers to be investigated. However, no one has described the acoustic propagation mechanisms for the range of characteristic dimensions of nanoscopic fibres, although a few researchers have attempted to demonstrate fluid flow behaviour in channels and pipes in the micro- and nano-scale range (Beskok and Karniadakis 1999; Niu et al. 2004; Karniadakis et al. 2005; Ansumali et al. 2006; Zhang 2011).

The mechanisms of sound absorption for conventional porous acoustic materials have been described by a number of researchers (Mechel and Ver 1992; Ingard 1994; Bies and Hansen 2003; Fahy 2005), and are associated with the propagation of air molecules within the pores or interstices in the material, and the interaction of the sound with the structure of the material. Viscous losses are associated with friction of the air molecule oscillations within the pores, as well as the loss of momentum caused by the changes in

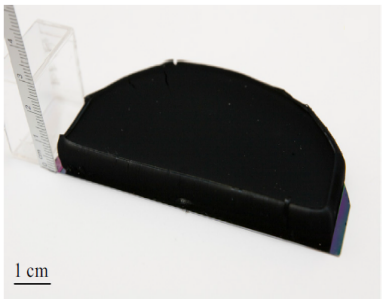

(a) 12 mm long CNT array.

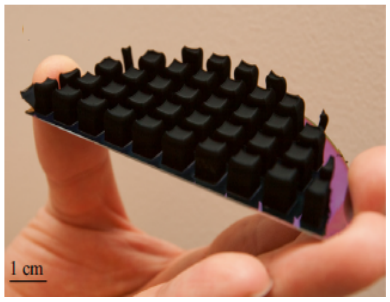

(b) Patterned CNT array.

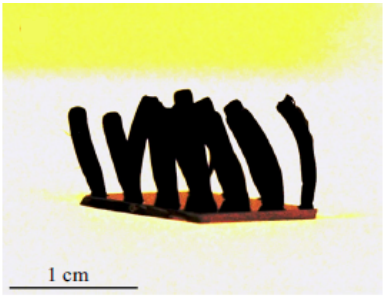

(c) CNT arrays with 1 mm diameter posts.

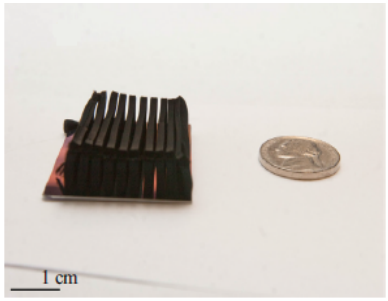

(d) 2 mm thick rectangular CNT arrays consisting of multiple tiles.

Figure 1.3: Various shapes of CNT arrays grown for different applications at the University of Cincinnati (UC). Figures from Cho et al. (2014a), by collaborators in Nanoworld laboratories at University of Cincinnati, USA.

flow direction and expansion and contraction of the air as it passes through the irregular arrangement of pores in the material. Heat conduction from the air to the absorber material is also responsible for thermal losses. The forced mechanical oscillation of the frame or structure of the porous material is also responsible for losses in some instances. However, the size of the thermal and viscous boundary layers relative to the characteristic dimensions of the material and the wavelength of the sound of interest will be significantly different for nanoscale acoustic absorber structures. In addition, nanotubes have been shown to be highly flexible (see for example CSIRO (2005)), so the interaction of sound waves with nanotubes is expected to be significantly different to that with the relatively rigid glass and mineral fibres commonly used in conventional absorber materials. Thus, models are required that account for these effects (Beltman 1999).

The controlling parameters of acoustic absorption for structures at the nanoscale will differ from those of conventional absorber materials. Developing an applicable analytical framework will involve extending the application

of the current theory for fibrous acoustic materials from the microscale (for example, synthetic fibre diameters of $2 \sim 25$ μm and natural fibre diameters of $8 \sim 38$ μm (Arenas and Crocker 2010)) to the nanoscale. Because the length scales of nanotubes (CNT: diameter 3 to 50 nm; BNT: diameter 10 to 80 nm;TNA: diameter 20 to 100 nm) are of the same order as the mean free path (65 nm) of particles in air at ambient temperature and pressure, the commonly used acoustic assumptions, such as continuity, are invalid. In addition, viscous effects which are assumed negligible in deriving the wave equation for acoustics will be important for nanotube acoustic absorbers. Modelling flow and acoustic propagation within a nanotube acoustic absorber will thus require the application of analytical or numerical approaches appropriate to the nanoscale such as the Lattice Boltzmann Method (Karniadakis et al. 2005), Direct Simulation Monte Carlo (Bird 1994) or Molecular Dynamics (MD) (Allen 2004; Frenkel and Smit 2002). These methods have successfully been applied to modelling nonlinear acoustic wave propagation (Hadjiconstantinou and Garcia 2001; Danforth and Long 2004a; Hanford and Long 2007). It is likely that the thermal interactions between the nanotubes and the fluid will also need to be considered.

In continuum models, internal flow properties such as density, velocity, pressure and temperature are usually considered to be constant or follow a linear relation and change according to well-defined theoretical and empirical relations (Hanford 2008). However, such assumptions are not always valid in the case of real gases confined in a small channel at the nanoscale (Czerwinska 2009). Quantification of the validity of continuum models and deviation from this behaviour can be established by a non-dimensional parameter known as the Knudsen number, $Kn = \frac{\lambda_{\text{mfp}}}{H}$, which is a ratio of the molecular mean free path (λ_{mfp}) and characteristic length scale (H). For $Kn = 0$ to 0.001, the medium is considered to be in the continuum regime. However, for $Kn \geq 0.1$ the continuum approximation is considered to be invalid (Czerwinska 2009; Hadjiconstantinou 2002). Flows can also be classified more specifically according to their Knudsen number using the different features of the flow regimes. For instance, in $0.001 < Kn < 0.1$, the regime is known as the slip flow regime (Karniadakis et al. 2005); and for $0.1 < Kn < 10$, the regime is regarded as the transition regime, which represents the transition between diffusive (continuum) and ballistic (free molecular flow) molecular behaviour (Hadjiconstantinou and Garcia 2001; Hadjiconstantinou 2002). For the nanoscale structures of CNTs, acoustic waves are propagating in air (a polyatomic gaseous media), and the flow is through (and around) cylindrical channel nanotubes. The average molecular free path of air at

STP, which is 65 nm (Karniadakis et al. 2005) and the average diameter of the tube, which is between 50 to 100 nm (maximum values considered), should be considered for the relative values of Knudsen number. Thus, the characteristic scale is comparable to the molecular mean free path, which places sound propagation in a transition flow regime (for CNT: $Kn = \frac{65}{50} = 1.3$), as exhibited in Figure 1.4. Molecules thus have the possibility to collide with the nanotube walls more frequently than between themselves (Czerwinska 2009). Therefore, surface effects will be dominant and, depending on the wall boundary condition, the flow behaviour will be modified by interactions with the wall and rarefaction of the medium, and hence tend to exhibit large flow disturbances and complex physical effects; thus continuum assumptions will be invalid (Czerwinska 2009; Prasanth and Kakkassery 2006). In this case, the Boltzmann equation of kinetic theory should be applicable; in order to solve this equation, particle collision simulation techniques should be considered. In other words, the value of the Knudsen number for air flow in nanoscopic fibres indicates that particle-based non-continuum approaches such as the Lattice Boltzmann Method (LBM), Direct Simulation Monte Carlo Method (DSMC) and Molecular Dynamics (MD) method should be implemented for the investigation of the flow behaviour.

In addition, in situations in which the non-continuum (non-equilibrium) effects cannot be neglected, the velocity distribution function is a very important quantity for identifying deviations from continuum behaviour. At thermodynamic equilibrium, the velocity distribution function of gas molecules,

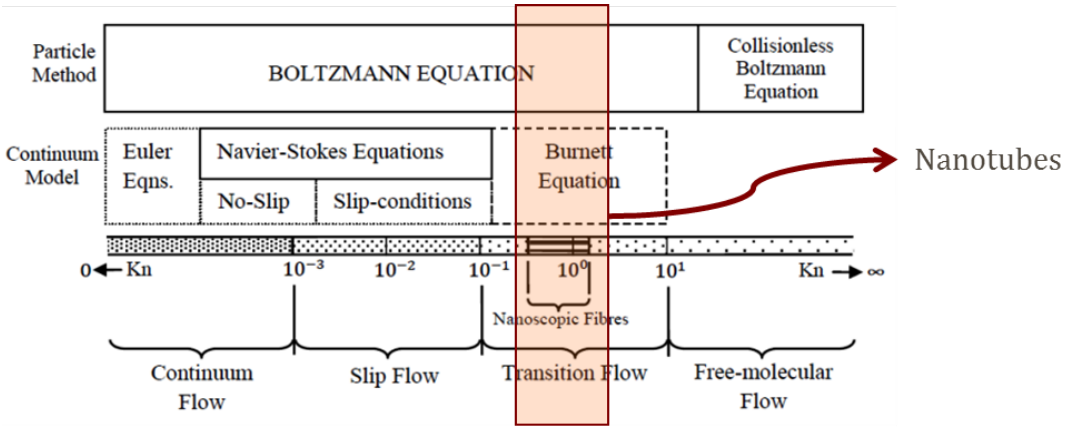

Figure 1.4: Applicability range of the models based on Knudsen number (Adapted from Ivanov et al. (2007); Hanford (2008)).

f_M, is Maxwellian with a distribution of the form (Karniadakis et al. 2005)

$$f_M = \frac{\rho}{2\pi RT^{3/2}} \exp\left[-\frac{(\xi - u)^2}{2RT}\right], \tag{1.1}$$

where R is the universal gas constant, T is the temperature and ξ is the molecular velocity. In the case where the temperature T, the velocity u, and the density ρ are functions of x and t, the velocity distribution function, defined by (Karniadakis et al. 2005)

$$f_{loc}(x, \xi, t) = \frac{\rho(x,t)}{2\pi RT(x,t)^{3/2}} \exp\left[-\frac{(\xi - u(x,t))^2}{2RT(x,t)}\right], \tag{1.2}$$

is referred to as being locally Maxwellian. The continuum theory assumes that (i) as discussed earlier, the Knudsen number is sufficiently small compared with unity, (ii) the velocity distribution function f_M is locally Maxwellian with a distribution given by f_{loc}, and (iii) the difference between f_M and f_{loc} is of the order of the Knudsen number (Karniadakis et al. 2005). Hence, the deviation of the velocity distribution function from the local Maxwellian also needs to be checked to ensure the validity of the continuum theory for the phenomena concerned.

Overall, the following specific research gaps can be identified based on the discussion that has been provided in the previous sections:

- The mechanisms of acoustic absorption in CNTs have not been investigated in previous research.
- Application of numerical and analytical modelling methods to this problem is still at an early stage.
- Acoustic flow simulation has not been conducted to model acoustic absorption effects of nanomaterials using non-continuum (molecular) methods.
- Experimental results are not available for the acoustic characteristics of CNT absorbers.

1.4 Research Scope

The current research aims to implement an accurate simulation method to model the acoustic absorption mechanisms of carbon nanotubes. In general, the practical realisation of an acoustic absorber would be formed by

thousands of nanotubes in an array grown on a substrate with various arrangements such as vertical/horizontal alignment of the tubes. Figure 1.3a shows an example CNT porous absorber formed from a vertical array of nanotubes grown on such a substrate. To investigate and understand the absorption mechanisms in this structure it is necessary to develop a sequential modelling scheme which will describe the various acoustic absorption mechanisms. For instance, Figure 1.5 exhibits a schematic of a model for vertically aligned (with the substrate) nanotubes (CNT forest with millions of nanotubes per square centimetre grown on a silicon substrate), which shows a simplified representation of the physical system for the interaction of sound waves within the tubes and also between the tubes. However, in order to understand the interaction of multiple tubes with acoustic waves, it is first necessary to reveal the sound wave propagation behaviour around a single tube, as the sound absorption by each tube is also expected to contribute significantly to the total absorption.

Therefore, the research presented in this thesis intends to model the acoustic absorption effects of a CNT considering only interactions between the acoustic wave and outer surface of the CNT. A suitable particle-based non-continuum approach must be chosen to model the sound propagation and absorption effects of the CNT, in order to simulate the likely phenomena associated with the interactions between the acoustic wave and the CNT at the nanoscale. In addition, the chosen method must be validated for each phenomenon. Hence, independent studies are required to examine the

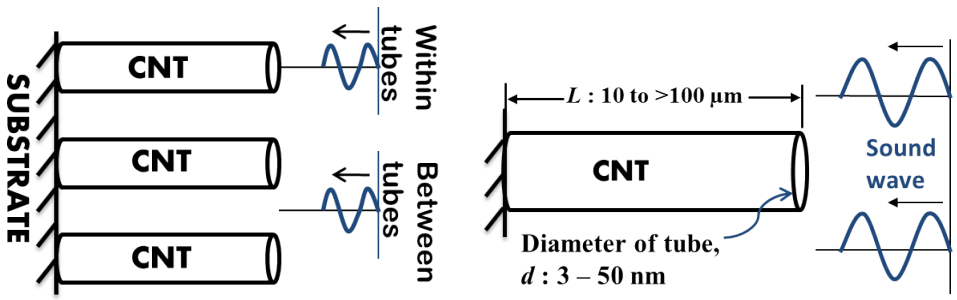

(a) Target modelling stage (b) Current modelling stage

Figure 1.5: Schematics of the modelling (a) as a long term goal showing the arrangement of the multiple tubes for wave propagation (here 3 tubes are shown for illustration) in the target modelling stage, but it is first important to understand the interactions with a single CNT as represented by (b) the scale of the nanotube in the current modelling stage. Interactions of the acoustic wave were limited to the exterior of the CNT at the current stage.

physical phenomena likely to be involved in acoustic interactions between the gas atoms and the CNTs. Consequently, previous studies of non-continuum methods must also be identified that represent the phenomena associated with the acoustic interactions of the CNT. Moreover, simulations must be performed for sound wave propagation in a simple medium without and with the CNT present so that a quantitative comparison of the acoustic parameters can be made to distinguish the absorption effects of the CNT from the classical absorption in the propagation medium. Furthermore, an exploratory experimental investigation is needed to characterise the acoustic absorption behaviour of a real CNT acoustic absorber and to identify possible deviations of the absorption behaviour from that of conventional materials. The contributions of this work to the discipline are as follows:

- Experimental results for acoustic absorption behaviour of a CNT forest.
- Theoretical analysis of the measured absorption coefficient of CNTs based on classical absorption mechanisms.
- Understanding of the acoustic flow behaviour of high frequency sound using molecular dynamics (MD) simulations.
- A platform developed to perform MD simulations of sound wave propagation in a gas.
- Quantification of sound attenuation in a conservative MD system.
- The first application of MD for simulating acoustic absorption effects of a gas and a CNT.

1.5 Chapter Outline

This thesis is divided into eight chapters. Chapter 1 describes the research undertaken in this thesis, the current state of the research, the research gaps and the motivation behind the work performed in this study. Chapter 2 presents a literature review of the previous studies in this field. This chapter also provides justification for the numerical methods and tools used in this study. Chapter 3 presents the exploratory experimental investigation of the acoustic absorption properties of carbon nanotubes. Chapter 4 describes the methodology used for the numerical studies and the implementation of the numerical methods at the nanoscale. Chapter 5 outlines the cases examined to validate the numerical results. Chapters 6 and 7 present the numerical results from the study of sound wave propagation in a simple monatomic gas

without and with the CNT present in the simulation domain, respectively. Finally, Chapter 8 summarises the conclusions from the research presented in this thesis and describes the achievements of this study. This chapter also presents an outlook of possible further work.

2 Literature Review

2.1 Introduction

In this chapter, a literature review is presented that provides an overview of potential approaches for the exploration of acoustic absorption mechanisms of nanofibres. It demonstrates the necessity of non-continuum particle-based simulation for the current problem (as highlighted in Chapter 1). The review is focused mainly on the application of non-continuum particle based approaches such as the Lattice Boltzmann Method (LBM), Direct Simulation Monte Carlo (DSMC) and the Molecular Dynamics (MD) method. In addition, a detailed description is presented of the numerical methods that have been implemented for various micro- and nano-scale analyses of relevance to the acoustics of nanotubes. Moreover, a comparison of the modelling approaches based on their advantages, disadvantages and limitations, provides the basis to choose an accurate simulation method for the flow simulations of carbon nanotubes.

Furthermore, at the beginning of the review, previously explored absorption mechanisms (classical and microscopic) for conventional porous materials are introduced to demonstrate how sound is absorbed in a fluid medium at the boundary interface. Both mechanisms were developed based on two important branches of classical mechanics: continuum mechanics and kinetic theory. Understanding the classical mechanisms is important for developing an understanding of absorption mechanisms at the nanoscale.

2.2 Nanoscopic Fibres: Carbon Nanotubes

Carbon nanotubes belong to a family of carbon allotropes named Buckminster fullerenes because of the resemblance of the molecule to the architect and scientist Buckminster Fuller's geodesic domes. They were only discovered in 1985 (Kroto et al. 1985). The first described fullerene was spherical, and is referred to as a buckyball. Six years later, a cylindrical fullerene was

discovered (Iijima 1991). It is known as a buckytube, or carbon nanotube (CNT), a one-atom thick wall of graphene rolled up into a seamless cylinder with a diameter of the order of a nanometre (50,000 times smaller than the width of a human hair). These hollow fibres of pure carbon display extraordinary properties including high resistance to heat, high ductility, high tensile strength, high electrical conductivity and a relatively low chemical reactivity. Many of their properties are still being explored and novel ways in which these nanoscale structures can be used are being discovered at an astounding rate.

A typical carbon nanotube structure has characteristic dimensions on the order of nanometres. In general, carbon nanotubes are produced in a bundle of tubes with an average tube diameter that varies from 3 nm to 50 nm and an average length from 10 µm to hundreds of micrometres (Seetharamappa et al. 2006). A carbon nanotube is formed by folding a single graphene sheet to form a hollow tube composed of carbon hexagons (Natsuki et al. 2004). Based on the number of rolled up graphene layers, carbon nanotubes can be divided into two groups: single-walled carbon nanotubes (SWCNTs) and multi-walled carbon nanotubes (MWCNTs). An illustration of the structure of a SWCNT is presented in Figure 2.1. The periodically repeating hexagon pattern of carbon atoms in space is a major feature in the structure of carbon nanotubes (CNTs) (Ruoff et al. 2003). Each atom in the hexagon pattern is covalently bonded to three neighbouring atoms. The hexagon structure is formed mainly due to the sp^2 hybridisation process (Brown et al. 1999) which combines one s-orbital and two p-orbitals to form three hybrid sp^2-orbitals at 120° to each other within a plane (Ruoff et al. 2003). Mixing between the sp^2-hybridised orbitals on adjacent carbon atoms produces a σ-bond. In addition, a relatively weak and out-of-plane bond known as a π-bond is also

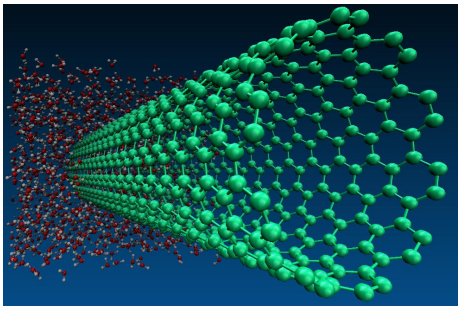

Figure 2.1: Molecular structure of a (10,10) single-walled carbon nanotube. The structure was drawn using "nanotube builder", a plugin of VMD (Visual Molecular Dynamics) software.

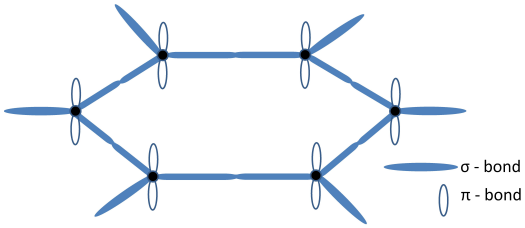

Figure 2.2: Basic hexagonal bonding structure (Ruoff et al. 2003) for one graphite layer (the 'graphene sheet'). Carbon nuclei shown as filled circle, out-of-plane π-bonds and σ-bonds connect the C nuclei in-plane. Figure adapted from Ruoff et al. (2003).

formed between the additional unhybridised p-orbital on each carbon atom. Figure 2.2 shows the basic hexagonal bonding structure in a graphene sheet. The covalent bond is responsible for the impressive mechanical properties of CNT's and the π-orbitals contributes to the interaction between the layers in multi-walled carbon nanotubes (MWCNTs) (Ruoff et al. 2003).

A convenient and widely used approach to classify the types of SWCNTs is by representing them in terms of their helicity (Dresselhaus et al. 1995; Natsuki et al. 2004), the direction in the hypothetical graphene sheet is rolled up to form the nanotube (Ruoff et al. 2003). They can be identified in terms of a pair of integers (n,m), corresponding to a lattice vector $\mathbf{C_h}$ on the graphite plane. The lattice vector $\mathbf{C_h}$ is expressed as a linear combination of unit vectors $\mathbf{a_1}$ and $\mathbf{a_2}$ oriented along the unit hexagonal cell of the two-dimensional graphene sheet (Natsuki et al. 2004). Following the notation in Dresselhaus et al. (1995), Ruoff et al. (2003), and Natsuki et al. (2004) and Figure 2.3, it can be written as

$$\mathbf{C_h} = n\mathbf{a_1} + m\mathbf{a_2}, \tag{2.1}$$

where the integer pair (n,m) determines the categories of carbon nanotubes. The groups of SWCNTs are denoted by the following three categories of tubes (Ruoff et al. 2003; Natsuki et al. 2004):
$m = 0$: 'zigzag',
$m = n$: 'armchair',
other: 'chiral'.

The integers (n,m) also uniquely determine the size of the nanotubes. The length L_c of the chiral vector $\mathbf{C_h}$ (the circumference of the nanotube) can be determined as (Dresselhaus et al. 1995; Natsuki et al. 2004)

$$L_c = |\mathbf{C_h}| = \sqrt{3}a_{\text{C-C}}\sqrt{n^2 + m^2 + nm} \tag{2.2}$$

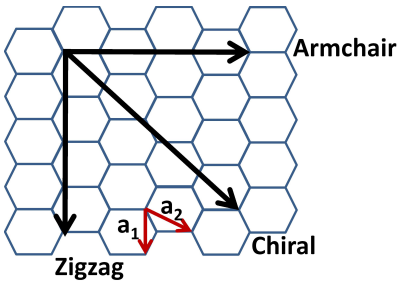

Figure 2.3: The chiral or lattice vector as a linear combination of unit vectors $\mathbf{a_1}$ and $\mathbf{a_2}$. Figure adapted from Ruoff et al. (2003)

where $a_{\text{C-C}}$ (= 1.421 Å) is the carbon-carbon bond length.

The diameter d_c of the nanotube can be evaluated as (Dresselhaus et al. 1995; Natsuki et al. 2004)

$$d_c = \frac{L_c}{\pi} = \frac{\sqrt{n^2 + m^2 + nm}}{\pi} \sqrt{3} a_{\text{C-C}}. \tag{2.3}$$

Considering the effective wall thickness t_c of the SWCNT, the effective diameter d_{ce} is defined as (Natsuki et al. 2004)

$$d_{ce} = \frac{\sqrt{n^2 + m^2 + nm}}{\pi} \sqrt{3} a_{\text{C-C}} + t_c. \tag{2.4}$$

As mentioned earlier, MWCNTs are formed by multiple layers of graphite rolled in on themselves to form a tube shape and they have an interlayer spacing of ∼3.4 Å (Seetharamappa et al. 2006; Ruoff et al. 2003; Saito et al. 1993; Zhou et al. 1994). Hence, MWCNTs are essentially nested SWCNT shells as shown in Figure 2.4 (Ruoff et al. 2003). The outer diameter of MWCNTs may range from 1 nm to 50 nm, while the inner diameter is usually several nanometres (Seetharamappa et al. 2006). The number of layers N_c and the effective cross-sectional area A_{ce} can be represented in terms of the innermost and outermost diameter d_{ci} and d_{co} of the tubes as (Natsuki et al. 2004)

$$N_c = 1 + \frac{d_{co} - d_{ci}}{2h} \tag{2.5}$$

and

$$A_{ce} = 2\pi t_c \left\{ \frac{N_c d_{ci}}{2} + \sum_{i=1}^{N_c} (i-1)h \right\} \tag{2.6}$$

respectively, where h is the distance between layers of the MWCNT.

SWCNTs can have either open ends or closed ends by capping each end of the open tubes with half of a fullerene (C_{60}) molecule (Dresselhaus et al.

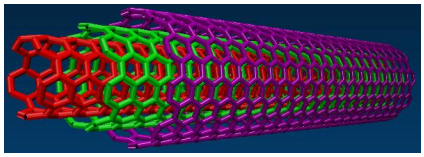

Figure 2.4: Molecular structure of a multi-walled carbon nanotube. The structure was drawn using "nanotube builder", a plugin of VMD (Visual Molecular Dynamics) software.

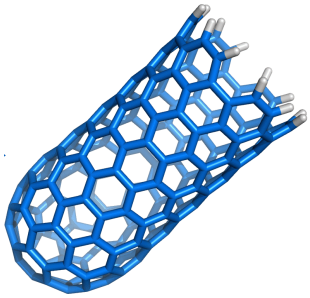

Figure 2.5: Schematic of a closed cap single-walled carbon nanotube[1].

1995; Ruoff et al. 2003). Figure 2.5 shows an example of a closed-end SWCNT capped with a fullerene molecule. It has been suggested that closed-end CNTs should have a diameter larger than the (5,5) and (9,0) tubes to have stable closed ends (Ruoff et al. 2003; Fujita et al. 1992; Dresselhaus et al. 1996; Dresselhaus et al. 1993).

2.3 Acoustic Absorption Mechanisms

Classical acoustic absorption mechanisms have been described by a number of researchers such as Mechel and Ver (1992), Ingard (1994), and Bies and Hansen (2003). The following description of the classical absorption mechanism for wave propagation through a narrow channel is based on the book by Ingard (2009). For a nanoscale wave propagation domain such as one containing CNTs, it is necessary to also understand the microscopic contributions to the absorption mechanism, as absorption deviates from the classical mechanism and occurs via the interactions of molecules. Therefore, a brief description of the sound absorption mechanism in a gas on a molecular level is also included based on the book by Fahy (2005), which follows the classical method but considers molecular interactions as well.

[1] http://oasys2.confex.com/acs/235nm/techprogram/images/1146216-0.gif

2.3.1 Classical Sound Absorption Mechanism in a Narrow Channel

Acoustic absorption occurs in a channel during sound wave propagation largely due to acoustic power dissipation at the bounding surfaces via viscous and thermal losses. Viscous loss, which is proportional to the square of the velocity amplitude tangential to the boundary, occurs due to the shear stress in the viscous boundary layer. Thermal loss, which is proportional to the square of the pressure amplitude at the boundary, occurs due to heat conduction in the thermal boundary layer (Ingard 2009).

The viscous boundary layer is produced by the change in the tangential velocity from zero at the wall (as imposed by viscosity with the assumption of the no-slip condition) to the free stream value far away from the wall. This viscous interaction with a solid boundary (interaction force on the wall and the corresponding reaction force on the fluid) involves a force component proportional to the velocity and a component proportional to the fluid acceleration due to the inertia of the oscillating flow. The thickness of the viscous boundary layer increases with shear viscosity, and decreases with frequency and density.

The thermal boundary layer is developed by the change in the temperature gradient during the transition of a fluid element (wave propagating media) from the isothermal condition at the wall to the isentropic (adiabatic) condition far from the wall. Sound wave propagation in a free field, far from the boundaries, produces a temperature fluctuation due to the isentropic (adiabatic) compression and rarefaction in the wave. On the other hand, the significant heat conduction and heat capacity of the solid compared with the air prevents temperature fluctuations at the wall and creates an isothermal condition. In both of these regions (isothermal at wall and isentropic at free field), during a compression, the pressure of a fluid element and the velocity at the surface of a volume element will be 90 degrees out of phase. Therefore, during the pressure increase, no net work will be done in one period of harmonic motion. However, the velocity and pressure will not be out of phase within the thermal boundary layer where the conditions are neither isothermal nor isentropic (Ingard 2009). This will allow a compression leading to a delayed heat leakage from the sound field into the gas and then via conduction into the boundary, due to diffusion in the air into the boundary (Ingard 2009).

Based on the above discussion, it can be understood that heat conduction is an important and substantial factor in acoustic energy dissipation in acoustic channel flow. CNTs have low thermal conductivity and heat capacity,

which indicates that the temperature of the wall will increase rapidly during the compression of the gas. This will produce a temperature fluctuation at the boundary which prevents an isothermal condition, violating the assumed classical behaviour of acoustic wave propagation in a narrow channel. Therefore, a different heat transfer mechanism for wave propagation is expected in this case.

2.3.2 Microscopic Sound Absorption Mechanism in Gases

Sound energy in gases is dissipated by a combination of viscous and heat conduction processes as discussed in the previous section describing the classical mechanism. In microscopic phenomena, it is observed that the molecular relaxation loss mechanism dominates substantially for diatomic or polyatomic gases (Fahy 2005). Sound absorption occurs due to the fluctuation of the fluid motion and heat conduction to the solid wall, which generates viscous and thermal boundary layers at the surface of the solid. According to the molecular bases of these boundary layer phenomena, viscosity is developed due to the existence of shear stress in fluids and the changing shear rate, which can be attributed to the discontinuity of the tangential velocity of the molecules at the interface layer of the media and the continuous variation of the tangential velocity with distance from the interface (Fahy 2005).

In the presence of a rigid surface at the boundary of a gas flow, the surface shear stresses exerted on the fluid by the solid surface arises from the interaction between the molecules of the two media. Due to the attractive forces of the wall molecules, when fluid molecules approach near to the solid surface, they are captured and dwell or stick in the vicinity of the point of impact for a brief period before leaving. During that time, an energy exchange may occur between the fluid and solid molecules, which causes a change of momentum upon the impacting molecules and generates skin friction drag on gases moving past the static wall surfaces. Subsequent collisions between the gas molecules that have not impacted the surface and the released molecules from the impacted surface tend to reduce the relative mean velocity between the gas and the solid, which can be attributed to the action of a stress component tangential to the surface known as the shear stress (Fahy 2005). These effects result in a variation of the mean flow velocity from zero at the surface and the free stream velocity in the centre of the channel or the flow that is unaffected by the surface interaction. This region forms the viscous boundary layer with the presence of the surface interaction effect within that region. The presence of this field causes a viscous loss of sound energy as the viscous stresses oppose the fluid motion and dissipate

the fluid kinetic energy into heat (Fahy 2005).

Another form of energy conversion occurs during sound wave propagation caused by thermal/molecular diffusion and molecular relaxation in the case of diatomic or polyatomic gases. The thermal diffusion process can be attributed to the heat flow that occurs in the acoustic wave, where a proportional change in the temperature gradient exists between the regions of periodic and simultaneous compression and rarefaction of the gases. In the compression region, the pressure, temperature and density temporarily increase and simultaneously decrease in the regions of rarefaction. The weak flow of heat during this process is irreversible, leading to a loss of sound energy (Fahy 2005).

The molecular relaxation effect can also cause loss of sound energy in diatomic or polyatomic gases. In general, relaxation is an effect related to the delay between the application of an external stress to a system and its response (Faller, 2010). During the wave propagation of sound, sudden compression of the gas causes the kinetic energy of the translational motion to increase virtually instantaneously, and raises the pressure, density and temperature. Subsequently some of this energy contributes to the rotational and vibrational energy of the molecules, and the pressure falls. If the pressure oscillations occur rapidly, then the process can be reversible due to the negligible loss of translational energy during expansion. If the compression-expansion cycle is slow, then the process will have sufficient time to reach thermodynamic equilibrium. However, if the pressure fluctuations occur at intermediate frequencies, then a relaxation effect is observed, and a re-adjustment of the equilibrium condition will lag behind the pressure variation within the gas, which will cause some sound energy to be irreversibly lost to the internal energy of the gas (Fahy 2005; Faller 2010).

2.4 Numerical Models: Continuum vs Non-Continuum Methods

Wave propagation in micro- and nano-scale flows is usually characterised by the confinement of the fluid environment (Czerwinska 2009). The hierarchy of mathematical models available to solve such types of fluid dynamics problems can be divided into two groups: continuum and non-continuum methods, despite the varying degrees of approximation (Hanford 2008). Continuum models consider the fluid as a continuous medium, which allows the average bulk properties of the fluid domain to be described at the macroscopic level using physical quantities such as the velocity, density, temperature and

viscosity (Czerwinska 2009). The continuum assumption is valid as long as the characteristic length of the problem is much larger than the mean free path of gas molecules, which can be characterised by the dimensionless Knudsen number Kn (Hanford 2008). It is also a parameter that defines the non-equilibrium or viscous effect of the gas. If the system has a value of $Kn \ll 1$, the continuum assumption is applicable (Hanford 2008). Several engineering applications including acoustics have used this continuum approximation with the implementation of Euler or Navier-Stokes equations for the simulation of flow. However, continuum models have limitations for the approximation of thermal equilibrium, as they consider negligible deviations from equilibrium, which is generally only applicable at the macro scale (Hanford 2008). In the case of nano- or micro-scale modelling, molecules might not even have sufficient time to reach equilibrium for momentum and energy transport due to solid-fluid interactions (Czerwinska 2009). Moreover, for such complex physics, additional equations need to be included to consider non-equilibrium and nonlinear effects which make simulations complicated and computationally costly (Czerwinska 2009). Therefore, there is a need to apply non-continuum methods, preferably via a molecular approach, to understand and consider the influence of the molecules.

In non-continuum methods, which are developed based on molecular models, the state of the gas at the microscopic level is realised by the particle nature of the gas and described by the particle position and velocity in 3D space (Hanford 2008; Czerwinska 2009). A comparison between continuum and molecular approaches is presented in Table 2.1, which is adapted from the literature (Bernsdorf 2008; Hanford 2008; Czerwinska 2009). The limitations and disadvantages of continuum methods as stated in Table 2.1 suggest that continuum models do not have the necessary features for the simulation of phenomena likely to be required to accurately model the acoustic absorption of nanoscale fibres, whereas a non-continuum particle-based simulation approach provides the required capabilities. The comparison indicates that particle-based methods have favourable attributes for solving this kind of flow problem. There are several molecular simulation techniques for computational modelling such as Molecular Dynamics (MD), Stochastic Rotational Dynamics (SRD), Dissipative Particle Dynamics (DPD), Cellular Automata, Lattice Boltzmann Method (LBM) and Direct Simulation Monte Carlo (DSMC) (Czerwinska 2009). In the last two decades, the most popular simulation methods in acoustics and fluid dynamics for channel flow at the micro- and nano-scale have been MD, LBM and DSMC.

Table 2.1: Comparison of continuum and non-continuum particle-based approaches.

Approach	**Continuum approach** (Euler and Navier-Stokes Equations)	**Molecular particle-based approach** (LBM, DSMC, MD etc.)
Features:	• Assumes properties from other theories or experiments and only the motion is simulated (Czerwinska 2009).	• Provides bulk properties as well as the motion at the same time and simulates molecular behaviours in a more realistic way (Czerwinska 2009).
Advantages:	• Continuum models of fluidic systems are very well developed. Therefore computational methods applied for such models are expected to give relatively fast, accurate and predictable results (Czerwinska 2009). • Flow properties follow simple well-defined theoretical and empirical relations which makes it easier to evaluate bulk properties during the simulation.	• Applicable for any kind of flow regime. • Flow properties defined by the molecular behaviour. Hence it can be extended beyond the continuum range. • Simple implementation of boundary conditions.
Disadvantages:	• Additional equations need to be incorporated to simulate complex flow behaviour (Czerwinska 2009). • Requires considerable computational resources during simulation (Hanford 2008). • Numerical instability (Hanford 2008).	• High computational cost, as it requires enormous computational resources significantly higher than that required for continuum simulation. • Difficulty during the simulation of multidimensional flows as it requires large amounts of memory. • Simulation domain has to be kept to a limited characteristic length in order to maintain a reasonable computational time and cost.

Limitations:

- Inability to simultaneously model the following conditions (Hanford 2008):
  - Non-equilibrium conditions
  - Diatomic or polyatomic molecules or gas
  - Nonlinearity
  - Relaxation effect
- Based on continuum assumptions.
- Limited in the range of validity, indicated by the Knudsen number.
- Infinitesimally short time of solid-fluid interactions, which rules out the capability of simulating thermal transportation created by solid-fluid interactions (Czerwinska 2009).
- Some of the methods are limited to predefined collision rules and a particular collision grid or domain such as LBM and DSMC.
- Other methods are limited by the force potential models and the time scale range for collisions such as MD.

LBM has been widely used due to its simplicity, despite some deficiencies in the results, especially in the case of high Knudsen number *transition flow* regimes (see Figure 1.4). On the other hand, DSMC has been used for the simulation of gaseous media more frequently than LBM because it overcomes the errors related to compressibility issues, whereas MD has been applied for the simulation of solids (Mohan and Liang 2008), liquids (Karniadakis et al. 2005), gases (Barisik et al. 2010) and gas mixtures (Kandemir and Sevilgen 2008) with complex flow physics (Maruyama 2002; Karniadakis et al. 2005). Nevertheless, LBM is preferable over MD and DSMC, if both methods are capable of simulating the similar problem, mainly because of LBM's simple collision rules and numerical efficiency. The drawback with MD and DSMC is their large computation time. MD requires more computational time and cost than DSMC, but provides better accuracy than DSMC. A general overview of the various models can be found in papers by Benzi et al. (1992), Chen and Doolan (1998), Succi (2001), Bird (1994), Oran et al. (1998), Karniadakis et al. (2005), Cieplak et al. (2000) and Allen (2004). Following the consideration of continuum versus non-continuum approaches as discussed here, the capability of the simulation method needs to be carefully checked before the particular method is chosen so that it has all the features necessary to simulate physical phenomena that are likely to be important.

2.5 Non-continuum Methods: Molecular Simulation Models

In the following sections, each of the three most commonly used non-continuum particle-based simulation methods is outlined, and their application to problems involving acoustics and micro- and nano-channel flows are discussed. The relative advantages and disadvantages of the methods and their applicability to the problem of interest here are presented in Section 2.7.

2.5.1 Lattice Boltzmann Method (LBM)

The Lattice Boltzmann Method is a mesoscopic approach based on the theory of cellular automata with the Boltzmann equation approximation, which considers the particle distribution on a lattice divided into solid and fluid points (Aaltosalmi 2005; Hanford 2008). During one lattice time step, idealised particles move from one node to another with unit speed and propagate to adjacent lattice points, subsequently redistributing their momentum with predefined simple collision rules for succeeding collisions, which also involves boundary conditions and external forces (if any) at the

solid-fluid interfaces (Aaltosalmi 2005; Hanford 2008). The particle collision rules are replaced by a relaxation term known as the collision operator, which produces the new particle distributions after the collisions (Bernsdorf 2008). The Lattice-Boltzmann equation for the particle density f_i can be written as (Aaltosalmi 2005; Bernsdorf 2008)

$$f_i(r + \lambda c_i, t + \eta) = f_i(r + t) + \Omega_i(r, t), \tag{2.7}$$

where f_i (r, t) is the particle density distribution on a lattice site r at time t with a velocity c_i pointing in the lattice direction i; and λ and η are the lattice spacing and lattice time interval, respectively. The term Ω_i (r, t) represents the collision operator which is a model-dependent term. It is expressed in the lattice BGK (Bhatnagar-Gross-Krook) model (Bhatnagar et al. 1954) as (Aaltosalmi 2005)

$$\Omega_i(r, t) = \frac{1}{\xi}\,[f_i^{(0)}(r, t) - f_i(r, t)], \tag{2.8}$$

where ξ is the relaxation time and $f_i^{(0)}$ is the equilibrium distribution of particles, which can be chosen to produce the required behaviour of the particle. Details of this method along with the derivation of the aforementioned equations can be found in the literature (Aaltosalmi 2005; Bernsdorf 2008; Viggen 2009).

It should also be noted that the LBM is equivalent to the Navier-Stokes method as it uses the symmetry of Chapman-Enskog expansion in the Navier-Stokes limit to provide Navier-Stokes-level solutions using only a few discrete velocities. Hence, the LBM is effectively a continuum method and thus likely not applicable to the systems studied in this thesis.

2.5.1.1 Applications of LBM in Micro Channel and Acoustics Problems

Numerous researchers have conducted molecular simulations using the Lattice Boltzmann Method (LBM) with applications in acoustics (Buick et al. 1998; Buick et al. 2000; Viggen 2009) for different aspects. For instance, in the LBM study conducted by Viggen (2009), a point acoustic source method was proposed to perform a simulation of viscously damped cylindrical and plane waves. Good agreement was exhibited with the numerical results for the simulation of the Doppler effect, diffraction and damped standing waves. However, application of LBM was only feasible in the ultrasound frequency range and on small spatial scales and required long computation times for lower frequencies or larger scales (Viggen 2009). Buick et al. (1998) applied LBM to simulate linear sound waves propagating in an unbounded region and in a tube, in situations where the density variation was small compared

with the mean density. Good agreement with the analytical expressions were obtained. Even for a nonlinear sound wave simulation at higher intensity, the expected features were observed using the LBM simulation. They showed that LBM can successfully be employed for sound wave propagation and accordingly they extended their study for nonlinear acoustic wave propagation to simulating the development of a shock front from a high-amplitude sinusoidal source (Buick et al. 2000).

Many computational studies of micro flows (Niu et al. 2004), gas flows (Niu et al. 2007; Tang et al. 2008), and flows in micro channels (Aminfar and Mohammadpourfard 2008) or nanochannels (Suga et al. 2010) have investigated the implementation of the LBM in transition regimes at Knudsen numbers ranging from 0.01 to 1. Niu et al. (2004) applied a new approach of the lattice Boltzmann BGK model developed based on the entropic LBM (Ansumali and Karlin 2002), which uses a modified relaxation time in terms of the Knudsen number, for the simulation of planar Coquette flow and pressure-driven micro-channel flows. They studied the flow behaviour in the Kn range from 0.01 to 0.5 and found that the proposed model could predict the micro-fluidic behaviour well. They extended the study (Niu et al. 2007) using the same method to address issues related to the boundary conditions, relaxation time and regularisation for micro-scale gas flow, and suggested that flows over a range of Knudsen numbers can be modelled using LBM by introducing the effective mean free path with boundary effects and a regularisation procedure to ensure the presence of nonequilibrium moments of LBM within the defined Hermite space. Suga et al. (2010) also used the modified expression for the effective relaxation time in conjunction with the bounce back/specular reflection (BSBC) and diffuse scattering (DSBC) wall boundary conditions to evaluate force-driven flow behaviour in a combined nanochannel that consisted of a narrow channel with $Kn = 1.1$ inserted into another large channel with $Kn = 0.14$. Satisfactory results were obtained for the wider channel flow region, whereas the flow rate was over-predicted for the narrower channel region, as $Kn > 0.5$. Tang et al. (2008) showed that current high-order and modified LBMs are not yet able to capture the nonlinear flow behaviour in the Knudsen layer (i.e. evaporation layer) for nonequilibrium gas flows. They proposed a wall function approach for the standard lattice BGK model, which could predict the nonlinear velocity profile accurately. However, they identified the need for an improved model for the quantitatively accurate prediction of transition-regime gas flows. Aminfar and Mohammadpourfard (2008) employed LBM to study the flow behaviour of isothermal pressure-driven microchannel flow within the transition region $0.1 < Kn < 0.5$ and at low Reynolds number $Re < 1$, using an expression for

the complete momentum accommodation coefficient and a relaxation time based on the Knudsen number. They showed that the modified method could improve the results and reduce the number of iterations significantly for the large aspect ratio channel investigated, leading to reduced CPU time, which is very sensitive and important for large lattice size.

As described above, most of the studies evaluated the transitional flow regime at high Knudsen numbers only in canonical flows such as gaseous flow in long microchannels, pressure-driven flow in microchannels, isothermal Coquette and Poiseuille flow, and flow in a combined nanochannel (Suga et al. 2010). Good accuracy was only obtained in the range of $Kn < 1$, with very good predictions obtained for the range within $Kn \leq 0.5$, indicating a clear research gap in the case of nanoflows for the range of $Kn \geq 1$ using LBM. However, LBM shows promising results in this Knudsen number range ($Kn < 1$) considering the outcomes from other molecular simulations to be discussed in the following sections. Beyond this range ($Kn \geq 1$), it seems that the relaxation time model needs to have more sensitivity to Kn, as suggested by Suga et al. (2010). This implies that for solving the current case of acoustic propagation within nanoscopic fibres in air using LBM, it is necessary to develop an effective relaxation time model that can simulate the flow behaviour without the over-prediction caused by the sensitivity issues typically encountered for high Knudsen number flows.

2.5.2 Direct Simulation Monte Carlo (DSMC) Method

DSMC is a particle-based simulation method that describes the bulk properties of gas using the physical modelling of particle motion and collisions based on kinetic theory (Oran et al. 1998; Hanford 2008). The distinct attribute of this model is that the particle motions and collisions are treated separately. The particle motions are modelled deterministically, while the collisions are modelled statistically (or probabilistically) (Oran et al. 1998; Hanford 2008). Due to the employment of a probabilistic procedure for the computation of collisions, the computing requirement in this model becomes manageable and it gives flexibility during the simulation (Prasanth and Kakkassery 2006). The DSMC approach, similar to a CFD (computational fluid dynamics) calculation, proceeds from a set of prescribed initial conditions and consists of four essential routine processes for each time step (Oran et al. 1998; Hanford 2008), namely:

1. *Moving simulated particles and applying the boundary conditions*: In this stage, a computational domain is defined and the initial state of the molecules is specified in the domain of physical space, which is ini-

tialised by their molecular weight, diameter, number of internal degrees of freedom, internal energy, location in space and velocity. During the particle movement for each time step, appropriate boundary conditions are applied for each molecule that can include diffuse boundaries, specular boundaries, periodic boundaries, inflow/outflow boundaries, and moving boundaries such as a piston boundary condition (Hanford 2008).

2. *Sorting, indexing and tracking particles*: In this stage of the simulation, particles are sorted to determine their cell location, which is a prerequisite for the next two steps: modelling collisions and sampling the flow field.

3. *Simulating collisions*: Collisions are simulated stochastically in this step. Several collision modelling techniques have been employed successfully between randomly selected pairs of molecules within each cell. However, the preferred model is a no-time-counter technique (Bird 1994), used together with the sub-cell technique, which enhances accuracy by ensuring that collisions occur only between near neighbours (Oran et al. 1998).

4. *Sampling macroscopic properties*: Macroscopic flow properties are sampled in this final process, which is performed by using the spatial coordinates and velocity components in a particular cell.

2.5.2.1 Applications of DSMC in Micro Channel and Acoustics Problems

Various applications in the field of nonlinear acoustics have been examined using DSMC, such as molecular relaxation effects in monatomic and diatomic gas (Danforth and Long 2004b; Danforth and Long 2004a; Danforth-Hanford et al. 2006) and numerical simulation of acoustics problems in planetary environments (Hanford 2008). It was observed that the deviation from continuum predictions for high Knudsen number flows could be distinguished with DSMC. In addition, application of DSMC in various acoustic problems indicated that for a large range of Kn flows, all physical properties of wave propagation at the molecular level, such as absorption, dispersion, nonlinearity and molecular relaxation can be simulated without any modification to the model (Hanford 2008). Moreover, DSMC can be expected to be useful for efficient modelling of other acoustical phenomena related to boundary layer problems and boundary interactions, despite some imposed limitations in the wavelengths and sound source type, which are usually restricted during

the simulation with the target of low computational cost and time (Hanford 2008). This prior research gives insight into and aspiration for the possible implementation of DSMC for the nonlinear boundary interactions in the case of sound propagation through nanotube structures.

Extensive simulations of sound wave propagation using DSMC were conducted by Hadjiconstantinou and Garcia (2001), Hadjiconstantinou (2002), and Hadjiconstantinou and Simek (2003) in micro- and nano-channels and in simple gases in the transitional flow regime, for continuum and non-continuum transport conditions. During the molecular simulation of sound wave propagation in high Knudsen number flows (Hadjiconstantinou and Garcia 2001), DSMC was implemented to predict the variation of the wave speed and attenuation constant as a function of oscillating frequency in the gaseous medium argon, which was modelled as dilute hard-sphere particles for small amplitude oscillations. The acoustic wavelength was considered as the characteristic length for comparison with the molecular mean free path. Simulations were performed for conditions in which the behaviour deviates substantially from the classical phenomena. For instance, the speed of sound deviates from the classical adiabatic constant when the period of oscillation is comparable to the molecular collision time, and similarly, at high frequencies the attenuation rate seems to show significantly different non-classical behaviour in the low attenuation limit. For both of these cases, DSMC produced good agreement with the experimental data and approximate solutions of the Boltzmann equation. Moreover, these simulations using DSMC (Hadjiconstantinou and Garcia 2001) offered accurate and consistent results for the variation of the sound speed and attenuation constant over the whole frequency range, whereas classical theories and molecular kinetic formulations based on the Boltzmann equation could not capture the variation appropriately, especially at high frequencies, as reported in the surveys done by Cercignani (1988). In other simulations of acoustic wave propagation in micro- and nano-channels (Hadjiconstantinou 2002; Hadjiconstantinou and Simek 2003), where channel height was considered as the characteristic length, DSMC was used for the simulation of a dilute monatomic gas to verify the theoretical results produced by their extension of the theory of continuum wave phenomena devised by Lamb. Characteristics of axial plane waves such as wave propagation and the complex propagation constant were investigated in two-dimensional narrow channels where the height was much smaller than the characteristic diffusion length based on the wave frequency, placing this case in the transition regime. Again, in this case, DSMC was able to capture the physics fairly accurately and showed consistent agreement with theoretical results. Further investigations in channel flow with

non-continuum conditions have been conducted by these researchers using DSMC (Hadjiconstantinou 2006). This continued research work for channel flow in the transitional regime indicates that DSMC has potential attributes to simulate wave propagation and absorption for nanoscopic fibres.

2.5.3 Molecular Dynamics (MD) Methods

Molecular Dynamics (MD) follows a similar approach to other molecular based methods such as LBM and DSMC, which have the basic steps of molecular collisions and other interactions, except it involves a different calculation procedure. While DSMC uses a stochastic approach for the simulation of collisions, MD uses a deterministic approach for collision modelling. MD uses an appropriate inter-atomic potential to describe the intermolecular potentials between the molecules and then uses the classical equations of motion, such as Newton's equations, for calculating the changes in position and velocity and to integrate them for the whole ensemble with suitable boundary conditions (Voter et al. 2002).

MD computes the trajectory of particles that interact within the defined physical domain of the system. It uses ensembles of molecules to calculate certain physical properties that obey statistical mechanics, by satisfying a particular thermodynamic state. Several types of ensembles are used for the simulation based on the thermodynamic state of the system, such as the micro-canonical ensemble (NVE) for a state that has a fixed number of molecules (N) with constant volume (V) and constant energy (E); the isobaric-isothermal ensemble (NPT), which has a fixed number of molecules, pressure and temperature; and the canonical ensemble (NVT), which has a fixed number of molecules, volume and temperature (Karniadakis et al. 2005).

In MD simulations, the microscopic state of an ensemble containing a set of N interacting particles selected to represent a molecular system can be specified in terms of the Cartesian coordinates ($r_i = r_1, r_2 \cdots r_N$) and the particle moment ($p_i = p_1, p_2 \cdots p_N$). The trajectory of the particles is computed according to classical equations of motion,

$$F_i(t) = m_i \frac{d^2 r_i(t)}{dt^2} \text{ and } \frac{dp_i(t)}{dt} = F_i(t), \tag{2.9}$$

where m_i is the mass of atom i, $\frac{d^2 r_i(t)}{dt^2} = a_i$ is its acceleration, and $F_i(t)$ is the force acting on atom i. Trajectories of each particle are defined by both the position and velocity with the time evolution of the system. As the particles move due to the instantaneous force acting on them, the change in

the position and velocity can be evaluated in the finite time interval using various numerical integrators, for instance the Verlet algorithm (Frenkel and Smit 2002; Allen 2004). These changes can be used to determine velocity-dependent properties such as the kinetic energy and temperature in the system (Meller 2001). The equations of motion are then solved until the properties of the system no longer change with time (in the cases where the equilibrium or steady-state properties are of interest) (Karniadakis et al. 2005; Werder 2005). The routine process or algorithm of the MD simulations can be presented sequentially by the following key steps (Karniadakis et al. 2005):

1. Initialisation of the positions and velocities for all particles.
2. Calculation of interaction forces between the particles at each time step using various intermolecular potential models such as the Lennard-Jones potential.
3. Integration of the equations of motion to obtain the average properties (e.g. temperature, pressure, volume) of the system.
4. Storing and analysing the data collected from the previous steps.

2.5.3.1 Application of MD in Micro/Nanochannel and Acoustics Problems

The Molecular Dynamics (MD) method has been implemented as a viable simulation approach for the investigation of sophisticated flow physics in micro-channel and acoustics problems, mainly at an industrial level due to its higher computational time, cost and requirement of the faster computing performance from the computational tool. However, with recent developments in computational performance, MD has emerged as a popular simulation tool for nanoscale flow simulation and has come within the grasp of general researchers or academics. In the last decade, MD has been consistently applied for the simulation of fluid-solid interactions, heat transfer and their implications for the development of various unknown physical characteristics of nanoscale flow such as flow in carbon nanotubes, shear-driven nano flow, and flow of helium-argon gas mixtures (Kandemir and Sevilgen 2008; Karniadakis et al. 2005; Kim 2009; Banerjee 2008). A detailed review of the implementations of MD simulation in a wide range of applications for the complex physics of flow problems in micro- and nano-channels and acoustics is given in Chapter 4.

2.6 Capability Requirements of the Methods

In the following sections the physical phenomena that are likely to be of importance for acoustic propagation and absorption in carbon nanotubes are examined, as well as the ability of continuum and non-continuum methods to capture these phenomena at the characteristic length scales of interest.

2.6.1 Wave Propagating Media (compressible fluid and polyatomic molecules)

In the case of acoustic wave propagation through[2] CNT structures, the propagating media will be air, which is a polyatomic, gaseous, and compressible medium. Compressibility of the medium will be an important factor for acoustic losses by heat conduction (Fahy 2005; Ingard 1994; Ingard 2009). This compression effect will be far greater for nanoscale wave propagation than for microscale flow due to the frequent collisions of molecules with the wall, together with collisions between the molecules. Compressibility will also be responsible for variations of the velocity and temperature profiles of the flow. In the case of diatomic or polyatomic gas molecules, relaxation effects will dominate due to the transformation of translational energy into other forms of molecular energy involving rotation and vibration (Fahy 2005). Thus, the absorption and dispersion of sound in a gas will have losses associated with the redistribution of the internal energy of the molecules known as relaxation losses (Hanford 2008). Hence, it is essential for the selected method to be able to model the complex compressibility effect and relaxation process for diatomic or polyatomic molecules (Hanford 2008).

2.6.2 Acoustics (pressure fluctuation and wave front)

A sound wave is a combination of compression and expansion of the propagating medium with rapid pressure fluctuations, which cause rapid changes in the velocity, density, and temperature of the medium. Due to these changes of temperature and velocity, thermal and velocity gradients will coincide with variations of pressure and density. As a consequence, in the case of nanoscale flow, boundary motion or body forces and momentum and heat transfer will occur simultaneously (Kim 2009; Banerjee 2008), and will have a substantial effect on the acoustic absorption mechanisms. Therefore, coupling

[2] In the following discussion, acoustic propagation within the CNTs is mentioned, however the findings apply equally to the interaction of acoustic waves with the exterior of CNT structures.

of momentum and heat transfer during the simulation is essential for the selected method.

Nanoscale wave propagation involves acoustic flows with large disturbances due to frequent collisions with the wall (Bird 1994), which will cause large variations in the temperature and density profile. In order to distinguish the large flow disturbances, a large system size with a large number of molecules must be simulated, which requires long simulation times (Bird 1994). Therefore, it is necessary for the selected method to be suitable for large flow disturbances while yielding low statistical error. Due to the oscillatory motion of acoustic waves and the small characteristic length of the channel, there will be a possibility of transient and simultaneous heating and cooling of the gas across the channel. This effect is known as the thermo-acoustic effect (Swift 2002), which the simulation method will be required to model.

2.6.3 Structural Vibration (fluid-structure interaction and pressure-vibration)

For a CNT forest grown on a substrate material, the thinness of the CNT walls, the mounting conditions of the tubes (which will act like a cantilever beam), and the pressure waves associated with sound propagation will induce structural vibrations of the tube. Moreover, thermal molecular interactions at the interface between the gas molecules and nanotube atoms will create thermal vibrations of the solid atoms (Kim 2009). These oscillations will create axial and rotational vibrations of the tube, which will also occur simultaneously with the oscillatory pressure wave. Hence the ability of the selected method to model fluid-structure interactions and structural vibrations is required.

2.6.4 Heat Transfer (thermo-acoustic effect and heat conduction)

Based on previous studies of nanoscale heat transfer (Kim 2009; Banerjee 2008), heat transfer plays a major role in nonlinearity and deviations from continuum behaviour in acoustic wave propagation. Although thermal interface resistance is the major factor contributing to the anomalous behaviour of nanoscale heat transfer, there will also be bi-directional heat transfer between the fluid and solid for CNTs in air: heat conduction through the solid wall and to the fluid outside the wall will occur, due to the fluctuating motion of the acoustic flow with the combination of compression and expansion. These various heat transfers will contribute significantly to the development of the thermal boundary layer, which is important for sound absorption at a boundary in a gas. Therefore, the selected method must be able to simulate

bi-directional heat transfer, which should also be coupled with the variation in momentum.

2.7 Justification of the Methods: LBM, DSMC and MD

Based on the discussion in the previous sections, it can be suggested that wave propagation through CNTs will be a multi-physics problem that will likely need to include the following effects:

1. wave propagating media: polyatomic gas, compressibility of the media (changing density).
2. acoustics: gas compression, oscillating piston in a simultaneous motion to generate wave front, hard wall.
3. vibration: structural wall, pressure induced vibration, vibration induced pressure (fluid-structure interaction).
4. heat transfer: gas-solid-gas, gas-gas, solid-solid, thermo-acoustics: compressed gas heated and expanded gas cooled.
5. multi-physics coupling: bi-directional effects/coupling between the fluid and structure for fluid-structure interaction and heat transfer.

A graphical representation of these effects is illustrated in Figure 2.6, showing how each of these effects will impact the nanotube structures.

As discussed in earlier sections, both LBM and DSMC have been implemented successfully for flow simulations in acoustics problems and in various size ranges of micro channel. However, simulation using LBM has been conducted mostly for flow behaviour in channels with low Knudsen

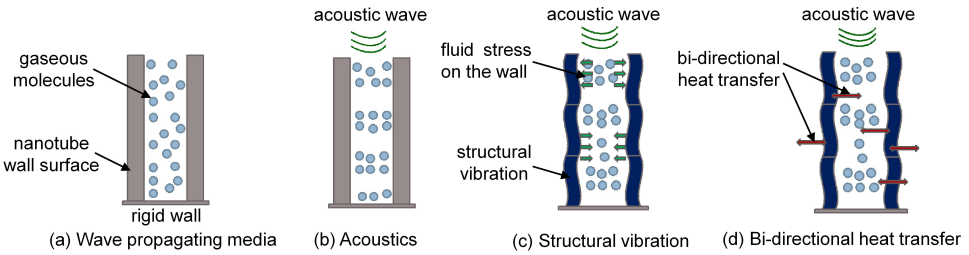

Figure 2.6: Schematics of physical phenomena required for acoustic modelling of carbon nanotubes.

number and partially in acoustics, whereas DSMC has been employed frequently for sound wave propagation in acoustic problems with small-scale channels. MD has been applied consistently in recent decades for simulations of nanoscale flow because of its extensive applicability for complex flow physics and its higher accuracy. Nevertheless, it cannot be judged which method would be more suitable for flow simulations with nanoscopic fibres based only on the range of previous applications of the methods. It would be more reasonable and practical if the method is chosen considering the limitations, capabilities, advantages and disadvantages associated with application to any particular problem. A comparison between LBM, DSMC and MD is presented in Table A.1 based on a literature review of the application of LBM, DSMC and MD in fluid dynamics and acoustics. The table lists the advantages and disadvantages of the methods along with their limitations that constrain those models to be selected for a particular problem, which can also be a selection criterion for a phenomenon to be simulated.

As indicated in Table A.1, it was found that LBM gives inadequate results for the simulation of highly compressible media (i.e. gaseous media such as air) and is unable to simulate substantial heat transfer effects, which are two important mechanisms that must be considered for the thermo-vibro-acoustic analysis of nanotubes. On the other hand, DSMC does not have any boundary condition constraints and is applicable for the whole Knudsen number range of flow regimes as it is independent of continuum limitations. Moreover, Hanford (2008) indicated that sound propagation properties such as nonlinear phenomena and absorption are inherent in the algorithm, which makes DSMC applicable for sound wave propagation. However, there are other factors that need to be considered for the nanoscale simulation of acoustic wave propagation through CNTs, such as coupled simulations of momentum and heat energy transfer, structural vibration coupled with fluid pressure fluctuations (fluid-structure interactions), and the bi-directional nature of heat transfer, which might also create a transient effect. Based on the previous application of these methods, DSMC method seems inapplicable, particularly for structural vibrations, as the method has limited applications restricted to rarefied gas flows with density variations (Bird 1994). Additionally, DSMC is still in the early stages of development for the simulation of bi-directional heat conduction, and needs major modification to include coupled momentum and heat energy transfer. This creates a great challenge for DSMC simulation solvers to extend their features (Darbandi and Roohi 2011). In contrast, MD has been efficiently implemented for the simulation of coupled fluid/solid interactions, structural vibrations, and bi-directional heat transfer. For instance, MD has been used to simulate flexural and tensile dy-

namic deformation behaviour including the vibrational frequencies of nickel (Ni) nanowire beams due to flexural bending (Mohan and Liang 2008). In addition, MD was used successfully to simulate nanoscale effects by Kim (2009) and Banerjee (2008), in which coupled momentum and heat transfer were considered at the solid/fluid interface. MD has been used successfully in recent decades to simulate nanoscale flow because of its extensive applicability for complex flow physics and its accuracy. Moreover, rapid improvements in the computation performance and reduced cost enable complicated MD simulations and promote higher accuracy of molecular simulation with greater flexibility. Hence, one may conclude that the MD method has the necessary features to simulate the required physical phenomena simultaneously. A comparison of the simulation capabilities of the preferred methods, LBM, DSMC and MD, is shown in Table 2.2, which indicates that MD is currently the most suitable method for the simulation of acoustic wave propagation in CNTs.

Table 2.2: Comparison of the particle-based simulation methods based on the simulation capabilities to capture the physical phenomena required for nanoscale acoustic flow modelling, indicating MD as the most suitable method.

Approach	Structural Vibration	Bi-directional Heat Transfer	Compressible Media	Acoustics
LBM	×	×	×	✓
DSMC	×	×	✓	✓
MD	✓	✓	✓	✓

2.8 Summary

The literature review presented here provides an overview of the potential simulation techniques to investigate the acoustic absorption of carbon nanotubes, including the advantages and disadvantages of the three most popular particle simulation methods (LBM, DSMC and MD). The phenomena most likely to be incorporated in the models for the simulation of nanoscopic fibres have also been described. Based on previous research in the transition-flow regime for various Knudsen numbers and their application in sound wave propagation, it can be concluded that MD is the most suitable method to be applied for this case as it has two major advantages; the ability to

simulate large Knudsen number flow and compressible media, as well as the effective simulation of heat conduction through the material.

3 Experimental Investigation of Acoustic Absorption Behaviour of a CNT Forest

3.1 Introduction

Carbon nanotubes (CNTs) are suitable for a wide variety of engineering applications as described in Chapters 1 and 2. Although CNTs have been suggested for acoustic damping applications there are only a few studies on the use of CNTs as a component of an acoustic absorption material in the form of composite foams (Bandarian et al. 2011; Verdejo et al. 2009; Basirjafari et al. 2012). In recent studies, it was shown that a CNT forest may enhance the acoustic absorption performance of a micro-perforated panel (MPP) absorber (Qian et al. 2014). However, none of these studies have characterised the acoustic absorption coefficient of CNTs alone. Hence, a preliminary experimental investigation of the acoustic absorption of CNT absorbers was conducted in order to quantify the acoustic characteristics and absorption performance of nanoscopic fibres compared with conventional porous materials. This chapter presents the findings from a preliminary experimental investigation of the acoustic absorption of CNT absorbers made of vertically aligned CNT forests. Experiments were conducted in an impedance tube using the two-microphone method with a normal incidence acoustic source. Theoretical predictions of the acoustic absorption properties of CNTs were made using classical acoustic theories including the Biot-Allard and Johnson-Allard models.

This chapter is organised as follows. First, a brief summary of previous investigations of the acoustic absorption behaviour of CNTs and the objective of the exploratory experiments are presented. Second, the methodology and sample preparation are detailed. Third, results for a 3 mm CNT sample from measurements using the impedance tube are presented and theoretical

predictions of the acoustic absorption coefficient using classical models are discussed. Fourth, the results are compared with those for a relatively thick CNT forest, and the differences in the absorption are analysed. Finally, conclusions on the absorption behaviour and performance compared with conventional materials are drawn.

In addition, a detailed description of the verification procedure of the measured results, including repeatability tests, reproducibility tests, and error analysis, is presented in Appendix B. A theoretical comparison of the absorption characteristics of a CNT absorber and the conventional porous materials is also described in Appendix C to highlight the significance of the absorption performance of nanoscopic fibres.

3.2 Background

Advances in nanotechnology have provided acoustic researchers with a number of new materials such as nanofibres and nanopores that can potentially be implemented as acoustic porous absorbers. The molecular behaviour of these new nanoscopic materials may have a significant influence on their sound absorption properties. In addition, their properties could play an important role in reducing the thickness of absorbers compared with currently available materials. In a study conducted by Qian et al. (2014), it was shown that super-aligned CNTs grown on the surface of a micro-perforated panel (MPP) surface can improve the acoustic absorption performance of MPP absorbers at low frequencies. Investigations were also conducted for nano-integrated polyurethane foam using multi-walled CNTs (Cherng 2006). Test results showed that the integration of CNTs improved the acoustic absorption performance by $5-10\,\%$ in the frequency range $800-4000\,\mathrm{Hz}$. Several other studies on the use of CNTs for enhancement of the acoustic absorption of conventional porous materials, such as CNTs incorporated into flexible polyurethane foams have been reported (Bandarian et al. 2011; Verdejo et al. 2009; Basirjafari et al. 2012). CNTs have also been suggested for reducing airplane noise by encapsulating the CNTs in a polymer nanocomposite to create electrospun fibres (Crawford 2012). It was suggested that the nanotubes may improve the sound absorption performance of the polymer nanocomposites as the individual nanotubes will oscillate with the sound waves, helping further absorb sound energy (Crawford 2012). These developments in nanotechnology offer exciting possibilities as the basis for acoustic absorption materials using nanotubes.

A fundamental understanding of the physical mechanisms associated with the use of nanotubes acting as acoustic absorbers has not as yet been

developed, and their potential benefits have not been quantified. A preliminary experimental investigation of the acoustic absorption characteristics of a CNT forest, as reported in this chapter, is the first step in the establishment of a fundamental understanding of nanoscale absorption. Development of this understanding will advance the knowledge base of the discipline, and will also allow a number of novel arrangements for acoustic absorbers to be investigated. However, measurements of the acoustic absorption properties of nano materials on their own have not been reported to date. This chapter presents the acoustic absorption characteristics of a CNT forest based on experimental measurements and theoretical predictions using classical methods. Characterising the acoustic absorption behaviour of the CNT forest will allow researchers to determine the degree to which the acoustic absorption mechanisms of nano materials are likely to deviate from continuum phenomena and modelling approaches applicable to conventional porous materials. Finally, it is worth noting that the research presented here forms a foundational study, with experiments performed on a few CNT samples of a limited size that are not intended to be commercial-grade acoustic absorbers.

3.3 Materials and Methods

The acoustic absorption coefficient of the CNT forests was measured in an impedance tube using the two-microphone technique (Chung and Blaser 1980a; Chung and Blaser 1980b) in accordance with the ASTM standard (ASTM E1050 1998).

3.3.1 Impedance Tube Method and Apparatus

A schematic of the setup for the two-microphone impedance tube method is illustrated in Figure 3.1a. A specimen to be tested is placed in a sample holder at the end of the tube. A sound source generates a plane wave inside the tube that propagates through the sample and is reflected back from the rigid termination. Thus, a standing wave develops inside the tube. The transfer function H_{12} ($= \frac{G_{12}}{G_{22}}$) is measured between the two microphones located at positions 1 and 2. The reflection coefficient, R, and absorption coefficient, α, at the face of the sample can be evaluated as (Chung and Blaser 1980a; Chung and Blaser 1980b; Han et al. 2007)

$$R = e^{2jkz_1} \frac{H_{12} - e^{-jkd}}{e^{+jkd} - H_{12}}, \tag{3.1}$$

$$\alpha = 1 - |R|^2, \tag{3.2}$$

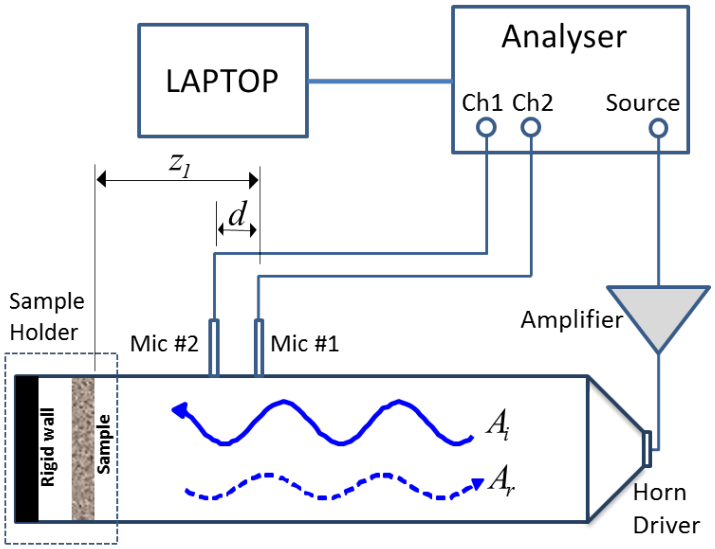

(a) Schematic of impedance tube set up

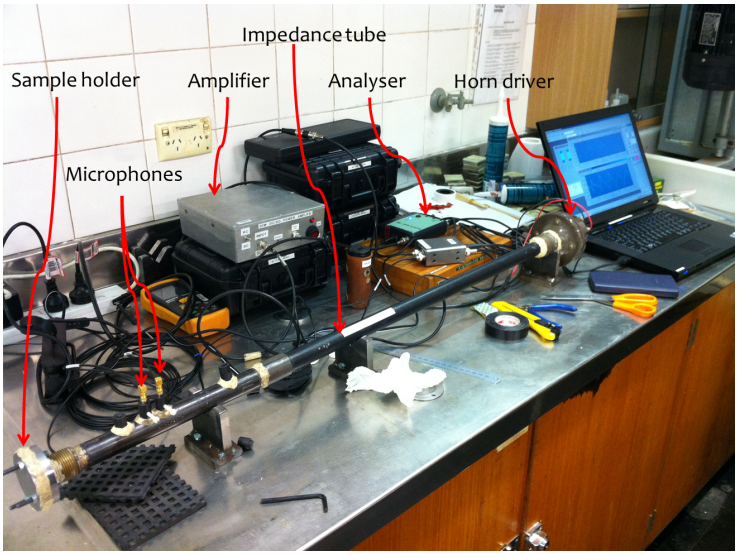

(b) Photograph of impedance tube arrangement

Figure 3.1: (a) Schematic and (b) photograph of impedance tube and instrumentation used to measure the absorption coefficient of the CNT sample.

where $e^{-jkd} = H_i$ and $e^{+jkd} = H_r$ represent acoustic transfer functions associated with the incident and reflected wave components, respectively (Chung and Blaser 1980b), z_1 is the distance of the furthest microphone from the surface of the termination, d is the separation distance between the two microphones and k is the wavenumber. The specific surface acoustic impedance Z_s of the sample can also be determined from the measured reflection coefficient using the following relation

$$Z_s/\rho c = \frac{1+R}{1-R}, \tag{3.3}$$

where ρ is the density of air and c is the sound speed in air.

A custom-made 22.10 mm internal diameter steel impedance tube was used to measure the normal incidence absorption coefficient of the CNT acoustic absorber. The impedance tube was constructed from a number of pipe lengths, a horn driver, and a pipe section which holds the two microphones that measure the acoustic pressure in the tube. A photograph of the experimental apparatus is shown in Figure 3.1b. Overall, four microphone spacings of 20.43 mm, 29.17 mm, 50.13 mm, and 140 mm are available to conduct the measurements with different operating frequency ranges, which can be determined as (Oldfield and Bechwati 2008; ISO 10534-1 2001; ISO 10534-2 2001)

$$f_u < \frac{0.45c}{d}, \tag{3.4}$$

$$f_l < \frac{0.05c}{d}, \tag{3.5}$$

where f_u and f_l are the upper and lower frequency limits. A list of the the upper and lower frequency limits for each of the microphone spacings of the impedance tube calculated using Equations (3.4) $-$ (3.5) is given in Table 3.1. It should be noted that the impedance tube has a cut-on frequency of 4.2 kHz for the first higher order acoustic mode based on the tube diameter of 22.10 mm. This limits the useful frequency range of the impedance tube even though the different microphone spacings would have permitted measurement at higher frequencies.

The instrumentation comprised two $\frac{1}{4}$-inch Brüel & Kjær (B&K) type 4958 array microphones, a four-channel B&K Photon+^{TM} data acquisition system, and LDS Dactron software (LDS Group 2013). The B&K microphones have a free field frequency response (re 250 Hz) of ± 2 dB within the frequency range 50 Hz to 10 kHz. A B&K type 4230 pistonphone calibrator was used to calibrate the microphones to 94 dB at 1 kHz. Measurement data was acquired to give a 4 Hz frequency resolution, with a sampling interval of 7.6 µs,

Table 3.1: Operating frequency range for different microphone spacings.

Microphone spacing d **(mm)**	**Frequency range (**kHz**)**
20.43	0.8 – 4.2
29.70	0.6 – 4.2
50.13	0.4 – 3.0
140.00	0.125 – 1.0

(with 12800 lines and 32768 points) and sample records of finite duration of approximately 106 s for 300 averages using a Hanning window. A B&K type 3545 sound intensity probe was used to verify the phase difference between the microphone pairs by placing them in an identical sound field generated in a B&K type UA0914 sound intensity coupler with a B&K type ZI0055 broadband sound source.

3.3.2 Correction for Microphone Phase Mismatch Error and Tube Attenuation

The acoustic impedance was measured using the two-microphone method (Chung and Blaser 1980a; Chung and Blaser 1980b). When the transfer function between two microphones is measured, phase error between the microphones is unavoidable and must be corrected. The standard sensor-switching technique (Chung and Blaser 1980a) was used to calibrate the microphones used in the impedance tube. Each transfer function H_{12} measured between the microphones was corrected (e.g., $H_{12}^{\text{corrected}} = H_{12}/H_{\text{cal}}$) by a calibration transfer function $H_{\text{cal}} (= \sqrt{H_{12} \times H_{21}})$ (Katz 2000), which ensured that any variation in the magnitude and phase of the measured transfer function due to differences in the two sensors was eliminated. The transfer functions H_{12} and H_{21} were obtained by switching the locations of microphone 1 and microphone 2 shown in Figure 3.1a, then measuring the transfer function. An additional correction was applied for the tube attenuation due to viscous and thermal losses at the tube walls, as well as damping and leaks using a method developed by Han et al. (2007). The real wavenumber k in the wave equation is replaced by a complex wavenumber

$$k' = k - jk'', \tag{3.6}$$

where $k = 2\pi f/c$, with f and c the frequency and sound speed, respectively, and k'' the attenuation constant, which can be predicted theoretically using an empirical relationship provided in the standards ASTM E1050 (1998) and

ISO 10534-2 (2001) (Han et al. 2007),

$$k'' = A\sqrt{\frac{f}{cD}}, \tag{3.7}$$

where D is the diameter of the tube and A is a constant. Values of A = 0.02203 (ASTM E1050 1998) and A = 0.0194 (ISO 10534-2 2001) have been specified previously. The attenuation constant k'' can also be measured directly as an alternative to Equation (3.7) from the measured transfer function for an (assumed) rigid termination. The attenuation constant is estimated based on the relationship between reflection coefficient R and transfer function H_{12}, with the assumption of $R = 1$ for the rigid termination (Han et al. 2007),

$$H_{12} = \frac{\cos[(k - jk'')(z_1 - d)]}{\cos[(k - jk'')z_1]}. \tag{3.8}$$

Equation (3.8) can be solved numerically for k'' using the Newton-Raphson iteration scheme (Han et al. 2007; Bhat 2004). Estimation of k'' from Equation (3.7) and from the measured transfer function using Equation (3.8), as detailed in Section B.3.2, shows that the tube has significant attenuation, which indicates this tube performs as a lossy waveguide. Hence the tube attenuation correction is necessary for this setup.

This correction method is also justified by the difference between measured absorption coefficients described in Section 3.4.1, the evidence of which is shown in Figure 3.7. It can be seen in the figure that the estimated absorption coefficient by applying this correction is comparable with the difference between the experimentally measured absorption coefficients of a sample and of the tube with a rigid termination.

These newly estimated complex wavenumber k' can also be used to predict the acoustic impedance Z_i of the closed tube normalised to the characteristic impedance of air (ρc) using the analytical expression (Kinsler et al. 2000; Boonen et al. 2009)

$$z_i^{\mathrm{t}} = Z_i/\rho c = -j \cot k' L, \tag{3.9}$$

where L ($\approx$ 984 mm) is the tube length and z_i^{t} is the normalised surface acoustic impedance. Figure 3.2 presents the analytical estimates of the normalised acoustic impedance real and imaginary values as solid line. The analytical estimate of the acoustic impedance of the closed tube was also compared with the experimental value estimated using the load impedance of the rigid termination. The normalised acoustic impedance z_i^{e} of a closed tube can be calculated from the measured surface acoustic impedance of the rigid

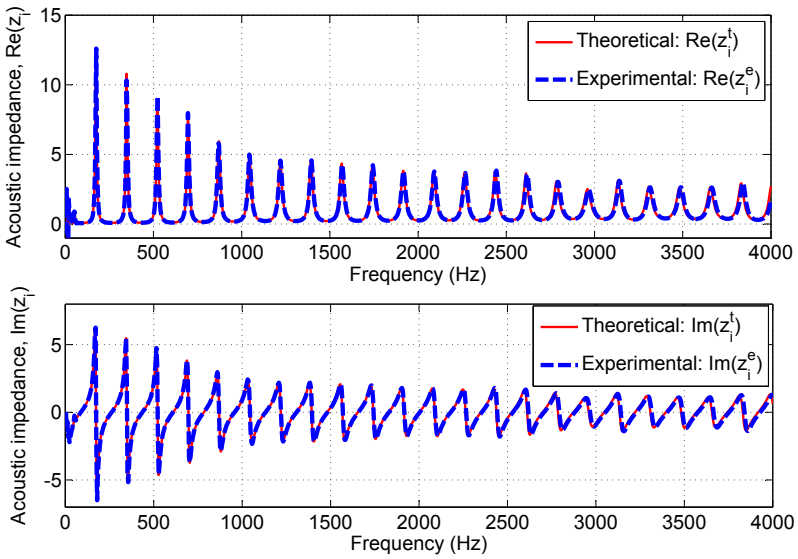

Figure 3.2: Experimental and theoretical estimates of the normalised internal acoustic impedance of the closed tube terminated with a rigid wall. Here superscripts e and t indicate the experimental and theoretical estimates of the impedance, respectively.

termination using the expression (Kinsler et al. 2000)

$$z_i^{\mathrm{e}} = \frac{z_r + j \tan k' L}{1 + j z_r \tan k' L}, \tag{3.10}$$

where z_r (= $Z_r/\rho c$) is the normalised surface acoustic impedance of the rigid wall termination. The real and imaginary parts of the normalised impedance are displayed in Figure 3.2 as dashed lines. It can be observed that both plots show consistency between the numerical and experimental results. The impedance measurement below 50 Hz is limited by the amplitude response of the microphones at low frequencies.

3.3.3 Sample Preparation and Configuration

The CNT samples were manufactured by a research team in the Nanoworld Laboratories at the University of Cincinnati, USA. A vertically aligned CNT forest was grown on a silicon wafer substrate to produce the absorber sample as exhibited in Figure 3.3. Each sample was 3 mm thick and cut to a diameter of 22.10 mm to match the internal diameter of the impedance tube.

The vertically aligned CNT array was grown in a 50.8 mm (2 inch) quartz tube reactor (ET 1000 by FirstNano) using a water-assisted Chemical Vapor

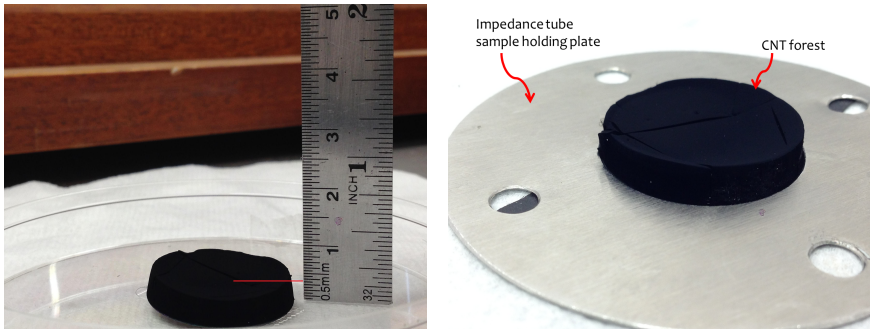

(a) Fabricated CNT sample (b) CNT forest and sample holder

Figure 3.3: Fabricated sample of 3 mm forest of CNT arrays. Figure 3.3a shows the total thickness of the CNT sample with the attached 0.5 mm substrate.

Deposition (CVD) process. The substrates were prepared as follows: (1) deposition of 20 nm Al (aluminum) film on a 101.6 mm (4 inch) Si wafer (100) coated with a (500 nm) SiO_2 layer by electron beam evaporation, (2) oxidation of the Al film to form an Al_2O_3 buffer layer, and (3) deposition of (1.5 nm) Fe/Gd thin film on the formed $Al_2O_3/SiO_2/Si$ substrate structure by e-beam evaporation. The growth parameters were 400 SCCM (standard cubic centimetres per minute) Ar, 100 SCCM H_2, 75 SCCM C_2H_4 and 900 ppm H_2O vapor. The deposition temperature was maintained at 780 °C. Details are presented in previously published works (Cho et al. 2014a; Cho et al. 2014b). The micro-morphological surface features and material characteristics of a CNT sample can be examined using scanning electronic microscopy (SEM) and transmission electron microscopy (TEM). SEM and TEM images of this type of sample can be found in previous works (Cho et al. 2014a; Cho et al. 2014b).

The CNT samples were held in an annular mounting plate as shown in Figure 3.4. Several orientations of the CNT sample were tested in order to separate the influence of the substrate material and the acoustic characteristics of the impedance tube. Figure 3.4b shows the configuration used to measure the acoustic absorption coefficient of the sample for the case of an incident acoustic wave striking the CNT forest and substrate. The CNT forest was oriented such that the long axis of the CNTs was perpendicular to the substrate and aligned with the direction of propagation of the incident acoustic wave. Figure 3.5a shows a similar configuration with only the substrate, in which the incident acoustic wave strikes the substrate material. This configuration was used to quantify the acoustic absorption coefficient of the substrate material. Figure 3.5b shows a configuration in which no sample was

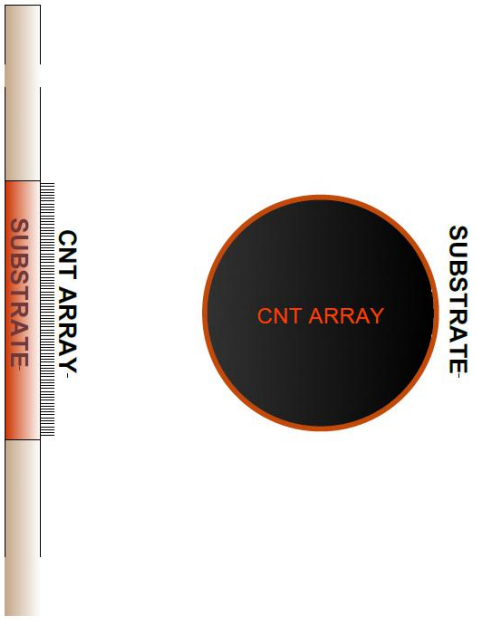

(a) Mounting schematic

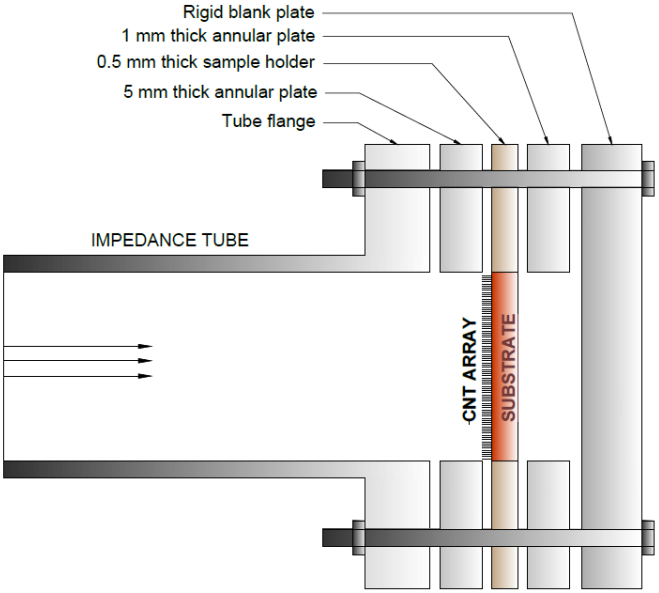

(b) Mounting configuration for CNT array

Figure 3.4: Arrangement of (a) the sample mounting plate to keep the CNT facing towards the acoustic source and (b) the sample configuration for CNT array. Note that components are shown as separated for illustrative purpose.

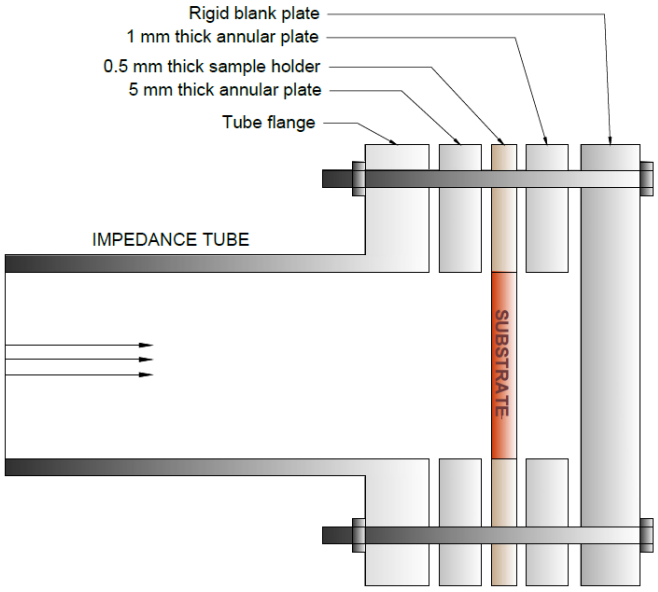

(a) Substrate only

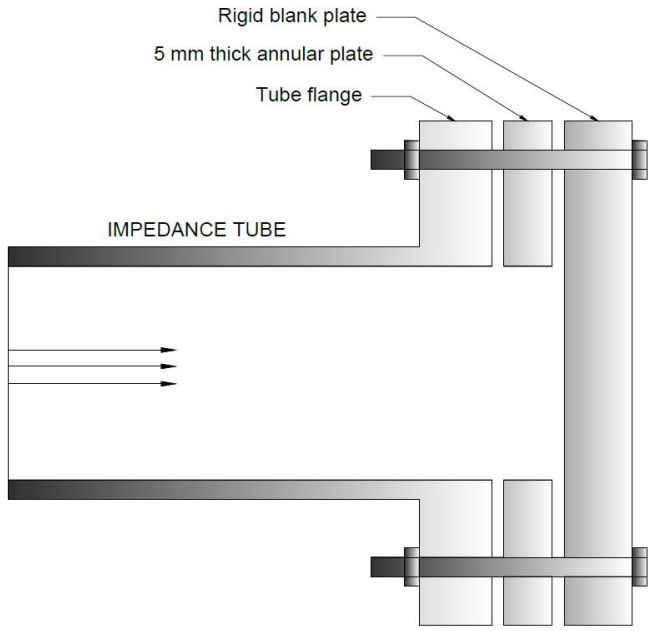

(b) Blank tube with rigid termination

Figure 3.5: Arrangement of the sample configuration for (a) the substrate and (b) the blank impedance tube with rigid termination. Note that components are shown as separated for illustrative purpose.

installed in the impedance tube, which was used to determine the absorption coefficient of the impedance tube apparatus. These two configurations allow the mounting condition of the CNT forest and substrate material to be the same for tests with and without the CNT forest exposed to the incident acoustic wave, without having any effect on the insertion loss during the measurements.

3.4 Results and Observations

The experimental investigation of the test samples using the impedance tube comprised measurements of the normal incidence sound absorption coefficient of the CNT forest for a maximum frequency of 4.2 kHz. However, the associated coherence (between the acoustic source and the microphone signals) for the tests conducted here, as displayed in Figure B.11a, was found to be excellent for the frequency range from approximately 125 Hz to 4 kHz. Hence, the results are presented here only for that frequency range. The results were compared with those of the substrate (Si) material alone, a blank impedance tube, and conventional absorptive materials. The accuracy and reliability of the test results were also verified by conducting repeated measurements and by evaluating the errors in the measurements and calculations. A detailed description of the verification procedure can be found in Appendix B.

3.4.1 Experimental Results

Measurements were conducted for several orientations of the sample to yield the acoustical absorption capability of CNT forest. The mounting configurations shown in Figures 3.4b and 3.5a were used for the measurement of the absorption coefficient of the CNT forest and substrate material, respectively. The measurement for solely the substrate material was conducted to determine the influence of the substrate material on the CNT forest absorption measurements. The absorption coefficient of the blank impedance tube was also measured using the mounting configuration shown in Figure 3.5b to estimate the acoustic absorption by the impedance tube itself. The comparison of the acoustic absorption coefficient by these three configurations is necessary to determine the absorption of the CNT forest alone. The sound absorption coefficient α of the CNT forest, the substrate material, and the blank impedance tube were estimated from the transfer function (H_{12}) measured between the two microphones placed with a separation distance of 20.175 mm (where the measured distance was corrected using the frequency null method

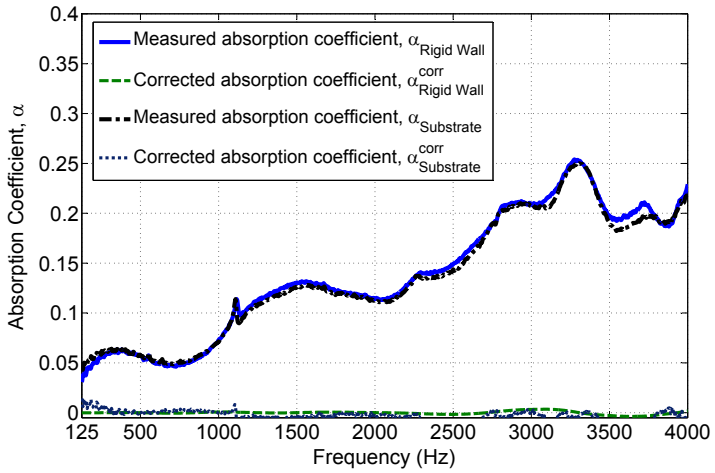

Figure 3.6: Measured and corrected normal incidence sound absorption coefficient of substrate material and tube with rigid termination.

(Katz 2000), as discussed in Appendix B.3). The assumed rigid termination consisted of a 5 mm thick mild steel blanking plate. Figure 3.6 shows the measured absorption coefficient of the blank impedance tube (with the rigid termination) and that of the substrate material for the sample configurations shown in Figure 3.5, with and without the implementation of the correction for tube attenuation. It may be observed that both the substrate and the rigid wall termination show almost the same amount of absorption, which indicates that the substrate material can be considered as a rigid wall for the comparison of the absorption behaviour with that of the CNTs. As shown in Figure 3.6, the impedance tube exhibits an absorption of less than 25%, which occurs predominantly due to the attenuation associated with the small tube diameter (Han et al. 2007), as well as sound leakage around the tube end and background noise. However, the expected result of zero absorption for the rigid wall termination is nearly achieved once the correction for tube attenuation (Han et al. 2007) is applied. Figure 3.7 shows the measured absorption coefficient of the CNT forest for the sample configuration shown in Figure 3.4b. The absorption coefficient is estimated by applying the correction to the measured results, which is also comparable with the difference of absorption coefficients between that of the CNT forest and the bare tube with rigid termination. It can be seen that the CNT forest shows a $5-10\,\%$ normal incidence acoustic absorption coefficient over the mid and high frequency range and less than 5% absorption at low frequencies below 1000 Hz.

The thickness of the sample used in this test was very thin compared with the wavelength and there was a concern that the incident noise had little

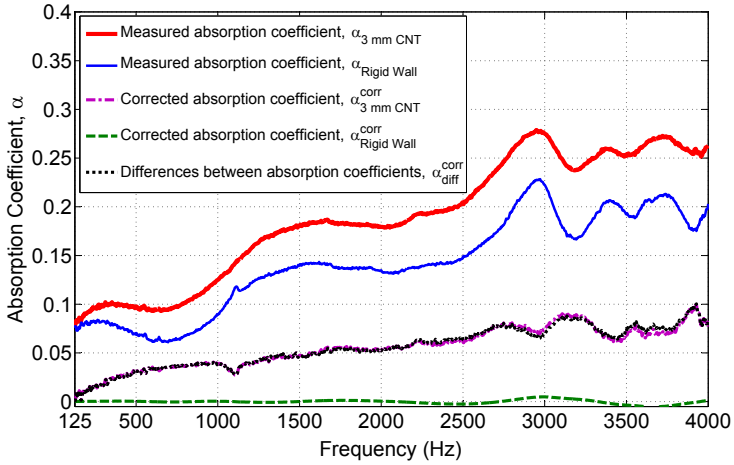

Figure 3.7: Measured and corrected normal incidence sound absorption coefficient of CNT forest sample compared with that of the tube with rigid termination. The ”differences" curve was obtained by taking the difference between the measured absorption coefficient of the bare rigid walled tube and that with the CNT forest present.

chance to dissipate before being reflected back from the rigid wall (Choy et al. 2009). Hence, it was anticipated that the acoustical behaviour of the CNT forest could be more accurately captured if the sample was combined with conventional materials and an air gap to increase the absorber thickness. This method would also increase the sound absorption coefficient above the noise floor of the lossy waveguide (impedance tube) and the effect of losses (by the rigid walled tube) on the results would be avoided. Therefore, additional measurements were conducted with the CNT forest combined with conventional porous materials to check the reliability of the previously obtained acoustic absorption coefficient of the CNT forest. In addition, an improvement in the acoustic absorption of a conventional absorber can be observed if the CNT forest is combined with the conventional porous materials to make a composite absorber panel. A conventional absorptive material of 14.5 mm polyurethane (PU) foam (0.1176 g, 21.1 kgm^{-3}) was placed in front of the CNT forest as shown in Figure 3.8. Previous arrangements of the sample configuration shown in Figures 3.4 and 3.5 were used to carry out the measurements for an equivalent absorber of three different mounting conditions of the CNT forest, substrate material, and rigid wall. To isolate the contributions of the CNT to the acoustic absorption, the following configurations were experimentally measured:

- *panel A*- 14.5 mm PU (polyurethane foam) + 37 mm AG (air gap) +

3 mm CNT + RW (rigid wall)

- *panel B*- 14.5 mm PU + 40 mm AG + ST (Substrate)
- *panel C*- 14.5 mm PU + 40 mm AG + RW
- *panel D*- 14.5 mm PU + 40 mm AG + 3 mm CNT + RW

The configurations of *panel A*, *panel B*, and *panel C* were chosen to represent arrangements (combined with the PU foam) equivalent to that of the CNT forest, substrate material, and rigid wall shown in Figures 3.4b, 3.5a, and 3.5b, respectively. A schematic of the mounting configuration for *panel A* is shown in Figure 3.8b. The estimated absorption coefficient results from the tests are shown in Figure 3.9. As expected, *panel A* of the polyurethane foam backed by the CNT forest (dashed bold line in the figure) exhibits a higher acoustic absorption coefficient than that of *panel B* and *panel C* of the substrate material and rigid wall. Replacing the 3 mm air gap with the 3 mm CNT forest in the composite *panel C* comprising 14.5 mm PU foam, 40 mm air gap and the rigid wall, decreased the surface impedance above a frequency of 1500 Hz. It reduced the mismatch between the impedance of the absorber and the characteristic impedance of air, resulting in higher acoustic absorption by the composite *panel A*. Similarly, a fourth type of composite panel with the 14.5 mm PU foam, 40 mm air gap, and 3 mm CNT forest (*panel D*) increased the acoustic absorption coefficient at low and high frequencies. This result supports the reliability of the earlier assessment of the absorption capability of CNTs. The findings also highlight the ability of CNTs to enhance the acoustic absorption coefficient of conventional porous materials. In order to demonstrate the significance of the absorption performance of nanoscopic fibres, the absorption characteristics of a CNT forest are also compared with those of conventional porous materials for samples of equivalent thickness and equivalent mass. A detailed analysis of this comparison is presented in Appendix C.

Consequently, it should be clarified that the estimated acoustic absorption coefficient of the CNT forest samples available to this study as shown in Figures 3.7 and 3.9 is very small and not sufficient to consider CNT forests as beneficial as sound absorbers in their current form. In addition the arrangement of the CNTs has not been optimised in any way for acoustic absorption considerations. Advanced manufacturing methods are allowing researchers to create CNTs in the range of the centimetre (cm) length scale (Cho et al. 2014a; Cho et al. 2014b; Zhang et al. 2013; Hooijdonk et al. 2013; Beckman 2007; Berger 2013). It is anticipated that a forest of CNTs of greater length

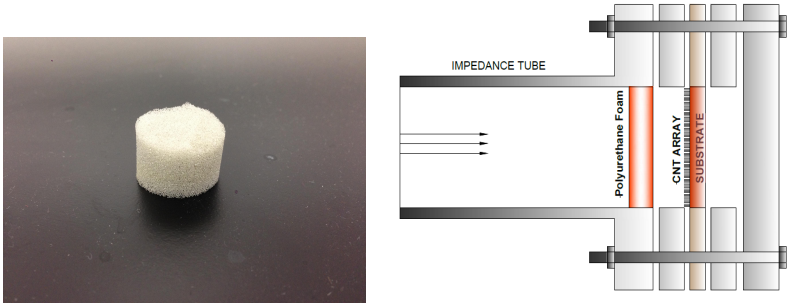

(a) Polyurethane foam sample

(b) Sample configuration of the composite absorber panel

Figure 3.8: The arrangement of sample configuration for a 14.5 mm polyurethane foam (0.1176 g, 21.1 kg m^{-3}) backed by a 37 mm air gap and the 3 mm CNT forest.

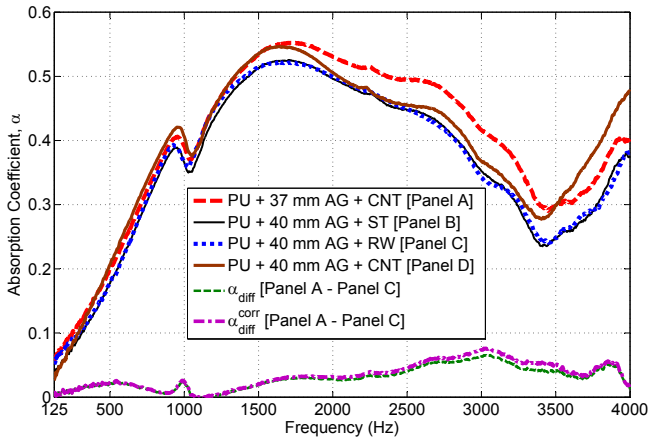

Figure 3.9: Comparison of the absorption coefficient for combinations of polyurethane foam and the CNT forest. Here, α_{diff} and $\alpha_{\text{diff}}^{\text{corr}}$ correspond to the difference between the measured and corrected absorption coefficients of the CNT and rigid wall. PU, CNT, AG, ST and RW stand for the polyurethane foam (14.5 mm), CNT forest (3 mm), air gap, substrate, and rigid wall, respectively.

(in the cm range), lower density, and possibly a variation in the arrangement of the nanotubes could be used to provide enhanced acoustic absorption. Advances in nanotechnology show that centimetre-long CNT forest can be grown efficiently using water-assisted thermal CVD (chemical vapour deposition) with a controlled growth time (Cho et al. 2014a; Cho et al. 2014b). In addition, it has been shown that a wide range of forest densities can be synthesised by controlling the catalyst nano particle formation process (Sakurai et al. 2013). Long CNT arrays with low forest density may permit the CNTs to vibrate with the sound waves, which will induce additional absorption. Furthermore, patterned CNT arrays can currently be fabricated with various densities of CNTs, for example, CNT arrays in which the nanotubes are bunched together in 1 mm diameter post-like structures (Cho et al. 2014a) and for which the density of the forest could be optimised to increase acoustic absorption. Several other arrangements of CNT are also possible (Cho et al. 2014a; Cho et al. 2014b), including super-aligned arrays (Qian et al. 2014). This experimental study conducted here on a CNT forest of a limited size indicates that promise. Further experiments are needed to measure the absorption coefficient of a CNT sample of greater length and possibly lower forest density with the aim of observing an increased absorption coefficient sufficient for practical application as a CNT-based acoustic absorber. Theoretical estimates of the absorption coefficient for different length of CNTs and bulk density of the CNT forest, presented in Appendix D, show that the absorption performance could be improved significantly with a lower forest density of CNTs. A similar observation of enhanced acoustic absorption performance of the CNT forest with lower forest density can also be observed in the experimental results presented in Section 3.5.4. Overall, these results indicate that it is worth pursuing further study of CNTs as acoustic absorbers.

3.4.2 Theoretical Prediction using Classical Methods

It is anticipated that the acoustic absorption mechanisms and the acoustic behaviour of CNTs would be different compared with that of conventional porous materials considering the physical structure and size scale of the CNTs. Thus, the classical methods applicable for conventional materials might not be able to characterise the acoustic behaviour of the CNTs. Therefore, it was of interest to analyse the acoustic behaviour using classical methods to explore how experimental estimates of the absorption coefficient of the CNTs deviate from theoretical predictions.

The simple empirical and classical method of Bies-Hansen (see Bies and Hansen (2003), p623, Appendix C), Garai-Pompoli (Garai and Pompoli 2005)

Table 3.2: Measured parameters and estimated physical properties of the CNTs and CNT forest that were used to predict the acoustic absorption characteristics using classical methods.

Parameters	**Value**
Sample thickness, t (mm)	3.0
Fibre diameter, d_f (nm)	12
Mass of the sample, m (g)	0.0499
Bulk density, ρ_b (kg m^{-3})	43.4
Nanotube (Multi-walled) density, ρ_m (kg m^{-3}), (Seetharamappa et al. 2006)	2100
Shear modulus, N (GPa), (Guhados et al. 2007)	1.4
Poisson's ratio, ν, (Hall et al. 2008)	0.20
Predicted properties	
Flow resistivity, σ (Pa s m^{-2}):	
(a) $\sigma_\text{Bies-Hansen} = 3.18 \times 10^{-9}\ \frac{\rho_b^{1.53}}{d_\mathrm{f}^2}$,	7.06×10^9
(Bies and Hansen 2003; Kino and Ueno 2008; Beranek and Ver 1992)	
➢ Developed for fibre glass products with $d_\mathrm{f} < 15\,\mu$m,	
➢ Range of d_f used for experimentation: $1 - 20\,\mu$m	
(b) $\sigma_\text{Ballagh} = 490\ \frac{\rho_\mathrm{b}^{1.61}}{d_\mathrm{f}}$, (Ballagh 1996)	1.77×10^7
➢ Developed for polyester fibre with mean d_f = 33 μm,	
➢ Range of d_f used for experimentation: $18\ -\ 48\,\mu$m	
(c) $\sigma^\text{modified}_\text{Garai-Pompoli} = 25.989\ \frac{\rho_\mathrm{b}^{1.404}}{d_\mathrm{f}^2}$, (Garai and Pompoli 2005)	3.59×10^7
➢ Developed for wool with mean d_f = 29 μm,	
➢ Range of d_f used for experimentation: $22\ -\ 35\,\mu$m	
Porosity, ϕ :	
$\phi = 1 - \frac{\rho_\mathrm{b}}{\rho_\mathrm{m}}$, (Kino and Ueno 2008)	0.979
Tortuosity, α_∞:	
$\alpha_\infty \approx \frac{1}{\sqrt{\phi}}$, (Attenborough 1993)	1.0105
Viscous characteristic length, Λ (μm):	
$\Lambda = \frac{1}{\pi d_\mathrm{f} l}$, (Allard and Champoux 1992; Allard 1993)	0.145
where $l = \frac{4\rho_b}{\pi d_\mathrm{f}^2 \rho_\mathrm{m}}$	
Thermal characteristic length, Λ' (μm):	
$\Lambda' = 2\Lambda$, (Allard 1993)	0.290

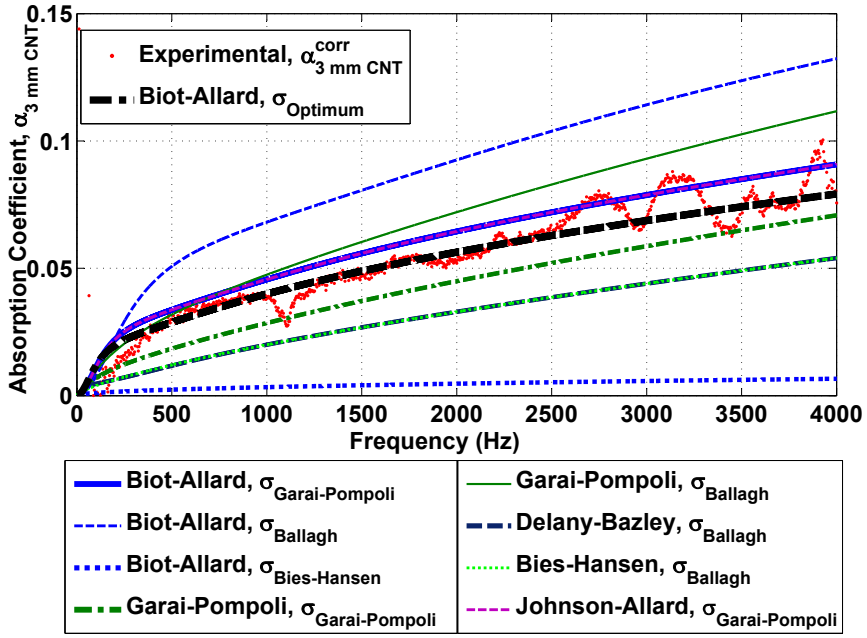

Figure 3.10: Theoretical prediction of the absorption coefficient of the CNT forest using the classical models of Biot-Allard (Hosseini Fouladi et al. 2011; Allard 1993), Johnson-Allard (Kino and Ueno 2008; Allard 1993) and Bies-Hansen (Bies and Hansen 2003). The predicted absorption coefficient of the Biot-Allard and Johnson-Allard models using the flow resistivity value of $\sigma_{\text{Garai-Pompoli}}$ and of the Bies-Hansen and Delany-Bazley empirical models using the flow resistivity value of σ_{Ballagh} are identical and coincide with each other in the figure. Note that the maximum range of the absorption coefficient in this figure is 0.15.

(both are actually a modified Delany-Bazley model (Delany and Bazley 1970)), Biot-Allard (Biot 1962; Allard 1993) and Johnson-Allard (Allard 1993) models were used to predict the acoustic absorption behaviour of the CNT forest. The estimated non-acoustical parameters of the CNTs used here to calculate the theoretical acoustic absorption coefficient are listed in Table 3.2. The geometrical and physical properties given in Table 3.2 were measured by the research group in the Nanoworld Laboratories at the University of Cincinnati, USA, and the details have been presented previously (Cho et al. 2014a; Cho et al. 2014b). The predicted absorption coefficient of the CNT forest based on the estimated non-acoustical properties using the five theoretical methods is shown in Figure 3.10. It can be noticed that the predicted acoustic absorption coefficients were significantly influenced by the value of the estimated flow

resistivity parameters. As listed in Table 3.2, the flow resistivity relationships by Bies-Hansen (Bies and Hansen 2003) and Ballagh (Ballagh 1996) give two significantly different values of the flow resistivity of 7.06×10^9 Pa s m^{-2} and 1.77×10^7 Pa s m^{-2}, respectively. The effect of these estimates is reflected in the predicted absorption coefficient by the Biot model ($\sigma_{\text{Bies-Hansen}}$ and σ_{Ballagh}) shown in the figure. It can be seen that the use of a flow resistivity value of 1.77×10^7 Pa s m^{-2}(σ_{Ballagh}), overestimates the acoustic absorption coefficient of the CNT forest compared with that of the experimental measurement. On the other hand, the Biot model with the use of a flow resistivity value of 7.06×10^9 Pa s m^{-2}($\sigma_{\text{Bies-Hansen}}$), severely under-predicts the absorption coefficient of the CNT forest. Similarly, other empirical models such as the Delany-Bazley (Delany and Bazley 1970) and Bies-Hansen (Bies and Hansen 2003) models under-predict the acoustic absorption coefficient with the flow resistivity value σ_{Ballagh}, whilst the Garai-Pompoli (Garai and Pompoli 2005) model over-estimates. This kind of inconsistency among the empirical models is expected considering the flow resistivity value of the CNT sample is six orders of magnitude larger than the applicable flow resistivity range of 10^3 to 5×10^4 Pa s m^{-2} for accurately predicting the absorption coefficient using these models (Bies and Hansen 2003). In addition, the predicted flow resistivity value in the range of 10^9 Pa s m^{-2} to 10^{10} Pa s m^{-2} is excessively high for an absorber material of 3 mm thickness. Hypothetically, an absorber material with a very high flow resistivity will have a high surface acoustic impedance for a small thickness of the material; thus it will result in a high impedance mismatch with the characteristic impedance of air and reduce the chance of incident sound waves entering the absorber and being dissipated. Hence, the classical models using a flow resistivity value of 7.06×10^9 Pa s m^{-2} given by $\sigma_{\text{Bies-Hansen}}$ predict a low absorption coefficient. However, the two estimates of the flow resistivity value given by σ_{Ballagh} and $\sigma_{\text{Bies-Hansen}}$ may be taken as representative of extreme values for theoretical estimates of the flow resistivity of a CNT forest, considering their effect on the predicted absorption coefficient, as shown by the Biot-Allard model. Furthermore, it can be demonstrated that a flow resistivity value chosen between these two extreme values of σ_{Ballagh} and $\sigma_{\text{Bies-Hansen}}$ can be used to predict an acoustic absorption coefficient similar to that of the experimental measurements. A modified equation of $\sigma_{\text{Garai-Pompoli}}$ (Garai and Pompoli 2005), given in Table 3.2, was used to predict the new flow resistivity value to be 3.59×10^7 Pa s m^{-2}. It can be seen that a flow resistivity of 3.59×10^7 Pa s m^{-2} ($\sigma_{\text{Garai-Pompoli}}$) in the Biot-Allard (Biot 1962; Allard 1993) and Garai-Pompoli (Garai and Pompoli 2005) models predicts acoustic absorption coefficients similar to the experimental values for the CNT forest, except for the uneven pattern

of the curve. Nevertheless, an optimum value of flow resistivity, $\sigma_{\text{Optimum}} = 4.7 \times 10^7$ Pa s m^{-2} gives a better prediction.

Consequently, it is evident from Figure 3.10 that most of the classical methods based on microscopic mechanisms either over-estimate or under-predict the acoustic absorption behaviour of the CNT forest. The reason for the discrepancies between the theoretical and experimental estimates of the acoustic absorption coefficient can be attributed to the significantly different values for the flow resistivity and characteristic lengths of the CNT forest compared with conventional materials. Compared with conventional porous materials, the estimated flow resistivity of the CNT forest is very high given the small thickness of the material. The large material density (43.4 kg m^{-3}) and the thin fibres (nanotube diameter = 12 nm) of the CNT forest, may contribute to the high flow resistivity, which influences the viscous and thermal losses substantially. Moreover, as listed in Table 3.2, the estimated characteristic length (viscous length = 145 nm) is only one order of magnitude larger than the fibre (nanotube) diameter of 12 nm, whereas typical porous materials have characteristic lengths many orders of magnitude larger than the fibre diameter (Ballagh 1996). For example, the typical fibre diameter of 6.1 μm and 5.58 μm of glass wool and melamine foam has characteristic thicknesses of 132 μm and 199 μm, respectively (Kino and Ueno 2008). These factors will affect the thermal and viscous layer thicknesses, and as a result, the relative influences of the various mechanisms are expected to change for CNTs or materials with pores or fibres at the smaller nanoscale (down to 1 nm). Despite having thin fibres (12 nm), CNTs have another extraordinary feature in the natural hollow structure of the fibre (i.e. nanotube), which potentially provides increased frictional resistance between the sound waves and the nanotubes and will also transfer the air particle vibrations into fibre vibrations more easily (Xiang et al. 2013). As a result, CNTs may provide a different mechanism for structural vibration and heat transfer interaction with the gas molecules, which would contribute in a different manner to the viscous and thermal boundary layers considered for conventional materials. Thus, accurate estimates of the viscous and thermal effects during the interaction between the material and the sound wave would be crucial to predict the acoustic absorption of a CNT acoustic absorber.

Although these are plausible explanations of the acoustic behaviour of CNTs based on the experiments conducted on limited samples, further investigations and measurements of the non-acoustical parameters are required to confirm these concepts. Overall, it can be concluded that the microscopic absorption mechanism applicable to conventional materials is not applicable to nanoscopic fibres such as CNTs. In order to develop an understanding of

the nanoscopic acoustic absorption mechanisms, acoustic modelling in the nanoscale range using molecular simulation is essential. Further research on modifications to the analytical methods is required as well. An overview of potential simulation methods such as Molecular Dynamics (MD), Direct Simulation Monte Carlo (DSMC) and the Lattice Boltzmann Method (LBM) can be found in Section 2.5.

3.5 Absorption Behaviour of a Long CNT Forest

It is anticipated that a forest of CNT arrays of greater length and lower forest density and possibly with a variation in the arrangement of the nanotubes can be used to provide enhanced acoustic absorption. In order to explore to what degree the absorption can be enhanced by a longer CNT forest (larger than 3 mm), an independent impedance tube test was conducted to measure the acoustic absorption coefficient of a 6 mm CNT forest using a newly fabricated impedance tube of inner diameter 25.4 mm. It should be noted that the CNT arrays in this particular sample were not attached to the substrate. Moreover, the bulk density of this sample was approximately 20.7 kgm^{-3} which is lower than that of the previous CNT sample of 3 mm thickness, where $\sigma_{3\,\mathrm{mm\,CNT}} = 43.4\,\mathrm{kgm}^{-3}$. A photograph of the 6 mm CNT forest detached from the substrate is shown in Figure 3.11. The measured acoustic absorption coefficient of the 6 mm CNT forest were compared with that of the 3 mm CNT sample. The comparison of the results is shown in Figure 3.12. It can be seen that the absorption behaviour of the 6 mm-long CNTs is significantly different from that of the 3 mm CNTs. The results show a considerable increase in absorption compared with that of the 3 mm CNTs at high frequencies above 2500 Hz, which is not anticipated for a 6 mm CNT sample considering that the thickness is just twice that of the 3 mm CNTs. The repeatability of the result obtained for the 6 mm CNT forest was checked by measuring absorption coefficients for four repeated tests with the same sample but rotating it to different surface positions. The results for the repeated tests are displayed in Figure 3.13, which confirm the repeatability of the measured absorption coefficient. In addition, a reliability test (similar to the test configuration shown in Figure 3.8) was conducted using a composite absorber sample consisting of a conventional material of 9.5 mm polyurethane (PU) foam, 11.5 mm air gap, and the 6 mm CNT forest. Comparative results of the acoustic absorption coefficient of two equivalent configurations of the sample with and without the CNT forest, but replaced with an air gap of equivalent thickness, are shown in Figure 3.14. A similar trend of absorption

increase above 2500 Hz was found for the absorber sample incorporating the 6 mm CNT forest.

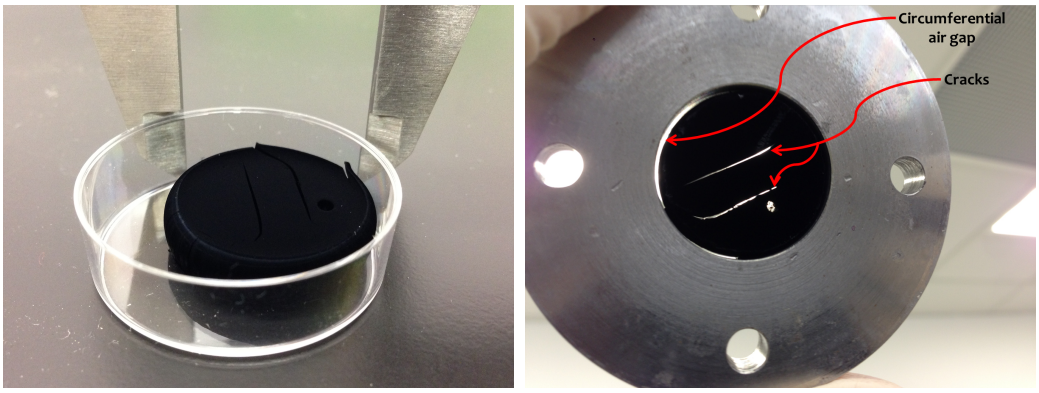

(a) Photographs of a 6 mm CNT forest.

(b) Photographs of a 6 mm CNT forest placed inside a sample holder

Figure 3.11: Photographs of a 6 mm CNT forest placed inside an impedance tube sample holder.

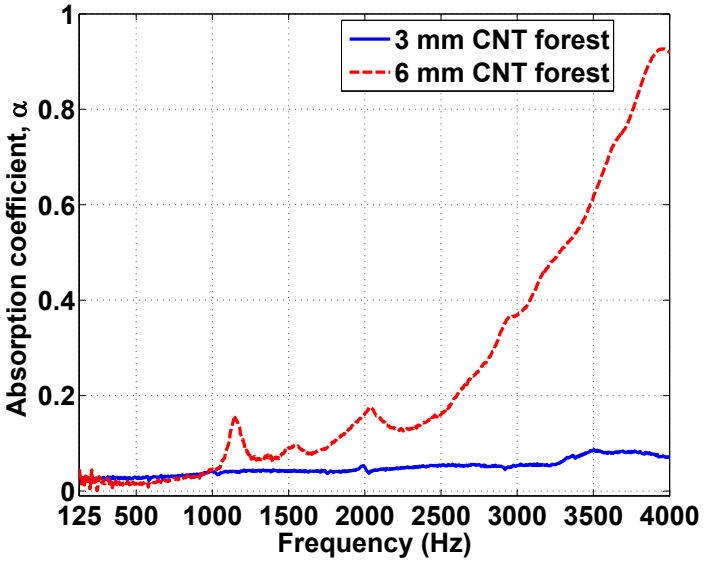

Figure 3.12: Acoustic absorption coefficient of a 6 mm and a 3 mm-long CNT forest measured using the impedance tube of inner diameter 25.4 mm.

Several explanations for the absorption increase of the 6 mm CNT sample were considered and analysed to understand this unusually enhanced absorption above the frequency of 2500 Hz. It should be noted that an appropriate

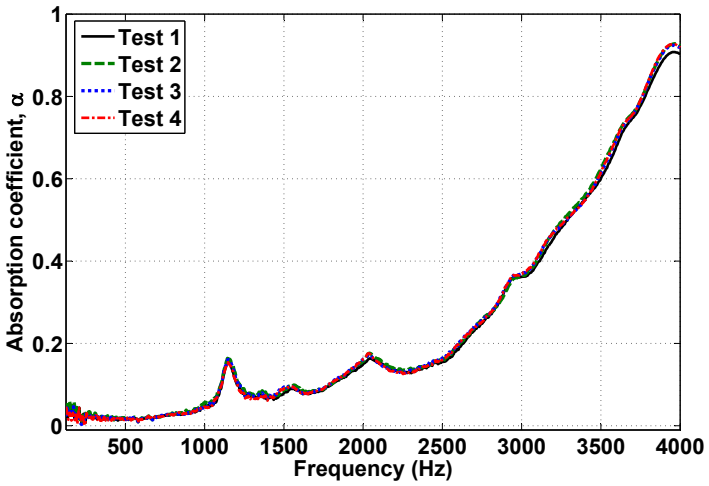

Figure 3.13: Acoustic absorption coefficient of a 6 mm-long CNT forest measured using the impedance tube for a number of repeated tests obtained by rotating the sample.

quantitative analysis of absorption behaviour of the CNT forest, as presented in this chapter, is currently very difficult due to the lack of theoretical models for nanomaterials. Hence, the following theoretical analyses are performed based on the classical methods to explain anomalies in the measured acoustic absorption coefficient. In addition, due to the lack of CNT samples and the limited availability of CNT samples for each test setup, the analyses have not been verified experimentally (specifically by repeating measurements for a given setup using a number of similar CNT samples) at this stage and should be the subject of future investigation. The following factors were considered for the analysis and their effects on the measured absorption coefficient are elaborated in the subsequent sections:

- circumferential air gap,
- sample mesoporosity,
- catalyst layer in the sample,
- nanotube forest density, and
- bending vibrations and frame resonance of the sample.

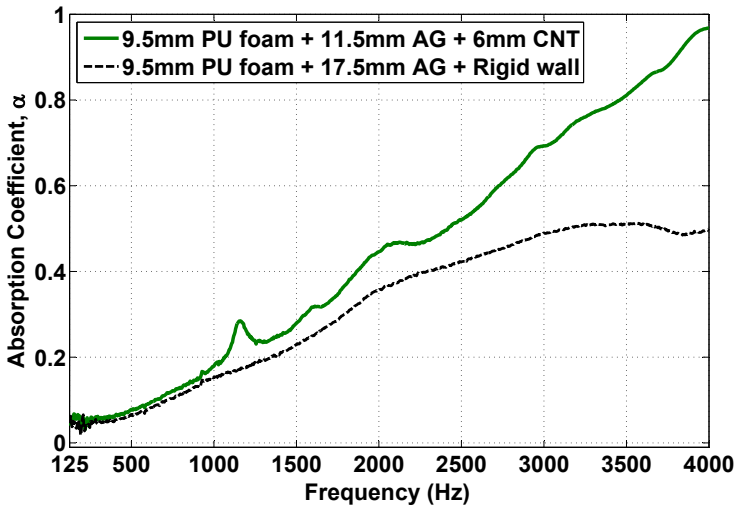

Figure 3.14: Comparison of the absorption coefficient for a composite absorber sample made of a 9.5 mm polyurethane foam, 11.5 mm air gap and the 6 mm-long CNT forest using a sample configuration shown in Figure 3.8.

3.5.1 Effect of Circumferential Air Gap

It can be noticed from Figure 3.11b that the CNT sample created a circumferential air gap with a thickness of approximately 0.83 mm when mounted inside the impedance tube sample holder, as the fabricated sample did not have a uniform circular dimension and also had a smaller diameter than the inner diameter of the holder. Hence, the effect of the circumferential air gap on the measured absorption coefficient of the CNT forest was analysed. Previous research by Pilon et al. (2004) showed that the presence of a circumferential air gap usually causes a global decrease in the measured absorption, while a material with an extremely high flow resistivity exhibits an absorption increase due to its high permeability contrast (a dimensionless parameter constructed by the ratio of the static visco-inertial permeability of the micro-and macro-porous network of a representative double porosity material). However, it has been suggested that this phenomenon might not be efficient for a thin sample. In the analysis conducted by Pilon et al. (2004), a criterion, based on the given material sample and experimental setup, was developed to identify materials that are affected by the presence of a circumferential air gap. This criterion, referred to as the acousto-visco-inertial criterion, relies on the estimates of the permeability contrast between the micro- and macro-porous network. Through the use of this criterion, an educated guess can be made to identify which absorption is measured:

the actual absorption of the material or one affected by the presence of the circumferential air gap. A similar strategy was employed for the 6 mm CNT sample to determine the effect of the circumferential air gap on the measured absorption coefficient. The permeability ratio of the 6 mm CNT sample was evaluated using the approximate values of the non-acoustical parameters of the 6 mm CNT forest. It was found that the presence of the circumferential air gap leads to a significant increase in the measured absorption coefficient from the actual value. However, most of the approximate values of the non-acoustical properties of the 6 mm CNT forest that were used for the evaluation of permeability ratio are out of the prescribed range suggested by Pilon et al. (2004) as suitable for making an educated guess on the effect of a circumferential air gap.

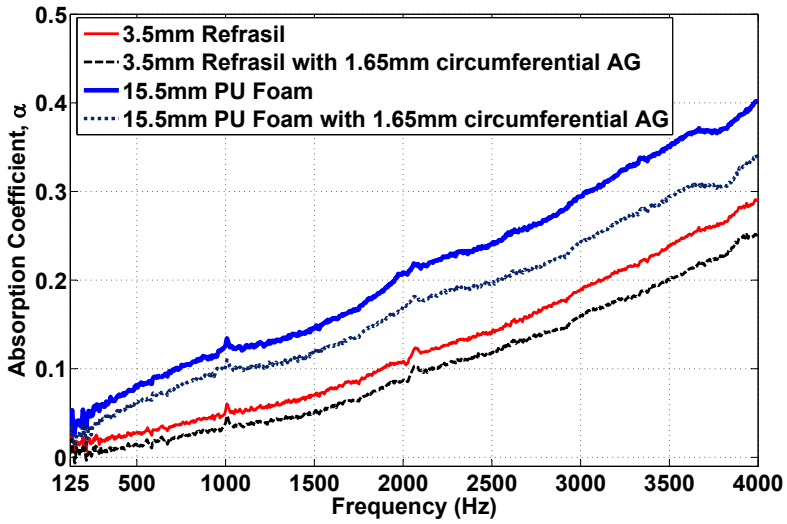

Figure 3.15: Absorption coefficient as a function of the frequency in the 25.4 mm impedance tube for a sample thickness of 3.5 mm refrasil and 15.5 mm PU foam without and with a 1.65 mm circumferential air gap.

In order to verify how this phenomenon would actually affect a thin sample of high flow resistivity material (which emulates the physical properties of CNTs) and a thick sample of low flow resistivity material, tests were conducted using an impedance tube for a low and a high flow resistivity material, polyurethane (PU) foam and refrasil, respectively. A thin sample of 3.5 mm refrasil and a relatively large thickness of 15.5 mm of PU foam with and without a 1.65 mm circumferential air gap were used for the tests. A comparison of the absorption coefficients for both materials with and without the circumferential air gap is shown in Figure 3.15. It can be seen that for

both cases the presence of the circumferential air gap reduces the acoustic absorption. It indicates that the effect of the circumferential air gap on the measured absorption coefficient of the 6 mm CNT sample could be different from the earlier observation made based on the acousto-visco-inertial criterion of Pilon et al. (2004). Therefore, an additional experiment was conducted with a loosely-supported sample holder setup (details can be found in previous work by Satoh et al. (2014)) by placing the 6 mm CNT sample of diameter 25.4 mm inside an impedance tube of smaller diameter of 22.1 mm. This kind of setup reduces the effect of the circumferential air gap and unwanted flexural vibrations of the sample on the measured absorption coefficient (Satoh et al. 2014). The CNT sample in the 22.1 mm impedance tube was backed with an air gap of 2 mm during the test as required to protect the CNTs from being crushed when the sample was placed inside the tube of smaller diameter. A comparison of the absorption results for both impedance tube tests is presented in Figure 3.16. It can be observed that the the sample with the loosely-supported setup (solid line) exhibits a significant increase in the absorption coefficient from the standard test (dotted line) in the mid to high frequency range. Therefore, it may be assumed that the reduced circumferential air gap may have contributed to the increase in the acoustic absorption which is similar to the observation made for a thin sample of high flow resistivity material of 3.5 mm refrasil. The presence of the air gap of a thickness of 2 mm with the absorber is unlikely the reason for the higher absorption of the 6 mm CNTs, as an air gap of thickness larger than 25 mm would be required to observe a shift of resonance peak at a frequency of 3.5 kHz or less as shown in Figure 3.16.

3.5.2 Effect of Sample Mesoporosity

As shown in Figure 3.11b, the CNT sample had two cracks in the middle of the sample structure. These cracks develop during the growth of the CNTs on nanoparticles. Strong intramolecular forces allow the CNTs to stick to each other, and if reaction conditions (as described in Section 3.3.3) during the growth of CNTs are not optimal, the stickiness may cause the CNTs to form cracks in the structure (Bourzac 2009). These cracks can act like additional mesopores in the microporous material, which usually affect the acoustic absorption behaviour of the porous material, as shown in several theoretical and experimental studies by Sgard et al. (2005). Thus, this CNT sample could be modelled as a meso-perforated material, also referred to as a double porosity material (Sgard et al. 2005), to investigate the effect of the meso-perforation and its contribution to increasing the acoustic absorption of the CNT sample.

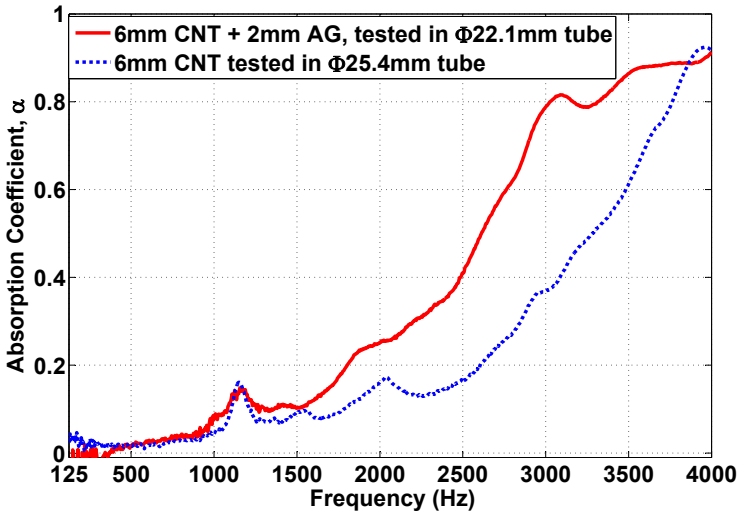

Figure 3.16: Absorption coefficient of the 6 mm CNT sample tested in two different impedance tubes of diameters 25.4 mm and 22.1 mm with the standard sample holder setup and the loosely-supported sample holder setup (Satoh et al. 2014), respectively.

The acoustic absorption behaviour of the meso-perforated CNT sample was analysed theoretically using the model developed by Sgard et al. (2005). Each of the cracks in the sample was approximately 0.33 mm wide and 1.32 mm long. Along with these cracks an additional cylindrical hole of diameter approximately 1.8 mm can also be seen in the sample structure in Figure 3.11. With the assumption of one representative equivalent circular hole for the aforementioned perforations, the corresponding radius and mesoporosity were estimated as $R = 1\,\text{mm}$ and $\phi_\text{p} = 0.0068$ (defined as the ratio of the area of the hole to the total sample area), respectively, for a representative double porosity configuration of the CNT sample. The acoustic absorption coefficient was then calculated based on the analytical model of Sgard et al. (2005) using the estimates of the non-acoustical parameters for the 6 mm CNT forest identical to those in Table 3.2. Figure 3.17 shows a comparison of the theoretically predicted acoustic absorption coefficient of the simple nanoporous CNT sample and the double porosity CNT sample. It can be seen that the theoretical prediction of the acoustic absorption for the double porosity CNT sample is enhanced in the frequency range of $1000-3000\,\text{Hz}$ due to the presence of cracks. Therefore the effect of meso-perforation can be substantial considering that the overall theoretical absorption performance of the CNT forests is low. However, these results also suggest that the effect could be in the wrong frequency range, i.e. the absorption increases in the

mid and low frequency range rather than in the relatively high frequency range where the increase in absorption is observed in the experimental results. The shape of the mesopores may have an effect in the prediction as the calculation was performed with the assumption of an equivalent circular pore.

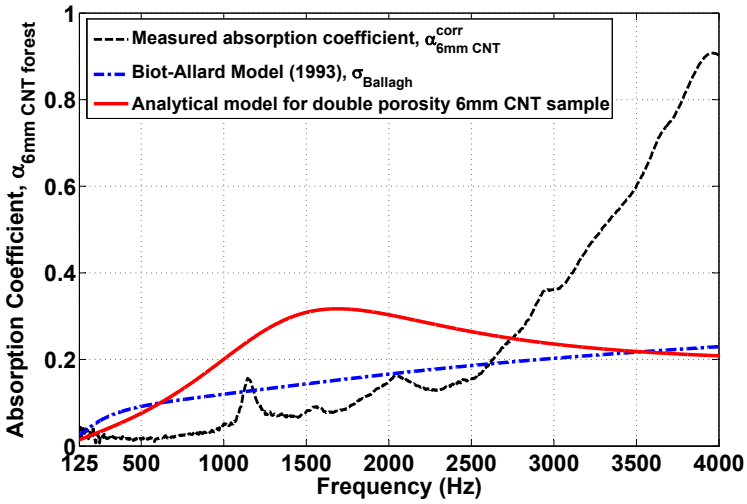

Figure 3.17: Theoretical prediction of the acoustic absorption coefficient of a 6 mm CNT sample calculated for a usual nanoporous CNT sample and a representative double porosity CNT configuration, of radius $R = 1$ mm and mesoporosity $\phi_p = 0.0068$. Experimentally measured absorption coefficient of the 6 mm CNT sample are also exhibited in this figure to illustrate the difference between the experimental results and the theoretical estimation based on the classical methods.

3.5.3 Effect of Catalyst Layer in the Sample

The fabrication process of the CNTs, as described in Section 3.3.3, comprises the deposition of a thin catalyst layer of Fe/Gd on the substrate structure, on which the vertical arrays of CNTs are grown. During the fabrication of the detached CNT forest, there is a possibility that the catalyst layer can be retained on the CNT arrays once they are detached from the substrate. For long CNTs, the catalyst layer could be anywhere between 2 to 5 nm in thickness. This layer can act like an acoustic membrane when excited by sound waves, which might have an effect on the measured acoustic absorption of the detached CNT forest. The resonance created by the membrane might also contribute to the peak observed around a frequency of 1150 Hz, which

will be discussed later in Section 3.5.5. The results suggest that a CNT forest attached to a substrate and a CNT forest detached from the substrate can behave differently for acoustic excitation. In addition, the frame resonance of the CNTs will be affected by the presence of the catalyst layer. Hence, the catalyst layer may have an effect on the acoustic absorption of a CNT forest detached from the substrate and the ways in which it may act to acoustic excitation. However, there is no specific evidence for these effects and a means of estimating the membrane effect for the catalyst layer is not available at this stage of the current investigation.

3.5.4 Effect of Forest Density

It is anticipated that lowering the forest spatial density (number per unit area) of the nanotubes will increase the acoustic absorption of the CNT arrays. Although during the fabrication process it was not intended to reduce the forest density of the particular sample of the 6 mm-long CNT forest, the measured bulk density (which is nearly half that of the 3 mm CNTs) suggests that the forest density might be lower than that of the 3 mm sample. However, the reality is a bit more complicated. During the growth of the long CNTs, the nanotubes, due to their stickiness, have a tendency to tug on their neighbours as they grow on the nanoparticles, speeding the growth of long CNTs (Bourzac 2009; Cho et al. 2014a; Cho et al. 2014b). Hence, long CNT arrays tends to have high forest densities at the upper part of the forest and relatively low forest densities at the lower part of the forest near to the catalyst layer and the substrate (Cho et al. 2014a). As a result, a long CNT forest may have a lower bulk density compared with a shorter CNT forest. Consequently, having a comparatively low bulk density in the long CNT forest provides a higher porosity and lower flow resistivity than that of a shorter CNT forest, which ideally contributes to increasing the acoustic absorption of a relatively high flow resistivity material such as the CNT forest. Theoretical estimates of the flow resistivity of the 3 mm CNT sample indicate that the values vary from $1.77 \times 10^7\,\mathrm{Pa\,s\,m^{-2}}$ to $3.59 \times 10^7\,\mathrm{Pa\,s\,m^{-2}}$ whereas for the 6 mm CNT sample, it varies from $5.37 \times 10^6\,\mathrm{Pa\,s\,m^{-2}}$ to $1.27 \times 10^7\,\mathrm{Pa\,s\,m^{-2}}$.

3.5.5 Effect of Bending Vibrations and Frame Resonance of the Sample

It is hypothesised that the peak observed at a frequency of around 1150 Hz in the absorption curve of Figure 3.13 for the 6 mm CNT sample could either be due to the bending vibration of the CNT sample or the frame resonance induced by the individual vibrations of the CNTs. Theoretical

values of the frequencies corresponding to the bending vibration modes of a similar circular plate made of CNTs for a simply supported condition (as the CNT sample was simply inserted into the holder without any additional constraints around the edge as shown in Figure 3.11b) are predicted using the relation (see Leissa (1969), Chapter 2, p8-10)

$$\lambda^2 = \omega a^2 \sqrt{\frac{\rho}{D}}\,, \tag{3.11}$$

where λ is the eigenvalue, ω is the natural frequency of bending vibration modes in rad/s, a is the radius of circular plate, ρ is the mass density per unit area of the plate, and D is the flexural rigidity which can be estimated as (see Leissa (1969), Chapter 1, p1)

$$D = \frac{Eh^3}{12(1-\nu^2)}\,, \tag{3.12}$$

where E is the Young's modulus, h is the plate thickness and ν is the Poisson's ratio. There are several factors that affect the calculation of the frequencies of the bending vibrations of the 6 mm CNT sample. For instance, the theoretical calculation was performed using the Young's modulus of the CNT forest as 1 MPa, which usually varies within the range of 1-10 MPa (Olofsson et al. 2009). In addition, the stiffness is highly directional for a vertically aligned CNT forest array. Individual estimates of the elastic modulus and the moments of inertia of CNT are not feasible which affects the quantitative determination of the flexural rigidity of the sample (Ni et al. 2008). It should also be noted that the forest density of the CNT is not uniform throughout the sample. Hence, the natural frequencies of the bending vibrations of this material were estimated theoretically using the mass densities of $10.85 \times 10^{-2}\,\mathrm{kgm}^{-2}$ and $26.04 \times 10^{-2}\,\mathrm{kgm}^{-2}$ of the 6 mm and 3 mm CNT sample, respectively, and an average value of the two mass densities of both CNT samples as $18.45 \times 10^{-2}\,\mathrm{kgm}^{-2}$. The corresponding natural frequency values estimated based on the classical theory of plates (Leissa 1969) for these mass densities are approximately 2065 Hz, 1354 Hz and 1608 Hz, respectively. It can be seen that the last two frequencies are close to the experimental value observed in the absorption curve displayed in Figure 3.13, whereas the value of 2065 Hz does not match with the frequency of the peak observed. This indicates that the dispersion in the approximate value of the surface density of the CNT sample greatly affects the theoretical values of the frequencies corresponding to the bending vibration modes of the CNT sample. Hence it is likely that the peak observed at a frequency around 1150 Hz is due to the bending vibrations of the sample inside the sample holder. The study

performed by Swift et al. (2000) suggested a similar absorption behaviour due to the sample bending vibrations.

The possibility of the peak being related to the frame resonance of the CNT sample cannot be excluded. Previous research by Dahl et al. (1990) on the acoustic absorption behaviour of fibrous materials suggests that the frame resonance is substantially affected by the fibre orientation to the sound wave propagation. They conducted impedance tube measurements on Kevlar fibres to investigate the frame resonance of fibrous materials using two different orientations of the fibres in the tube by placing the fibre planes parallel and normal to the direction of sound propagation. It was found that the material with fibres normal to the direction of sound propagation had an additional peak at low frequency in the absorption curves induced by the excitation of a frame resonance, which was confirmed and thoroughly analysed using theoretical models such as the fibre-motion model of Kawasima (1960). On the other hand, the material with the fibres parallel to the direction of sound propagation did not show any frame resonance in the measured absorption coefficient. The excitation of the frame resonance was attributed to the fibre motion induced by the viscous drag and pressure gradient across the length of the fibre (Dahl et al. 1990). It was concluded that when the fibres are oriented normal to the direction of the sound propagation the forces are strong enough to laterally displace (vibrate) the materials (or fibres), whilst the forces created along the fibres, in the case of fibres orientated parallel to the direction of sound propagation, are not strong enough to cause the fibres to vibrate (Dahl et al. 1990). The study of Dahl et al. (1990) suggests that the frame resonance in the measured absorption coefficient of the 6 mm forest could potentially be neglected due to the orientation of the CNTs, which was parallel to the direction of sound propagation. However, in the case of CNTs, even though the fibres are oriented in the direction parallel to the sound propagation, the forces might be strong enough to vibrate the nanotubes and generate frame resonance in the sample, considering their nanoscale dimension, high length-to-diameter ratio, and light weight. In addition, the strong intermolecular van der Waals forces between the nanotubes may influence the frame resonance. This behaviour could possibly be confirmed with the molecular simulation of the acoustic behaviour of CNTs.

It can be summarised that the low forest density of the nanotubes, presence of mesoporosity, and catalyst layer in the sample may be responsible for the absorption increase in the 6 mm CNT forest compared with the 3 mm. The presence of a circumferential air gap may have contributed to the absorption increase as well. However, analysis based on the experimental results of a conventional materials indicates that the presence of circumferential air gap

may cause a decrease in the measured absorption of a thin sample of high flow resistivity material such as a CNT forest. The peak at low frequency in the absorption curve may have been induced by the bending vibration of the sample. This additional peak at low frequency could also be related to the frame resonance of the CNT sample.

Based on the above analyses, it can be noted that not all the speculations regarding the absorption behaviour of CNTs have been verified in this study, as there is no definitive evidence to substantiate all of the claims at this stage of the investigation. However this analysis at least provides a demonstration of the possible factors that might affect the acoustic absorption behaviour of nanomaterials, which illustrates that the contributing factors can also depend on how the materials were fabricated, the physical and geometrical conditions of the fabricated sample, the orientation of the nanotubes inside the impedance tube, how they were prepared for the impedance tube tests, and finally the consistency of the mounting conditions of each sample during the tests. These exploratory experiments and theoretical analysis will provide an understanding of the possible conditions required for performing simulations to investigate the nanoscopic absorption mechanisms for nanomaterials. In addition, they indicate potential factors/parameters that should be considered during the setup of a simulation domain for an efficient numerical investigation. For instance, it was identified from this study that a molecular dynamics simulation of sound wave propagation, by placing a CNT normal to the direction of wave propagation, would potentially be useful to understand and verify the excitation of frame resonance.

3.6 Difficulties and Limitations in CNT Sample Preparation

It is essential to highlight the difficulties in handling CNT samples during the tests and the limitations in preparing CNT samples suitable for a particular test setup. It is very well known that impedance tube test results are significantly affected by sample mounting conditions, which in the case of CNTs, depends on how the CNT samples are prepared and the handling of the CNTs during tests. CNTs are very fragile: even a simple touch can change the surface of the sample, creating non-uniformities in the sample. Thus, variance in repeated test results may occur for the same sample. Hence careful handling of the CNT sample is very important during the tests. Some of the difficulties and limitations that were faced repeatedly during the experimental investigation of the acoustic absorption properties of CNTs are as

follows:

- fabricating a circular CNT sample such that it fits the inner diameter of the impedance tube.
- maintaining uniformity/regularity in the sample structure and sample surface (a planar surface is difficult to achieve).
- maintaining the same sample geometry throughout repeated tests (which depends on how the samples were handled in tests).
- samples without a substrate (i.e. detached CNT) would be a better choice for an appropriate test as it allows the nanotubes to move freely in the sample rather than being constrained at one end of the tube by the attached substrate. This will replicate the appropriate sample conditions for standard tests used for conventional porous materials.
- cracks appearing in the fabricated sample may induce some sort of double porosity in the material that influence the measured absorption coefficient and require a different procedure to conduct a theoretical analysis.

These aforementioned difficulties and limitations may be avoided with the careful design of the sample holder for each CNT sample or by growing the CNTs in a sample holder of predetermined design for a particular test setup of the impedance tube.

3.7 Summary

This chapter presents the acoustic absorption characteristics of a CNT absorber based on an experimental investigation of the acoustic absorption coefficient of a forest of aligned CNTs within the frequency range of 125 Hz to 4.2 kHz. It was found that a CNT forest with a material thickness of 3 mm can provide as much as 10% acoustic absorption and can enhance the acoustic absorption of a combined panel consisting of the CNT forest and a conventional porous material by $5-10\,\%$. Although, only a small enhancement in absorption was demonstrated for the CNT samples investigated, it was achieved by a small mass (0.0499 g) and thickness (3 mm) of the CNT forest. It was also shown that the absorption is reproducible. This investigation exposes the limitations of classical methods, based on microscopic mechanisms, to accurately predict the performance of the CNTs for acoustic absorption. Theoretical predictions using the models developed for

conventional acoustic materials do not agree well with the experimentally measured acoustic absorption coefficient of the CNT forest. Furthermore, an independent measurement of the acoustic absorption coefficient of a relatively long CNT forest of 6 mm indicates that a larger length and lower forest density of the CNTs may improve the absorption performance of CNT-based acoustic absorbers. The physical reasons for the differences in the absorption between the 3 mm and 6 mm CNTs are still under investigation. The results also suggest that the acoustic absorption mechanisms are likely to deviate from those for continuum phenomena. The overall findings highlight the necessity of acoustic modelling at the nanoscale to develop an understanding of the nanoscopic absorption mechanisms of CNTs. Future work should also involve measuring the absorption coefficient with the sound wave striking normal to the direction of orientation of CNTs in the CNT forest.

4 Acoustic Simulation of Nano-channels using Molecular Dynamics

4.1 Introduction

Modelling acoustic mechanisms at the nanoscale requires molecular simulations as the flow behaviour at the nanoscale is in the transition regime based on Knudsen number. In Chapter 2, molecular dynamics (MD) was identified as a suitable method for simulating the physical phenomena of acoustic absorption at the nanoscale. This chapter presents a review of previous MD simulations of relevance to the physics of acoustic absorption mechanisms at the nanoscale that have included micro- and nanoscale flow properties and acoustic wave propagation. It also discusses additional simulations that can be performed to assess whether MD models can be used to correctly simulate acoustic absorption at the nanoscale.

In the first section, an overview of the MD simulation method including the force fields, boundary conditions, barostats and thermostats involved in a simulation of acoustic wave propagation, is given. In the next section, a brief description of the simulation tools that were used in this study, namely LAMMPS, VMD, Tcl script and Topotools, is presented. The following sections include a review of previous applications of MD in nanoscale flow simulations and acoustics problems and its limitations in the audible frequency range. Potential validation cases for the MD simulation of acoustic absorption mechanisms are also discussed.

4.2 Basics of Molecular Dynamics

The basic working concept of molecular dynamics (MD) simulations is to generate particle trajectories in a microscopic system of interacting particles

by solving Newton's equations of motion (Li 2005; Allen 2004; Hofmann 2003). All macroscopic quantities like pressure and temperature in the system can be described in terms of positions and velocities of individual molecules or atoms interacting with each other for a specified inter-particle interaction potential $U(\mathbf{r}^N)$ (Li 2005; Allen 2004; Hofmann 2003). For a simple atomic system, the classical equations of motion to calculate the forces $\mathbf{F}_i$ acting on the atoms may be written in terms of the interaction potential as

$$\mathbf{F}_i(\mathbf{r}^N) = -\nabla_i U(\mathbf{r}^N) = m_i \ddot{\mathbf{r}}_i = m_i \frac{\partial \dot{\mathbf{r}}_i}{\partial t}, \tag{4.1}$$

where $\mathbf{r}^N = (\mathbf{r}_1, \mathbf{r}_2, \mathbf{r}_3 \ldots \mathbf{r}_N)$ represents the complete set of $3N$ atomic co-ordinates, $\mathbf{F}_i \equiv (\mathbf{F}_{ix}, \mathbf{F}_{iy}, \mathbf{F}_{iz})$, $\nabla_i \equiv (\frac{\partial}{\partial x_i}, \frac{\partial}{\partial y_i}, \frac{\partial}{\partial z_i})$, $\ddot{\mathbf{r}}_i \equiv \frac{\partial^2 \mathbf{r}_i(t)}{\partial t^2}$, $\dot{\mathbf{r}}_i \equiv \mathbf{v}_i \equiv \frac{\partial \mathbf{r}_i(t)}{\partial t}$. The potential $U(\mathbf{r}^N)$ can be parameterised to represent the generic physical properties of molecules or atoms or to match the quantum calculations or experimental values of known properties of molecular systems of interest. The trajectory of the atoms is propagated numerically based on the forces acting on the atoms derived from the potential energy.

4.2.1 Force Fields

The forces on the particles are obtained from the gradient of potential energy as mentioned earlier in Equation (4.1). That is usually described using the potential energy model for the inter-particle interactions (Wahnström 2013; Allen 2004). The force field is the set of parameters and equations that is used to describe the inter-particle interactions. The potential energy of a molecular system $U(\mathbf{r}^N)$ can be represented as a sum of bonded (valence) interactions (U_{val}) and non-bonded interactions (U_{nb}) as (Mayo et al. 1990; Allen 2004)

$$U(\mathbf{r}^N) = U_{\text{val}}(\mathbf{r}^N) + U_{\text{nb}}(\mathbf{r}^N). \tag{4.2}$$

The bonded interactions depend on the specific bonds of the structure, and the non-bonded interactions depend on the distance between the atoms (Mayo et al. 1990). Intramolecular bonding interactions (U_{val}) typically consist of bond length/stretch (U_{bond}, two-body), bond-angle bend (U_{angle}, three-body), and dihedral torsion (U_{dihedral}, four-body) terms (Mayo et al. 1990; Allen 2004; Alexiadis and Kassinos 2008)

$$U_{\text{val}}(\mathbf{r}^N) = U_{\text{bond}}(\mathbf{r}^N) + U_{\text{angle}}(\mathbf{r}^N) + U_{\text{dihedral}}(\mathbf{r}^N), \tag{4.3}$$

while non-bonded interactions (U_{nb}) include long-range electrostatic forces (U_{q}) and shorter range dispersive (van der Waals) and repulsive overlap

force (Pauli repulsion) interactions (U_{vdw}) (Mayo et al. 1990; Alexiadis and Kassinos 2008)

$$U_{\text{nb}}(\mathbf{r}^N) = U_{\text{vdw}}(\mathbf{r}^N) + U_{\text{q}}(\mathbf{r}^N). \tag{4.4}$$

Non-bonded interactions in MD simulations are generally assumed to consist only of two-body terms between pairs of particles.

4.2.1.1 Non-bonded Interactions

A well-known mathematical model that combines van der Waals attractions and Pauli repulsions is the Lennard-Jones potential (also known as the LJ 12-6 potential) (Allen 2004; Alexiadis and Kassinos 2008). The functional form of the LJ potential (Kim 2009; and Banerjee 2008) is

$$U_{\text{vdw}}(\mathbf{r}^N) = U(r_{ij}) = 4\varepsilon_{ij}\left[\left(\frac{\sigma_{ij}}{r_{ij}}\right)^{12} - \left(\frac{\sigma_{ij}}{r_{ij}}\right)^{6}\right], \tag{4.5}$$

where $U(r_{ij})$ denotes the interaction potential between the molecules i and j separated by a distance r_{ij}, ε_{ij} is the binding energy (depth of potential), and σ_{ij} is the distance at which the intermolecular potential is zero, i.e. $U(r_{ij}) = 0$, which can be thought of as a measure of the molecular diameter. A graphical illustration of the Lennard-Jones potential is shown in Figure 4.1. A cut-off distance of r_{c} beyond which the pair interaction is set to zero is generally used to save computational time, although care must be taken in doing this as too small a value of r_{c} can drastically impact the thermodynamics of the simulated system. A truncated version of the LJ potential can be defined as (Allen 2004; Le 2010)

$$U(r_{ij}) = \begin{cases} 4\varepsilon_{ij}\left[\left(\frac{\sigma_{ij}}{r_{ij}}\right)^{12} - \left(\frac{\sigma_{ij}}{r_{ij}}\right)^{6}\right] & \text{for } r_{ij} \leq r_c, \\ 0 & \text{for } r_{ij} > r_c. \end{cases} \tag{4.6}$$

In applications in which attractive interactions are not important or are of less concern than excluded volume effects, a purely repulsive potential force can be used by truncating the potential at the position of its minimum $2^{\frac{1}{6}}\,\sigma_{ij}$ and shifting upwards (Allen 2004; Le 2010). This truncated and shifted pairwise interaction, shown in Figure 4.1, is known as the WCA (Weeks-Chandler-Andersen) potential (Weeks et al. 1971) which can be defined as (Le 2010)

$$U(r_{ij}) = \begin{cases} 4\varepsilon_{ij}\left[\left(\frac{\sigma_{ij}}{r_{ij}}\right)^{12} - \left(\frac{\sigma_{ij}}{r_{ij}}\right)^{6}\right] + \varepsilon_{ij} & \text{for } r_{ij} < 2^{\frac{1}{6}}\sigma_{ij}, \\ 0 & \text{for } r_{ij} \geq 2^{\frac{1}{6}}\sigma_{ij}. \end{cases} \tag{4.7}$$

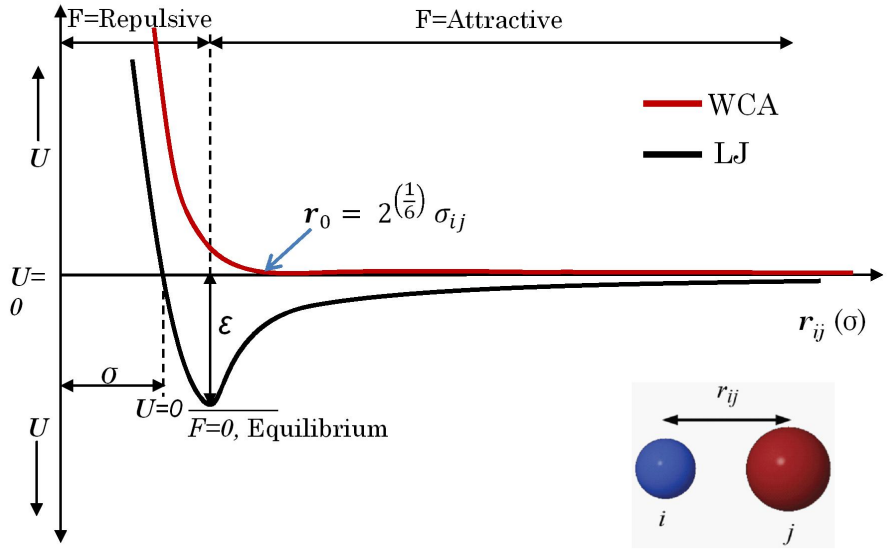

Figure 4.1: Graphical representations of Lennard-Jones and WCA potentials for non-bonded interactions between atoms i and j.

The electrostatic potential is included if there is a non-uniform distribution of electron density in the molecules, which is generally represented by point charges on the atoms; the interaction energy between a pair of such charges follows the known Coulomb law (Allen 2004; Alexiadis and Kassinos 2008)

$$U_{\mathrm{q}}(\mathbf{r}^N) = U(r_{ij}) = \frac{1}{4\pi\epsilon_0}\frac{q_i q_j}{r_{ij}}, \tag{4.8}$$

where q_i and q_j are the charges and ϵ_0 is the permittivity of free space.

4.2.1.2 Bonded Interactions

Each contribution of the bonded interactions presented in Equation (4.3) is typically modelled by the following equations for bond-lengths, bond-angles and dihedral angles, respectively (Allen 2004; Alexiadis and Kassinos 2008)

$$\text{Bond lengths} : U_{\text{bond}}(\ell_{ij}) = \frac{k_{ij}}{2}\left(\ell_{ij} - \ell_{ij,0}\right)^2, \tag{4.9}$$

$$\text{Bond angles} : U_{\text{angle}}(\theta_{ijk}) = \frac{\kappa_{ijk}}{2}\left(\theta_{ijk} - \theta_{ijk,0}\right)^2, \tag{4.10}$$

$$\text{Dihedral angles} : U_{\text{dihedral}}(\phi_{ijkl}) = \sum_{n=0}^{4} A_{ijkl}\cos^n\left(\phi_{ijkl}\right), \tag{4.11}$$

where ℓ_{ij} is the instantaneous bond length for an equilibrium bond position $\ell_{ij,0}$, θ_{ijk} is the instantaneous bond angle for an equilibrium angle $\theta_{ijk,0}$, and

ϕ_{ijkl} is the torsion angle of three connected bonds between atom pairs ij, jk, and kl. A simplified graphical representation of these contributions is shown in Figure 4.2. The parameters k_{ij}, κ_{ijk}, and A_{ijkl} measure the strength of the interactions and are specified by various force fields (Allen 2004). Some widely used force fields are AMBER (Pearlman et al. 1995), GROMACS (Van Der Spoel et al. 2005), CHARMM (Brooks et al. 1983), OPLS (Jorgensen et al. 1996), MM3 (Allinger et al. 1989), MM4 (Allinger et al. 1996), MMFF94 (Halgren 1996), DREIDING (Mayo et al. 1990), AMOEBA (Piquemal et al. 2006), and many others (Ponder and Case 2003; Gao and Kong 2004), which have been developed for certain applications and tested against the experimentally known properties (Allen 2004; Alexiadis and Kassinos 2008).

4.2.1.3 REBO Potentials

In this study, a second-generation reactive empirical bond order (REBO) potential (Brenner et al. 2002) was employed for the MD simulation of carbon nanotubes. A brief description of the REBO potential is given in this section.

The analytical formulation of the potential energy E_b in the Brenner model (REBO potential) for carbon structures is expressed as a sum of the

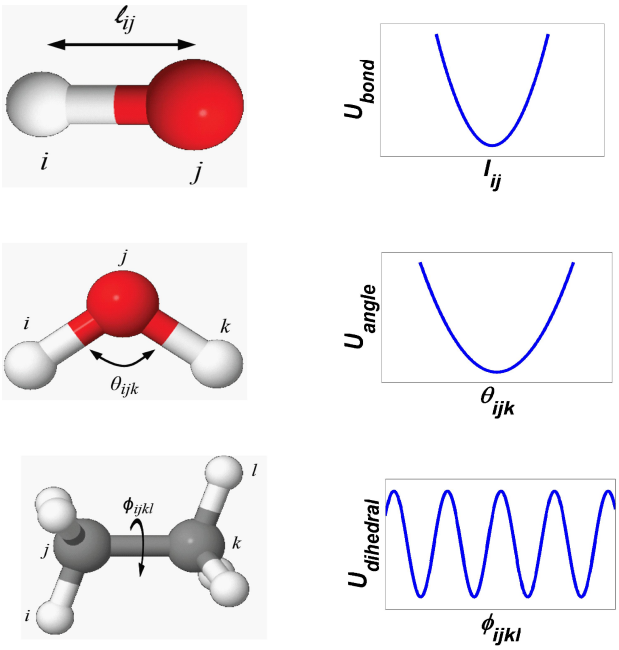

Figure 4.2: Illustration of bond-lengths, bond-angles and dihedral-angles and the graphical representations of their generalised potentials. Figure adapted from Huang (2013).

bonding energy of each bond between carbon atoms i and j by (Brenner et al. 2002; Lindsay and Broido 2010; Carlborg et al. 2008)

$$E_{\mathrm{b}} = \sum_{i} \sum_{j(>i)} \left[V^{\mathrm{R}}(r_{ij}) - \overline{b}_{ij} V^{\mathrm{A}}(r_{ij}) \right], \tag{4.12}$$

where V^{R} and V^{A} are attractive and repulsive pairwise energy terms, receptively, r_{ij} the distance between nearest-neighbour atoms i and j, and $\overline{b}_{ij}$ is the bond order term. Following the second-generation REBO potential (Brenner et al. 2002) expression, the pair potentials V^R and V^A are given by (Brenner et al. 2002; Lindsay and Broido 2010)

$$V^{\mathrm{R}}(r_{ij}) = f_{ij}^{C} \left(1 + \frac{Q}{r_{ij}} \right) A e^{-\alpha r_{ij}}, \tag{4.13}$$

and

$$V^{\mathrm{A}}(r_{ij}) = f_{ij}^{C} \sum_{n=1}^{3} B_n e^{-\lambda_n r_{ij}}, \tag{4.14}$$

respectively, where f_{ij}^{C} is a cutoff term limiting the range of covalent interactions only to nearest neighbours. The parameter f_{ij}^{C} assumes a value of unity for nearest neighbours and zero for all other interaction distances (Brenner et al. 2002). However, a switching function is used to define the value of f_{ij}^{C} of the form (Brenner et al. 2002)

$$f_{ij}^{C} = \begin{cases} 1 & \text{for } r_{ij} < D_{ij}^{\min}, \\ \frac{1}{2} \left[1 + \cos\left((r_{ij} - D_{ij}^{\min}) / (D_{ij}^{\max} - D_{ij}^{\min}) \right) \right] & \text{for } D_{ij}^{\min} < r_{ij} < D_{ij}^{\max}, \\ 0 & \text{for } r_{ij} > D_{ij}^{\max} \end{cases} \tag{4.15}$$

where the difference between $D_{ij}^{\max}$ and $D_{ij}^{\min}$ defines the distance over which f_{ij}^{C} varies from zero to one. Parameter values of $D_{ij}^{\max} = 2.0\,\text{Å}$ and $D_{ij}^{\min} = 1.7\,\text{Å}$ for the carbon-carbon pair terms is obtained by Brenner et al. (2002) that are consistent with fitting graphite and diamond lattices. The bond order function $\overline{b}_{ij}$ is given as a sum of terms (Brenner et al. 2002; Lindsay and Broido 2010)

$$\overline{b}_{ij} = \frac{1}{2} \left[b_{ij}^{\sigma-\pi} + b_{ji}^{\sigma-\pi} \right] + \prod_{ij}^{\mathrm{RC}} + b_{ij}^{\mathrm{DH}}, \tag{4.16}$$

where

$$b_{ij}^{\sigma-\pi} = \left(1 + \sum_{k \neq i,j} f_{ik}^{C} g_{ijk} \right)^{-\frac{1}{2}}, \tag{4.17}$$

and

$$g_{ijk} = \sum_{i=0}^{5} \beta_i \cos^{i}\left(\theta_{ijk} \right). \tag{4.18}$$

Here, the values of the functions $b_{ij}^{\sigma-\pi}$ and $b_{ji}^{\sigma-\pi}$ depend on the local coordination of atoms around atom i and the angle between atoms i, j, and k (θ_{ijk}) (Brenner et al. 2002; Lindsay and Broido 2010). The term $\prod_{ij}^{\mathrm{RC}}$ accounts for various radical characters of a bond between atoms i and j, such as vacancies, and is part of a conjugated system (Brenner et al. 2002; Lindsay and Broido 2010). The term b_{ij}^{DH} is a dihedral bending function that depends on the dihedral angle for carbon-carbon double bonds. The dihedral function is given by (Brenner et al. 2002; Lindsay and Broido 2010)

$$b_{ij}^{\mathrm{DH}} = \frac{T_0}{2} \sum_{k,l \neq i,j} f_{ik}^{C} f_{jl}^{C} \left[1 - \cos^2\left(\phi_{ijkl}\right)\right], \tag{4.19}$$

where T_0 is a parameter and ϕ_{ijkl} is the dihedral angle of atoms i, j, k, and l, and is given by (Lindsay and Broido 2010; Brenner et al. 2002)

$$\cos\left[\phi_{ijkl}\right] = \boldsymbol{\eta}_{jik} \cdot \boldsymbol{\eta}_{ijl}, \tag{4.20}$$

where

$$\boldsymbol{\eta}_{jik} = \frac{\mathbf{r}_{ji} \times \mathbf{r}_{ik}}{|\mathbf{r}_{ji}||\mathbf{r}_{ik}| \sin(\theta_{ijk})}. \tag{4.21}$$

In the above equations, $\boldsymbol{\eta}_{jik}$ and $\boldsymbol{\eta}_{ijl}$ are unit vectors normal to the triangles formed by atoms j, i, k, and i, j, l, respectively.

4.2.2 MD Algorithms

MD algorithms involve performing step-by-step numerical integration of Newton's equation of motion in Equation (4.1) in order to calculate the atomic trajectories. Several algorithms have been developed to perform the numerical integration of the equations of motion such as the (Frenkel and Smit 2002; Allen 2004; and Stote et al. 1999):

- Verlet algorithm
- Leap-frog algorithm
- Velocity-Verlet algorithm
- Beeman's algorithm
- Gear predictor-corrector algorithm

The MD algorithm can be chosen based on the following criteria considering one's specific requirements (Frenkel and Smit 2002; Allen 2004; Cai 2005; and Stote et al. 1999):

- it satisfies the conservation law of energy (important for a simulation in the microcanonical ensemble)
- it permits the use of a long time step for integration (i.e. allows infrequent and accurate evaluations of forces)
- it is computationally efficient (i.e. low memory storage and high computational speed)
- it copes with both the long and short time scales relevant to the problem of interest in terms of stability, accuracy and energy conservation (i.e. low energy drifts for overall time scales)
- it has a simple form of the algorithm and is easy to implement
- it is time reversible

In this study, MD simulations were performed using the 'velocity-Verlet algorithm', which tends to have moderate energy conservation and limited long-term energy drifts (Frenkel and Smit 2002). This algorithm is one of the simplest and most widely used algorithms (Frenkel and Smit 2002; Allen 2004; and Czichos et al. 2011). It has important features such as exact time reversibility, simplicity of the algorithm, permits large time steps and is easy to program (Allen 2004). Thus, the following discussion is focused only on the 'velocity-Verlet algorithm'. This algorithm yields positions $\mathbf{r}(t)$ and velocities $\mathbf{v}(t)$ at time t as (Frenkel and Smit 2002)(see page 65)

$$\mathbf{r}(t+\Delta t) = \mathbf{r}(t) + \mathbf{v}(t)\Delta t + \frac{\mathbf{F_i}(\mathbf{r}(t))}{2m_i}\Delta t^2, \tag{4.22}$$

and

$$\mathbf{v}(t+\Delta t) = \mathbf{v}(t) + \frac{\mathbf{F_i}(\mathbf{r}(t+\Delta t)) + \mathbf{F_i}(\mathbf{r}(t))}{2m_i}\Delta t, \tag{4.23}$$

where

$$\mathbf{F}_i(\mathbf{r}^N(t+\Delta t)) = -\nabla_i U(\mathbf{r}^N(t+\Delta t)). \tag{4.24}$$

It can be noted that the velocity-Verlet algorithm uses information of positions, velocities and forces from the current time steps to advance the atomic positions and velocities with a discrete (i.e. non-continuous) time step Δt. In order to carry out a simulation the initial positions and velocities must first be assigned to all atoms in the system. The initial particle positions $\mathbf{r}^N(0)$ can be chosen based on the lattice structure of the systems that are to be simulated. The initial velocities $\mathbf{v}(0)$ of every atom can be drawn from a velocity distribution such as Maxwell-Boltzmann or Gaussian distribution

(Frenkel and Smit 2002; Allen 2004; Cai 2005; and Stote et al. 1999) at a given temperature T. The force term $\mathbf{F}$ is calculated from the specified force potential using Equation (4.1). A typical flow chart for the progress of an MD simulation is shown in Figure 4.3 (Cai et al. 2010).

4.2.3 Periodic Boundary Conditions and Minimum Image Convention

Molecular dynamics aims to provide information about the macroscopic properties from the simulation of atomic trajectories of a microscopic system of atoms or molecules (Cai 2007; Frenkel and Smit 2002). Hence, the system is designed with a small number of atoms from a real system of interest with atoms or molecules of a macroscopic sample size. However, surface effects can dominate the bulk properties in the small systems that are feasible to simulate. For instance, a system of 1000 atoms arranged in a simple $10 \times 10 \times 10$ cube will have 488 ($= 10^3 - 8^3$) atoms at the surface, which is nearly half of the system size (Nakano 2014; Frenkel and Smit 2002; Allen 2004). Even a large system with $\sim 10^{23}$ atoms will have 6% surface atoms in total (Cai 2007; Frenkel and Smit 2002; Allen 2004). The influence of these surrounding atoms cannot be ignored for a small system of 10^3 to 10^6 atoms in MD simulations. Therefore, a special treatment of boundary conditions in the simulation volume is essential to mimic the presence of an infinite bulk of surrounding atoms in a model system. This is usually achieved by employing periodic boundary conditions (PBCs), which surround the simulation box with replicas of itself to avoid including too many atoms in the simulation domain, while maximising the numerical efficiency and eliminating surface artefacts (Cai 2007; Frenkel and Smit 2002; Allen 2004). Simulations can be performed efficiently for bulk materials with a microscopic system of atoms and molecules by employing PBCs (Cai 2007; Allen 2004).

An illustrative representation of PBCs is shown in Figure 4.4. The atoms in the image cells are assumed to behave in exactly the same way as the primary cell and they can freely enter or leave any cells. Hence, if an atom moves in the primary cell, the replica of that atom in all image cells moves in a concerted manner by the same amount (Cai 2007; Frenkel and Smit 2002; Allen 2004; Le 2010). For instance, if an atom leaves the cell by crossing a boundary, their images simultaneously enter through the opposite face of that cell. It is not possible to compute the interactions between each particle and the periodic images of every other particle, so the *minimum image convention* is generally applied, in which the only non-bonded interactions that are considered for a particle in the primary cell are those with the nearest images

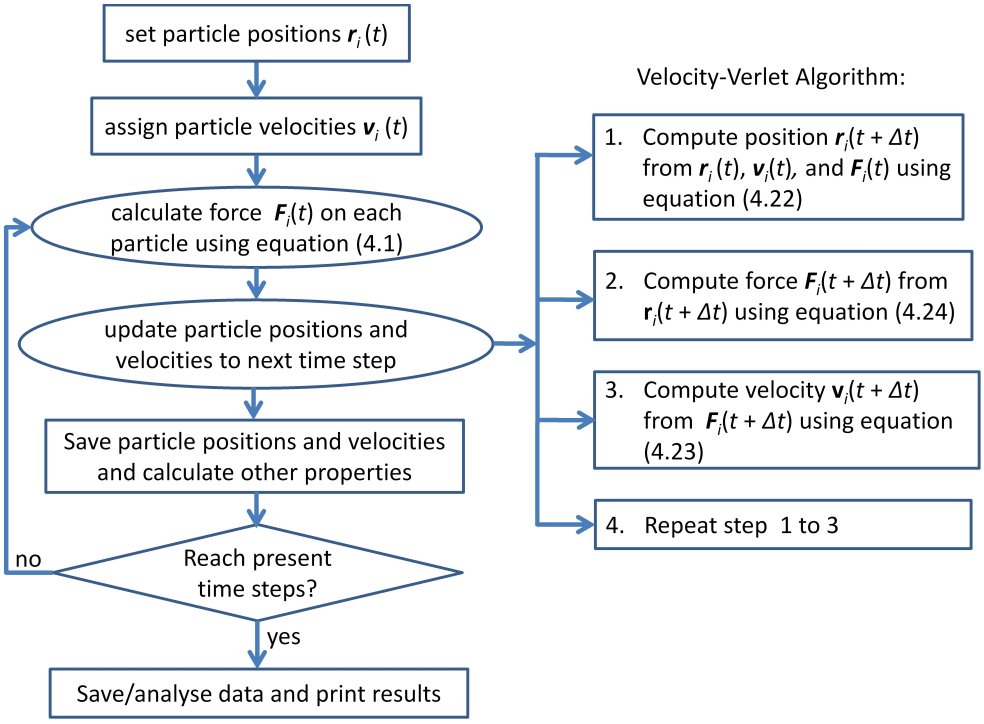

Figure 4.3: Flow chart of typical MD simulation using velocity-Verlet algorithm (Adapted from Cai et al. (2010)).

of other particles in the system (Wahnström 2013; Allen 2004; Frenkel and Smit 2002). The minimum-image convention is exact if the side length of the simulation box is at least twice the cut-off radius of the interactions. To avoid finite-size effects associated with simulating a finite system, the simulation box side length should be at least twice the correlation length between pairs of particles. In addition, electrostatic interactions cannot be truncated without introducing an infinite error to thermodynamic quantities such as the system energy, so alternative methods must be used to calculate electrostatic energies and forces in periodic systems (Hockney and Eastwood 1989; Plimpton et al. 1997).

4.2.4 Thermostats and Barostats

In classical MD simulations, it is necessary to control the temperature of the system in order to simulate a particular thermodynamic state (e.g. constant temperature), which is difficult in a finite system (Karniadakis et al. 2005). Adding a thermostat allows one to do this efficiently. In general, a target temperature is specified according to the user's requirement and the ther-

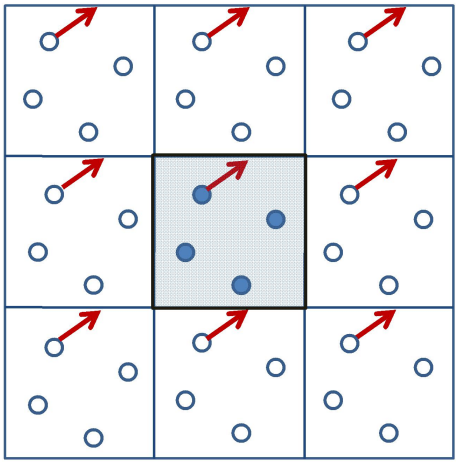

Figure 4.4: An illustrative view of periodic boundary conditions. As a particle moves out of the primary cell (shaded box), a replica image of the atom moves in to replace it (Adapted from Allen (2004)).

mostat attempts to equilibrate the system to the target temperature. Many algorithms exist to simulate the target or constant temperature. Some of the most commonly employed temperature coupling schemes (which are also applied to the MD simulations in this study) are (Karniadakis et al. 2005):

- Velocity scaling
- Berendsen thermostat
- Langevin thermostat
- Nosé-Hoover thermostat

The *Velocity scaling* method scales the particle velocities at intervals to alter the temperature of the system. In MD simulations, the instantaneous temperature of the system is related via the momentum of the particles as (Rühle 2007)

$$\sum_{i=1}^{N} \frac{|\mathbf{p}_i|^2}{2m_i} = \frac{k_B T}{2}(3N - N_C), \tag{4.25}$$

and

$$T = \sum_{i=1}^{N} \frac{m_i {v^2}_i}{N_{\text{dof}} k_B}, \tag{4.26}$$

where ($3N$ - N_C) = N_{dof} is the total number of degrees of freedom with N_C being the number of constraints, $\mathbf{p}$ is the momentum, T is the instantaneous

temperature at any time t and k_B is the Boltzmann constant. In order to alter the current temperature T, the velocities are multiplied by a factor λ, then the change of temperature can be calculated as (Rühle 2007; Tuckerman 2010)

$$\Delta T = \sum_{i=1} \frac{m_i(\lambda v_i)^2}{N_{\text{dof}} k_B} - \sum_{i=1} \frac{m_i {v_i}^2}{N_{\text{dof}} k_B}, \tag{4.27}$$

$$\Delta T = (\lambda^2 - 1)T. \tag{4.28}$$

Thus, the average temperature of the system can be maintained at a desired temperature T_0 by scaling the velocities of the particles with the factor $\lambda = \sqrt{\frac{T_0}{T}}$ at each time step. Hence, a thermostat using velocity rescaling is straightforward to implement and useful for controlling temperature in the warm-up/initialisation phase of a simulation (Johnson et al. 2012; Hünenberger 2005). However, a drawback of this method is that as it does not allow temperature fluctuations that corresponds to the canonical ensemble (Karniadakis et al. 2005; Frenkel and Smit 2002; Rühle 2007).

The *Berendsen thermostat* uses an external (hypothetical) heat bath with fixed temperature T_0 to maintain the temperature of the system. The heat bath is coupled to the system following a coupling strength parameter τ, which determines how tightly or loosely the system is coupled with the heat bath and the rate at which the system temperature reaches the desired temperature (Karniadakis et al. 2005; Rühle 2007). The deviation of the system temperature from T_0 is slowly corrected according to (Karniadakis et al. 2005; Rühle 2007)

$$\frac{dT}{dt} = \frac{1}{\tau}(T_0 - T). \tag{4.29}$$

As shown in Equation (4.29), the *Berendsen thermostat* produces an exponential decay of the system temperature towards the desired temperature. Thus, at each time step the velocities of the particles are rescaled by a factor λ, where (Rühle 2007)

$$\lambda = \left[1 + \frac{\Delta t}{\tau}\left\{\frac{T_0}{T(t - \frac{\Delta t}{2})} - 1\right\}\right]^{\frac{1}{2}}. \tag{4.30}$$

In practice, the value of the coupling parameter τ is chosen with care to avoid unrealistic temperature fluctuations. However, the fluctuations generated using the *Berendsen thermostat* do not correspond to the canonical ensemble.

The *Langevin thermostat* controls the temperature in the system by considering the motion of particle through an interaction with a background implicit solvent as if the particle is immersed in a bath of smaller particles. The smaller particles (solvent) create a damping force to the momenta of the

particles and give random pushes to the particle to adjust the temperature. The total force on each particle i has the form (Schneider and Stoll 1978; Yuan 2010; Dünweg and Paul 1991; Hünenberger 2005)

$$m_i \ddot{\mathbf{r}}_i = F_\mathrm{c} + F_\mathrm{f} + F_\mathrm{r}, \tag{4.31}$$

where

$$F_\mathrm{f} = -\frac{m_i}{\zeta}\dot{\mathbf{r}}_i \tag{4.32}$$

and

$$F_\mathrm{r} \propto \sqrt{\frac{k_\mathrm{B} T m_i}{\Delta t\, \zeta}}. \tag{4.33}$$

Here, F_c is the conservative force term computed from the inter-particle interactions (Equation (4.1)), F_f is a frictional or viscous drag force term proportional to the particle's velocity $\dot{\mathbf{r}}_i$ computed for each particle using a user-assigned damping factor ζ, and F_r is the random force due to the solvent atoms at a temperature T derived from the fluctuation-dissipation theorem (Johnson et al. 2012; Tuckerman 2010; Dünweg and Paul 1991; Hünenberger 2005). The Langevin thermostat provides approximate thermal behaviour for the canonical ensemble and allows the use of larger time steps. However, the Langevin thermostat is not suitable for a system where diffusion coefficients are of interest, as momentum transfer is destroyed in this approach (Johnson et al. 2012; Tuckerman 2010).

The *Nosé-Hoover thermostat* uses an extended-ensemble approach, in which an extra thermal reservoir variable and a frictional term is introduced in the equations of motion to extend the system Hamiltonian (Karniadakis et al. 2005). The equation of motion of a particle is then given by

$$\frac{d^2\mathbf{r}_i}{dt^2} = \frac{\mathbf{F}_i}{m_i} - \xi\frac{d\mathbf{r}_i}{dt}. \tag{4.34}$$

In this equation, ξ is a variable introduced to include the frictional force via a factor proportional with the particle's velocity. The friction variable is a dynamic quantity and the time derivative of this quantity is calculated from the difference between the kinetic energy corresponding to the instantaneous temperature T and the reference temperature T_0 (Karniadakis et al. 2005). It can be written as (Karniadakis et al. 2005)

$$\frac{d\xi}{dt} = \frac{1}{Q}\left(\sum_{i=1}^{N} m_i \dot{r}_i^2 - 3Nk_B T_0\right) = \frac{1}{Q}\left(T - T_0\right), \tag{4.35}$$

where N is the number of particles in the system and Q is a constant referred to as the effective mass, which represents the coupling to the thermal reservoir/bath. Hence the coupling strength of the thermostat is determined by

the value of Q. In this approach, although the Hamiltonian (energy) of the simulated system fluctuates, the total Hamiltonian in the extended system is conserved and produces the canonical ensemble in the primary simulation system for microcanonical dynamics in the extended system (Finnerty 2011). However, the extended system is not guaranteed to be ergodic (the hypothesis which states that the time average equals the ensemble average (Stote et al. 1999)).

At times it is desirable to perform a simulation at constant pressure, and sometimes at both constant system temperature and pressure. In a simulated system, constant pressure is maintained by controlling the system volume. Several barostat algorithms exist to simulate a constant/target pressure by adjusting the volume of the simulated system. Some of the commonly used barostats are the (Shell 2012):

1. Berendsen barostat: A similar technique to the Berendsen thermostat. At each step, the system volume (size) is periodically rescaled to maintain the desired pressure. However, this thermostat approach does not reproduce a statistical mechanical ensemble.

2. Nosé-Hoover barostat: A similar approach to the Nosé-Hoover thermostat. The system is coupled with a fictitious pressure bath using an extended Lagrangian system to impose the desired pressure and reproduces the isothermal-isobaric (NPT) ensemble when combined with the Nosé-Hoover thermostat.

3. Parrinello-Rahman barostat: This is an extension of the constant-pressure method of the Nosé-Hoover barostat that allows dynamic shape change of the simulation box as well as size (volume).

4.2.5 Averages and Statistical Errors

In molecular dynamics simulations, useful information of a quantity is obtained by averaging the information generated on the system at the microscopic level. The average quantities are evaluated by performing time averaging of the microscopic quantities (Wahnström 2013). For an observable quantity A of the system in a molecular dynamics simulation, which is a function of time t, time-averages of A along the trajectory generated in phase-space can be obtained for a finite time interval τ as (Frenkel and Smit 2002; and Wahnström 2013)

$$\overline{A} = \frac{1}{M}\sum_{t=1}^{M} A_t, \quad (M = \text{total number of time steps} = \frac{\tau}{\Delta t}) \tag{4.36}$$

In statistical mechanics, thermodynamic quantities are related to ensemble averages of system properties, in which an *ensemble* can be considered as a large collection of different microscopic states in a system that share an identical/constant macroscopic state (Stote et al. 1999; Wahnström 2013). The average of a quantity A is defined in terms of *ensemble average* $\langle A \rangle$, which is an average taken over states of the system consistent with the statistical ensemble corresponding to the experimental observables. According to the *ergodic* hypothesis, if the system is allowed to evolve for an infinite amount of time, the system will eventually visit all possible states, then the time average equals the ensemble average (Stote et al. 1999; Wahnström 2013). Hence, at equilibrium, if $\tau \to \infty$:

$$\langle A \rangle = \overline{A} \tag{4.37}$$

Some example time averages in MD simulations are (Stote et al. 1999; Cai et al. 2010)

$$\text{Potential energy} : \overline{U} \approx \langle U \rangle = \frac{1}{M} \sum_{j=1}^{M} U_j \tag{4.38}$$

$$\text{Kinetic energy} : \overline{K} \approx \langle K \rangle = \frac{1}{M} \sum_{j=1}^{M} \left\{ \sum_{i=1}^{N} \frac{m_i}{2} \mathbf{v}_i . \mathbf{v}_i \right\}_j \tag{4.39}$$

$$\text{Temperature} : \overline{T} = \frac{1}{3Nk_B} \frac{1}{M} \sum_{j=1}^{M} \left\{ \sum_{i=1}^{N} m_i \mathbf{v}_i . \mathbf{v}_i \right\}_j \tag{4.40}$$

where M is the number of configurations ($= \frac{\tau}{\Delta t}$) with τ being the total simulation time and Δt being the timespacing.

To generate exact averages for a given model from the molecular simulations, it is essential to perform the simulation for an infinitely long time (Frenkel and Smit 2002). Since the results of the MD simulations are obtained by averaging over a finite time period, the simulation results are always subject to statistical errors (Frenkel and Smit 2002; Wahnström 2013). Therefore, it is important to estimate the statistical errors or error bounds associated with the average value obtained from the MD simulations. The error can be estimated from the variance of the mean value with the assumption of Gaussian approximation (Frenkel and Smit 2002; Wahnström 2013). The variance in the mean of an observable quantity A can be written as (Frenkel and Smit 2002; Wahnström 2013)

$$\sigma^2(\overline{A}) \approx \frac{2\tau_c}{\tau} (\overline{A^2} - \overline{A}^2), \tag{4.41}$$

where $\frac{\tau}{(2\tau_c)}$ is an estimate of the number of uncorrelated data points of A in a simulation of length τ and τ_c is the characteristic decay time of the

correlations in fluctuations of A, which can be evaluated as (Frenkel and Smit 2002; Wahnström 2013)

$$\tau_c \equiv \frac{1}{(\overline{A^2} - \overline{A}^2)} \int_0^\infty dt \langle [A(t) - \overline{A}][A(0) - \overline{A}] \rangle. \tag{4.42}$$

The relative variance in $\overline{A}$ is therefore given by (Frenkel and Smit 2002)

$$\frac{\sigma^2(\overline{A})}{\overline{A}^2} \approx \frac{2\tau_c}{\tau} \frac{(\overline{A^2} - \overline{A}^2)}{\overline{A}^2}. \tag{4.43}$$

As shown in Equation (4.43), the root-mean-square error in $\overline{A}$ is proportional to $\sqrt{\frac{\tau_c}{\tau}}$, which indicates that the variance is inversely proportional to the number of uncorrelated data points (Frenkel and Smit 2002).

Another method to estimate the statistical error is to perform *block averaging*. The block averaging method is a powerful tool to determine the simulation length (total time) required to yield a reliable estimate of a quantity (Frenkel and Smit 2002). A block average is a time average over a given block length t_B (Frenkel and Smit 2002)

$$\overline{A}_B \equiv \frac{1}{t_B} \int_0^{t_B} dt A(t). \tag{4.44}$$

To obtain the variance in the block averages of a given value of t_B, simulation can be performed for a number of blocks n_B of block size t_B. Then, the variance can be evaluated from the block averages of n_B adjacent blocks of length t_B as (Frenkel and Smit 2002)

$$\sigma^2(\overline{A}_B) = \frac{1}{n_B} \sum_{b=1}^{n_B} (\overline{A_B} - \overline{A})^2. \tag{4.45}$$

Similar to Equation (4.41), the variance in the mean can be expressed as (Frenkel and Smit 2002)

$$\sigma^2(\overline{A}_B) \approx \frac{\tau_c}{t_B} (\overline{A^2} - \overline{A}^2). \tag{4.46}$$

Since τ_c is as yet unknown, defining (Frenkel and Smit 2002)

$$P(t_B) \equiv t_B \times \frac{\sigma^2(\overline{A}_B)}{[\overline{A^2} - \overline{A}^2]}. \tag{4.47}$$

It can be seen that in the limit of $t_B \gg \tau_c$, $P(t_B)$ must approach τ_c. The limit of $P(t_B)$ for $t_B \to \infty$ can be estimated by plotting $P(t_B)$ versus t_B (Frenkel and Smit 2002; Wahnström 2013). The limit of $P(t_B)$ can be used to determine whether the simulation is of sufficient duration to estimate the mean of a particular quantity. If $P(t_B)$ is strongly dependent on t_B for the total simulation duration $t_B = \tau$, then it can be assumed that the run is not long enough for the estimation of any particular quantity.

4.3 Simulation Tools: LAMMPS, VMD, Tcl Script, TopoTools

An open source classical MD simulation code, LAMMPS (Large-scale Atomic/ Molecular Massively Parallel Simulator), developed at Sandia National Laboratories, a US Department of Energy facility, was used to conduct the MD simulations (Plimpton 1995; LAMMPS-Manual 2013). A post-processing software package, VMD (Visual Molecular Dynamics) was used for 3D visualisation, modelling, and analysis of molecular structures. Tcl, an embedded scripting language of the VMD, along with TopoTools, an additional plugin for VMD, was used to create the initial configuration files for the molecular systems for the MD simulations.

LAMMPS has a wide range of force potentials, ensembles and boundary conditions built in C++ code for running molecular simulations under different physical conditions. It allows the code to be modified or extended for new capabilities such as new force fields, atom types, boundary conditions, or diagnostics. It can model an ensemble of particles in a solid, liquid or gaseous state for atomic, polymeric, biological, metallic, granular and coarse-grained systems. LAMMPS allows the particles to interact via short- or long-range forces with a variety of force fields and boundary conditions (Plimpton 1995; LAMMPS-Manual 2013). It is specially designed to run efficiently on massively parallel computers. To run the simulation in multiple processors on parallel machines, LAMMPS uses spatial-decomposition techniques which partition the simulation domain into small 3D sub-domains based on the number of processors assigned to run the simulation, with each sub-domain assigned to each processor (Plimpton 1995; LAMMPS-Manual 2013).

VMD is an interactive graphics program originally designed for molecular visualisation and analysis of bio-polymers such as proteins, nucleic acids, lipids, and membranes. It is an open source software developed by the Theoretical and Computational Biophysics Group at the University of Illinois at Urbana-Champaign (Stone 2012; VMD-Guide 2012).

TopoTools is a VMD plugin developed for manipulating topology information, which can be used for generating complete input data structure files for MD codes such as LAMMPS by replicating or combining multiple molecular systems in the VMD platform (Kohlmeyer 2013).

A typical input script for LAMMPS, the data file specifying the initial configuration, and the Tcl script for creating the data file are provided in Appendix E.

4.4 Implementation of MD for Nano-channel Flow and Acoustics Problems

This section presents a review of previous MD simulations of relevance to molecular modelling of nanoscopic acoustic absorption mechanisms. The purpose of this review is to provide an overall assessment of the capability of MD simulations for various applications in nanoscale flow and acoustic problems and, in addition, to present a comparison of previously simulated physics with the phenomena relevant to the current problem. The challenges associated with simulations in the audible frequency range will also be considered. This review is primarily focused on the capabilities of MD methods, based on their previous application to simulate the phenomena that are expected to be crucial for accurate modelling of nanoscale acoustic absorption in CNTs.

4.4.1 Wave Propagating Media at the Nanoscale

A number of MD simulation studies have investigated fluid transport and diffusivity in nanochannels. Mutat et al. (2012) simulated methane (CH_4) gas flow through a single-walled carbon nanotube (SWCNT) by equilibrium (EMD) and non-equilibrium (NEMD) molecular dynamics to investigate molecular diffusion (self and transport diffusivity) of gas inside nanopores at various tube fluid loadings. Ban and Huang (2012) studied gas permeation of CO_2/N_2 through a carbon nanotube membrane using MD to investigate the potential of flue gas separation. The purpose of the study was to develop and validate transport theory for gas separation and to gain a fundamental understanding of gas permeation through CNT membranes. Results showed that the simulations agreed with experimental measurements. Arora and Sandler (2006) conducted a similar study using EMD simulations to determine the separation performance of a nanotube membrane by simulating mass transport of pure N_2, O_2, and an air mixture in a SWCNT at 100 K. Mao and Sinnott (2000) used MD simulations to study the movement of polyatomic molecules through nanotubes by modelling the diffusive and dynamic flow of methane, ethane, and ethylene through SWCNTs at room temperature, while Tuzun et al. (1996) used MD to study helium and argon flow inside CNTs. Similarly, Liu et al. (2010), Sokhan et al. (2004), and Ackerman et al. (2003) used MD simulations effectively to study the self and transport diffusivity of N_2, Ar, and Ne. In most of these cases, MD simulations captured the nanoscale transport properties successfully.

Other MD studies have been mainly concerned with flow properties such

as the frictional stress, slip velocity, and slip length of typical compressible fluids flowing through the nanotubes. Kandemir and Kaya (2012) simulated lid-driven micro-cavity gas flow using hard-sphere molecules and a single-species gas. They investigated the major flow characteristics of lid-driven cavity flow (such as the formation of the primary vortex, pressure variations, and the velocity profile) under varying subsonic speeds and lid temperatures. Interesting behaviour of the compressibility in the micro-cavity was observed at low Mach numbers even though the regime is widely considered to be within the incompressible flow region. It was concluded in this work that compressibility and temperature variations in the flow could easily be included in MD with current computational capabilities; however, it was suggested that greater computational resources would be required to simulate higher Reynolds number (*Re*) flows. Mantzalis et al. (2011) used MD simulation to examine layering of CO_2 gas transported through a SWCNT subjected to variations of pressures and temperatures of 1-20 bar and 300 - 400 K, respectively, while Hu et al. (2007) simulated air flow through an array of carbon nanotubes using MD.

Longhurst and Quirke (2007) simulated temperature-driven pumping of decane through SWCNTs to investigate the possible applications of nanotubes for dynamic nanoscale reaction vessels. Although their simulation results were qualitatively accurate, they showed that very high pressures can develop in the miniature vessels of nanotubes due to the strong capillary forces, which also act to draw the molecules into nanopores. Chaudhri (2005) implemented MD methods to understand the fluid flow properties inside nanotubes by simulating argon gas flow inside SWCNTs. He studied the transport behaviour and structure of argon atoms for flow simulation cases similar to those of Tuzun et al. (1996), Dendzik et al. (2004), Lee and Sinnott (2004), and Mao and Sinnott (2000). Sokhan et al. (2002) studied steady-state Poiseuille flow in nanopores using NEMD by simulating the gravity-driven flow of methane through a long cylindrical pore of SWCNT at ambient conditions. Lee and Sinnott (2004) conducted NEMD simulations of gas flow of methane in several open-ended SWNCTs to study the transport behaviour of flow through nanotubes. They found that the molecular flow rate depends on the tube diameter but does not depend on the symmetric helical structure of the nanotubes, i.e. the methane gas transport is not affected by the difference in helicities (armchair/zigzag) of the CNTs. They observed non-equilibrium transport behaviour of methane flow caused by the minuscule dimensions of the systems, indicating the unique mechanism for nanoscale flow. Liu et al. (2012) conducted an experimental investigation and MD simulations of gas flow characteristics through nanopores with an emphasis on the friction and

gas viscosity. They conducted an experiment with controlled flow rates in a flow tube with a pressure drop across nanopore membranes. Their MD simulations were of argon gas and an argon nanopore made of fixed atoms. MD results showed that the nanoscale flows have a much lower viscosity and friction coefficient than those in a microscale channel, due to less frequent intermolecular collisions between the gas molecules and more frequent collisions with the wall.

Barisik et al. (2010) used MD for the simulation of linear Couette flow of argon at a Knudsen number of $Kn = 10$, which created a new benchmark for the simulation of high Knudsen number transition flows using MD. In their further work (Barisik and Beskok 2011), they used MD for simulating shear-driven gas flows in nanochannels and revealed that the surface (solid)-gas (fluid) interactions had a significant effect on the velocity, density, shear stress, and normal stress distributions at the interface. These kinds of behaviour were previously confirmed by other researchers (Kim 2009; and Banerjee 2008) for nanoscale flow channels, which indicate the potential capability of the MD method, without requiring major modifications other than slight modifications to the boundary wall model or potential energy model based on the requirements of the application under consideration.

4.4.2 Acoustics (pressure fluctuation and wave front)

Various MD studies of acoustic problems have been performed to simulate shock wave propagation in gaseous media. Yano (2012) applied large-scale MD simulations to clarify the presence of nonlinear and non-equilibrium processes in large amplitude and high frequency ($\sim$ GHz) sound wave propagation in a gas (argon). It was observed that the wave front exhibited a stream-like profile instead of a wave-like profile, with the direct transport of mass, momentum, and energy, which moves with a larger speed than the sound speed of an ideal gas (Yano 2012). This behaviour confirms the deviation from the classical behaviour of high-frequency linear standing-wave analysis. Deladerriere et al. (2008) used MD to measure the variation of the velocity of acoustic wave propagation in simplified nuclear glasses and pure silica, in order to understand the decrease in the Rayleigh velocity in materials subjected to elastic irradiation (Deladerriere et al. 2008). Makeev et al. (2009) conducted a similar molecular simulation to study shock-wave propagation in a CNT-reinforced composite material in an amorphous silicon carbide matrix. Their objective was to understand the effect of the presence of aligned nanotubes and their dynamic and structural changes on the shock wave structure and the composite materials. It was found that the presence of

CNTs reduced the shock-wave velocity and modified the wave-front structure in a wide range of impact velocities, which was considered to be due to changes in the degree of shock-induced heating and the resultant variation of viscosity in the shock-loaded target. Hofmann (2003) applied MD for shock-wave simulations in argon at the critical density and a temperature of 306 K. He simulated steady and unsteady effects of shock-wave formation by using a piston set in impulsive motion (with velocities ranging from 300 to 900 m/s) to demonstrate the resulting density and temperature variations and directional temperatures across the shock waves. Valentini and Schwartzentruber (2009) studied the structure of normal shock waves in dilute argon by coupling the MD domain with a computational fluid dynamics (CFD) solver using a realistic Lennard-Jones (LJ) potential. The continuum solver was coupled with the atomistic region to correctly generate the inflow and outflow particle reservoirs, which allowed the simulation to achieve sufficient statistical accuracy to calculate the structure of the normal shock wave. A detailed comparison of DSMC and MD results showed near-perfect agreement for density and temperature profiles in the high temperature range of 300-8000 K. However, it was shown that the DSMC simulation with the variable-hard-sphere (VHS) collision model was not capable of reproducing the shock profiles, particularly the temperature profiles, over a broad temperature range. It was concluded that MD might be a valuable tool for more complex flows, including highly non-equilibrium molecular processes for which experimental data is not available. Valentini et al. (2013) studied the structure of normal shock waves in noble gas mixtures of Xe/He and Ar/He of various compositions. The MD results showed an overall good agreement with experimental data, although two discrepancies were found: the prediction of the monotonic rise in the density profile for Xe/He shocks instead of an overshoot as observed in experiments, and the prediction of an overshoot in the temperature profile for Ar/He mixtures that was absent in the experiments. They showed that MD simulations are computationally feasible and capable of reproducing the experimental results for shock-wave structures at low densities. These implementations of MD again confirm its wide range of applicability for the complex physics of flow problems in acoustics.

4.4.3 Structural Vibration at the Nanoscale (fluid-structure interactions)

Chen et al. (2011) simulated water flow passing a SWCNT using MD and continuum mechanics (CFD) to investigate the flow resistance and energy

transfer between water molecules and CNTs induced by the nanoscale fluid-structure interactions. They observed a linear dependence between the drag force and flow velocity at small Reynolds numbers up to 0.1, which could be predicted by Stokes law. However, at higher speeds (i.e. elevated Reynolds numbers), a significant deviation from linearity was identified from the MD simulations, indicating a reduction in the viscosity due to friction-induced local heating and flow-induced structural vibrations, resulting in a weaker drag force, which was not captured by the CFD simulations. A significant increase in the CNT vibration was observed at higher flow speeds, induced by the excitation of low-frequency vibration modes, which had a substantial effect on the energy transfer between the water molecules and the nanotube, indicating the importance of fluid-structure interactions for nanoscale flows. Li and Hong (2007) simulated the gas transport of Ar molecules through silver (Ag) nanochannels using MD. They investigated the diffusion of gas under the combined effects of the vibration of the channel, gas-wall binding energy, and channel size. It was found that the vibration of the channel played an important role in gas transport through the nanochannels for strong fluid-structure binding energies. Insepov et al. (2006) used MD simulations to predict a new "nanopumping" concept using carbon nanotubes that would enable the pumping of gases or liquids through nanochannels. Fluid-surface interactions between the H_2 and He gas atoms and the SWCNT were explicitly incorporated in MD simulations to properly capture the "nanopumping" effect (i.e. activation of an axial gas flow inside the nanotubes at a high macroscopic velocity in the direction of a travelling surface wave). However, the characteristic frequency of the wave for activating the nanopumping effect was high compared with the frequency required for the velocity to reach a hyperthermal value and the maximum effect was observed at approximately 38 THz (based on the chosen nanotube length of 10 nm). The effect was found to depend on the ratio of nanotube length and the wavelength of the surface wave.

4.4.4 Heat Transfer at the Nanoscale (thermo−acoustic effect and heat conduction)

Banerjee (2008) used MD to simulate hydrogen storage in CNTs and CNT growth and heat transfer in order to characterise nanoscale charge, mass, and thermal transport. He identified discontinuities in thermal transport and a novel growth mode for nanotubes that was successfully validated by experiment. Kim (2009) applied MD to simulate heat transfer in nanoscale liquid films. He simulated fluid-solid thermal interactions by accounting for thermal

oscillations of the wall molecules and their influence on the fluid molecules, overcoming the limitations of previous simulations that considered the wall molecules as fixed molecules, and which were therefore unable to simulate the work done by moving wall molecules on the fluid. This method was found to model heat conduction in nanochannels successfully, allowing coupled momentum and energy transport to be simulated simultaneously (Kim 2009). Osman and Srivastava (2005) used MD to investigate transient heat-pulse propagation in SWCNTs of varying chirality and diameter. They studied temporal and spatial variations of the kinetic temperature in CNTs using MD simulations and observed the propagating wave packets induced by the heat pulse. It was found that heat pulses of picosecond (ps) duration generated several wave packets that propagated at the speed of sound corresponding to longitudinal acoustic (LA) phonons and twisted phonon modes (TW), second sound waves, and diffusive components. The simulations revealed that zigzag CNTs carry more heat energy than armchair nanotubes, which explains why zigzag CNTs show higher steady-state thermal conductivity than armchair CNTs, as reported in previous investigations. Thomas et al. (2010) applied MD simulations to examine the thermal conductivities (transition to fully diffusive phonon transport) of empty and water-filled SWCNTs with varying diameter and tube length. It was found that the required length to obtain fully diffusive thermal transport and the magnitude of the conductivity in empty CNTs decreased with tube diameter and that the conductivity was 20-35% higher than that in water-filled CNTs. The reduction of the thermal conductivity in water-filled CNTs was attributed to substantial low-frequency phonon scattering due to interactions with water molecules, indicating the influence of solid-liquid interactions on the thermal conductivity of nanotubes.

4.5 Potential Cases for MD Simulation of Acoustic Absorption Mechanisms

No MD simulations have been carried out previously for either compressible or incompressible nanoscale flow in which all physical phenomena relevant to acoustic absorption within CNTs in air were simultaneously considered. All of the cases discussed were evaluated by comparing their simulated physics against the phenomena deemed relevant to acoustic absorption. This comparison is given in Table 4.1. As indicated in the table, most previous MD simulations of nanoscale phenomena have been conducted to investigate flow properties. None have accounted for fluid-structure interactions, bi-directional heat transfer, or acoustic wave propagation in the audible fre-

quency range or even in the ultrasonic frequency range. In order to assess whether MD can simulate acoustic absorption mechanisms, for which a number of multi-physics criteria must be considered simultaneously, we have considered four different cases of previous molecular simulations, those conducted by Chen et al. (2011), Carlborg et al. (2008), Sokhan et al. (2002), and Hadjiconstantinou and Garcia (2001). These validate the physics of structural vibration, bi-directional heat transfer, flow properties and compression effects, and acoustic effects, respectively. While each of these simulation cases does not replicate all of the physics that is relevant to the current problem, each case captures a subset of the relevant phenomena and together they can certainly demonstrate the ability of MD to account for all of the required physics at the nanoscale. The case presented by Chen et al. (2011) can be used to validate fluid-structure interactions between CNTs and water molecules and structural vibrations of CNTs induced by energy transfer between the fluid and solid wall. The disadvantages of this case are the incompressible nature of the fluid flow and lack of consideration of flow inside the CNT. Flow inside the CNT might be important for acoustic wave propagation. Regarding the validation of acoustic effects, Hadjiconstantinou and Garcia (2001) simulated sound waves propagating in a dilute hard-sphere gas through a rectangular microchannel (not a CNT) using DSMC. These DSMC results can be compared with MD simulation results for an analogous physical arrangement. The MD simulation of transient heat-pulse propagation in a CNT conducted by Osman and Srivastava (2005) provides a suitable platform for simulating heat transfer in nanotubes, as the effects of phonon modes were taken into consideration. However, the ideal validation case would include the influence of solid-liquid thermal interactions. Nevertheless, Osman and Srivastava's (2005) study is an appropriate example for validating the simulation capability of MD for thermal energy transport in nanotubes. The simulation case of thermal boundary resistance conducted by Carlborg et al. (2008) can be considered to simulate the effect of fluid-structure interactions on heat transfer for capturing the bi-directional nature of heat flow. Their (Carlborg et al. 2008) study used NEMD to simulate the heat pulse propagation in SWCNTs surrounded by argon matrices and demonstrated the contribution of the surrounding matrix and matrix phase (solid/liquid) on the energy transfer between the SWCNT and matrix. The simulation of methane gas flow in CNTs performed by Sokhan et al. (2002) is useful for validating the flow properties for a fluid within a CNT, as the properties were examined with variations of methane/CNT interactions with the effect of solid surfaces on the fluid taken into consideration.

Table 4.1: Comparison of potential validation cases for MD simulation of nanoscale flow indicates the suitability of those cases for each physical phenomenon.

Case References	**Structural Vibration**	**Bi-directional Heat Transfer**	**Compressible Media**	**Acoustics**	**Approach**	**Material-Media**
Mantzalis et al. (2011)	×	×	✓	×	MD	SWCNT - CO_2
Ban and Huang (2012)	×	×	✓	×	MD	SWCNT - CO_2/N_2
Mutat et al. (2012)	×	×	✓	×	DCV-GCMD & NEMD	SWCNT - CH_4
Liu et al. (2010)	×	×	✓	×	GCMC & MD	SWCNT bundle - Ar
Jalili and Majidi (2007)	×	×	✓	×	MD	SWCNT - Xe, Kr
Li and Hong (2007)	✓ (partially)	×	✓	×	MD	2 nanochanel of Silver (Ag) - Ar
Hu et al. (2007)	×	×	✓	×	MD	SWCNT - Air
Arora and Sandler (2006)	×	×	✓	×	EMD	SWCNT - N_2/O_2/Air
Insepov et al. (2006)	✓	×	✓	×	MD	SWCNT - H_2/He
Chaudhri (2005)	×	×	✓	×	MD	SWCNT - Ar
Tuzun et al. (1996)	×	×	✓	×	MD	SWCNT - He/Ar
Liu et al. (2012)	×	×	✓	×	MD	Solid Ar - Gaseous Ar
Dendzik et al. (2004)	×	×	✓	×	MD	SWCNT - Ar
Kosmider et al. (2004)	×	×	✓	×	MD	SWCNT - Ar
Lee and Sinnott (2003)	×	×	✓	×	MD	SWCNT - O_2
Lee and Sinnott (2004)	×	×	✓	×	MD	SWCNT - CH_4

Table 4.1: Comparison of potential validation cases for MD simulation of nanoscale flow indicates the suitability of those cases for each physical phenomenon.

Case References	Structural Vibration	Bi-directional Heat Transfer	Compressible Media	Acoustics	Approach	Material-Media
Mao and Sinnott (2000)	×	×	✓	×	MD	SWCNT - $CH_4/C_2H_6/C_2H_4$
Sokhan et al. (2004)	×	×	✓	×	MD	SWCNT - N_2
Ackerman et al. (2003)	×	×	✓	×	DCV-GCMD & NEMD	SWCNT - Ar/Ne
Sokhan et al. (2002)	×	×	✓	×	NEMD	SWCNT - CH_4
Chen et al. (2011)	✓	×	✓ (partially)	×	MD, CFD	Rigid/flexible SWCNT - SPCE/TIP3P Water
Osman and Srivastava (2005)	×	✓	×	×	MD	SWCNT
Thomas et al. (2010)	×	×	✓	×	MD	SWCNT - Water
Yano (2012)	×	×	×	✓ (partially)	MD	Rectangular box - Ar
Hadjiconstantinou and Garcia (2001)	×	×	×	✓	DSMC	Rectangular domain - Ar
Carlborg et al. (2008)	×	✓	×	×	MD	SWCNT - Solid/liquid Ar
Study in this thesis	✓	✓	✓	✓	MD	SWCNT - Gaseous Ar

Abbreviations: DCV-GCMD: Dual control volume-grand canonical MD; DSMC: Direct Simulation Monte Carlo; EMD: Equilibrium Molecular Dynamics; GCMC: Grand Canonical Monte Carlo; MD: Molecular Dynamics; NEMD: Non-Equilibrium Molecular Dynamics; S/DWCNT: Single/Double walled carbon nanotube.

4.6 Limitations of MD simulation in Audible Frequency Range

MD has been applied to simulate solids, liquids, and dense gases because of its simplicity and accuracy, since it requires only the specification of a potential energy function to describe the interactions between the atoms (Valentini and Schwartzentruber 2009). The use of potential energy functions to describe complex systems makes MD ideal for the type of multi-physics simulation presented in this study (Valentini and Schwartzentruber 2009; and Valentini et al. 2013). However, the feasibility of a molecular simulation is limited by the required simulation time, which is determined by the mean collision time. For instance, in a simulation of a rarefied gas (density $\sim 10^{-4}\,\mathrm{kgm}^{-3}$), the mean collision time, τ, will be on the order of microseconds, as τ scales as the inverse of density. There is a wide separation of time scales between τ and the simulation time step of femtoseconds required to capture the interactions between colliding molecules, resulting in the need for substantial computational resources (Valentini and Schwartzentruber 2009; and Valentini et al. 2013). Molecular simulations of acoustic wave propagation in gaseous media in the audible frequency range (0.02-20 kHz) are similarly limited, and must be able to simulate times of milliseconds ($\sim 10^{-3}$ s), thus requiring the simulation of time scales separated by 12 orders of magnitude. This is the reason why no MD studies to date have treated acoustic wave propagation in dilute gases in the acoustic frequency range. Previous molecular simulations using MD, DSMC, or LBM for acoustic wave propagation at the nanoscale were instead conducted with large amplitudes and high frequencies in the MHz and GHz range (Hadjiconstantinou and Garcia 2001; Hadjiconstantinou 2002; Hadjiconstantinou and Simek 2003; Danforth and Long 2004b; Buick et al. 2000; Yano 2012; and Makeev et al. 2009). To achieve faster computations using MD simulations, atoms can be modelled as hard spheres, providing computationally inexpensive inter-atomic potential functions and creating strictly elastic collisions and allowing the system to be propagated with a variable time step corresponding to the time interval between collisions (Jover et al. 2012; and Hofmann 2003). Salomons and Mareschal (1992) conducted pioneering MD simulations of a monatomic hard-sphere gas to obtain fluid properties across a shock wave (Valentini and Schwartzentruber 2009). The description of molecules as hard spheres may provide a simplifying representation of intermolecular interactions that results in a less computationally expensive MD simulation, but long-range attractive interactions, coupling to continuous structural vibrations, and inelastic collisions cannot be readily captured (Valentini and Schwartzentruber 2009). Furthermore, none of

the widely available simulation packages, such as GROMACS, DL_POLY, LAMMPS and NAMD, are suitable for handling discontinuous potential functions natively (Jover et al. 2012). Several alternative approaches have been used to reduce the computational expense of MD simulations. For example, Valentini and Schwartzentruber (2009) used MD simulation to compute parameters and determine functional relations for collision models in DSMC, which could then produce accurate results more efficiently than MD. Hence, currently available computational resources leads to the conclusion that MD simulations within the audible frequency range are highly challenging. However, performing a large-scale MD simulation at the millisecond scale can potentially be achieved using supercomputers (Shaw et al. 2010).

4.7 Summary

This chapter presents a review of previous research on the application of molecular dynamics (MD) to study phenomena relevant to investigating nanoscale acoustic absorption mechanisms. A review of the use of MD simulations to study nanoscale flow and acoustics found that most of these simulations have been employed to explore nanoscale flow properties. Few simulations have considered fluid/structure interactions by accounting for vibrations. No MD simulations of acoustic wave propagation have been conducted in the audible frequency range. This review provides insight into the requirements of MD methods for successfully conducting molecular simulations to explore acoustic absorption mechanisms at the nanoscale. In particular, MD capabilities must be extended to the millisecond time scale to permit the study of acoustic wave propagation in the audible frequency range, which requires considerable computational resources. In addition, in this review four cases of previous molecular simulations were identified that can be performed for validating MD simulations to model each of the phenomena relevant to acoustic absorption mechanisms. Overall simulations can be performed to assess whether MD can simulate acoustic absorption mechanisms at the nanoscale by validating the results against these following reference studies:

- nanoscale fluid-structure interaction between water and carbon nanotubes (Chen et al. 2011): to simulate the structural vibrations induced due to fluid/structure interactions
- thermal boundary resistance between CNT and surrounding fluid matrix (Carlborg et al. 2008): to simulate bi-directional heat transfer between a liquid and a solid structure

- molecular simulation of sound wave propagation in a monatomic gas (Hadjiconstantinou and Garcia 2001): to simulate acoustic wave propagation in a gaseous media
- fluid flow in nanopores (Sokhan et al. 2002): to simulate flow properties and compression effects.

5 Validation Cases for MD Simulation

5.1 Introduction

In Chapters 2 and 4, it was demonstrated that the modelling of a system for simulating acoustic wave propagation in the presence of CNTs is a multi-physics problem. It was revealed that molecular simulations carried out thus far have not accounted for all relevant aspects of this multi-physics problem, simultaneously, namely fluid/structure interactions, bi-directional heat transfer, and acoustic wave propagation. Hence, it was identified (in Section 4.5) that four previous molecular simulation studies, those conducted by Chen et al. (2011), Carlborg et al. (2008), Sokhan et al. (2002), and Hadjiconstantinou and Garcia (2001), can each be considered suitable for validating the use of MD simulations for modelling a subset of the relevant phenomena. However, due to the limitations of computational resources, only three of these simulations were performed to validate the three major phenomena, as stated earlier. The case presented by Chen et al. (2011), referred to as *Case 1* here, is re-simulated in this study to validate the fluid/structure interaction between a carbon nanotube and water molecules, the fluid flow properties, and the excitation of vibrational modes of the carbon nanotube due to their interactions. The molecular simulation conducted by Carlborg et al. (2008) is validated in this study to verify the effect of fluid/structure interactions on heat transfer for capturing the bi-directional nature of heat flow for a single-walled carbon nanotube surrounded by a matrix of liquid argon, which is referred to as *Case 2* here. Finally, molecular dynamics (MD) simulations are performed to study sound wave propagation in a simple monatomic gas (argon) and the simulation results are validated by comparison with the previous study by Hadjiconstantinou and Garcia (2001), which is represented as validation *Case 3* here.

In the present study, a single carbon nanotube is modelled using the REBO

potential (Brenner et al. 2002) in all MD simulations. The REBO potential has been used widely by other researchers (Carlborg et al. 2008) to perform MD simulations of carbon nanotubes. It has been successfully used to calculate the thermal transport properties of carbon nanomaterials (Carlborg et al. 2008). In addition, it is known for its accuracy to reproduce the phonon-dispersion relations of CNTs, which is very important for heat transfer mechanisms (Carlborg et al. 2008; Maruyama 2003; Maruyama 2002; Shiomi and Maruyama 2006). Hence, the MD simulations for CNT are performed using this potential to validate the results against the original simulations of the reference papers (Chen et al. 2011; Carlborg et al. 2008; Sokhan et al. 2002), which were conducted with different potential models for the CNTs. The non-bonded interactions between the atoms are described by a Lennard-Jones (LJ) 12-6 type potential, U as (Carlborg et al. 2008)

$$U(r_{ij}) = 4\varepsilon_{ij}\left[\left(\frac{\sigma_{ij}}{r_{ij}}\right)^{12} - \left(\frac{\sigma_{ij}}{r_{ij}}\right)^{6}\right], \tag{5.1}$$

where r_{ij} is the intermolecular distance between atoms i and j, and ε_{ij} and σ_{ij} are the Lennard-Jones parameters for the atoms. The results are also validated against the potential parameters that will be used consistently for the simulations performed in the rest of the studies of this thesis. A list of the LJ potential parameters used in the simulations of this study for the interactions of Ar (argon), C (carbon), O (oxygen) and N (nitrogen) atoms is summarised in Table 5.1. The parameters were chosen based on their applications in a similar study of the phenomena relevant to this study. They were obtained from the reference papers of the validation cases studied here.

Furthermore, it should be clarified that even though the study presented in this chapter reproduces the simulation conditions and validates the results for the three different reference cases, each of the simulations carried out in

Table 5.1: Lennard-Jones potential parameters (ε_{ij} and σ_{ij}) for interactions between C-O, Ar-C, Ar-Ar, C-N, N-N, Ar-N (Chen et al. 2011; Carlborg et al. 2008; Sun et al. 2014).

Interactions	ε_{ij} (meV)	σ_{ij} (Å)
C-O (95.3 ° contact angle)	4.0626	3.19
Ar-C	4.98	3.38
Ar-Ar	10.33	3.40
C-N	2.746	3.349
N-N	3.126	3.297
Ar-N	5.68	3.3485

these validation cases represents a novel scientific contribution in terms of the simulation method or the potential energy function used for the CNT molecules. For instance, *Case 1* confirms that the REBO potential can simulate the structural vibrational modes of the CNT found using the Dreiding potential (Mayo et al. 1990), *Case 2* shows that the phonon energy spectrum of the CNT obtained with the Brenner potential (Brenner 1990) can be reproduced using this potential while the thermal boundary conductance of the fluid/structure interaction can also be predicted approximately, and *Case 3* demonstrates the development of an entirely different platform for molecular simulation of sound wave propagation in a gas using the MD method instead of the DSMC method (Hadjiconstantinou and Garcia 2001; Danforth and Long 2004a). Table 5.2 illustrates the differences in the simulation approaches between the current study and the reference cases.

Table 5.2: Major differences in the simulation approaches between the current study and the reference cases (Chen et al. 2011; Carlborg et al. 2008; Hadjiconstantinou and Garcia 2001) that were used for validation.

Validation cases	**Reference**	**Differences in simulation approaches**
Case 1	Chen et al. (2011)	DRIEDING potentials for CNT
Case 2	Carlborg et al. (2008)	Brenner potential (Brenner 1990) of first generation for CNT
Case 3	Hadjiconstantinou and Garcia (2001)	DSMC method and hard sphere gas

5.2 Case 1: Nanoscale Fluid/Structure Interaction Between Water and Carbon Nanotubes

In order to validate the MD code for flow-induced structural vibration of a carbon nanotube, a molecular dynamics simulation was performed to simulate the nanoscale fluid/structure interaction when water flows around a single-walled carbon nanotube (SWCNT). An open-end armchair (5,5) CNT with a diameter d_{CNT} = 0.69 nm and length l_{CNT} = 5 nm was immersed in a simulation box of water molecules. A gravity-driven water flow was applied in the direction perpendicular to the tube axis to simulate the fluid flow passing around the CNT. The interaction and energy transfer between the water molecules and CNTs were observed in order to analyse the flow-induced excitation of structural vibration of the CNT.

5.2.1 Simulation details

A rectangular simulation domain filled with water molecules with dimensions of $L_x = L_y = 4\,\text{nm}$ in the x- and y-directions, and $L_z = 5\,\text{nm}$ in the z-direction was designed to simulate the nanoscale fluid/structure interactions. A 5 nm long open-end (5,5) armchair CNT was placed at the centre of the simulation domain in the z-direction. A snapshot of the simulation domain is shown in Figure 5.1. The water molecules were described by an extended simple-point-charge (SPC/E) model (Berendsen et al. 1984; Berendsen et al. 1987), which is the same as that used by Chen et al. (2011). The geometrical and potential parameters of O (Oxygen) and H (Hydrogen) atoms and the water (H_2O) molecules of the SPC/E model are listed in Table 5.3. The SHAKE algorithm was applied to constrain the bond length and angle of water molecules. As mentioned earlier, the REBO potential was used for carbon-carbon interactions in this MD simulation, unlike the original simulation performed by Chen et al. (2011), in which the interactions were modelled by the Drieding force field (Mayo et al. 1990). A list of the parameters of the REBO potential function can be found in the papers of Brenner et al. (2002) and Stuart et al. (2000). In the simulation software LAMMPS, a built-in parameter file named 'CH.airebo' is available for use without listing the parameters separately in the input files. The interaction between the carbon nanotube and water is described by the Lennard-Jones potential of oxygen and carbon atoms corresponding to a contact angle of 95.3 ° for water over graphene. The values are given in Table 5.1.

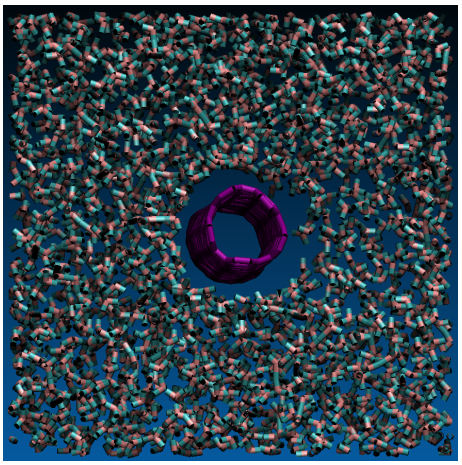

Figure 5.1: Snapshot of the MD simulation domain for nanoscale fluid (water)-structure (CNT) interaction.

Table 5.3: Parameters for SPC/E water model (Berendsen et al. 1984).

Parameters	**Value**
O mass	15.999 g/mol
H mass	1.008 g/mol
O charge	-0.8476e
H charge	0.4238e
$r_{\text{O-H}}$	1.0 Å
θ_{H-O-H}	109.47 °
LJ $\varepsilon_{\text{O-O}}$	6.734 meV
LJ $\sigma_{\text{O-O}}$	3.166 Å
LJ $\varepsilon_{\text{O-H, H-H}}$	0.0 meV
LJ $\sigma_{\text{O-H, H-H}}$	0.0 Å

The simulation setup and other simulation conditions were similar to those of Chen et al. (2011). The simulation was initiated at a temperature of 300 K with a small timestep of 0.001 fs in order to relax the system and the timestep gradually increased to 0.5 fs to speed up the relaxation process. A constant temperature was maintained with a Nosé-Hoover thermostat (NVT). Thereafter the system was equilibrated for 300 ps at a temperature T = 300 K and a pressure P = 1 bar using a Nosé-Hoover thermostat and barostat applied to water molecules. Then the system was switched to the NVT ensemble during the water flow around the CNT. A thermostat in the directions (x and y) perpendicular to the fluid flow was applied to maintain the temperature of the flow. A body force was applied to each water molecule in the x-direction to drive the flow. During the water flow, the CNT was allowed to deform with the centre of the CNT fixed. Once the flow reached a steady state, the velocity, density, and temperature along the flow direction of the fluid, were recorded every 1 ps and averaged over 4 ns. Flow profiles were obtained by dividing the simulation domain into slices of 2 Å thickness in the x and y-directions.

5.2.2 Validation Results

In the original simulation by Chen et al. (2011), interfacial slippage and viscosity change at the nanoscale, and deviations from classical hydrodynamic predictions were studied. It was shown that local heating and restructuring of the solvent around the CNT have a significant effect on the drag force, interfacial slippage, the viscosity change, and the deviation from the classical hydrodynamic theory. In addition, the vibrational coupling between the water-CNT structure induced heating of the water molecules around the CNT.

As mentioned earlier, observing the excitations of low-frequency structural vibration modes in the CNT and energy transfer between the CNT and water molecules were of interest in this validation study. Consequently, the change in the water structure and the flow properties due to the fluid/structure interaction were also captured and verified against the results of Chen et al. (2011).

To verify the simulation results of flow-induced structural vibrational modes of the CNT, a MD simulation was initially validated for properties such as the flow velocity, mass density, and temperature of the water molecules with the results given by Chen et al. (2011). The distribution of the flow velocity, mass density, and temperature of water molecules around the flexible CNT are plotted in Figure 5.2. It can be seen from Figure 5.2a that water flows in parallel layers without disruption between the layers, developing a laminar flow pattern around the carbon nantoube in which the velocity converges to the flow direction in the far field (Chen et al. 2011). Flow-induced local heating of water molecules around the carbon nanotube can also be observed in Figure 5.2c, which shows a higher temperature near to the CNT compared with other regions in the simulation domain, even though the system was coupled globally to the thermostat. It was found that the excess kinetic energy, due to vibrational coupling between the CNT and the fluid, which facilitates significant mechanical energy transfer from the water to the CNT structure, induces dramatic heating of the nantoube and surrounding fluid molecules (Chen et al. 2011). The local flow velocity profile in the x-direction and temperature at the mid-plane (dashed line shown in Figure 5.2a) of the simulation domain of the present MD simulation were also compared with those computed by Chen et al. (2011), as shown in Figure 5.3. Both results are in good agreement. The small axial shift in the velocity profile from the centre of the box in MD simulation results is due to the movement of the CNT with the flow, even though the motion of the centre of mass of the CNT was eliminated by zeroing the linear and angular momentum of the CNT. The momentum of the CNT is zeroed in each timestep by adjusting the velocities of the atoms, for which the momentum is required to be estimated for any movements of the atoms. It creates a time lag between the calculation of new momentum due to the movements and zeroing of that momentum in each time step, which results in a small shift of the CNT. In addition, a significant interfacial fluid slippage at the wall of the CNT was observed in the local velocity profile at the midplane of the simulation domain, which corresponds to the slip length of 1 nm. A similar observation was made in the results by Chen et al. (2011) regarding the boundary slippage at the water-CNT interface.

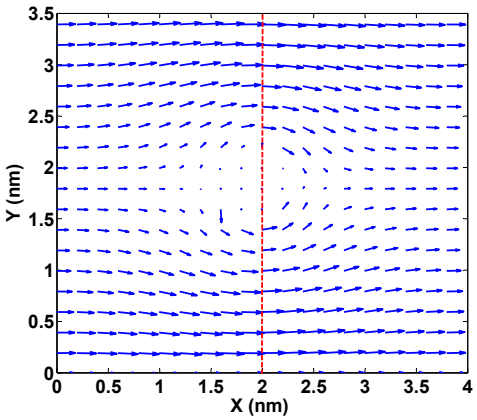

(a) Flow velocity (scale of velocity can be observed from Figure 5.3a)

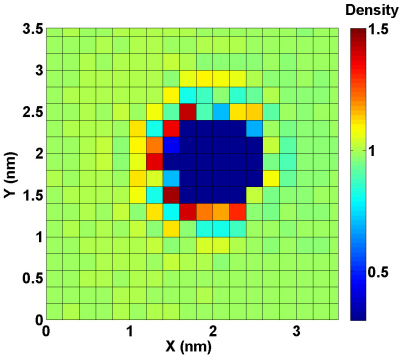

(b) Density

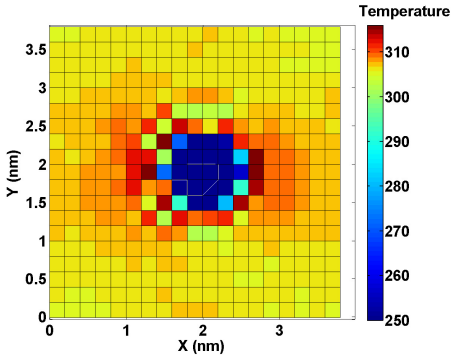

(c) Temperature

Figure 5.2: Distribution of flow velocity, mass density, and temperature in the plane normal to the direction of the carbon nanotube, i.e., the x-y plane. The values of these variables are quantitatively consistent to those measured by Chen et al. (2011).

The excitation of flow-induced structural vibration in the carbon nanotube was quantified by principal component analysis (PCA) (Chen et al. 2011; Shenai et al. 2012). To perform PCA, an atomic trajectory matrix is constructed from the input data set of Cartesian coordinates for an N-atom system collected at each output timestep. A covariance matrix C_{ij} is then generated from the trajectory matrix, which can be written as

$$C_{ij} = \langle (x_i - \langle x_i \rangle)(x_j - \langle x_j \rangle) \rangle, \tag{5.2}$$

where x_i and x_j are atomic coordinates at each timestep and $\langle \cdots \rangle$ denotes the time average performed over all timesteps. The eigenvalues of the covariance matrix C_{ij} give the contributions of the principal modes (Chen et al.

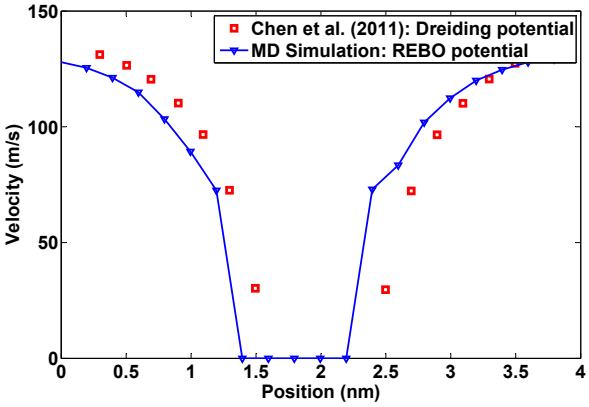

(a) Local flow velocity

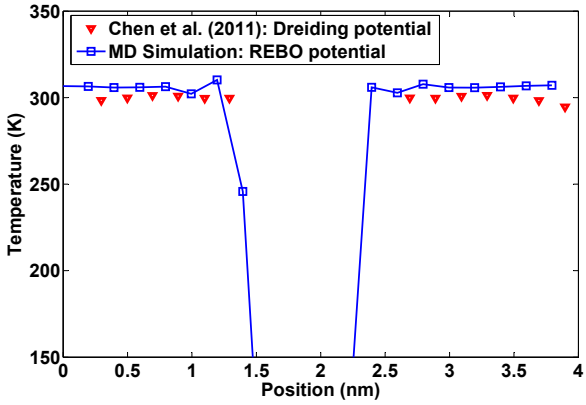

(b) Local flow temperature

Figure 5.3: Local flow velocity and temperature in the x-direction recorded along the dashed line in Figure 5.2a.

2011). The normalised eigenvalue for motion of the CNT atoms is plotted against eigenvector index in Figure 5.4a and some of the most occupied vibrational modes excited by the water flow are shown in Figure 5.4b. As shown in Figure 5.4, the most occupied modes excited by the fluid flow are bending modes, breathing modes, and the coupling of these two modes (at higher frequencies). These findings of the structural vibrational modes due to the fluid/structure interaction are similar to those observed by Chen et al. (2011). The scree plot shown in Figure 5.4a is also in good agreement with the results presented by Chen et al. (2011).

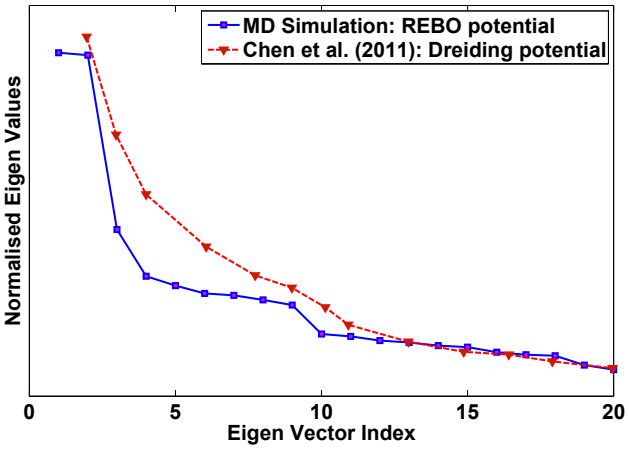

(a)

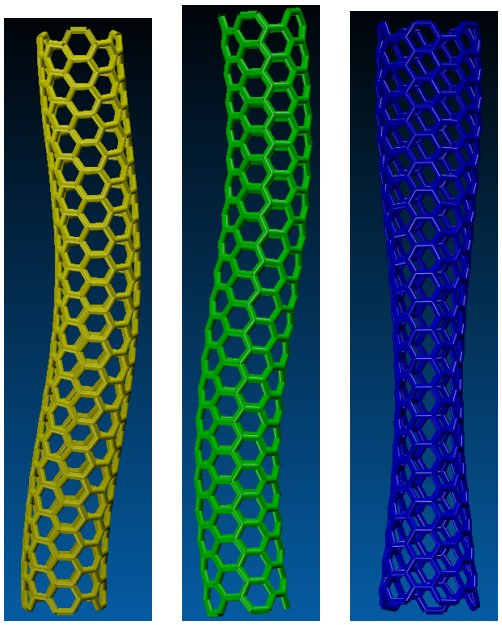

(b)

Figure 5.4: (a) Scree plot showing the normalised eigenvalues against eigenvectors obtained from PCA; (b) Vibrational modes excited by fluid flow interaction with the CNT which suggests considerable mechanical energy transferred from the fluid flow.

5.3 Case 2: Thermal boundary resistance between CNT and surrounding fluid matrix

In order to validate the MD simualtion for the heat transfer mechanisms at fluid/structure interfaces, the thermal boundary resistance between a SWCNT and surrounding liquid argon matrix was studied during heat pulse propagation in the CNT. In the current study, the contribution of the modal energy transfer between the SWCNT and the liquid argon matrix and its effect on phonon behaviour was studied and the effect on the phonon energy spectrum of the CNT was analysed.

The simulation was reproduced from the study conducted by Carlborg et al. (2008). In their study, it was shown that the thermal boundary conductance (TBC) depends strongly on the local properties of the adsorption layer of the liquid matrix formed on the surface of the solid structure. Consequently, it was observed that the TBC does not vary considerably with the length of the CNT, although a length effect was evident for short nanotubes. In addition, a linear coupling was observed between the low-frequency oscillations in the SWCNT and the surrounding adsorbed layer of argon atoms on the solid surface, which was demonstrated by phonon spectral analysis. In this study, the TBC was calculated at the solid-liquid interface and validated against the simulation results of Carlborg et al. (2008). The phonon energy spectrum of the CNT was also estimated to validate the frequencies of excited phonon oscillations.

5.3.1 Simulation details

MD simulations were performed for a 225 Å-long open-ended (5,5) armchair SWCNT with a diameter of 6.9 Å. A rectangular box with a cross-sectional area of 35×35 Å^2 filled with liquid argon at a density of 1200 kg/m^3 was used as the simulation domain. The CNT was placed in the centre of the box and periodic boundary conditions were applied in all directions of the simulation domain. A snapshot of the molecular structure of the simulation setup is shown in Figure 5.5. The Lennard-Jones potential function was used to model the van der Waals forces between argon atoms and the interactions between argon and carbon atoms. The potentials parameters are given in Table 5.1.

The system (both CNT and liquid argon) was initially equilibrated at 300 K (in the supercritical phase for argon) using an auxiliary velocity rescaling thermostat for 500 ps with a timestep of 0.5 fs. Then both systems were cooled at a rate of 1 K/ps to a target temperature of 120 K to arrive at the liquid phase

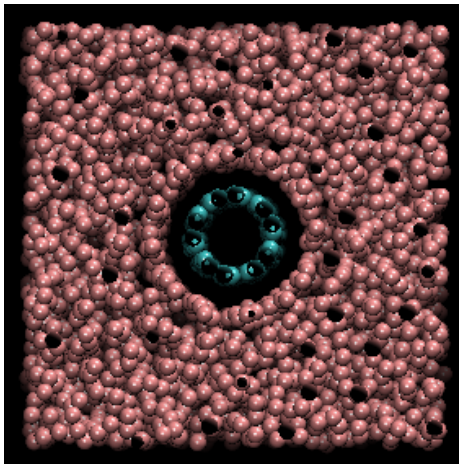

Figure 5.5: Snapshot of the MD simulation domain of liquid argon surrounding a CNT.

of argon. Thereafter the system was further equilibrated at 120 K for 200 ps. After equilibration, a picosecond heat pulse was propagated through the tube by ramping up the temperature of the CNT by 200 K over 10 ps, which pushed the liquid matrix out of equilibrium. Then the system was adiabatically relaxed towards equilibrium without any temperature control. A complete temperature history of the cooling, heating, and equilibration process is shown in Figure 5.6. In order to estimate the thermal boundary conductance of the liquid-solid interface, the temperature difference between the CNT and the surrounding liquid matrix was recorded during the relaxation period. In addition, the velocity components of the atoms were also sampled to calculate the phonon energy spectrum.

5.3.2 Validation Results

To characterise the equilibrium distribution of argon around the CNT, the radial density of the liquid argon matrix was measured during the simulation. The computed radial density distribution of liquid argon during the equilibration of the system and the heat flow are shown in Figure 5.7. It can be seen that the density distribution features a sharp peak at around 3.38 Å, which corresponds to the equilibrium carbon-argon distance. The peak in the density distribution indicates that the molecular structure of the equilibrated argon matrix forms a dense adsorption layer around the SWCNT at the CNT surface (Carlborg et al. 2008), which is visible in the MD snapshot of the molecular structure shown in Figure 5.5. Two additional peaks are also

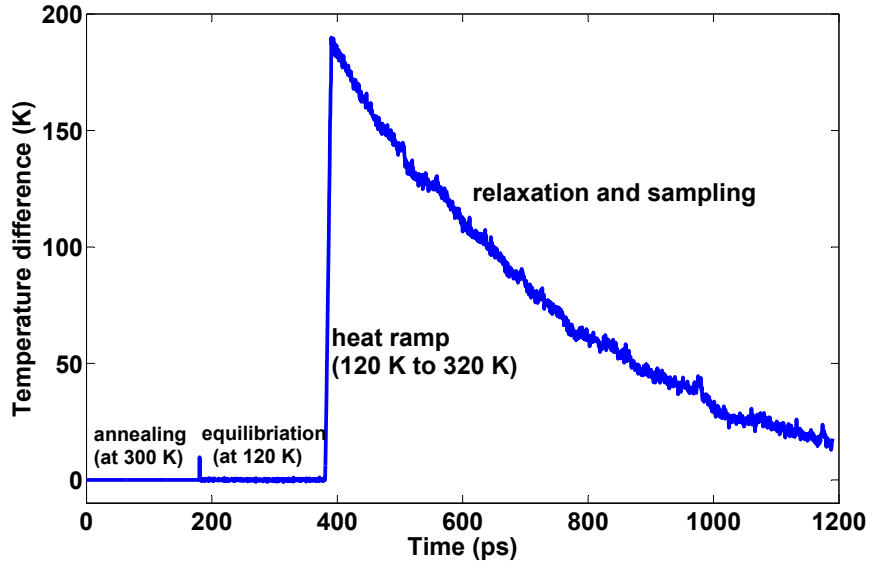

(a)

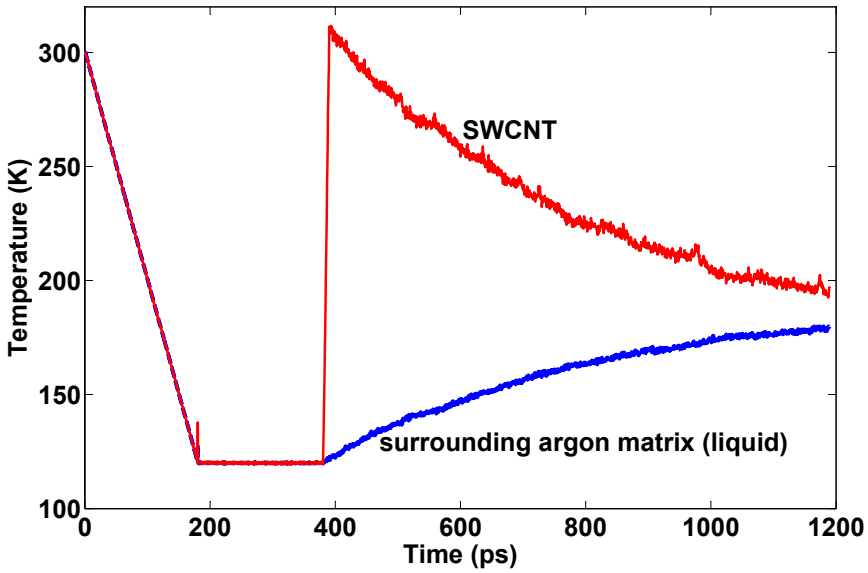

(b)

Figure 5.6: Time evolution of (a) the temperature difference between the SWCNT and liquid argon at different stages of the MD simulation and (b) the recorded temperature for both argon and the CNT during relaxation.

observed in the radial density distribution, which reveals the formation of two other dense layers of liquid argon. It can also be noted that the structure and density distribution were unchanged during heat flow, even though the matrices were disturbed from equilibrium by ramping up the temperature of the CNT.

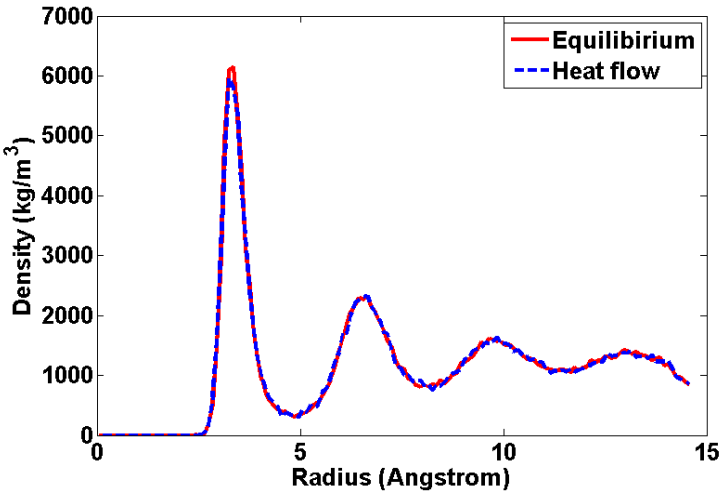

Figure 5.7: The radial density distribution of liquid argon from the surface of the CNT showing density oscillations with three distinct peaks within 10 Å of the CNT surface.

To estimate the thermal boundary resistance (TBR) at the solid-liquid interface, the temperature difference between the CNT and the argon matrix during the relaxation (without any temperature control) was recorded. The temperature difference versus time is displayed in Figure 5.6a, which shows an exponential decay, resulting from the heat flow predominately limited by thermal boundary resistance at the solid-liquid interface (Shenogin et al. 2004). An exponential function with a relaxation time τ can be fitted to the temperature difference recorded from the simulation to estimate the TBC (Carlborg et al. 2008). The thermal boundary conductance (i.e. inverse of thermal boundary resistance) of the SWCNT-argon interface was determined using the lumped-heat-capacity method from Equation (5.3) (Carlborg et al. 2008), derived from the expression for the temperature difference between two coupled domains as a function of time during the relaxation period:

$$\Delta T = \Delta T_0 e^{[-(1/m_{\mathrm{Ar}}c_{\mathrm{Ar}}+1/m_{\mathrm{CNT}}c_{\mathrm{CNT}})]KSt}, \tag{5.3}$$

and

$$S = \pi L_{\mathrm{CNT}}(d + \sigma_{\mathrm{C\text{-}Ar}}), \tag{5.4}$$

where $\Delta T = T_{CNT} - T_{Ar}$ is the temperature difference at time t, ΔT_0 is the initial temperature at time $t = 0$, m_{Ar} and m_{CNT} are the masses of the argon and CNT atoms, respectively c_{Ar} = 312 J/kgK and c_{CNT} = 1000 J/kgK are the heat capacities, and S is the contact area calculated from Equation (5.4) with L the length of the tube and d =6.9 Å the diameter of the (5,5) tube. The estimated TBC, K, of the CNT-liquid matrix interface was found to be nearly constant at a value of 1.4 MW/m^{2}K at 120 K, which is similar to the average value of 1.6 MW/m^{2}K estimated by Carlborg et al. (2008).

To verify the excitation of phonon modes of the CNT and the corresponding vibrational frequency range due to the heat transfer between the adsorbed argon layer and the CNT, the phonon energy spectral density of the CNT was estimated. The phonon energy spectrum of the nanotube was calculated from the power spectral density of the velocity fluctuations of carbon atoms in the nanotube as (Carlborg et al. 2008)

$$g(f) = \frac{1}{N}\sum_{j}^{N}\left|\int e^{-2\pi i f t}\mathbf{v}_j dt\right|^2, \tag{5.5}$$

where f is the frequency at which the velocities are sampled from the simulation, $\mathbf{v}_j$ is the velocity of carbon atom j, and N is the total number of atoms in the tube. Similar to the calculation performed by Carlborg et al. (2008), the velocities were sampled at 133 THz for 57344 time steps during heat transfer (i.e. relaxation without any temperature control) and ensemble averaged in 2048 sample windows. The calculated phonon energy amplitude of the CNT versus phonon frequency is shown in Figure 5.8a. It can be observed that the phonon modes are distributed over a broadband frequency spectrum in a random pattern and the highest frequency of the phonon modes for the CNT is as high as 50 THz. The sharp peak at 50 THz represents the intramolecular vibrations of covalently bonded C atoms in the CNT (Shenogin et al. 2004; Zhang et al. 2012). The calculated phonon energy spectrum shows a similar pattern to those calculated by Carlborg et al. (2008) and Shenogin et al. (2004), which validates the accuracy of the model used here to simulate the transport properties and heat transfer as heat transfer mechanisms are significantly influenced by phonon transport properties.

In addition, it can be seen that the low-frequency vibrations of the CNT are nearly damped out for frequencies below 3 THz as the closeup of the phonon spectrum shows in Figure 5.8b. In the study by Carlborg et al. (2008), it was shown that this frequency range corresponds to the vibrational spectrum of the adsorbed layer of liquid argon. Hence it was demonstrated that resonant coupling of the vibrational modes between the CNT and the

argon layer was responsible for significant damping of the low-frequency phonon modes of the CNT.

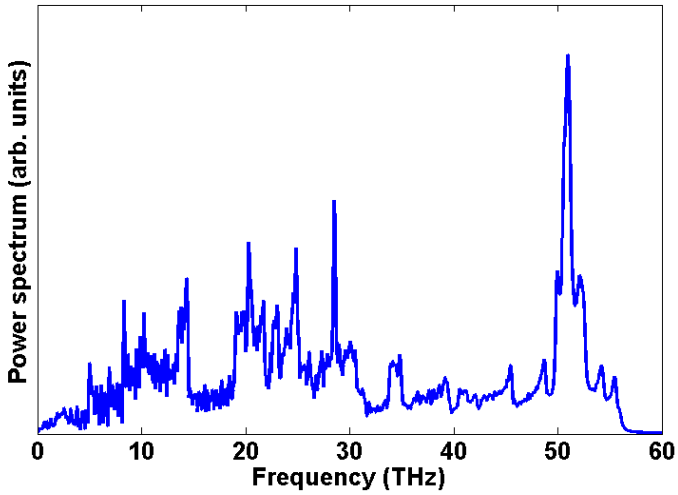

(a) Phonon energy spectrum

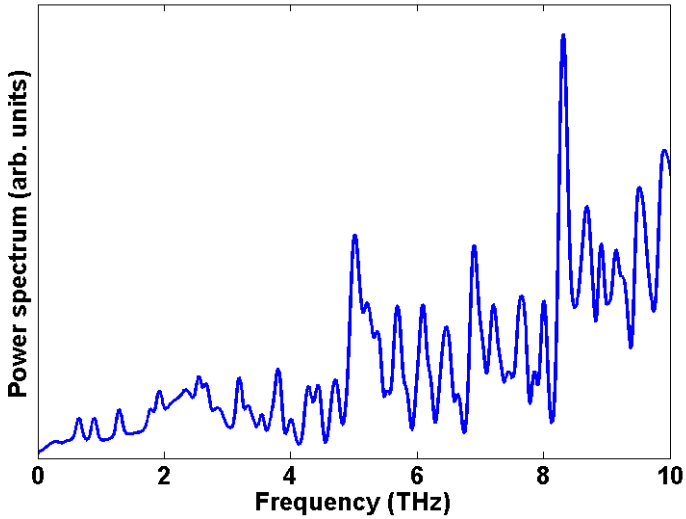

(b) Closeup of the first 10 THz

Figure 5.8: Phonon energy spectrum of the 225 Å long SWCNT submerged in a liquid argon matrix. The spectrum was calculated from the velocity fluctuations of carbon atoms in the nanotube in the MD simulations.

5.4 Case 3: MD Simulation of Sound Wave Propagation in a Monatomic Gas

In this case study, sound wave propagation in a simple gas was studied using molecular dynamics, a molecular method, and validated against the results of a DSMC study (Hadjiconstantinou and Garcia 2001). A plane sound wave was generated within a rectangular domain by oscillating a solid wall comprising Lennard-Jones atoms with the same intermolecular potential as the gas molecules. Simulations were conducted for high-frequency sound in the MHz to GHz range using as the wave-propagating medium a simple gas of a limited number of molecules due to the limitations of computational expense. Simulation results were compared with the theoretical estimate of the transmission matrix method (Beranek and Ver 1992).

Molecular dynamics simulations were performed for a plane sound wave propagating in a monatomic gas (argon) in a rectangular domain of length L_z as shown in Figure 5.9. The domain length was varied based on the acoustic wave frequency. An oscillating wall made of solid argon was used as a sound source and excited at $z = 0$ by imposing a sinusoidally varying velocity in the z-direction. The far end of the simulation domain was terminated by a reflecting wall, known as a specular wall, where the normal component of the velocity of any incident particle was reversed. In order to validate the MD results, the simulation domain was constructed to resemble that of the DSMC study reported by Hadjiconstantinou and Garcia (2001).

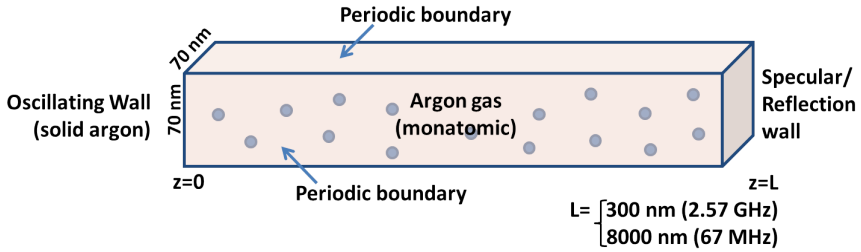

(a) Schematic of simulation geometry

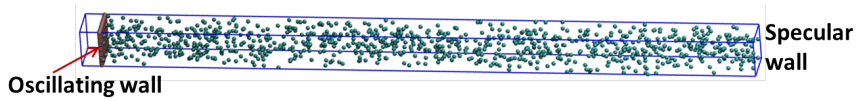

(b) Snapshot of MD simulation domain

Figure 5.9: Simulation domain and sound source model for acoustic wave propagation in argon gas.

The interactions between gas molecules (i.e. argon-argon) was described by a Lennard-Jones 12-6 type potential. The LJ parameters, $\varepsilon_{ij} = 10.33$ meV and σ_{ij} = 3.40Å were used for argon molecules (Carlborg et al. 2008). The interatomic interactions between the oscillating wall atoms (solid argon) were also expressed with the same potential parameters as the gas molecules. The cut-off distance for the Lennard-Jones function was set to 3σ for the interactions of the gas and wall molecules. A short range purely repulsive WCA (Weeks-Chandler-Andersen) potential (Weeks et al. 1971) was introduced for the interaction between the argon atoms of the solid wall and those of the propagating medium (gas) by truncating the Lennard-Jones potential at $2^{\frac{1}{6}}\,\sigma_{ij}$.

The wall oscillates harmonically in the z-direction with displacement Z_w and oscillation speed V_w as a function of time t according to

$$Z_w(t) = a(1 - \cos\omega t), \tag{5.6}$$

$$V_w(t) = a\omega \sin\omega t, \tag{5.7}$$

where the displacement and motion of the wall is characterised by the amplitude a and the angular frequency ω. The sound source yields a plane sound wave propagating in the z-direction leading to a velocity variation

$$v_i(z,t) = v_0 \exp\left[i(\omega t - kz) - mz\right], \tag{5.8}$$

with maximum gas velocity $a\omega$, which corresponds to the peak velocity of the oscillating wall, $v_0 (= a\omega)$, where $k = \frac{2\pi}{\lambda}$ is the wavenumber with λ the acoustic wavelength and m is the attenuation coefficient. Due to the specular wall at the far end of the domain, the propagating wave will be reflected at the termination as

$$v_r(z,t) = -v_0 \exp\left[i(\omega t - k(2L - z)) - m(2L - z)\right]. \tag{5.9}$$

Superposition of the incident and reflected waves leads to a standing wave of the form (Wang and Xu 2012; Hadjiconstantinou and Garcia 2001)

$$v(z,t) = A(z)\ \sin\omega t + B(z)\ \cos\omega t, \tag{5.10}$$

where

$$A(z) = v_0\left[e^{-mz}\ \cos kz\ -\ e^{-m(2L-z)}\ \cos k(2L - z)\right], \tag{5.11}$$

$$B(z) = -v_0\left[e^{-mz} \sin kz\ -\ e^{-m(2L-z)}\ \sin k(2L - z)\right]. \tag{5.12}$$

$A(z)$ and $B(z)$ are the components of the velocity amplitude of the standing wave, which can be extracted from the numerical solution based on a method

used by Hadjiconstantinou and Garcia (2001). In order to calculate these velocity components from the simulation results, the instantaneous velocity $v(z_{jj}, t_{ii})$ of the gas molecules in a number of bins/slices perpendicular to the z-axis along the box length was recorded at each time step after the initial transient had passed. Here, z_{jj} is the position of the bin and t_{ii} is the recorded time step with $jj(= 1, 2, 3 \cdots M)$ being the bin number index and $ii(= 1, 2, 3 \cdots N)$ the time sample index. Thereafter, a least-square method was used to evaluate $A(z)$ and $B(z)$ from the recorded data. Detailed equations can be found in Hadjiconstantinou and Garcia (2001). A non-linear fit of Equations (5.11) and (5.12) to the numerical solution of $A(z)$ and $B(z)$ was performed using the Nelder-Mead simplex method (Press et al. 1992; Hadjiconstantinou and Garcia 2001) to estimate the wave number k and the attenuation coefficient m. A phase shift was included in the wave equations for the parameter fits for theoretical prediction at higher frequencies in the GHz range due to the entrance effects near to the sound source (Hadjiconstantinou and Garcia 2001).

5.4.1 Simulation Details

Molecular dynamics (MD) simulations were carried out for acoustic wave propagation at two different frequencies of 67 MHz and 2.57 GHz, as required for validation against the DSMC results (Hadjiconstantinou and Garcia 2001). A simulation domain with transverse dimensions $L_x = L_y = 70$ nm (2.57 GHz) or 12 nm (67 MHz) was modelled with the domain length L_z chosen to be no longer than a few wavelengths ($L = \frac{7}{4}\lambda$) to reduce the simulation cost. Domain lengths of 300 nm and 8000 nm were used to simulate acoustic wave propagation at frequencies of 2.57 GHz and 67 MHz, respectively. A periodic boundary condition (PBC) was applied in each of the directions perpendicular to the propagating wave. The time step Δt of the simulation was taken to be 1 fs. This choice of time step satisfies the time step constraints suggested by Hadjiconstantinou and Garcia (2001) for accurate molecular simulation and to capture the time evolution of the wave profile, that is, the time step should be significantly smaller than the mean collision time and the characteristic time, which can be written as (Hadjiconstantinou and Garcia 2001)

$$\Delta t \ll \frac{\lambda_{\mathrm{mfp}}}{c_{\mathrm{m}}} \text{ and } \Delta t \ll \frac{2\pi}{\omega}, \tag{5.13}$$

where

$$c_{\mathrm{m}} = \sqrt{\frac{2k_B T}{M_m}}, \tag{5.14}$$

is the most probable velocity, λ_{mfp} (=7.28×10^{-8} m) is the mean free path, k_{B} is the Boltzmann constant, and T is the gas temperature.

A piston made of solid argon was used as sound source, where the interactions between the argon atoms of the solid wall and those of the gaseous media were described by a short range purely repulsive WCA potential. The piston wall of solid argon, combined with the thermostat applied on the gas (see Sections 5.4.2 and 5.4.4), was designed to mimic the diffuse reflection boundary condition. The wall was created by holding a collection of argon atoms (35645 atoms) stationary and setting the force on them to zero. The oscillation of the wall was generated with a velocity assigned to wall atoms collectively by imposing a sinusoidally varying velocity in the z-direction. During the simulation, the piston creates the sinusoidally varying velocity while the thermostat applied in the direction perpendicular to the wave propagation imposes the Maxwellian variance of the velocity.

Simulations were initiated with a Gaussian distribution of gas velocity components consistent with the desired temperature and were equilibrated at a temperature of $T = 273$ K and pressure of $P = 1$ atm with a gas density ρ = 1.8 kgm^{-3}. The velocity amplitude of the sound source was chosen to avoid nonlinear effects in the wave propagation, such as shock formulation, by ensuring that viscous forces dominate inertial forces (Wang and Xu 2012; Hadjiconstantinou and Garcia 2001), i.e. when the Reynolds number, $Re \ll 1$, which gives

$$v_0 \ll \frac{\omega\mu}{\rho c}, \tag{5.15}$$

where μ is the viscosity and c is the classical sound speed. This criterion can also be expressed as $v_0 \ll \frac{c}{R}$, where

$$R = \frac{c^2\rho}{\omega\mu}, \tag{5.16}$$

is the acoustic Reynolds number (Hadjiconstantinou and Garcia 2001). In the MD simulations, the velocity amplitude of the sound source was chosen to be $v_0 = 0.025c$ at the lower frequency of 67 MHz ($R \approx 20$); a larger amplitude of $v_0 = 0.15c$ was used at the higher frequency of 2.57 GHz ($R = 0.5$) as the acoustic wave is damped significantly due to the large attenuation at this frequency. However, v_0 was assumed to be smaller compared to the most probable molecular velocity c_{m} of the gas, which usually has the same order as the sound speed c.

5.4.2 Numerical Results and Validation

To evaluate $A(z)$ and $B(z)$, sampling was started when the change in the average velocity of particles at a position z with time had become relatively small, i.e. at a steady state condition of the flow. In order to determine the starting point for sampling, a monitoring point was set to observe the change in the average particle velocity at each moment of an integer number of periods of the propagating wave. The gas temperature and pressure fluctuations were also monitored during the wave propagation as a sanity check. Figure 5.10 shows the fluctuations of the mean spatial gas temperature and the gas pressure during the acoustic wave propagation at a frequency of $f = 67$ MHz ($R \approx 20$). As shown in Figure 5.10a, the maximum increase of the mean temperature due to dissipation was less than 2%; hence the change in the sound speed was less than 1.5%, since the sound speed varies as $\sqrt{T}$ (Hadjiconstantinou and Garcia 2001). The temperature and pressure of the gas fluctuates harmonically due to the oscillation of the piston.

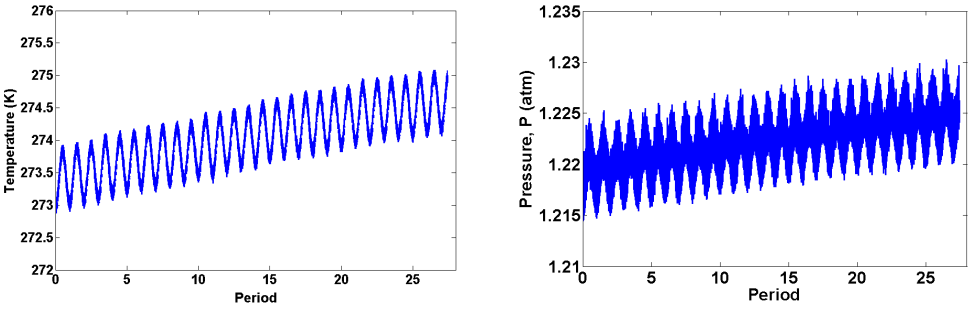

(a) Mean spatial gas temperature

(b) Mean spatial gas pressure

Figure 5.10: Mean spatial temperature and pressure oscillations of the gas for frequency $f = 67$ MHz ($R \approx 20$).

After the transient period had passed, sampling was done from 15 periods after the start of the simulation up to 27 periods, with 45 time samples in each period and 80 spatial bins per wavelength at a frequency of $f = 67$ MHz. Numerical estimates of the cosine and sine components, $A(z)$ and $B(z)$, of the velocity amplitude are presented as a function of distance z in Figure 5.11. A comparison between the MD results and the normalised (by velocity amplitude) DSMC (Hadjiconstantinou and Garcia 2001) results of the velocity amplitude $V(z) = \sqrt{A^2 + B^2}$ is also displayed. It can be seen that the MD results match the normalised DSMC results very well except for a small discrepancy attributable to insufficient sample averaging.

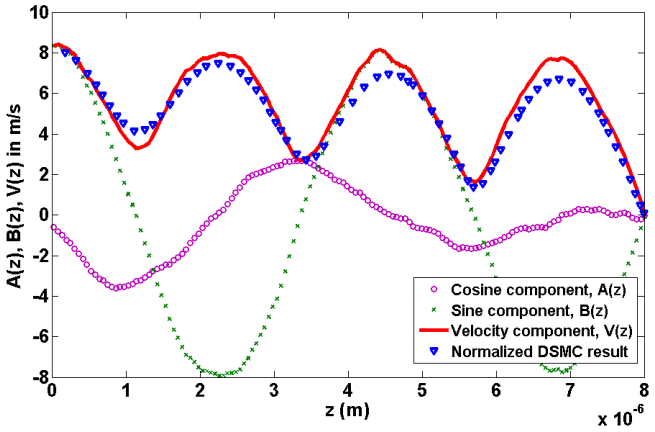

Figure 5.11: Velocity amplitude $V(z) = \sqrt{A^2 + B^2}$ as a function of distance for frequency $f = 67$ MHz ($R \approx 20$). The normalised DSMC result compared with the MD simulation result.

For the validation of the MD results at higher frequencies, simulations were performed at a frequency $f = 2.57$ GHz for an acoustic Reynolds number $R = 0.5$. A challenge of simulations at higher frequency is that the rapid oscillation of the sound source heats the system very quickly as the acoustic source continuously does work on the gas. Therefore, an auxiliary mechanism that is compatible with wave propagation modelling was required to remove the additional heat from the system. A Nosé-Hover thermostat (NVT) was coupled loosely with the system in directions perpendicular (x and y) to the propagating wave to control the increasing temperature. It was observed that thermostatting with a damping time equal to the period of the acoustic frequency can effectively control the temperature increase. Effects of the thermostatting damping time on the propagating wave are elaborated in Section 5.4.4. Figure 5.12 shows the fluctuations of the mean spatial gas temperature and gas pressure during the acoustic wave propagation at $f = 2.57$ GHz ($R = 0.5$). As shown in Figures 5.12a and 5.12b, the maximum increase of the mean temperature and pressure were kept to less than 2% of the equilibrium temperature and pressure; hence the change of sound speed was less than 1.5%.

To extract the cosine and sine components, $A(z)$ and $B(z)$, of the velocity amplitude at the higher frequency, sampling was done between 61 periods after the start of the simulation up to 100 periods (i.e. for a total duration of 40 periods), with 60 spatial bins in each wavelength. Figure 5.13a shows the comparison between the normalised DSMC data and MD results for $A(z)$

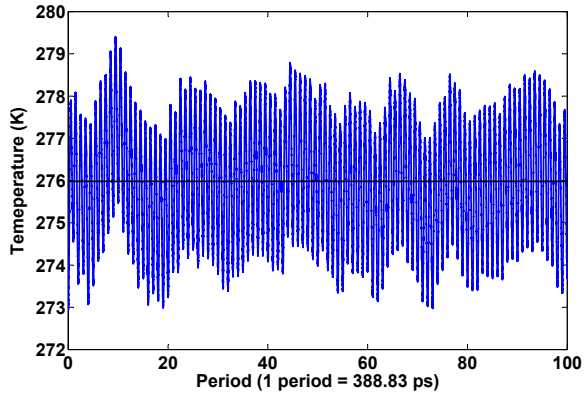

(a) Mean spatial gas temperature

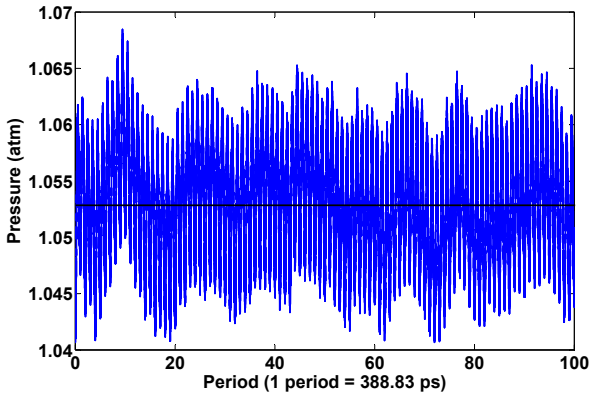

(b) Mean spatial gas pressure

Figure 5.12: Mean spatial temperature and pressure oscillations of the gas for frequency, $f = 2.57$ GHz ($R = 0.5$).

and $B(z)$. The normalised DSMC data for the components of the velocity amplitude show good agreement with the MD results. In previous analyses (Hadjiconstantinou and Garcia 2001; Sirovich and Thurber 1965; Greenspan and Thompson 1953), it was found that free molecular flow dominates near the acoustic source at higher frequency in a region smaller than one mean free path (λ_{mfp}). This effect was verified by applying a nonlinear fit to the cosine and sine components of the velocity amplitude, and restricting the fit to the region outside one mean free path ($z > \lambda_{\text{mfp}}$) or half a mean free path ($z > 0.5\lambda_{\text{mfp}}$) of the sound source, a method similar to that used by Hadjiconstantinou and Garcia (2001). Figure 5.13b shows that both restrictions give a good fit to the waveforms for a constant value of the sound speed

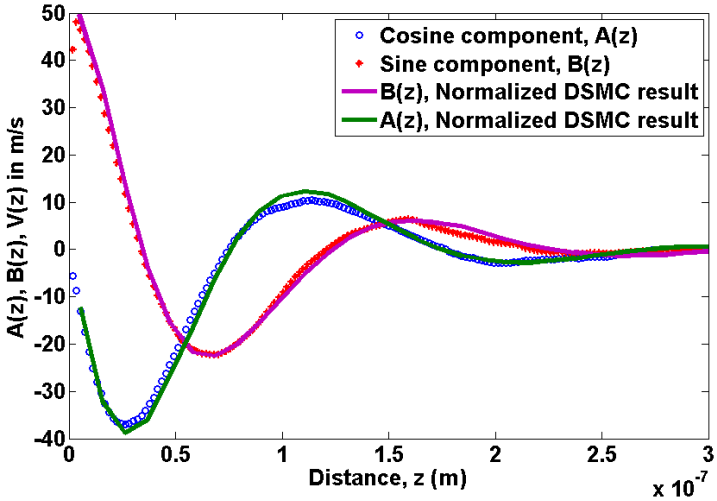

(a)

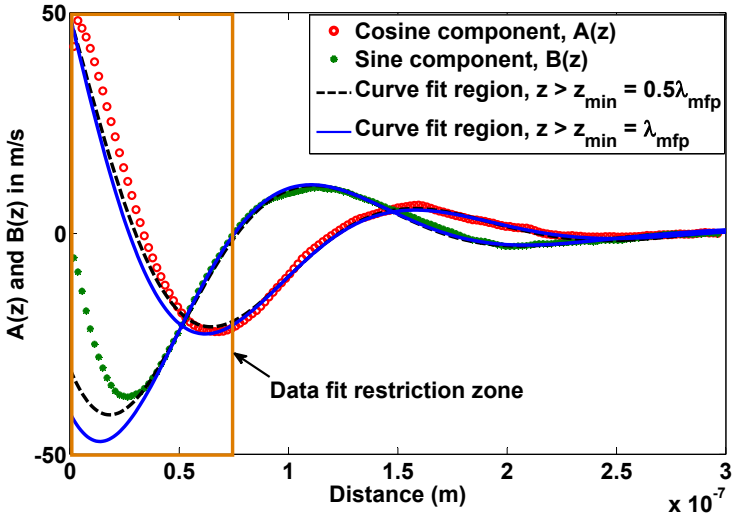

(b)

Figure 5.13: Cosine and sine components, $A(z)$ and $B(z)$, of the velocity amplitude as a function of distance for frequency $f = 2.57$ GHz ($R = 0.5$). (a) Normalised DSMC result compared with the MD simulation result. (b) Curve fit to cosine and sine components of velocity amplitude from MD simulation as a function of distance.

and attenuation coefficient in the domain further than half a mean free path from the source; however the waveforms in the domain further than one mean free path from the source show comparatively better fits. Consequently, the waveforms do not fit very well near to the acoustic source in the region $0 < z < \lambda_{\text{mfp}}$. This result verifies the observation made by Hadjiconstantinou and Garcia (2001) that the free molecular flow is important near to the source at domain length smaller than one mean free path. Unknown parameters, such as the sound speed (c) and attenuation coefficient (m) for the sound wave propagation in the monatomic gas, were also obtained using the nonlinear fitting of the waveforms to the simulated data. The values for the sound speed (c) and attenuation coefficient (m) that were determined from the MD simulation are listed in Table 5.4, which are similar to those obtained by the DSMC method. The effect of variation in the data fitting restriction zone is evident in the fitted parameters.

Table 5.4: Comparison of MD and DSMC results (Hadjiconstantinou and Garcia 2001) for fitted attenuation coefficient (m) and sound speed (c) for different range of λ_{mfp} values used in fitting the cosine and sine components, $A(z)$ and $B(z)$, respectively, of the velocity amplitude in Figure 5.13b.

λ range	MD results		DSMC results	
	m (m^{-1})	c (m/s)	m (m^{-1})	c (m/s)
$z > 0.5\lambda_{\text{mfp}}$	1.43×10^7	478.77	1.42×10^7	464.1
$z > \lambda_{\text{mfp}}$	1.50×10^7	495.34	1.45×10^7	515.7

Based on the above discussion and validation results, it can be concluded that the MD simulation results are consistent with those of previous molecular simulations, such as the DSMC method, for sound wave propagation in a gas, and that the MD method can be effectively used to model acoustic wave propagation. Additionally, it is worth mentioning that this study (in validation *Case 3*) presents the first ever MD simulations to study standing waves. The wave characteristics of sound wave propagation in argon gas are analysed using classical standing wave equations and verified against the results of the DSMC method. Yano (2012) performed a similar molecular dynamics study of progressive sound wave propagation in a gas. However, his study was focused on investigating the fundamental problem of propagation of plane waves in high frequency sound: nonlinear and nonequilibrium processes. Hence his system was designed to simulate large amplitude oscillations of a sound source ($v_0 = a\omega = 0.8c$) with a simulation box length sufficiently large to observe nonlinear effects. On the other hand, in the current study the amplitude of the sound source was kept to a relatively small value

of $v_0 = 0.15c$, nearly six times smaller than that of Yano (2012), to avoid nonlinearity in the sound waves by ensuring that viscous forces dominate. Consequently, the length of the simulation domain considered in this study is very small, within a few wavelengths, which ensures that the sound wave does not travel to distances where the wave significantly steepens due to nonlinear effects (Hadjiconstantinou and Garcia 2001) or at least minimises the effects of nonlinearities.

5.4.3 Theoretical Comparison with Transmission Matrix Method of Duct Systems

The transmission matrix method described by Beranek and Ver (1992) for the analysis of duct systems with plane waves can be used to make a theoretical comparison with the simulation results. A few modifications were made to the transmission matrix equations for a duct system with uniform cross section in order to adapt the method for the current simulation domain. A complex wave number, $k' = k - im$, was considered instead of the classical wave number k to include the attenuation term m in the wave equation. In addition, k_c (a wave number for a flow with mean velocity) is replaced with k', assuming no frictional energy loss along the simulation domain. The acoustic pressure, p_j, and mass velocity field, $\rho S v_j$, at the j-th location in the simulation domain can be obtained by (see Beranek and Ver (1992), p377),

$$\begin{bmatrix} p_j \\ \rho S v_j \end{bmatrix} = \begin{bmatrix} T_{11} & T_{12} \\ T_{21} & T_{22} \end{bmatrix} \begin{bmatrix} p_0(z=0) \\ \rho S v_0(z=0) \end{bmatrix} \tag{5.17}$$

where S is the cross section of the simulation domain and the transmission matrix is given by (see Beranek and Ver (1992), p377),

$$\mathbf{T} = \begin{bmatrix} T_{11} & T_{12} \\ T_{21} & T_{22} \end{bmatrix} = \begin{bmatrix} \cos(k'L_j) & i\frac{c}{S}\sin(k'L_j) \\ i\frac{S}{c}\sin(k'L_j) & \cos(k'L_j) \end{bmatrix} \tag{5.18}$$

Figure 5.14 shows the comparison between the transmission matrix and MD simulation results. It can be seen from Figure 5.14a that the MD simulation results show good agreement with the theoretical estimates of the velocity amplitude at the lower frequency. On the other hand, at higher frequency, the agreement is good at distance further than one mean free path ($z > \lambda_{\mathrm{mfp}}$) from the acoustic source, but deteriorates at distance closer than one mean free path. This indicates that the aforementioned effect of free molecular flow is important for higher frequency and linear acoustic theory is not applicable near to the source at this frequency.

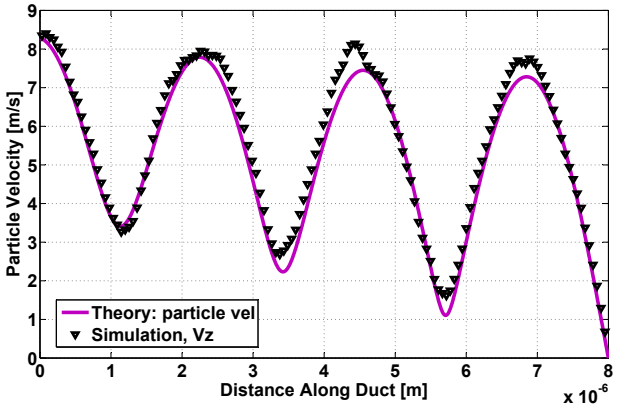

(a) R≈20

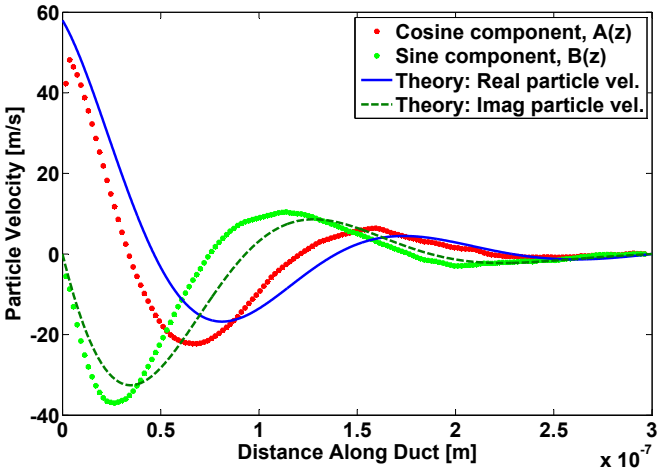

(b) R=0.5

Figure 5.14: Comparison of MD simulation results with theoretical estimates using transmission matrix method. (a) Velocity amplitude $V(z) = \sqrt{A^2 + B^2}$ as a function of distance for frequency $f = 67$ MHz ($R \approx 20$). (b) Cosine and sine components, $A(z)$ and $B(z)$, of the velocity amplitude as a function of distance for frequency $f = 2.57$ GHz ($R = 0.5$).

5.4.4 Effect of Thermostat

A comparison of the mean spatial gas temperature with and without the NVT thermostat and with varying thermostat damping times is presented in Figure 5.15. It can be observed that without the thermostat the gas temperature increases linearly with time due to the continuous work done by the piston on the gas, and with the inclusion of NVT thermostat the temperature can be controlled. However, thermostatting may also affect the pressure amplitude

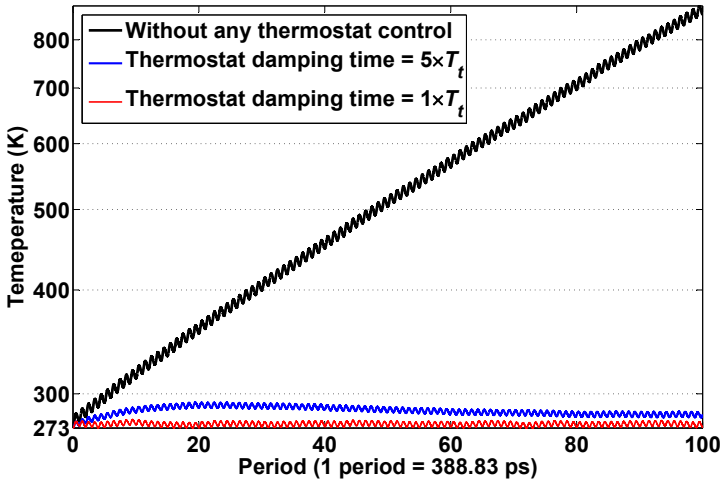

Figure 5.15: Variation of mean spatial gas temperature with and without NVT thermostat and for varying thermostat damping times. The thermostat with a damping time of 1 period shows the best temperature control of the three cases.

by injecting or extracting additional heat into/from the system. Hence, it was necessary to ensure that the use of a thermostat does not affect the propagating wave, which was done by adjusting the thermostatting damping time (τ) as a function of the number of periods (T_t) of the simulated acoustic frequency (ω), i.e. $\tau = n(\frac{2\pi}{\omega})$ with $n = 1, 2, \cdots$. It was found that a thermostat with a damping time of less than 1 period, i.e. a strongly coupled thermostat, affected the propagating wave by creating a large temperature fluctuation inconsistent with the oscillation of the piston. On the other hand, a thermostat damping time of 1 period or greater (e.g. 5 periods), i.e. a loosely coupled thermostat, was able to control the increasing temperature consistent with the oscillation of the piston, as shown in Figure 5.15, without affecting the propagating wave. It can be seen that the damping time of 1 period shows the best temperature control out of the cases studied, which aligns well with the fact that the additional energy input by each oscillation period of the piston is removed within each period by the thermostat. Therefore, higher frequency simulations were performed using the NVT thermostat with a damping time of 1 period.

5.5 Summary

This chapter presents MD simulations that were performed to validate each of the relevant phenomena required for the multi-physics problem of acoustic wave propagation in a system of CNTs, namely fluid/structure interactions, bi-directional heat transfer, and acoustic wave propagation. In *Case 1*, it was shown that the chosen MD method can accurately simulate the structural vibrational modes of a CNT excited by fluid/structure interactions and the flow properties of water molecules when compared with the reference study of Chen et al. (2011). The validation *Case 2* involves the study of the excitation of phonon modes of the CNT due to bi-directional heat transfer at the liquid-solid interface, which was analysed in terms of the phonon energy spectrum. In addition, the thermal boundary conductance and the formation of an argon adsorption layer around the CNT surface were also studied, which were compared with the study performed by Carlborg et al. (2008). In *Case 3*, MD simulation results were validated against theoretical calculations using the transfer matrix method and the DSMC results of Hadjiconstantinou and Garcia (2001). Comparison of the results indicates that the MD simulation method can be applied to understanding the sound field inside a standing wave tube. For all validation cases, the simulations in this study were performed with a different force field or simulation method to each of the reference simulations. Hence, this validation study demonstrates that a single approach (one force field - REBO, and one method - MD) can be used to study all of the phenomena that were modelled using different approaches in the reference studies. Consequently, based on the comparisons of the results of the current MD simulations with those of previous studies with similar simulation setups, it can be concluded that the chosen MD force field and method are capable of accurately modelling each of the phenomena required for solving the problem that has been undertaken in this project. In addition, successful validation of these simulations is very important to develop a platform that can be extended to perform MD simulations for nanomaterials with due consideration of all relevant phenomena simultaneously. Overall, this study demonstrates the usefulness of MD simulations and that the procedure can be followed to study the acoustic absorption behaviour of CNTs.

6 MD Simulation of Sound Wave Propagation and Classical Absorption in a Monatomic Gas

6.1 Introduction

Use of molecular dynamics simulation to model acoustic wave propagation in the presence of a nano-material is studied in this part of the thesis. Having a more complete understanding of the sound field inside an acoustic wave domain enables the simulation to be extended to the investigation of the CNT structural parameters controlling acoustic absorption. Simulations were initially performed for sound wave propagation in argon gas without CNTs present; thereafter it was extended to analyse the thermo-acoustic behaviour of CNTs in the presence of acoustic wave propagation in a gaseous media. This investigation will contribute to an improved understanding of the sound field and acoustic absorption behaviour in molecular dynamics simulations of acoustic wave propagation with and without the presence of a nanomaterial, which will lead to the investigation of the acoustic absorption mechanism of nanoscopic fibers.

Since this research is primarily aimed at clarifying the types of mechanisms involved that account for acoustic absorption due to the interaction between a gas and a CNT, only a relatively simple case of molecular simulation of sound wave propagation around a single CNT is considered in this study. Moreover, due to the limited availability of computational resources, simulations were restricted to a relatively short and narrow CNT. In the work presented in this study (see Chapter 7), the analysis of a single CNT fibre in a small acoustic domain was considered, where typical solution times were on the order of 25 days (per 100 periods of the wave cycle) using 96 cores of a supercomputer[1] with a peak performance of 24 teraFLOPS. Hence,

[1]For more details of the supercomputer: https://www.ersa.edu.au/service/hpc/tizard/

the analysis of a full-size CNT sample with millions of CNT units would be prohibitive with the available computational resources.

In addition, it was mentioned in Chapter 4 that simulations would need to be extended into the millisecond time scale to permit the study of acoustic wave propagation in the audible frequency range ($0.02 - 20\,\text{kHz}$), which would require considerable computational resources. Thus, it was concluded that performing MD simulations to explore acoustic absorption mechanisms at the nanoscale in the audible frequency range would not be feasible with the available computational resources. Therefore, the study of MD simulations for the CNT was limited to acoustic frequencies in the gigahertz (GHz) range.

The simulations reported in this study are an extension of the previously validated simulation presented in Section 5.4 to include a carbon nanotube (CNT). The focus of the study is on single-walled CNTs (SWCNTs) as representative nanoscopic fibres for acoustic absorption purposes. MD simulations were performed to capture the atomistic processes involved in the interaction between the acoustic wave and the CNT, which govern the energy transfer between them and control the acoustic absorption. The simulation domain was modelled with a CNT attached to the wall at the opposite end of the domain to the acoustic source and aligned parallel to the direction of the flow. Simulations were performed for high frequency sound wave propagation at a frequency of $f \approx 1.5\,\text{GHz}$ with a domain length equivalent to approximately half the wavelength of the acoustic wave to reduce the computational cost. Furthermore, it should also be reemphasised that at the high frequency considered, i.e. $f \approx 1.5\,\text{GHz}$, simulations were performed with a large initial velocity amplitude due to the considerable attenuation.

In order to observe the attenuation due to classical (viscous and thermal) losses occurring in the high-frequency sound propagation, additional simulations were performed for sound wave propagation without the CNT present for the same domain dimensions and conditions. The results were used to obtain a comparison of acoustic variables with and without the CNT present. This comparison was made in order to observe the acoustic damping due to the effect of fluid-structure interactions between the gas and the CNT induced by the acoustic wave. The results were used to demonstrate (and determine) the losses occurring in the fluid media without the presence of the CNT, which is very useful to differentiate between the classical acoustic energy losses in the fluid and the losses due to the CNT.

The study is divided into two major parts. In *Part 1*, presented in this chapter (Chapter 6), the analysis of the acoustic field inside the simulation domain without the CNT present is described. In *Part 2*, detailed in Chapter 7, the analysis and discussion related to the acoustic energy losses and

absorption behaviour of the CNT are presented. The associated classical acoustic losses in the fluid media causing attenuation in the high-frequency sound are also quantified and discussed in *Part 1*, which is an integral part of the investigation of the absorption mechanisms of the CNT. Moreover, the study presented in *Part 1* confirms that damping mechanisms are functional in the simulated acoustic domain with the current simulation setup using the MD method. The study in *Part 1* forms a platform for the analysis in this chapter. Thereafter the analysis is extended in *Part 2* in the following Chapter 7 for the explanation of the sound field and acoustic losses inside the simulation domain with the CNT present. Finally, conclusions are drawn from the analysis of the simulation results and possible extensions to the simulation and analysis approach presented in this study are discussed.

One challenge in MD simulations of high-frequency sound is describing the sound field inside the simulation domain, which must be defined properly before any quantification of the acoustic absorption can be done. In the current molecular dynamics simulations, data for acoustic variables such as the velocity, pressure, and density were collected in the time domain. The stochastic nature of atoms in a molecular simulation affects the measured values of these quantities. Hence, a significant portion of this chapter is devoted to describe the sound field inside the simulation domain. The methodology used here to analyse the sound field and to quantify the acoustic losses creates a platform to perform large-scale MD simulations in which the acoustic wave frequency can be reduced to the audible frequency range to study the acoustic behaviour of nanomaterials.

This chapter, *Part 1* of the study, is organised as follows. First, Sections 6.2-6.3 describe the simulation details and the relevant theories and modified calculation methods that were used to obtain the sound wave propagation parameters and absorption/losses in the wave medium. Second, Section 6.4 describes the study conducted to perform "sanity checking" of the simulations such as equilibration conditions of the simulations, convergence tests and statistical errors. These measurements demonstrate the effect on the simulation results that might be incurred due to variations in the system parameters. Finally, the simulation results are presented in Section 6.5. The sound field behaviour and the acoustic losses are also discussed in this section. It is very important that the MD simulation results of acoustic wave propagation in a fluid medium of a simulated acoustic domain are carefully analysed to determine deviations from classical methods. Since the simulation was performed for high-frequency sound in the GHz range, it carries even more importance to identify non-linearities in sound-wave propagation, which will have a very high attenuation coefficient. These analyses are useful to

differentiate the classical losses in the fluid medium and the non-linearities involved in the high-frequency sound from those of an analogous simulation domain containing a CNT.

6.2 Simulation Details

As mentioned earlier, simulations were performed for an equivalent system containing a CNT. The system was designed identically to the system modelled for the validation *Case 3* presented in Section 5.4, except with a smaller domain length. The simulation domain had transverse dimensions $L_x = L_y = 70\,\text{nm}$ and a domain length $L_z = 150\,\text{nm}$ chosen to be roughly equal to half the wavelength of the propagating wave. Figure 5.9 shows a sketch of the simulation domain. The far end of the simulation domain in the z-direction was terminated with a reflecting wall and the system was replicated in the transverse directions using periodic boundary conditions. The domain was filled with argon gas with a density of $\rho = 1.8\,\text{kgm}^{-3}$ to permit the propagation of acoustic waves.

Simulations were initiated with a Gaussian distribution of gas velocity components consistent with the desired temperature and were equilibrated for 2 ns at a temperature of $T = 273\,\text{K}$ and pressure $P = 1\,\text{atm}$. A Langevin thermostat was used to control the gas temperature during the equilibration period. Thereafter the system was switched to an NVT ensemble and further relaxed for 750 ps at the same temperature and pressure. Then the piston was sinusoidally oscillated at a velocity of $v_0 = 0.15c = 49.69\,\text{m/s}$ to excite the system with an acoustic wave of frequency 1.5 GHz. A timestep size of 0.5 fs was used during the equilibration of the gas and a 1 fs timestep was used during the wave propagation period. The simulation was run for nearly 39 ns, which is equivalent to 100 periods of the propagating wave cycle. As described earlier, the velocity amplitude of $v_0 = 0.15c$ was used to ensure that sufficient signal amplitude existed within the curve fit region ($z > 0.5\lambda_{\text{mfp}}$).

Similar to the system designed for validation *Case 3*, an NVT thermostat was coupled loosely with the system in directions perpendicular (x and y) to the propagating wave (z-direction) to extract the additional heat from the gas as the system was continuously heated due to the work done on the gas by the acoustic source. A detailed description of the implementation and the effect of thermostat on the propagating wave was given in Sections 5.4.2 and 5.4.4.

6.3 Theory: Calculation Methods

To analyse the sound field inside the simulation domain and to demonstrate the acoustic losses, the acoustic variables and sound energy parameters were evaluated based on the theory and calculation methods described in the following sections.

6.3.1 Fundamental Relationships of Acoustic Variables

For a plane wave travelling in a finite length waveguide, the standing wave equation for the sound pressure and particle velocity in the frequency domain can be written as (Kuipers 2013)

$$p(z,f) = A_p(f)\exp^{-ikz} + B_p(f)\exp^{ikz} = A_p(z,f) + B_p(z,f), \tag{6.1}$$

$$v(z,f) = \frac{1}{\rho c}\left[A_p(f)\exp^{-ikz} - B_p(f)\exp^{ikz}\right] = \frac{1}{\rho c}\left[A_p(z,f) - B_p(z,f)\right], \tag{6.2}$$

where A_p and B_p are the complex pressure amplitude of the incident and reflected plane wave, respectively, z is the spatial coordinate along the wave propagating direction (aligned perpendicular to the direction of piston face), ρ is the density of gas, c is the speed of sound, $k = \frac{2\pi f}{c}$ is the wavenumber and f is the simulated wave frequency. Solving the above equations for $A_p(z,f)$ and $B_p(z,f)$ yields (Kuipers 2013)

$$A_p(z,f) = \frac{1}{2}\left[p(z,f) + \rho c v(z,f)\right], \tag{6.3}$$

$$B_p(z,f) = \frac{1}{2}\left[p(z,f) - \rho c v(z,f)\right]. \tag{6.4}$$

Here, $p(z,f)$ and $v(z,f)$ are the Fourier transform of $p(z,t)$ and $v(z,t)$ at any position along the simulation domain. The incident and reflected sound waves, A_p and B_p, can then be associated with the incident and reflected sound intensity as (Kuipers 2013)

$$I_{\text{in}}(z,f) = \frac{|A_p(z,f)|^2}{2\rho c}, \tag{6.5}$$

$$I_{\text{ref}}(z,f) = \frac{|B_p(z,f)|^2}{2\rho c}. \tag{6.6}$$

Similarly, the active I_{ac} and reactive I_{reac} acoustic intensity can be associated with the particle velocity, $v(z,f)$, and sound pressure, $p(z,f)$, of the standing wave as (Jacobsen 1989)

$$I_{\text{ac}} = \frac{1}{2}Re[pv^*], \tag{6.7}$$

$$I_{\text{reac}} = \frac{1}{2} Im[pv^*]. \tag{6.8}$$

Here, v^* is the complex conjugate of the particle velocity $v(z, f)$ and the dependency of Equations (6.7) and (6.8) on z and f are omitted for brevity. To estimate the active and reactive intensity in terms of a double-sided spectrum of sound pressure, p_{ds}, and particle velocity, v_{ds}, Equations (6.7) and (6.8) become (Kuipers 2013)

$$I_{\text{ac}} = 2Re[p^*_{\text{ds}} v_{\text{ds}}], \tag{6.9}$$

$$I_{\text{reac}} = 2Im[p^*_{\text{ds}} v_{\text{ds}}]. \tag{6.10}$$

Combining Equations (6.3) to (6.6), the incident and reflected intensity parameters can also be expressed in terms of the power spectral density as (Kuipers 2013)

$$I_{\text{in}} = \frac{1}{4} \left[\frac{G_{pp}}{\rho c} + \rho c G_{vv} \right] + \frac{1}{2} Re(G_{pv}), \tag{6.11}$$

$$I_{\text{ref}} = \frac{1}{4} \left[\frac{G_{pp}}{\rho c} + \rho c G_{vv} \right] - \frac{1}{2} Re(G_{pv}). \tag{6.12}$$

The active and reactive intensity can be expressed as a function of the power spectrum using the cross-correlation between the sound pressure and particle velocity as (Kuipers 2013)

$$I_{\text{ac}} = Re(G_{pv}), \tag{6.13}$$

$$I_{\text{reac}} = Im(G_{pv}), \tag{6.14}$$

where G_{pp}, G_{vv} and G_{pv} are the single-sided auto- and cross-power spectral density of the sound pressure and particle velocity, respectively. Similarly, the transfer function between the sound pressure and particle velocity can be used to estimate the normalised acoustic impedance at any position as

$$z_s = \frac{Z_s}{\rho c} = \frac{1}{H_{pv} \rho c}, \tag{6.15}$$

where Z_s is the specific acoustic impedance of the propagating wave at any position along the wave propagation path and H_{pv} is the transfer function between the sound pressure and particle velocity. One can also calculate a localised absorption coefficient from the local active and incident acoustic intensity, I_{ac} and I_{in}, at any given position. The localised sound absorption coefficient, $\alpha_{\text{L}}(z)$, can be expressed as (Kuipers 2013)

$$\alpha_{\text{L}}(z) = 1 - \frac{I_{\text{ref}}(z)}{I_{\text{in}}(z)}. \tag{6.16}$$

The potential, kinetic and total energy density in a sound field can be written as

$$W_{\text{pot}} = \frac{|p|^2}{2\rho c^2} = \frac{G_{pp}}{\rho c^2}\,, \tag{6.17}$$

$$W_{\text{kin}} = \frac{\rho |v|^2}{2} = \rho G_{vv}\,, \tag{6.18}$$

$$W_{\text{tot}} = W_{\text{pot}} + W_{\text{kin}}\,. \tag{6.19}$$

6.3.2 Attenuation from Total Power and Exergy Concepts

The acoustic power losses in a conservative molecular dynamics simulation system cannot be estimated in a typical way, where the dissipated energy is calculated based on the rate of reduction of acoustic energy flowing along the wave path. Since the dissipated energy is converted to the random internal energy of the gas, keeping track of the change of total energy in the system at a given position is therefore a convenient way to estimate the losses occurring in the fluid medium. Hence, in order to estimate (demonstrate) dissipation of acoustic power in the simulation domain due to the classical losses in the fluid medium, the estimate of the acoustic power flowing in the medium is not the only power to consider for power balance of the system. Rather, the estimate of the total power in the system is of greater importance (see Swift 2002, Chapter 5, p128). The total power flowing in the wave propagation direction can be related to the enthalpy in moving gases using Rott's acoustic approximation (Swift 2002). The acoustic approximation of the total power flux in the z-direction can be written as (see Swift 2002, Chapter 5, p132)

$$\dot{H}_2(z) = \frac{1}{2}\rho \int Re[hv^*]dA - (A\kappa + A_{\text{solid}}\kappa_{\text{solid}})\frac{\mathrm{d}T_{\text{m}}}{\mathrm{d}z}, \tag{6.20}$$

where

$$h = U + PV = KE_{\text{gas}} + PE_{\text{gas}} + P/\rho \tag{6.21}$$

is the enthalpy per unit mass, κ is the thermal conductivity, A is the cross-sectional area and T_{m} is the mean temperature of the gas. The first term on the right side of Equation (6.20), $\frac{1}{2}\rho \int Re[hv^*]dA$, is the time-averaged enthalpy flux and the second term, $(A\kappa + A_{\text{solid}}\kappa_{\text{solid}})\frac{\mathrm{d}T_{\text{m}}}{\mathrm{d}z}$, is the conduction of heat both in the gas and in whatever solid is present in the system. Here, U is the internal energy per unit mass of the gas, which is the sum of the total kinetic energy, KE_{gas}, and total potential energy, PE_{gas}. The term PV is the product of the pressure and volume of the gas. The derivation of Equation (6.20) can be found in Chapter 5 of Swift (2002).

In order to present the power balance of the model and to estimate the total losses in the system, the concepts demonstrated by Swift (2002) for thermoacoustic engines and refrigerators based on the thermodynamics of efficiency are employed in this study. Similar to the method of accounting for efficiency in a complex thermodynamic system, all losses can be measured in terms of equivalent lost work, where a special temperature T_0 is identified as the temperature of the environment at which arbitrary amounts of heat of no economic value can be freely exchanged (see Swift 2002, Chapter 6, p147). The lost work (in terms of power) is expressed as the product of the temperature of the environment and the sum of all the entropy generated in the system as (see Swift 2002, Chapter 6, p150)

$$\dot{W}_{\text{lost}} = T_0 \sum \dot{S}_{\text{gen}}, \tag{6.22}$$

which is known as the Gouy-Stodola theorem (Bejan 1997). Here, $\sum \dot{S}_{\text{gen}}$ is the time-averaged entropy generation, expressed as an integral of the instantaneous rate of entropy generation over time and over the whole volume of the apparatus, which can be written as (see Swift 2002, Chapter 6, p151)

$$\sum \dot{S}_{\text{gen}} = \frac{\omega}{2\pi} \int_0^{\frac{2\pi}{\omega}} \int_V \rho \dot{s}_{\text{gen}} \, \mathrm{d}V \mathrm{d}t. \tag{6.23}$$

In the above equation, $\rho \dot{s}_{\text{gen}}$ is the instantaneous rate of entropy generation per unit volume, which is the sum of effects from different dissipative processes such as viscous, thermal, frictional, chemical, etc., involved with the various loss mechanisms and responsible for irreversibility in a thermoacoustic system (see Swift 2002, Chapter 6, p151). The sum $\sum$ indicates the total entropy generation can be calculated by adding together separate terms of entropy generation for each of the irreversible processes that accompany a total operation in a thermoacoustic system (Swift 2002).

The interpretation of losses was developed from a derivation of an acoustic approximation leading to the Gouy-Stodola theorem (Swift 2002; Bejan 1997) and from the concept of exergy. The exergy is the maximum amount of work that a system can do as it comes to equilibrium with a thermal reservoir. A brief description of the derivation of exergy based on the book by Swift (2002) is presented in this section. A generalised portion of the simulated system, as shown in the schematic in Figure 6.1, is considered to derive the acoustic approximation of losses (i.e. total entropy generated in the system) in terms of the exergy. For steady state of the portion shown in Figure 6.1, the difference between energy fluxes going out and going in must be zero, according to the First Law of Thermodynamics, which can be written as (see

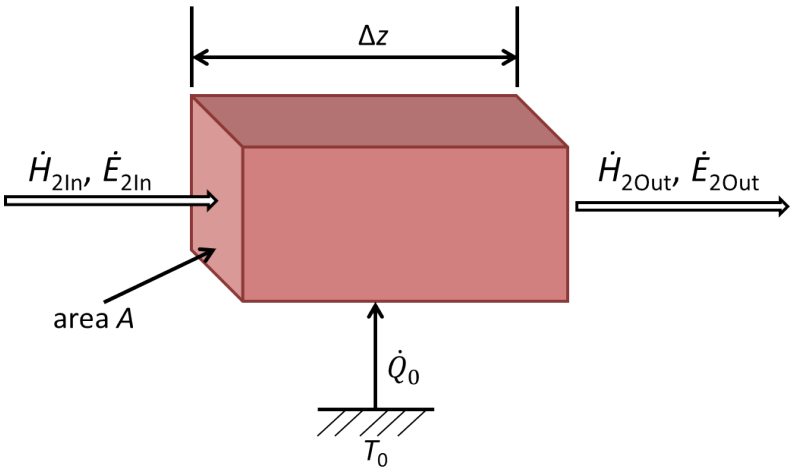

Figure 6.1: Schematic of a generalised microscopic portion of the simulation domain of the modelled acoustic system. The wave is propagating in the z-direction and the representative microscopic portion of the simulation domain with length Δz has acoustic power $\dot{E}_2$ and total power $\dot{H}_2$ flowing into and out of the left and right open end, respectively. In between the process, the system rejects (or absorbs) thermal power $\dot{Q}$ to ambient at T_0. The schematic is adapted from Swift (2002).

Swift 2002, Chapter 6, p154)

$$0 = \dot{H}_{2\mathrm{Out}} - \dot{H}_{2\mathrm{In}} - \dot{Q}_0. \tag{6.24}$$

Similarly according to the Second Law of Thermodynamics, the entropy generated within the portion must equal to the difference between the entropy fluxes going out and going in, which can be written as (see Swift 2002, Chapter 6, p154)

$$\sum \dot{S}_{\mathrm{gen}} = \frac{\dot{H}_{2\mathrm{Out}} - \dot{E}_{2\mathrm{Out}}}{T_{\mathrm{mOut}}} - \frac{\dot{H}_{2\mathrm{In}} - \dot{E}_{2\mathrm{In}}}{T_{\mathrm{mIn}}} - \frac{\dot{Q}_0}{T_0}, \tag{6.25}$$

where $\dot{E}_2$ is the acoustic power flowing at a mean temperature T_{m} along the wave path, which is equal to I_{ac} when presented as an acoustic power flowing per unit area in a plane wave propagation and $\frac{\dot{H}_2 - \dot{E}_2}{T_m}$ is the second-order entropy flux. Combining Equations (6.24) and (6.25) by eliminating the uninteresting heat $\dot{Q}_0$ yields (see Swift 2002, Chapter 6, p154)

$$T_0 \sum \dot{S}_{\mathrm{gen}} = \frac{T_0}{T_{\mathrm{mIn}}} \dot{E}_{2\mathrm{In}} + \left(1 - \frac{T_0}{T_{\mathrm{mIn}}}\right) \dot{H}_{2\mathrm{In}} - \frac{T_0}{T_{\mathrm{mOut}}} \dot{E}_{2\mathrm{Out}} - \left(1 - \frac{T_0}{T_{\mathrm{mOut}}}\right) \dot{H}_{2\mathrm{Out}}, \tag{6.26}$$

which can be written in terms of exergy as

$$T_0 \sum \dot{S}_{\text{gen}} = \dot{X}_{\text{2In}} - \dot{X}_{\text{2Out}}, \tag{6.27}$$

with $\dot{X}_2(z)$ being the time-averaged exergy flux in the z-direction in the simulation domain. The thermoacoustic approximation of exergy flux $\dot{X}_2(z)$ can be written as (see Swift 2002, Chapter 6, p155)

$$\dot{X}_2 = \frac{T_0}{T_{\text{m}}} \dot{E}_2 + \left(1 - \frac{T_0}{T_{\text{m}}}\right) \dot{H}_2. \tag{6.28}$$

Examining this equation for $\dot{X}_2$, it can be noticed that the exergy flux indicates the ability of the associated power to do work as defined earlier (see Swift 2002, Chapter 6, p155). Expressing $\dot{X}_{\text{2In}} = \dot{X}_2^i$ and $\dot{X}_{\text{2Out}} = \dot{X}_2^{i+1}$, where $i(= 1, 2, 3 \cdots M)$ is the bin[2] number index along the wave propagation, and presenting the difference between the exergy flux $(\dot{X}_{\text{2In}} - \dot{X}_{\text{2Out}})$ as the change in energy flux in two consecutive bins in the simulation domain, Equation (6.27) can be written as

$$T_0 \frac{\mathrm{d} \sum \dot{S}_{\text{gen}}}{\mathrm{d}z} = -\frac{\dot{X}_2^{i+1} - \dot{X}_2^i}{\Delta z} = -\frac{\mathrm{d}\dot{X}_2}{\mathrm{d}z}, \tag{6.29}$$

which results in a thermoacoustic approximation to the Guoy-Stodola theorem from letting $\Delta z \to \mathrm{d}z$. This equation shows that

$$-\frac{\mathrm{d}\dot{X}_2}{\mathrm{d}z} \leq 0, \tag{6.30}$$

expressing the combined First and Second laws of thermodynamics in thermoacoustics and indicating the conservation of exergy when no entropy is generated (see Swift 2002, Chapter 6, p155). It can also be shown that work lost and entropy generation can be related in a simple form, when $T_{\text{m}} = T_0$, as (see Swift 2002, Chapter 6, p155)

$$-\frac{\mathrm{d}\dot{X}_2}{\mathrm{d}z} = T_0 \frac{\mathrm{d} \sum \dot{S}_{\text{gen}}}{\mathrm{d}z} = -\frac{\mathrm{d}\dot{E}_2}{\mathrm{d}z}, \tag{6.31}$$

which indicates the losses as the dissipation of acoustic power per unit length in a channel along the wave path. In this study, the thermostat was considered as the environment to which waste heat was transferred at $T_0 = T_{\text{thermostat}} = 273\,\text{K}$, which is equivalent to the equilibrium gas temperature of the whole system, and $T_{\text{m}} = \langle T_i \rangle$ is the mean gas temperature of each microscopic bin along the z-direction.

[2]Virtual bins are created during a simulation by dividing the simulation domain (spatially) into evenly spaced slices of microscopic boxes (containing a number of atoms) relative to a coordinate value or origin in any direction along the domain (LAMMPS-Manual 2013).

The entropy generation calculated using Equation (6.29) gives the rate of energy lost per unit length of the microscopic portion of the thermoacoustic system. For a simulation domain of a thermoacoustic system of plane wave propagation of a volume V and cross-sectional area A and wavelength $\lambda = \frac{2\pi}{k}$ with k being the wavenumber, the rate at which the energy is lost from the wave can be obtained by integrating Equation (6.29) over the volume (see Kinsler et al. 2000, Chapter 8, p216). It can be written per unit volume as

$$\frac{\dot{W}_{\text{lost}}}{V} = -\frac{1}{V}\int_0^{\lambda} \nabla \,.\, \dot{X}_2 \mathrm{d}z. \tag{6.32}$$

Equation (6.32) gives the power lost per unit volume, which can then be used to obtain the attenuation coefficient m_{e} as, in this case based on exergy concepts,

$$m_{\text{e}} = -\frac{\left[\frac{1}{V}\int_0^{\lambda} \nabla \,.\, \dot{X}_2 \mathrm{d}z\right]}{2I}, \tag{6.33}$$

where $I(=\frac{1}{2}\rho c v_0^2)$ is the classical acoustic intensity for the simulated wave, $v_0 = 49.69\,\text{m/s}$ is the particle velocity amplitude chosen for the study and subscript 'e 'is used to indicate exergy concepts.

In a conservative molecular simulation domain, the coherent energy contained in an acoustic wave is transferred to atoms at random times via the stochastic nature of the interactions of atoms as the wave propagates, which leads to an eventual reduction of the magnitude of the rarefaction and compression. Hence, the lost work or entropy generation can be considered as the incoherent energy associated with the loss mechanisms. Therefore, distinguishing the incoherent energy from the coherent acoustic energy in each microscopic bin along the wave path would give the total losses in the system. In the above calculations of the exergy flux, it can be noticed that all power terms represent the coherent energy in the system, which means the lost work or entropy generation would be equivalent to the incoherent energy in the system as the lost work is converted to random energy of the gas atoms.

6.3.3 Attenuation from the Theory of Continuum Mechanics

For a simple-harmonic plane wave, the viscous loss of energy per unit volume per second (see Morse and Ingard 1968, Chapter 6, p275) can be expressed as

$$\frac{\mathrm{d}\epsilon_{\text{viscous}}}{\mathrm{d}t} = (\eta_{\text{B}} + \frac{4}{3}\mu)|\frac{\mathrm{d}u_z}{\mathrm{d}z}|^2 = \frac{4}{3}\mu|\frac{\mathrm{d}v}{\mathrm{d}z}|^2, \tag{6.34}$$

where $u_z = v$ is the particle velocity in the z-direction, μ is the dynamic viscosity in units of Pa s (for argon, $\mu = 22.2 \times 10^{-6}$ Pa s) and η_{B} is the bulk

viscosity of gas (for monatomic gas, $\eta_B = \simeq 0$). The losses due to thermal conduction can be evaluated as (see Morse and Ingard 1968, Chapter 6, p277)

$$\frac{d\epsilon_{\text{thermal}}}{dt} = \kappa\nabla^2 T = \frac{\kappa}{T}|\nabla T|^2 + T\nabla\,.\,(\frac{\kappa}{T}\nabla T), \tag{6.35}$$

where κ is the thermal conductivity in units of W/mK and T is the gas temperature in Kelvin. Here T represents the gas temperature in such a way that the magnitude of the temperature fluctuation in the wave would be equivalent to (see Kinsler et al. 2000, Chapter 8, p215)

$$|T - T_{\text{eq}}| = T_{\text{eq}}(\gamma - 1)\frac{p_0}{\rho c^2}, \tag{6.36}$$

where T_{eq} is the equilibrium temperature of the gas, p_0 is the pressure amplitude of the wave and γ is the specific heat ratio which is $\frac{5}{3}$ for a monatomic gas such as argon.

In Equation (6.35), the second term on the right is an oscillatory term whose time average is zero and can be approximated as (see Kinsler et al. 2000, Chapter 8, p216)

$$T\nabla\,.\,(\frac{\kappa}{T}\nabla T) \simeq 0. \tag{6.37}$$

The T's in the denominator in Equation (6.35) can be replaced by T_{eq} to make a consistent approximation with linear acoustics (see Kinsler et al. 2000, Chapter 8, p216). However, in a molecular system, the gas is heated up from its equilibrated temperature (273 K in the case investigated here) during the wave propagation, as shown in Figure 6.8a; hence, T_{eq} is replaced by the mean spatial gas temperature. The thermal losses can then be expressed as

$$\frac{\mathrm{d}\epsilon_{\text{thermal}}}{\mathrm{d}t} = \frac{\kappa}{T_{\text{eq}}}|\nabla T|^2. \tag{6.38}$$

The time-averaged rate of change of the acoustic energy density (rate of energy being lost from the acoustic wave) over the volume can then be estimated as

$$\mathrm{d}Q = \frac{S}{V}\left\langle \int_0^{\lambda} \left[\frac{\mathrm{d}\epsilon_{\text{viscous}}}{\mathrm{d}t} + \frac{\mathrm{d}\epsilon_{\text{thermal}}}{\mathrm{d}t}\right] \mathrm{d}z \right\rangle_t. \tag{6.39}$$

The attenuation coefficient for continuum approximations from the simulation results can be evaluated as (see Morse and Ingard 1968, Chapter 6, p277)

$$m_{\text{c}}^{\text{s}} = \frac{\mathrm{d}Q}{2I}, \tag{6.40}$$

where subscript 'c 'and superscript 's 'are used to indicate calculation based on continuum mechanics and simulation results, respectively.

Similarly, theoretical approximations of the classical losses based on continuum mechanics can be shown as (Morse and Ingard 1968; Kinsler et al. 2000)

$$\frac{\mathrm{d}\epsilon_{\text{viscous}}}{\mathrm{d}t} = \frac{4}{3}\mu|kv_{\text{rms}}|^2, \tag{6.41}$$

and

$$\frac{\mathrm{d}\epsilon_{\text{thermal}}}{\mathrm{d}t} = (\gamma-1)\frac{\kappa}{c_p}|kv_{\text{rms}}|^2, \tag{6.42}$$

where c_p is the heat capacity at constant pressure in J/kgK (for argon, c_p = 520.33 J/kgK), k ($=\frac{\omega}{c}$) is the wavenumber and v_rms is the root-mean-square of acoustic velocity amplitude, which is equivalent to $\frac{1}{\sqrt{2}}\times$ velocity amplitude v_0 for sinusoidal motion, which is used in this simulation. The continuum approximations of the classical attenuation coefficient results from letting $v_\text{rms} = \frac{1}{\sqrt{2}}v_0$ and $I = \frac{1}{2}\rho c v_0^2$ in Equation (6.40):

$$m_\text{c}^\text{t} = \frac{2}{3}\mu\frac{k^2}{\rho c} + \frac{1}{2}\frac{\kappa}{c_p}(\gamma-1)\frac{k^2}{\rho c}, \tag{6.43}$$

where subscript 'c 'and superscript 't 'are used to indicate calculation based on continuum mechanics and theoretical approximation, respectively.

The classical attenuation coefficient can also be calculated from the complex wavenumber k_c derived for plane wave propagation from the linearised wave equation. The complex wavenumber can written as (Pierce 1989; Howard and Cazzolato 2014)

$$k_c = \frac{\omega}{c}\left[1 + j\frac{\omega\nu}{c^2}\left(\frac{4}{3}+\frac{\gamma-1}{Pr}\right)\right]^{-1/2} = k - jm, \tag{6.44}$$

where ν ($=\frac{\mu}{\rho}$) is the kinematic viscosity, Pr ($=\frac{\mu c_p}{\kappa}$) is the Prandtl number, $k(=\frac{\omega}{c})$ is the classical wavenumber and m represents the attenuation rate of the acoustic field by the effects of viscous and thermal conductivity. At low frequency, for small ω, where visco-thermal affects are negligible, the complex wavenumber can be approximated as

$$k_c \approx \frac{\omega}{c}\left[1 - j\frac{1}{2}\frac{\omega\nu}{c^2}\left(\frac{4}{3}+\frac{\gamma-1}{Pr}\right)\right] = k - jm. \tag{6.45}$$

Thus the attenuation coefficient for low frequencies may be approximated as

$$m \approx \frac{1}{2}\frac{\omega^2\nu}{c^3}\left(\frac{4}{3}+\frac{\gamma-1}{Pr}\right). \tag{6.46}$$

It can be shown that the attenuation coefficient approximated for low frequencies given by Equation (6.46) is consistent with the continuum approximation

of the classical attenuation coefficient m_c^t in Equation (6.43). However at higher frequencies (for large ω) the dimensionless coefficient $\frac{\omega\nu}{c^2}$ approaches unity and the attenuation can be significant. Hence the higher order terms of the complex wavenumber cannot be ignored. Thus, at higher frequencies, evaluation of the attenuation coefficient using the complex wavenumber in its original form in Equation (6.44) gives a better approximation of attenuation. Hence, the attenuation constant ($m_{c_L}^t$) without an approximation for low frequencies is calculated from the complex wavenumber k_c using the relation in Equation (6.44) (Pierce 1989).

6.4 Sanity Check: Equilibration, Convergence Test, Statistical Errors and Wave Propagation

As mentioned earlier, the simulation domain was extended from the validation study presented for *Case 3* in Section 5.4. Therefore, the acoustic domain was initially designed to simulate acoustic wave propagation at a frequency $f \approx 2.5\,\text{GHz}$ (acoustic Reynolds number, $R = 0.5$). Hence a simulation that included the CNT was performed using the same frequency and the same simulation conditions despite reducing the domain length to accommodate the wave to the order of one wavelength. However, after analysing the acoustic field of the simulation domain (shown in Figure 5.9) for the classical acoustic absorption in the fluid medium, it was observed that the wave attenuation was too high to have sufficient acoustic energy near the termination. In addition, the wave became very noisy near the reflective wall due to the large attenuation, which can be observed in the results presented in Section 6.5. Hence, the acoustic wave frequency was reduced to $f \approx 1.5\,\text{GHz}$ ($R = 1$) to ensure that the wave had sufficient acoustic energy near the reflective wall and thereby improve the coherence with transmission of the acoustic wave. As such, some of the studies performed for sanity checking such as system size, sampling time, and statistical errors, presented in Sections 6.4.1, 6.4.2, and 6.4.3, respectively, are for the acoustic wave of frequency $f \approx 2.5\,\text{GHz}$ ($R = 0.5$), whereas the equilibration and steady state condition explained in Section 6.4.4 and 6.4.5, respectively, are for the current simulation at the frequency of $f \approx 1.5\,\text{GHz}$ ($R = 1$). The sanity check results verified at the frequency $f \approx 2.5\,\text{GHz}$ ($R = 0.5$) can still be considered valid for a relatively lower frequency at $f \approx 1.5\,\text{GHz}$ ($R = 1$) given that the ratio of mean free path and acoustic wave length (Knudsen number) for both frequencies is in the transition flow regime and the change in the value of Kn is in an acceptable range of 0.2-0.4.

6.4.1 Convergence Test: system size

In order to ensure that the simulation box was large enough to neglect finite-size effects, convergence tests for the system size were performed with respect to the dimensions of the box perpendicular to the wave propagation direction (z-axis). Simulations were performed by varying box dimensions L_x and L_y from $L_x = L_y = 20\,\text{nm}$ to $70\,\text{nm}$ with a fixed simulation domain length $L_z = 150\,\text{nm}$ in the z- direction. A comparison of simulation results for the particle velocity amplitude of the standing wave with varying system size is displayed in Figure 6.2. The simulation results presented in Figure 6.2 are for the velocity components $A(z)$ and $B(z)$ of the particle velocity amplitude $v(z)$, in Equations (5.11) and (5.12), respectively, as a function of wave travelling distance from the sound source in the z-direction. It should be noted that the simulation results were estimated after the transient period of the simulation had passed. It can be seen that the simulation results are slightly influenced by the change of the simulation domain size. The comparison indicates that simulation domains with dimensions L_x and L_y larger than $60\,\text{nm}$ (equivalent to $\frac{L_x \text{ or } L_y}{\lambda_{\text{mfp}}} \gtrsim 1$) give well-converged particle velocity components. Variance in the results for the simulations of smaller system size from $20\,\text{nm}$ to $40\,\text{nm}$ may be due to greater random error in

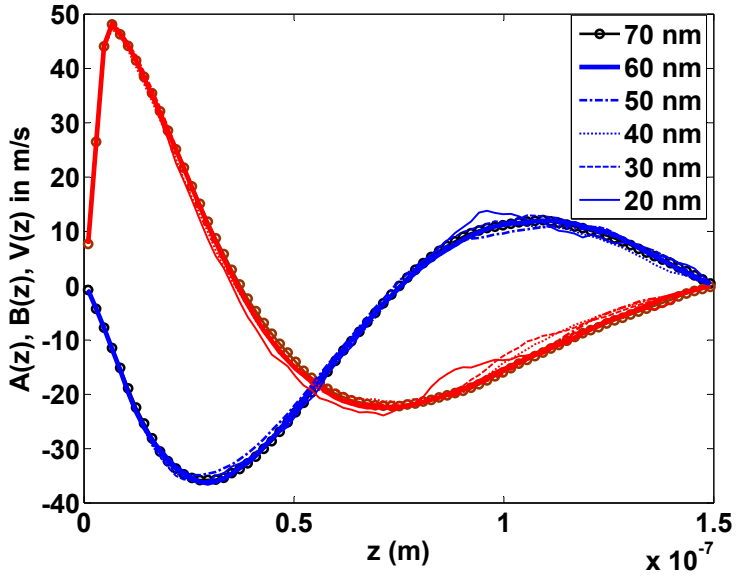

Figure 6.2: Velocity components $A(z)$ (blue lines) and $B(z)$ (red lines) as a function of distance from acoustic source for varying system size (width of the simulation domain).

simulation with smaller numbers of atoms in the system. For instance, a system size of $20 - 40$ nm have a number of argon atoms (gaseous region only) in the range of 1,800 to 7,500, whereas a system size of $50 - 70$ nm contains more than 10,000 atoms and up to 20,500 atoms. The precision of simulated properties improves with larger number of atoms in the system, as statistical errors in a property decreases proportionally with the inverse of square root of the number of atoms (Frenkel and Smit 2002). Hence, it can be considered that a simulation domain with the dimensions $L_x = L_y = 60$ nm (in the direction perpendicular to the wave propagation) achieves a well-converged simulation result with insignificant effects associated with the finite system size. However, in this study all simulations were performed with larger dimensions of $L_x = L_y = 70$ nm to ensure that the domain size was at least equal to one mean free path ($\lambda_{\text{mfp}} \approx 72$ nm) for argon atoms. Having a large enough system size to accommodate a full collision length for gaseous atoms would minimise/exclude inter-nanotube coupling interactions via the gaseous argon atoms as a result of the periodic boundary condition in the x- and y- directions.

6.4.2 Convergence Test: sampling time

A similar convergence test of sampling times for the collection of simulation data was performed to ensure that the sampling frequency was large enough to avoid any perturbation in the simulation results. The simulations were carried out for a fixed system size with dimensions $L_x = L_y = 70$ nm and $L_z = 150$ nm. In order to perform the convergence test, a number of MD simulations were conducted with different sampling times varying in the range of 0.5 ps to 20 ps for the collection of the velocity amplitude data. It should be clarified that a 20 ps sampling time indicates the time for the final averaged quantities generated from the average over 2000 repeated quantities computed in the preceding portion of the simulation every 10 fs timestep (LAMMPS-Manual 2013). Similarly a 15 ps sampling time would extract a final averaged value every 15 ps of the simulation computed from 1500 instantaneous values collected every 10 fs timestep. This implies that reducing the sampling time (in this case) does not only increase the sampling frequency but also reduces the sample size of the repeated quantities extracted for final averaging.

Figure 6.3 shows the simulation results for the velocity components $A(z)$ and $B(z)$ of the standing wave as a function of the distance the acoustic wave has travelled from the sound source for various sampling times. It can be seen that the simulation results change slightly with the sampling rate and

converge for high sampling rates. Sampling times less than 1 ps appear to give well-converged simulation results for the velocity components. Hence further MD simulations were performed with a 1 ps sampling time to record the velocity data during the wave propagation.

6.4.3 Statistical Errors

Classical MD simulations evolve in a step-by-step fashion with time and there are limits on the time and length scales that can be simulated on a typical computer (Allen 2004; Frenkel and Smit 2002). Hence, the statistical variation in simulation results must be taken into account. The simulations performed in this study were run for approximately 4×10^7 MD steps for 100 periods of the propagating acoustic wave at a frequency of $f \approx 2.5$ GHz, which corresponds to 39 ns of simulated time (which took 22.5 hours using 48 cores on a supercomputer with a peak performance of 24 teraFLOPS). Therefore, it is very important to check whether the simulation has reached the steady state before commencing the post-processing of the results. In addition, it is a common practice when conducting molecular simulations to estimate statistical errors in order to measure the influence of errors on the estimated average of a simulation quantity of interest. In addition, estimates of statistical errors can be used to confirm whether the simulation was

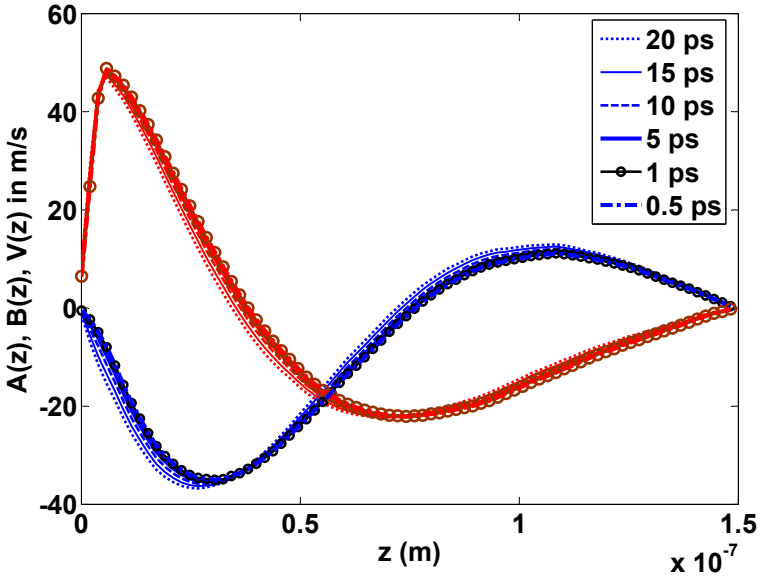

Figure 6.3: Velocity components, $A(z)$ (blue lines) and $B(z)$ (red lines) as a function of distance from sound source for varying sampling time.

actually run long enough before taking simulation averages of the quantity of interest. In this study, *block averaging*, as described in Section 4.2.5, was used to estimate statistical errors for the components of standing wave velocity amplitude. The calculation was carried out to estimate the overall standard error as (Grossfield and Zuckerman 2009)

$$SE(A, t_{\mathrm{B}}) = \frac{\sigma(\overline{A}_{\mathrm{B}})}{\sqrt{n_{\mathrm{B}}}}, \tag{6.47}$$

in the measured quantity (A) as a function of block size, which was varied as a multiple of the number of cycles of the wave. Here, t_{B} is the block length, n_{B} is the number of blocks and $\sigma(\overline{A}_{\mathrm{B}})$ is the standard deviation among the block averages $\overline{A}_{\mathrm{B}}$. Figure 6.4 illustrates the calculated value of the $SE(A, t_{\mathrm{B}})$ as a function of block size. It can be seen that the estimates of the overall

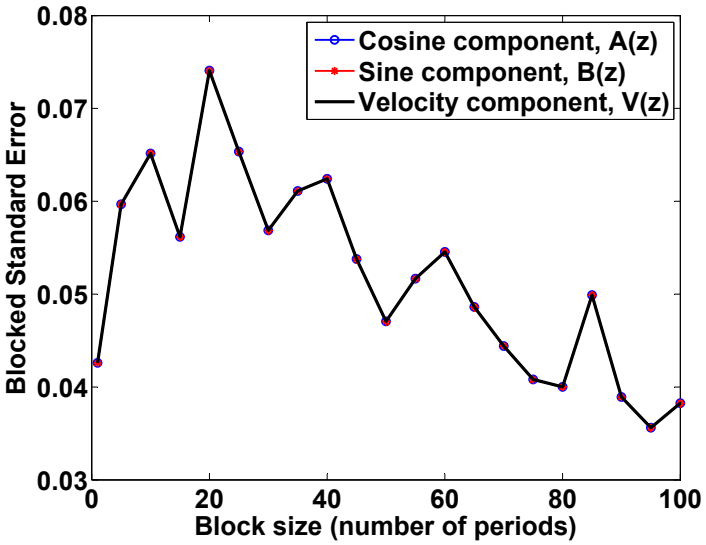

Figure 6.4: Estimates of the overall standard error $SE(A, t_{\mathrm{B}})$ using block averaging for wave frequency $f \approx 2.5\,\mathrm{GHz}$ ($R = 0.5$). The figure shows the approach to a plateau value of $SE(A, t_{\mathrm{B}})$ when the block size t_B is increased as a function of number of acoustic wave periods (T_t), reflecting essentially decay time of the correlations in fluctuations of the estimated velocity components, $A(z)$ and $B(z)$. The block averaging was calculated from simulation data of a length of 78 ns equivalent to 200 periods of wave propagation cycle.

standard error $SE(A, t_{\mathrm{B}})$ steeply increases as the block size is increased and reached a maximum at a block size of 20 periods, indicating the consecutive blocks smaller than 20 wave periods is highly correlated. Thereafter the error estimate decreases as the block size is increased further. This indicates that

the simulation would need to be run for at least 20 periods to yield a reliable estimate of a quantity. For large block sizes, only a few data points (number of blocks) were available which results in large standard deviation in the error (Frenkel and Smit 2002). In this study each simulation was run for 100 periods. The first 60 periods after the simulation had started was considered as a transient period for equilibration and the averaging of the results was conducted on the data for the remainder of the (40) simulation periods.

6.4.4 Equilibration of the System

Simulation conditions were monitored for the equilibration of the system properties such as temperature, pressure, velocity, kinetic and potential energy. The time evolution of these properties during the equilibration (before the wave propagation) are shown in Figures 6.5 and 6.6. Figure 6.5 shows the time evolution of the global temperature, pressure, kinetic and potential energy of the gas in the system. It can be seen that the system gradually

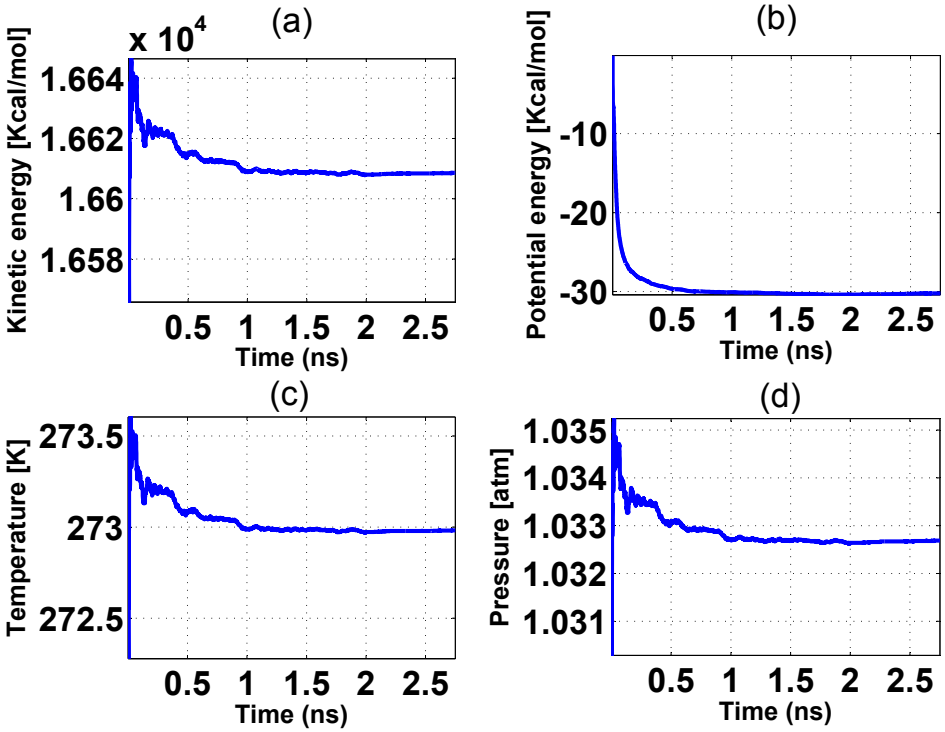

Figure 6.5: Illustration of the time evolution of global (a) kinetic energy, (b) potential energy, (c) temperature and (d) pressure of the gas in the simulation system during the equilibration process.

reached a constant value for each of the gas properties by the equilibration

time of 2.5 ns. Similarly, the time evolution of change of velocity, density, temperature and pressure of the gas in each microscopic bin along the z-direction of the simulation domain was monitored and the results are displayed in Figure 6.6. Again it can be observed that the system reached a well converged equilibrium condition along the simulation domain by 2.5 ns.

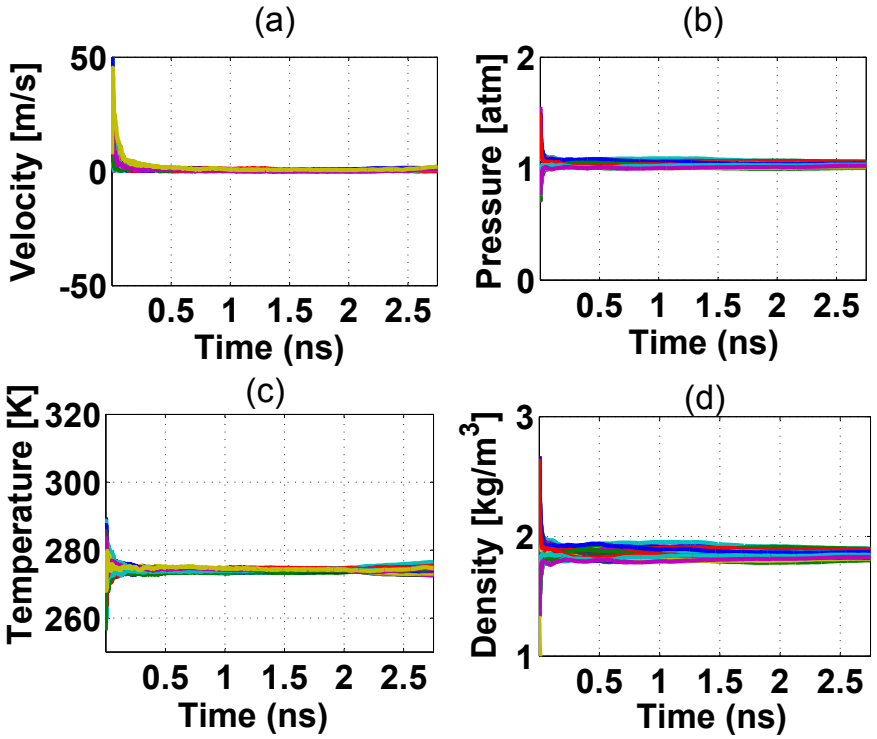

Figure 6.6: Illustration of the time evolution of change of (a) average velocity ($V = \sqrt{V_x^2 + V_y^2 + V_z^2}$), (b) pressure, (c) temperature and (d) density of the gas during the equilibration process in each microscopic bin (total 79 bins) along the z-direction of the simulation domain. Each colour represents the quantity for particular bin.

A histogram was constructed of the molecular velocities of gas atoms in the whole system to check the velocity distribution function of the molecules. Figure 6.7 shows the velocity distribution of the gas molecules during the equilibration. It can be seen that the velocity distribution develops into the Maxwellian form in the equilibration.

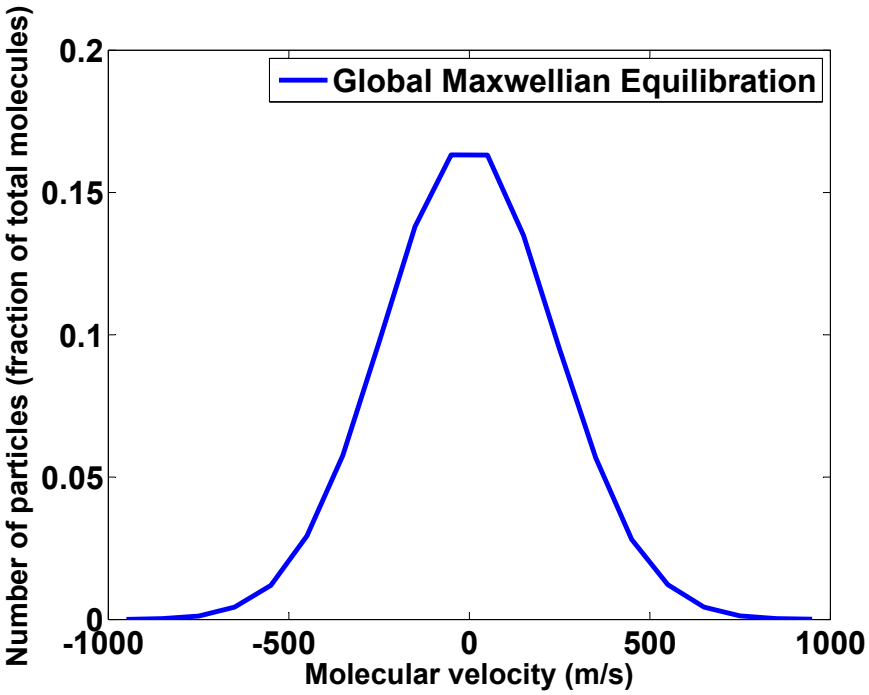

Figure 6.7: Maxwellian velocity distribution function of argon gas in equilibrium at 273 K.

6.4.5 Steady State Condition during the Wave Propagation

The variation of the temperature and pressure of the gas was monitored during the steady state of the wave propagation. It was observed that the variation in the mean temperature and pressure of the gas, shown in Figure 6.8, due to dissipation was less than 5% of the gas equilibrium temperature at 273 K or pressure at 1 atm, respectively. Hence the change in sound speed (which is proportional to $\sqrt{T}$ or $\sqrt{P}$) would be within 2.5%.

In order to check for deviations of the velocity distribution function of the gas molecules from the locally Maxwellian form, a histogram was constructed of the molecular velocities of all the gas atoms in the system (i.e. global) and those of the three spatial slices along the z-direction (i.e. local). Figure 6.9 shows the global and local velocity distribution of the gas molecules during the wave propagation. It can be seen that the velocity distribution of the gas molecules is both globally and locally Maxwellian and the deviation between them is insignificant.

The system was also checked for the input/output energy balance for the extraction of additional energy by the thermostat and the energy input

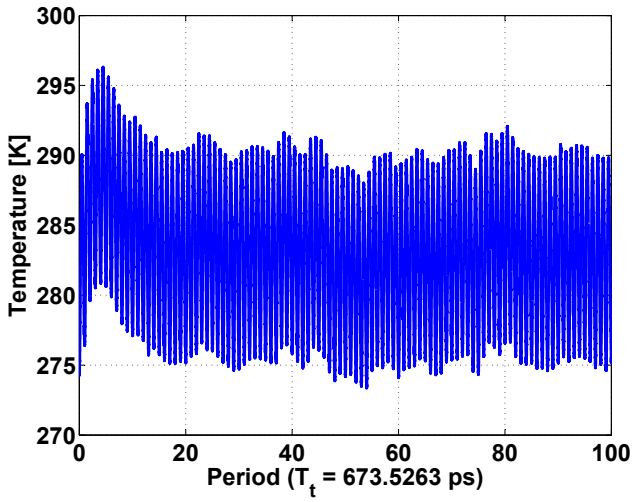

(a) Temperature

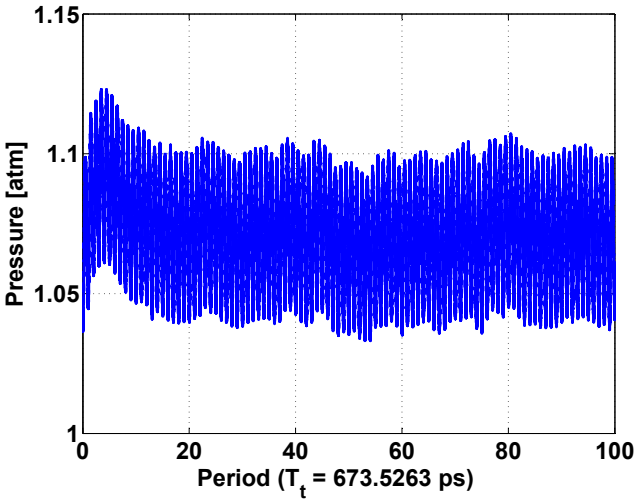

(b) Pressure

Figure 6.8: Variation of mean spatial (a) temperature and (b) pressure of the gas for a simulation of acoustic wave propagation at frequency $f \approx 1.5\,\text{GHz}$ ($R = 1$).

to the system by each oscillation period of the piston. The energy input to the system was monitored by observing the normal force acting on the gas atoms near to the piston. The input acoustic energy is equivalent to the work done by the pistons, which can be calculated from the recorded normal force on the gas and the oscillating displacement of the piston. The work done by

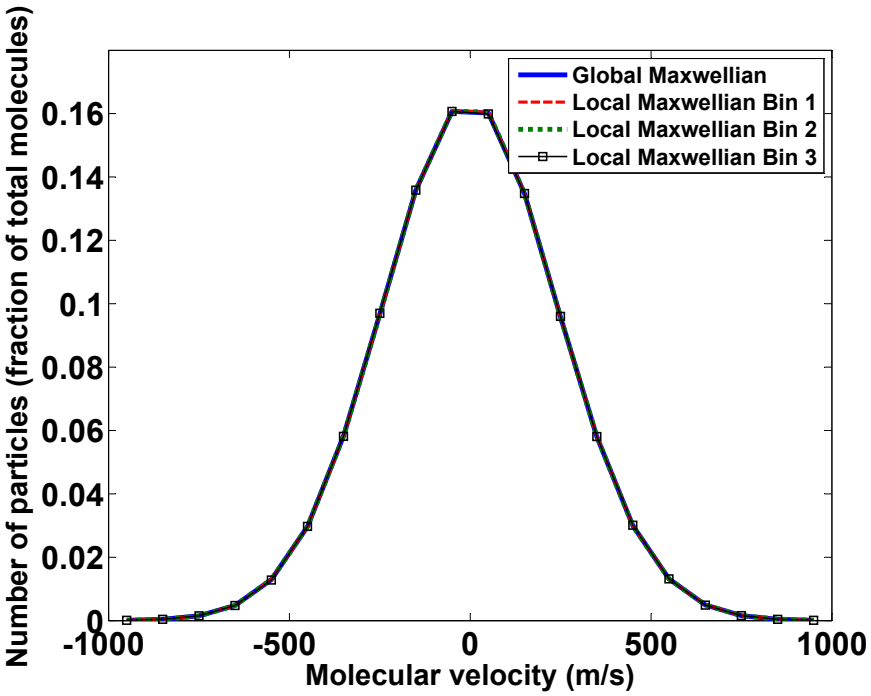

Figure 6.9: Maxwellian velocity distribution function of argon gas during the sound wave propagation of frequency $f \approx 1.5\,\text{GHz}$ (R=1) measured globally for the whole system and locally for three spatial bins along the z-direction. The values of molecular velocities and the number of molecules were averaged over the simulation time equivalent to 40 wave cycles. Here, spatial bins 1 - 3 represent the 3-dimensional slices of width 30 nm starting from the sound source, i.e Bin 1: $0 - 30\,\text{nm}$, Bin 2: $30 - 60\,\text{nm}$, and Bin 3: $60 - 90\,\text{nm}$.

the piston can be expressed as

$$W = \text{Force} \times \text{distance} = \left\langle \int_0^{\lambda} F_z \mathrm{d}z \right\rangle_T \tag{6.48}$$

The energy extracted by the thermostat was recorded during the simulations, which can also be estimated by balancing the recorded system's total energy and the energy of the gas and piston wall (refer to LAMMPS-Manual (2013)). A comparison of the work done and the energy extracted by the thermostat as a function of wave periods is shown in Figure 6.10. It can be seen that both curves show a similar trend of the energy slope indicating the amount of energy input to the system by each oscillation of the wave cycle is extracted by the thermostat. A linear fit of these curves reveals that both curves have

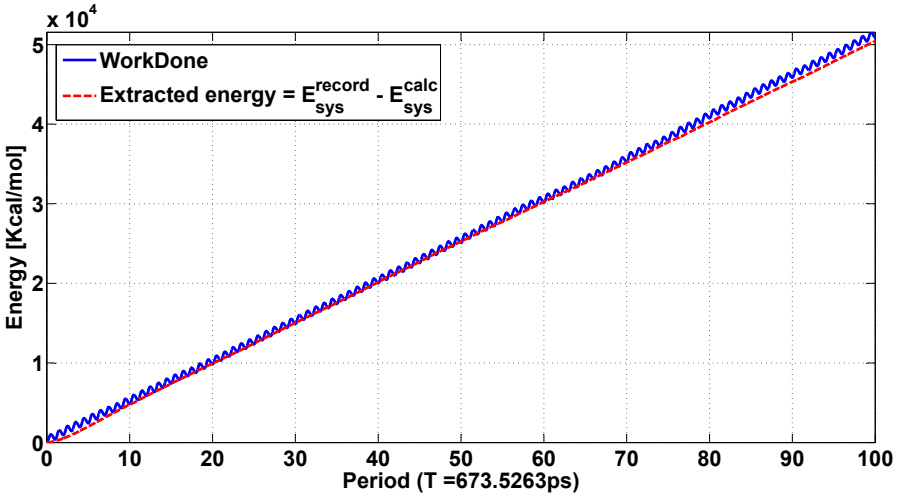

Figure 6.10: Estimates of work done on the gas by the piston and energy extracted by the thermostat as a function of time during acoustic wave propagation for a wave frequency $f \approx 1.5\,\text{GHz}$ (R=1).

the same slope and the amount of energy input to and extracted from the system per period is 511 kcal/mol.

6.5 Results and Discussion

6.5.1 Analysis of Sound Field in the Simulation Domain

As mentioned earlier, an acoustic system was modelled using a monatomic gas to perform MD simulations that account for the effects of classical absorption. In order to demonstrate that the molecular model can realistically simulate classical absorption mechanisms, an analysis of the sound wave propagation in the simulation domain is essential. In this way it can be confirmed that the simulation accurately represents a sound field with acoustic variables (such as velocity and pressure profile, sound intensity etc.) equivalent to a realistic acoustic system for particular boundary conditions. This section discusses the sound field characteristics of the simulated wave, including the attenuation of the wave due to classical losses occurring in the fluid medium. Some preliminary results were shown in Section 5.4.3 for validation *Case 3* that confirm that the simulation results do indeed match the analytical solutions predicted using the transfer matrix method. To analyse the sound field, most of the calculations herein were performed in the frequency domain instead of the time domain calculations presented in Section 5.4.

Simulations were carried out for three different frequencies to observe the changes in the sound field with the acoustic wave frequency. The three acoustic frequencies were $f \approx 1.5\,\text{GHz}$, 2 GHz and 2.5 GHz. The research of Jacobsen (1989), Jacobsen (1991), and Jacobsen (2011) in studying the acoustic field are followed herein to describe the sound field characteristics of the simulated wave. In addition, the calculations were performed with the assumption of a constant value of the sound speed in gaseous argon of 460 m/s. This value was calculated using non-linear curve fitting, as described in Section 5.4, of the waveforms to the estimated component of the velocity amplitudes $v(z)$ for a wave frequency $f \approx 2.5\,\text{GHz}$. The values of the sound speed computed using the non-linear fitting varied between 420 m/s and 515 m/s for the simulated frequencies.

The auto-spectral density of the acoustic pressure (G_{pp}) and particle velocity (G_{vv}) at each position of the domain along the wave path were evaluated to check the frequency of the acoustic wave propagating in the simulation domain. The auto-spectral densities displayed in Figure 6.11 for the simulation domain of $R = 1$ confirm that the simulated wave did indeed propagate with the drive frequency, which in this case was $f \approx 1.5\,\text{GHz}$.

Acoustic pressure and particle velocity

In order to check the effect of periodic boundary conditions (PBC) in the directions perpendicular to the direction of the wave propagation, the particle velocity profile of the wave was calculated as a function of distance in the y- and z-directions and are presented in Figure 6.12. It can be seen that the particle velocity near the periodic boundary is the same as that of the free flow in the middle of the domain, which indicates that there is no development of a velocity boundary layer confirming the semi-infinite nature of the flow field in the x- and y-directions.

The sound pressure and particle velocity of the standing wave at different positions along the simulation domain was estimated using the fast Fourier transform of the time domain data for these parameters. The time domain data was taken from the average of the number of atoms in each virtual bin in the computational domain at regular intervals along the propagation direction. Figures 6.13a and 6.13b display the half-wavelength standing wave pattern of the sound pressure and particle velocity for the molecular simulation of the sound wave frequency $f \approx 1.5\,\text{GHz}$ ($R = 1$). The zero velocity on the right side of the domain at z =150 nm and the particle velocity of 49.6 m/s on the left side, which is approximately equal to the piston velocity amplitude v_0 =49.69 m/s, indicate the position of the termination wall and the acoustic source of the domain, respectively. The wave pattern of the

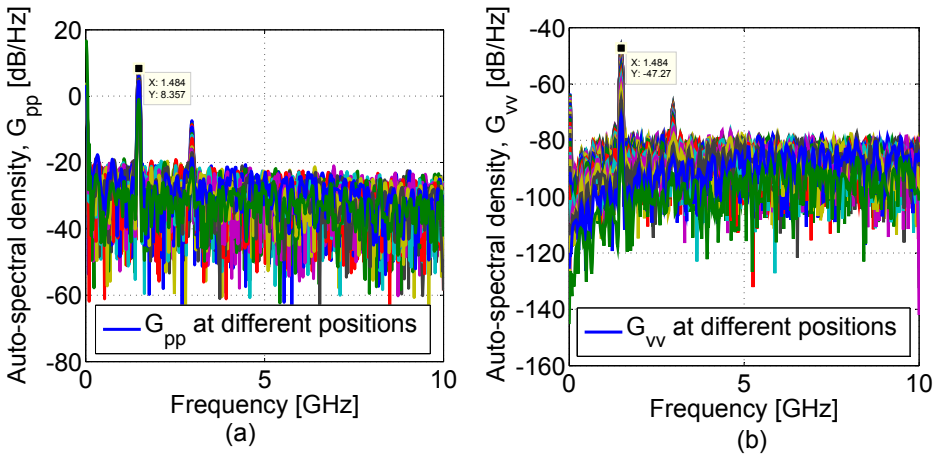

Figure 6.11: Auto-spectral density of (a) acoustic pressure and (b) particle velocity along the wave path in the simulation domain for wave frequency $f \approx 1.5\,\text{GHz}$. The peak at $f \approx 1.5\,\text{GHz}$ in both figures indicates that the acoustic pressure and particle velocity of the propagating acoustic wave at any given position in the domain maintain a wave frequency of $f \approx 1.5\,\text{GHz}$. Other smaller peaks represent the harmonics of the propagating wave. Each colour in these figures represents an estimated quantity for each microscopic bin along the z-direction.

particle velocity and acoustic pressure for the frequency $f \approx 1.5\,\text{GHz}$ confirm that the domain length was equivalent to half a wavelength of the acoustic wave propagating in the domain. A comparison between the sound pressure and the normalised particle velocity ($\rho c v$) presented in Figure 6.14 shows that the normalised particle velocity was larger than the sound pressure, which indicates that the sound field was dominated by a reactive field. This is expected considering that the length of the simulation domain was equal to half the wavelength of the acoustic wave, which is within the acoustic near field of a source. This behaviour can be explained rigorously using the description of sound intensity as detailed in the following paragraphs.

Active and reactive acoustic intensity

It is well known that the sound pressure and the particle velocity, at a given position in a sound field far from the source, are in phase in a plane propa-

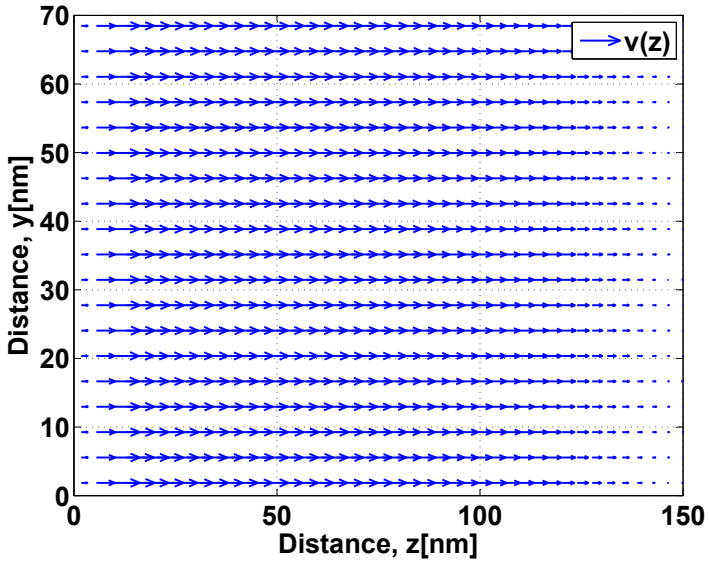

Figure 6.12: Particle velocity profile in yz-space of acoustic wave propagation along the z-direction at frequency $f \approx 1.5\,\mathrm{GHz}$ ($R = 1$). A "distance" of 35 nm corresponds to the centreline of the domain.

gating wave (Jacobsen 2011). Conversely, the sound pressure and the particle velocity near the source can be partly in phase and partly in quadrature (90 ° out of phase) (Jacobsen 1989). The in-phase sound components correspond to the active sound intensity and the out-of-phase components correspond to the reactive sound intensity (Jacobsen 1989). Hence, a sound field (near the acoustic source) in general can be characterised as active (i.e. progressive) and reactive (i.e. non-progressive) based on the phase relation between the sound pressure and the particle velocity of the propagating wave. The active and reactive sound intensity, respectively, express the flow of sound energy and the amount of energy which flows back and forth at a given position (Jacobsen 1989). In the near field of the sound source, the sound field is dominated by the reactive field, which represents a coherent but non-propagating, oscillatory sound energy flux (Jacobsen 1989; Jacobsen 2011). Since in this study the length of the simulation domain (in the case of $R = 1$) was approximately equal to half of a wavelength of the simulated acoustic wave, the developed acoustic field would be within the near field of the source. Hence, both the reactive and active acoustic sound field would be significant in the simulation domain. Figure 6.15 shows the estimated rate of active and reactive energy flowing per unit area of the simulation domain

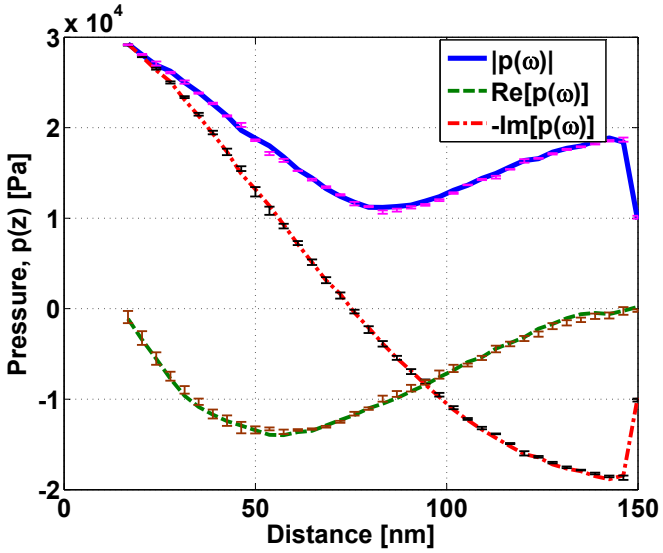

(a) Acoustic pressure

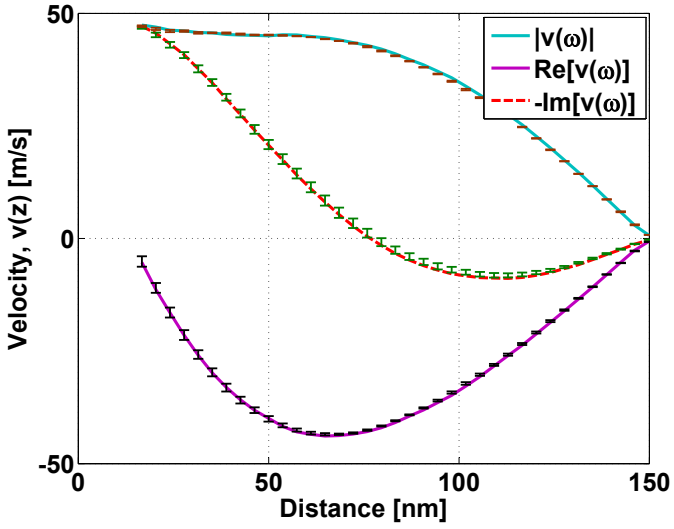

(b) Particle velocity

Figure 6.13: Real and imaginary components of (a) acoustic pressure and (b) particle velocity of acoustic wave propagation at frequency $f \approx 1.5\,\text{GHz}$ ($R = 1$). The values of particle velocity and acoustic pressure nearest to the sound source are displayed at a distance of 6 nm away from the maximum distance travelled by the piston. Error bars in the figure represent standard deviation in the estimated values of particle velocity and acoustic pressure. The standard errors were calculated using the block averaging method discussed in Section 6.4.3.

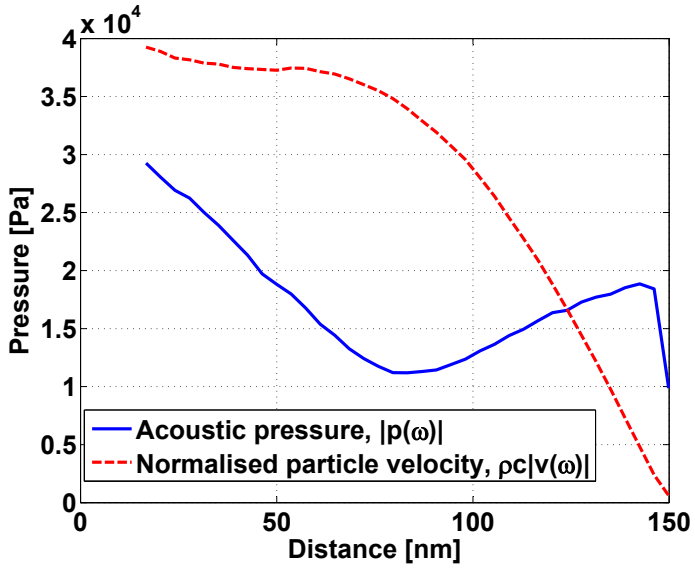

Figure 6.14: Acoustic pressure and normalised particle velocity (ρcv) of acoustic wave propagation at frequency $f \approx 1.5\,\text{GHz}$ ($R = 1$).

for an acoustic wave of frequency $f \approx 1.5\,\text{GHz}$ ($R = 1$). Here the intensity is measured in a direction normal (at 90 °) to the piston wall for a unit area of the simulation domain through which the sound energy is flowing. It can be seen that both the flowing active energy and oscillatory reactive energy are significant in the domain. However, the reactive field is stronger than the active field near the reflective wall due to the dissipative nature of the active energy (which will be discussed later in Section 6.6) as the wave is moving away from the source.

Figure 6.16 compares the oscillatory reactive energy for three different acoustic frequencies, $f \approx 1.5\,\text{GHz}$, 2 GHz and 2.5 GHz. It can be observed that the reactive energy increases as the frequency decreases within the same domain length, which is expected as the sound field becomes active at high frequencies and reactive at relatively low frequencies near the source (Jacobsen 1989). This can be attributed to the fact that the ratio of the distance between the source and receiver (i.e. the domain length L_z) and the wavelength of the acoustic wave (λ) increases from 0.5 to 1.5 with the change of frequency from 1.5 GHz to 2.5 GHz. This means, for a fixed domain length, that any given position in the domain represents a distance closer to the source as the frequency decreases. Hence the reactive sound field becomes stronger compared with the active field as the frequency decreases. In addition, a high value of the ratio of the active and reactive intensity as the

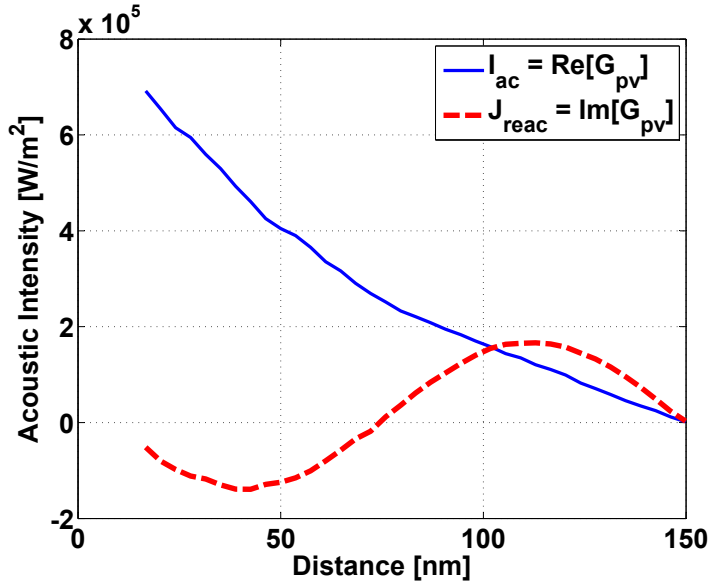

Figure 6.15: Illustration of active and reactive acoustic intensity, I_{ac} and I_{reac}, calculated using Equations (6.9) and (6.10) for $f \approx 1.5\,\text{GHz}$ ($R = 1$).

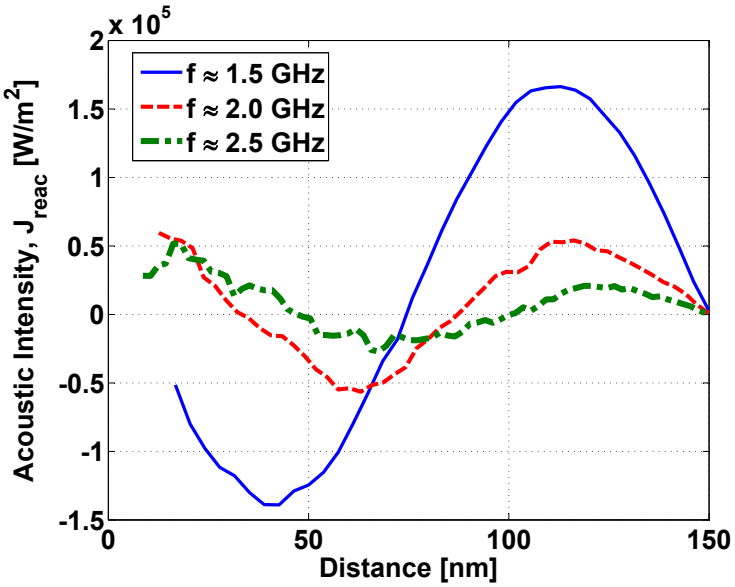

Figure 6.16: Comparison of reactive acoustic intensities for three different frequencies $f \approx 1.5\,,\,2$ and $2.5\,\text{GHz}$ ($R = 1, 0.75, 0.5$).

frequency decreases, which can be observed from both acoustic intensities for each frequency, confirms that the wave is in the near field of the acoustic source (the oscillating piston wall).

Kinetic and potential acoustic energy

The total acoustic energy within a sound field has two parts: kinetic and potential energy. Theoretically for a plane propagating wave both of these energy densities should be equal as shown in the mathematical relations (using the relation $p = \rho c v$) in Equations (6.17), (6.18) and (6.19). The estimated components of total acoustic energy density; the kinetic and potential energy density, W_{kin} and W_{pot}, are shown in Figure 6.17. It can be seen that there is a difference between the kinetic and potential energy densities, where the kinetic energy density exceeds the potential energy density with the exception of the rigid termination which has a zero velocity, which is a characteristic of the acoustic near field of a source as mentioned earlier. The inequality/difference between the kinetic and potential energies can be related to the acoustic intensities (active and reactive) of the simulated acoustic field using the relationship (Jacobsen 1989)

$$|I_{\text{ac}}|^2 + |I_{\text{reac}}|^2 \leq 4c^2 W_{\text{pot}} W_{\text{kin}} + c^2 (W_{\text{pot}} - W_{\text{kin}})^2. \tag{6.49}$$

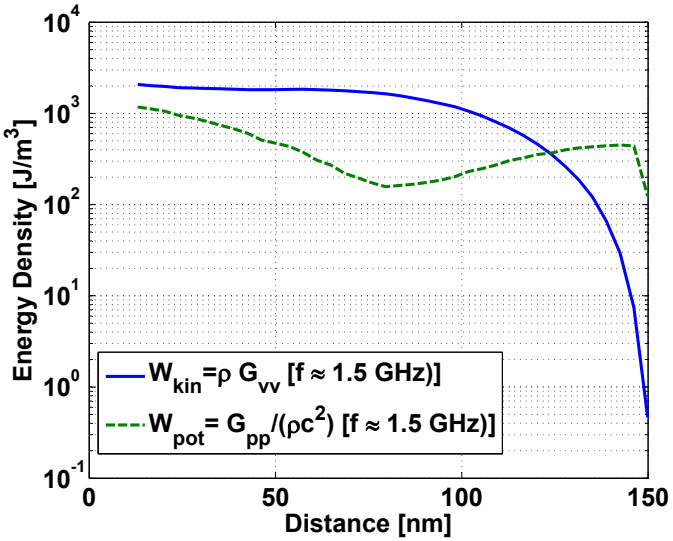

Figure 6.17: Kinetic and potential energy densities of the sound field propagating in the simulation domain with acoustic wave frequency $f \approx 1.5\,\text{GHz}$ ($R = 1$).

This relation is verified for the current simulation as the comparison between these two components shown in Figure 6.18.

Coherence

The coherence between the sound pressure and particle velocity is generally used in acoustics to check if both components are correlated and coherent in order to ensure that the measurements are valid. A similar approach is used in this study for the simulation results to quantify the correlation between the sound pressure, p, and the particle velocity, v, along the wave path in the simulation domain. The coherence between the sound pressure and the particle velocity, γ^2_{pv}, can be evaluated using the cross spectrum and the auto spectrum of both acoustic components as (Jacobsen 1989)

$$\gamma^2_{pv} = \frac{|G_{pv}|^2}{G_{pp}G_{vv}}, \tag{6.50}$$

where G_{pp} is the pressure autospectrum, G_{vv} is the velocity autospectrum and G_{pv} is the cross-spectrum between sound pressure and particle velocity. Figure 6.19 shows the estimated coherence between the sound pressure and the particle velocity of the propagating acoustic wave as a function of

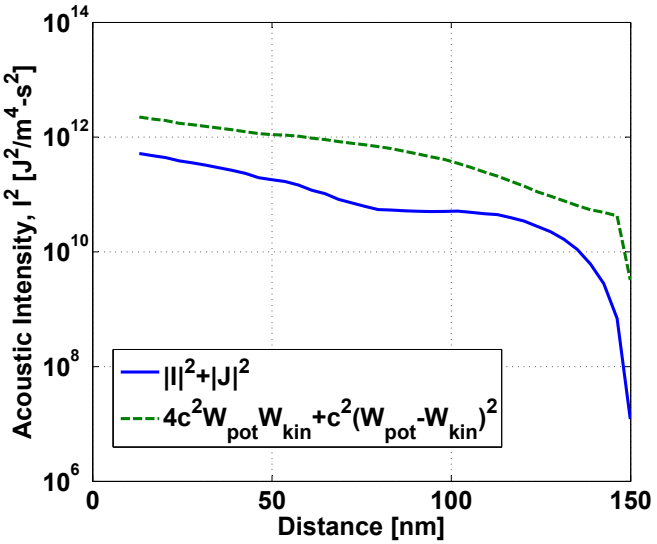

Figure 6.18: Relationship between acoustic intensities and total acoustic energy densities evaluated for $f \approx 1.5\,\text{GHz}$ ($R = 1$). Magnitude of complex acoustic intensity ($I_{\text{ac}} + iI_{\text{reac}}$) is compared with the kinetic and potential acoustic energy density.

propagation distance away from the source. It can be seen that the magnitude of the coherence is close to unity near the sound source and is high, varying in the range of $0.99 - 1$, for the majority of the wave path in the simulation domain. This indicates that both components are correlated along the wave path. The coherence value decreases near the termination wall due to the attenuation of the propagating wave as the wave moves away from the source and the fact there is no velocity at the boundary.

The coherence between the pressure signals measured at the sound source (p_0) and at any position (p_z) along the wave path away from source, $\gamma^2_{p_0 p_z}$, is also affected by the characteristics of the sound field (Jacobsen 1989). A comparison of the coherence value, $\gamma^2_{p_0 p_z}$, for three different frequencies is displayed in Figure 6.20a. It can be seen that the coherence remains near unity when close to the source for each frequency, but the value decreases from unity away from the source as the frequency increases. This is expected given that the attenuation increases with higher frequencies. The influence is more pronounced in the calculation of the transfer function, $H_{p_0 p_z}$, between the pressure measured at the sound source (p_0) and at any position (p_z). Figure 6.20b shows the estimated transfer functions $H_{p_0 p_z}$ for these frequencies as a function of distance along the wave path. It can be seen that the magnitude of the transfer function near the termination wall decreases as the wave fre-

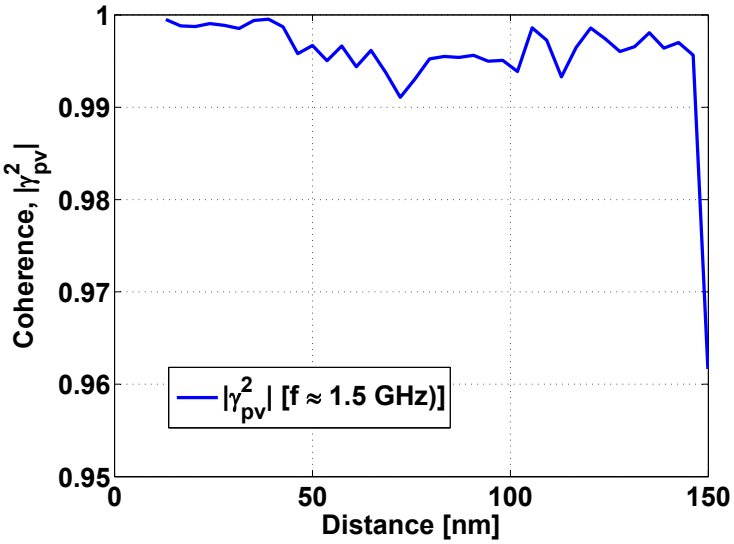

Figure 6.19: Coherence between the sound pressure and the particle velocity ($|\gamma^2_{pv}|$) of the acoustic wave as a function of propagation distance for a wave frequency of $f \approx 1.5\,\text{GHz}$ ($R = 1$).

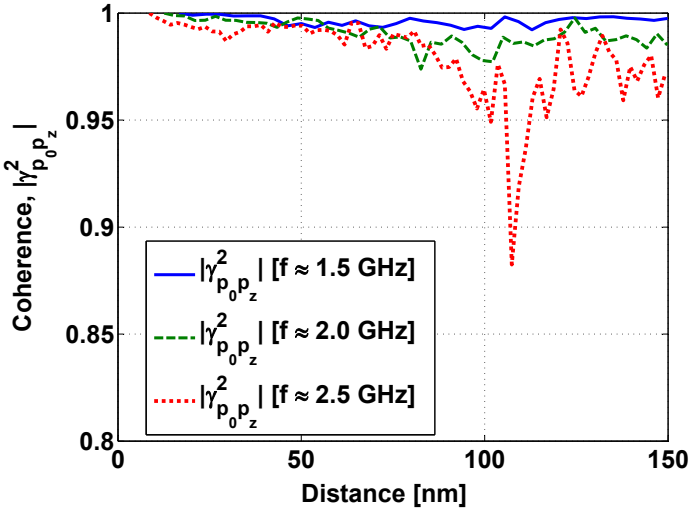

(a) Coherence, $\gamma^2_{p_0p_z}$

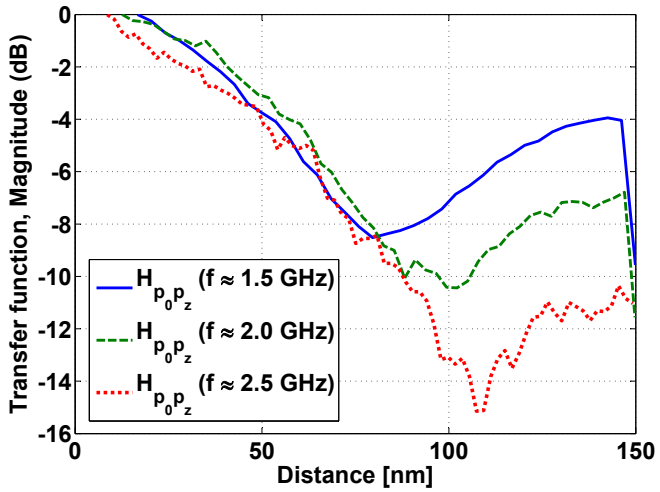

(b) Transfer function, $H_{p_0p_z}$

Figure 6.20: The coherence ($\gamma^2_{p_0p_z}$) and transfer function ($H_{p_0p_z}$) between the pressure signals measured at the sound source (p_0) and at any position (p_z) along the wave path away from source for simulated wave frequencies $f \approx$ 1.5 , 2 and 2.5 GHz ($R = 1, 0.75, 0.5$).

quencies change to higher values, with noisy behaviour (due to attenuation) of the signal for the relatively high frequency of 2.5 GHz. The high coherence value for each simulated wave frequency also confirms the accuracy of the spectral resolution used for the calculation of acoustic variables.

Acoustic impedance

The specific acoustic impedance Z_s of the propagating acoustic wave was also evaluated in the simulation domain along the wave path in order to observe the phase shift due to attenuation. A comparison of the estimated impedance of the sound wave normalised by the characteristic impedance of the medium (ρc) for three different frequencies is displayed in Figure 6.21. A shift in the phase and magnitude of the normalised acoustic impedance with frequency can be observed in Figure 6.21, indicating the change in attenuation with frequency.

Prediction of wave parameters: Plane wave theory

The non-linear fitting of the standing wave equations described in Section 5.4 can be used to predict the acoustic parameters such as the sound speed (c) and attenuation coefficient (m) from the wave pattern of the particle velocity. Figure 6.22 shows the waveforms fitted to the simulation data of the cosine and sine components of the velocity amplitude without any restriction to the zone over which the data is fit. The extracted parameters for the non-linear fitting without any restriction were $c = 435\,\mathrm{m/s}$ and $m = 0.914 \times 10^7\,\mathrm{m^{-1}}$. It can be seen that the fitting of the waveforms deteriorates near to the reflective wall. Consequently, if the fitting is restricted outside half a mean free path (λ_{mfp}) or one mean free path from the sound source, the waveforms give good fits of the velocity components. However, the waveforms give the best fit of the curve for the domain length $z > \lambda_{\mathrm{mfp}}$ by a constant sound speed $c = 447\,\mathrm{m/s}$ and attenuation coefficient $m = 0.967 \times 10^7\,\mathrm{m^{-1}}$. On the other hand, the fit deteriorates very quickly in the region $0 < z < \lambda_{\mathrm{mfp}}$. This indicates that free molecular flow near the source may be important at this frequency. It was anticipated that the simulated wave for $R = 1$ would be of sufficiently long wavelength, if not much greater than the mean free path of the gas molecules, to avoid free molecular flow in most of the simulation domain. However, the simulation results indicate this is not the case even though free molecular flow is dominant only within $z < 0.5\lambda_{\mathrm{mfp}}$ and is not as significant as it was for the relatively higher frequency at $R = 0.5$ (2.5 GHz). Further analysis on estimating the attenuation coefficient from acoustic energy losses predicted from the classical theory of continuum approximation is given in Section 6.6.

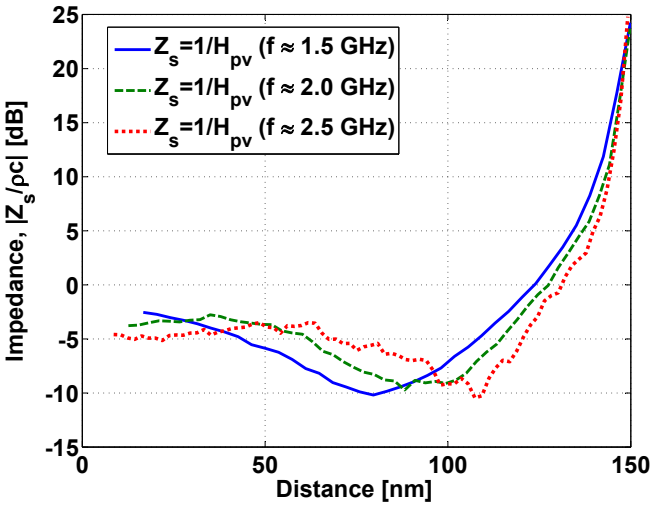

(a) Magnitude, $|\frac{Z_s}{\rho c}|$

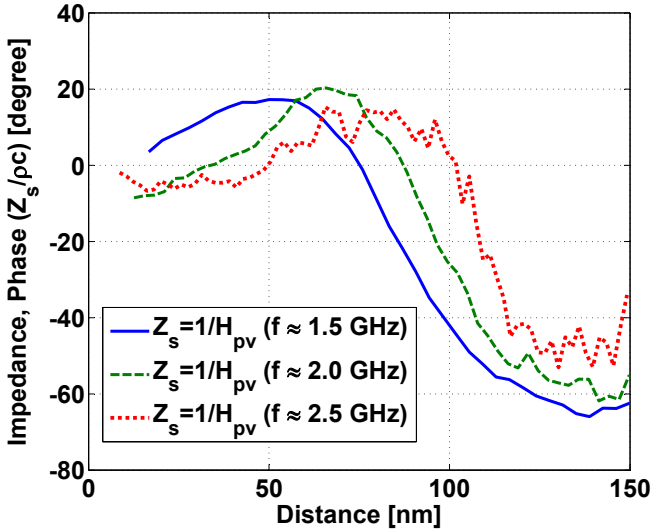

(b) Phase, $\Phi(\frac{Z_s}{\rho c})$

Figure 6.21: Normalised acoustic impedance $z_s = \frac{Z_s}{\rho c}$ of the acoustic wave propagating in the simulation domain as a function of distance for simulated wave frequencies $f \approx 1.5$, 2 and 2.5 GHz ($R = 1, 0.75, 0.5$).

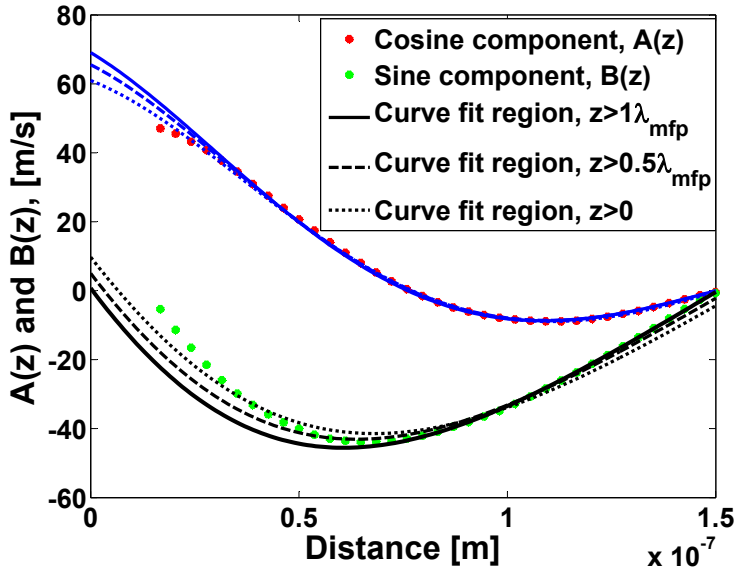

Figure 6.22: Non-linear curve fit to cosine and sine components, $A(z)$ and $B(z)$, of the velocity amplitude as a function of distance for acoustic wave frequency $f \approx 1.5\,\mathrm{GHz}$ ($R = 1$). The curve fitting was applied in the regions of the domain length $z > 0$, $z > 0.5\lambda_{\mathrm{mfp}}$ and $z > \lambda_{\mathrm{mfp}}$. The predicted values for each of these fits are: $c = 435\,\mathrm{m/s}$ and $m = 0.914 \times 10^7\,\mathrm{m}^{-1}$, $c = 442\,\mathrm{m/s}$ and $m = 0.957 \times 10^7\,\mathrm{m}^{-1}$, and $c = 447\,\mathrm{m/s}$ and $m = 0.967 \times 10^7\,\mathrm{m}^{-1}$, respectively.

Speed of sound and acoustic process

It was argued by Kinsler et al. (2000) (see Chapter 8, p214) that acoustic losses can be introduced into the acoustic wave by generating a phase angle between the pressure and density, as it modifies the adiabat relating acoustic pressure and condensation. The same can be thought of the acoustic processes occurring in the current molecular simulation and the behaviour can be verified by the transfer function between the acoustic pressure and density. Figure 6.23 shows the magnitude and phase of the transfer function $H_{\rho p}$ estimated between the acoustic pressure and density along the wave path. It can be seen that the phase between the acoustic pressure and density varies with the distance along the wave path, which indicates that acoustic losses are indeed induced by the introduction of a phase angle between the pressure and density. The larger phase angle as the wave moves away from the source suggests the characteristics of an attenuated wave away from the source. This behaviour can also be used to verify the adiabatic process occurring in the fluid medium during the wave propagation. The adiabatic relation between

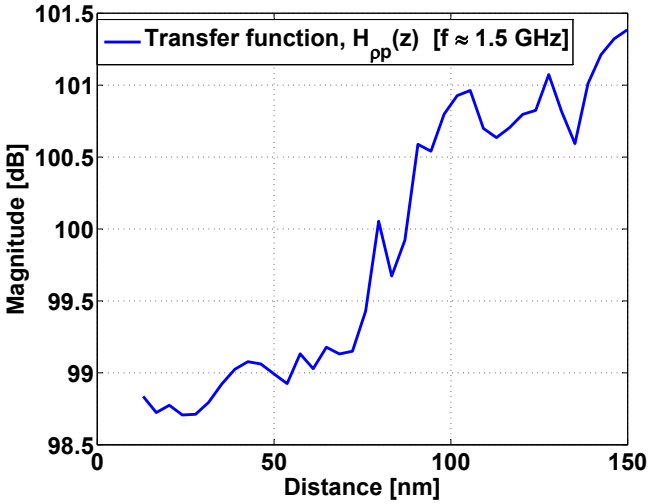

(a) Magnitude, $|H_{\rho p}|$

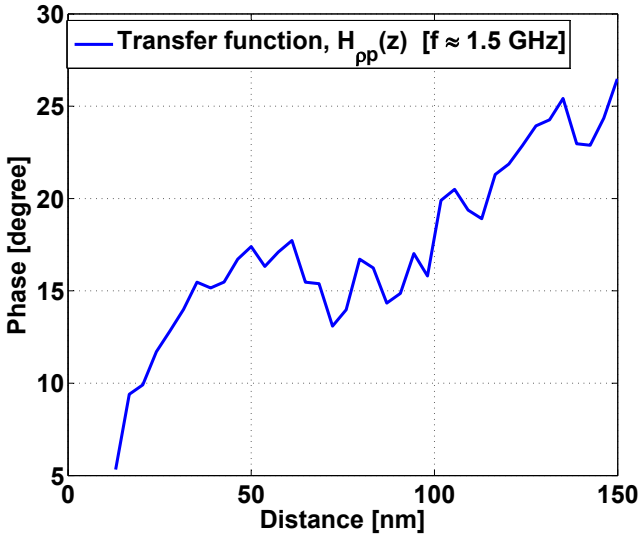

(b) Phase, $\Phi(H_{\rho p})$

Figure 6.23: The (a) magnitude and (b) phase of the transfer function ($H_{\rho p}$) between acoustic pressure and density as a function of distance for acoustic wave frequency $f \approx 1.5\,\text{GHz}$ ($R = 1$).

the pressure and density in a gas can be expressed in terms of the sound speed as (see Kinsler et al. 2000, Chapter 5, p120-121)

$$c^2 = \gamma \frac{p}{\rho}, \tag{6.51}$$

where c is the sound speed, γ is the specific heat ratio of the gas, p and ρ are the acoustic pressure and density. An estimation of the speed of sound was performed using the relation in Equation (6.51) with the assumption of $\gamma = \frac{5}{3}$ for the monatomic gas argon for the acoustic system simulated in this study. The value of sound speed as a function distance is displayed in Figure 6.24. The sound speed was found to be similar to the value predicted using the plane wave theory mentioned earlier. This implies that the acoustic processes in the monatomic fluid are indeed adiabatic.

It should also be noted from Figure 6.24 that the sound speed is not constant along the wave propagation direction and changes with distance, which indicates possible non-equilibrium effects. The simulation results presented in this thesis were not intended to discuss non-equilibrium effects at this stage of investigation but rather to demonstrate the acoustic behaviour in a MD simulation domain and to analyse and discuss the typical behaviour theoretically using continuum equations. The investigation of non-equilibrium

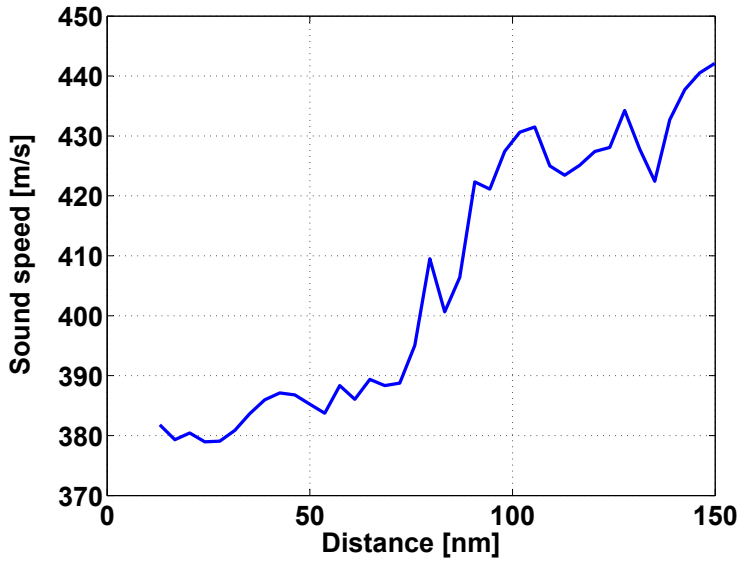

Figure 6.24: Speed of sound as a function of distance calculated from the simulation results for acoustic wave frequency $f \approx 1.5\,\mathrm{GHz}$ ($R = 1$).

effects is indeed an important part of this research area and of interest for future work.

Localised sound absorption coefficient
In the discussion of this study, the absorption coefficient is presented as a separate term from the attenuation coefficient. Here, the absorption coefficient is described as a ratio of the sound intensity attenuated and the intensity of the sound incident upon the termination wall. The intensity of the attenuated sound can be expressed as a difference between the incident and the reflected sound at a given position at any surface. The localised absorption coefficient as a function of distance along the wave path can be calculated using Equation (6.16). Figure 6.25 shows the calculated sound absorption coefficients for three different frequencies. It can be observed that the absorption coefficient decreases as the sound moves further away from the sound source and moves towards the termination wall. This is expected given that the absorption coefficient is defined as a ratio of the active and incident intensity at a position, and both of these quantities are reduced as the sound moves further away from the source due to the attenuation of the sound. On the other hand, the incident intensity near to the source is large and the reflection from the termination wall near to the source is very small. Hence the absorption coefficient is higher near to the source. A lossless medium without any attenuation along the wave path would have a fixed value of the absorption coefficient (a flat/horizontal curve) at any position in the domain. The trend in the curve in Figure 6.25 indicates the sound is absorbed as it moves away from the source, implying that the sound is only attenuated due to the classical loss mechanisms acting along the wave path. It can also be observed that the acoustic absorption coefficient in the domain increases as the frequency increases from 1.5 GHz to 2.5 GHz and the curves become very noisy with increasing frequency.

6.6 Attenuation of Sound in the Fluid Medium

Attenuation of sound occurs in a monatomic gas due to viscous and thermal losses (also known as classical losses) of acoustic energy. Viscous losses occur due to the differences in relative motions between adjacent portions of the medium such as during the compressions and expansions of the medium that accompany the transmission of an acoustic wave (see Kinsler et al. 2000, Chapter 8, p210). Thermal losses result from the heat conduction between adjacent portions of the medium generated from higher temperature condensations and lower temperature rarefactions (Kinsler et al. 2000). A

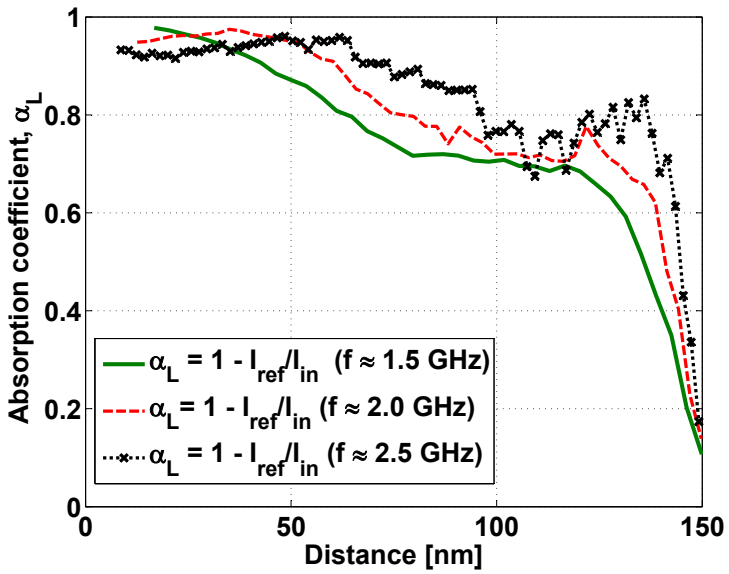

Figure 6.25: Comparison of the localised acoustic absorption coefficient (α_L) as a function of distance along the wave path for acoustic wave frequencies $f \approx 1.5\,,\,2$ and $2.5\,\text{GHz}$ ($R = 1, 0.75, 0.5$).

detailed description of loss mechanisms can be found in Section 2.3. In many situations, especially at low frequency, acoustic dissipation is insignificant and can be ignored for the distances and times of interest (Kinsler et al. 2000; Morse and Ingard 1968). However, in high frequency sound wave propagation (as in this study), the losses are significant, when within distances equivalent to a wavelength. Hence, estimation of losses in a medium for high frequency sound waves is very important to distinguish between the losses occurring in the fluid and the losses occurring due to the interaction between the fluid and any other components (in this case the CNT).

The method used to calculate acoustic losses and sound attenuation coefficients from a conservative MD simulation of acoustic wave propagation is described in Section 6.3.2. The calculations were performed using the concepts of total power and exergy demonstrated by Swift (2002). The results are also compared with the continuum approach of predicting the attenuation coefficient and nonlinear fitting of the waveforms using plane standing wave theory described in Sections 6.3.3 and 5.4, respectively.

Acoustic energy losses in the simulation domain based on exergy concepts can be evaluated using Equation (6.32). Thereafter the attenuation can be estimated using Equation (6.33). In the current simulation domain (without

the CNT), there is no solid included to induce any kind of heat conduction in the system. Hence $A_{\text{solid}}\kappa_{\text{solid}}\frac{dT}{dz} \approx 0$ in Equation (6.20). A thermostat was used to remove the additional energy pumped into the system by the piston for the repeated cycles of the wave. The thermostat was merely extracting the excess energy from the system at each cycle of the wave and is not contributing to the power balance of a thermoacoustic system for each period of the wave propagation. Therefore, the thermostat was not considered as similar to a heat exchanger requiring inclusion as heat conduction for the system. Thus the contribution from the thermostat was not included in the heat conduction term on the right side of Equation (6.20). Similarly, the acoustic losses and attenuation coefficient from the simulation results based on continuum mechanics can be evaluated using Equations (6.39) and (6.40). The values of the attenuation coefficient using theoretical approximations of classical losses based on continuum mechanics and the linearised wave equation can be calculated from Equations (6.43) and (6.44). The non-linear fits of the acoustic waveforms to the simulated particle velocity amplitude shown in Figure 6.22 can be used to predict the attenuation coefficient using plane wave theory.

A comparison of the attenuation coefficients estimated from the MD simulation results (using exergy concepts and continuum mechanics) and theoretical predictions (from continuum approximations and complex wavenumber) is presented in Table 6.1. The attenuation coefficients were calculated for three different frequencies at acoustic Reynolds numbers R=1, 0.75, and 0.5. It can be observed that the attenuation coefficient estimated from the MD simulation results using exergy concepts (m_{e}) matches well with the theoretical predictions ($m^{\text{t}}_{\text{c}_{\text{L}}}$) from the complex wavenumber without low-frequency approximations for each of the three simulated frequencies. The attenuation coefficient (m^{s}_{c}) for the MD simulation results were also evaluated using the equations of continuum mechanics for viscous and thermal losses and compared with the theoretical predictions (m^{t}_{c}) of the continuum approximations of the equations of classical absorption. Again, the estimates of the attenuation coefficient give consistent agreement between the simulation results and theoretical predictions. However, the theoretical predictions of attenuation coefficient using the continuum approximations of classical absorption (m^{t}_{c}) and the estimates of attenuation coefficient using exergy concepts (m_{e}) do not agree well. The approximation (m^{t}_{c}) of continuum theory gives an overestimation of the attenuation coefficients for both simulation results (m_{e}) and the predictions ($m^{\text{t}}_{\text{c}_{\text{L}}}$) from the complex number without low-frequency approximations. The discrepancies between these quantities can be explained by the range of validity of the continuum theory for predictions of the attenuation

Table 6.1: Comparison of theoretical predictions and simulation results of classical attenuation constant for three different frequencies simulated in this study. The attenuation coefficient values were also compared with different calculation methods of acoustic losses. Here superscripts 's', 't 'and subscripts 'e ', 'f ', 'c 'and 'c_L 'are used to indicate simulation results, theoretical value, exergy concepts, nonlinear fitting using standing wave theory, continuum mechanics, and continuum mechanics without low frequency approximation, respectively. The value of m_e was calculated from exergy concepts using Equation (6.33), the value of m_c^s was estimated from simulation results based on continuum theory of classical absorptions using Equation (6.40), the theoretical value of m_c^t based on continuum approximations was predicted using Equation (6.43) and the value of the attenuation coefficient without low frequency approximations $m_{c_L}^t$ was predicted from the complex wavenumber using Equation (6.44). Here, a constant value of the sound speed c =460 m/s was used for these estimates of the attenuation coefficient for all three frequencies. The mean temperatures of the gas during the steady state condition of the acoustic wave propagation were 284 K, 280 K and 279 K for wave frequencies of $f \approx 1.5$ GHz, 2.0 GHz, and 2.5 GHz, respectively. These temperatures are used as T_{eq} in Equation (6.38).

Approach	**Acoustic Reynolds Number**		
	$R = 1$ [$f \approx 1.5$ GHz]	$R = 0.75$ [$f \approx 2.0$ GHz]	$R = 0.5$ [$f \approx 2.5$ GHz]
MD results:			
$m_e \times 10^7$ (m^{-1})	0.98	1.14	2.58
$m_f^s \times 10^7$ (m^{-1}) ($z > 0.5\lambda_{mfp}$)	0.96	1.05	1.40
$m_f^s \times 10^7$ (m^{-1}) ($z > \lambda_{mfp}$)	0.97	1.10	1.51
$m_c^s \times 10^7$ (m^{-1})	1.94	1.78	2.64
$\frac{m_e}{f^2} \times 10^{-12}$ (Np $s^2 m^{-12}$)	4.49	2.90	3.91
$\frac{m_c^s}{f^2} \times 10^{-12}$ (Np $s^2 m^{-12}$)	8.80	4.52	3.99
Theoretical predictions:			
$m_c^t \times 10^7$ (m^{-1})	1.25	2.23	3.76
$m_{c_L}^t \times 10^7$ (m^{-1})	0.69	0.96	1.23
$\frac{m_c^t}{f^2} \times 10^{-12}$ (Np $s^2 m^{-1}$)	5.69	5.69	5.69
$\frac{m_{c_L}^t}{f^2} \times 10^{-12}$ (Np $s^2 m^{-1}$)	3.14	2.44	1.86

coefficient. The validity of the continuum theory is defined by the relaxation time for viscous and thermal absorptions. The relaxation time for viscous and thermal conduction in fluid is given by (see Kinsler et al. 2000, Chapter 8, p210-216)

$$\tau_S = \frac{4}{3}\frac{\mu}{\rho c^2}, \tag{6.52}$$

and

$$\tau_\kappa = \frac{1}{\rho c^2}\frac{\kappa}{c_p}, \tag{6.53}$$

respectively. To comply with the assumptions in the continuum theory for the fluid continuum, the wave frequencies, f, should be much smaller than the relaxation frequencies f_S and f_κ, respectively, for viscous and thermal absorptions (see Kinsler et al. 2000, Chapter 8, p210-216). This validity condition can be approximated by a dimensionless coefficient $\omega\tau_{S/\kappa}$ and a value much smaller than unity would confirm the validity of the continuum theory (see Kinsler et al. 2000, Chapter 8, p210-216). The dimensionless coefficient calculated for each frequency is listed in Table 6.2. It can be seen that $\omega\tau_{S/\kappa} \approx 1$ for each of the simulated frequencies, which indicates that the wave frequencies are approaching the relaxation frequency. This violates the validity of the continuum theory. Furthermore, Greenspan (1956)'s experimental data for sound wave propagation in monatomic gas show that the continuum theory is valid only if $\frac{\rho c^2}{\omega\mu\gamma}$ is greater than 10 (Pierce 1989). This validity condition was also verified for each of the simulated frequencies and a list of the values of parameter $\frac{\rho c^2}{\omega\mu\gamma}$ is given in Table 6.2. It can again be seen that the value is much smaller than 10, which confirms the violation of the applicability of the continuum theory for the attenuation coefficient using approximations of classical absorption. Hence, it can be concluded that the discrepancies in the attenuation coefficients are expected.

It can also be noticed that the attenuation coefficient increases as the Reynolds number decreases. This indicates that classical losses (attenuation) increase with the wave frequency. The changes in the attenuation coefficient with frequency also verifies that the MD method can simulate classical absorption due to viscous and thermal losses in a fluid medium and can also simulate the change in the effects of classical absorption due to a change in frequency.

Furthermore, in experimental investigations, it has been shown by previous researchers that the attenuation coefficient varies with the wave frequency, and the attenuation coefficient and the square of the frequency are essentially proportional (Kinsler et al. 2000). Therefore, attenuation data are usually presented as a function of $\frac{m}{f^2}$ in experimental measurements of attenuation

and plotted against the wave frequency f to demonstrate any departure from a horizontal line, which indicates deviations from the predictions of continuum (or classical) theory (Kinsler et al. 2000). A list of the calculated values of $\frac{m}{f^2}$ from the MD simulation results is included in Table 6.1. It can be observed that the value of the attenuation coefficients in the from of $\frac{m}{f^2}$ gives a constant value of 5.69×10^{-12} Np s^{2}m^{-1} for the theoretical prediction using continuum approximations, whereas the value of $\frac{m}{f^2}$ decreases with increasing acoustic frequency when the calculations were performed without the approximation for low frequency. The simulation results for this value of $\frac{m}{f^2}$ estimated using both exergy concepts and continuum equations similarly indicate a departure from the horizontal line with frequency (if $\frac{m}{f^2}$ is plotted as a function of f), implying deviation from the continuum theory. Thus, the simulation results confirm the deviation from the continuum theory for the attenuation coefficients at the high frequencies simulated in this study.

Based on the above analysis of the sound field and sound attenuation in an acoustic simulation domain without a CNT present, it can be concluded that the modelled molecular system is able to simulate the sound field and absorption effects due to classical losses in the fluid medium. The acoustic parameters in the simulation domain gave reasonably consistent results across the three acoustic frequencies simulated in this study. The attenuation due to classical absorption was estimated from the simulation results using exergy concepts. The careful analysis of the energy balance in the MD simulations gives confidence that the acoustic absorption is calculated correctly. Additionally, the calculated values of attenuation coefficients provide good approximation to the theoretical values estimated from the complex wavenumber of the linearised wave equation without low-frequency approximations, which indicates the reliability of the simulation results. These results confirm that the MD method can be used effectively to simulate the effects of

Table 6.2: Comparison of relaxation frequency for viscous (f_S) and thermal (f_κ) absorptions with wave frequencies (f). The dimensionless coefficients $\omega\tau_S$ and $\omega\tau_\kappa$ are also evaluated for each of the wave frequencies along with Greenspan (1956)'s validity parameter $\frac{\rho c^2}{\omega\mu\gamma}$.

Reynolds number	f_S (GHz)	f_κ (GHz)	$\omega\tau_S$	$\omega\tau_\kappa$	$\frac{\rho c^2}{\omega\mu\gamma}$
R=1 [$f \approx 1.5$ GHz]	13.02	11.96	0.72	0.78	1.12
R=0.75 [$f \approx 2.0$ GHz]	-	-	0.96	1.04	0.84
R=0.5 [$f \approx 2.5$ GHz]	-	-	1.24	1.35	0.64

classical absorption in a fluid and the attenuation behaviour can be predicted using the method described in this section. In the following chapter, the modelled system was then extended for the simulation of acoustic wave propagation in the same acoustic medium with a CNT present.

6.7 Summary

In summary, this chapter presented the study of high-frequency acoustic wave propagation using molecular dynamics simulation. A methodology was demonstrated for analysis of the sound field in a molecular dynamics (MD) simulation system of high-frequency wave propagation in a simple gas, in which the stochastic nature of atoms has a very significant effect on the evaluated acoustic (macroscopic) parameters. The characteristics of the sound field of the high-frequency wave propagation in a domain, in which the distance between the sound source and receiver is very small and the total length is smaller than that of a wavelength, were also discussed. In addition, the classical losses occurring in the acoustic medium (gaseous argon) were quantified and presented in terms of attenuation coefficients. Estimation of the attenuation coefficient from the MD simulation was performed based on thermodynamic exergy concepts. The attenuation coefficient results were verified against predictions using standing wave theory and theoretical approximations based on continuum mechanics. It was found that the simulation results provide consistent estimates of the attenuation coefficient across the three different frequencies studied in this thesis and give a good approximation to the theoretical predictions. Calculations of the attenuation coefficients as a function of the squared frequency indicate that the estimates deviate from the predictions of continuum theory for the high-frequency waves simulated in this study. Overall, based on the comparison of the theoretical calculations and MD simulation results, it can be concluded that MD simulations can be used effectively to model acoustic absorption effects in a simple fluid. This means that the MD simulation method can be applied confidently to understanding the sound field inside a standing wave tube with nanomaterials present and to study the absorption effects of the nanomaterials. Thereafter the study was extended in the following chapter to investigate acoustic (high frequency) wave propagation in the presence of a CNT using MD simulation.

7 MD Simulation of Acoustic Absorption in a CNT

7.1 Introduction

Acoustic wave propagation in a monatomic gas in the presence of a CNT is discussed in this chapter. This is the second part of the study of the MD simulation of sound wave propagation introduced in Chapter 6, which now includes a CNT in the simulation domain. Simulations were performed with the aim to investigate the acoustic losses due to the CNT and to capture the atomistic mechanisms involved. The preliminary objectives were to model the acoustic absorption effects due to the interaction between the gas and the CNT using MD simulations, and to quantify the acoustic energy losses that occur due to the CNT. Ensuring that damping mechanisms induced by the CNT are functional in a simulation model of molecular dynamics will lead to further understanding the loss mechanisms involved. In addition, the losses need to be distinguished from the classical losses in the fluid medium. The study presented in this part is mainly focused on modelling a molecular simulation domain to develop a protocol for measuring acoustic absorption by a CNT so that, in future, the analysis of the sound field can be extended further to investigate the loss mechanisms involved with one or more CNTs. Consequently, a major portion of this chapter is devoted to quantifying the acoustic energy losses in a conservative MD simulation domain with a CNT present.

With these aforementioned aims, a molecular simulation domain was modelled for acoustic wave propagation in a monatomic gas (argon) with a single CNT placed at the termination wall at the opposite end of the domain to the sound source. A schematic of the simulation geometry and a snapshot of the simulation domain are shown in Figure 7.1. The size (diameter and length) of the CNT was very small in order to reduce the computational expense and to simplify the atomistic mechanisms by ensuring that no gas

atoms could enter the interior of the CNT so that the interaction with gas atoms occurred only with the outside surface of the CNT.

This chapter is organised as follows. The simulation details and the equilibration of the system are described in Section 7.2. Section 7.3 presents the relevant theories and calculation methods that were used to estimate the acoustic losses and attenuation coefficient from the simulation domain in the presence of the CNT. Thereafter the simulation results in terms of the changes in the acoustic behaviour and acoustic losses compared with that of an acoustic system without the CNT (*Part 1* in Chapter 6) are discussed in Section 7.5. The effects on the CNT due to interaction with the acoustic wave are explained in Section 7.6. Finally conclusions regarding the modelling of the acoustic absorption effects by the CNT and the behaviour of the CNT are made based on the observations and analysis of the simulation results.

7.2 Simulation Details

An open-end (uncapped) (5,5) SWCNT of length L_{CNT} = 50 nm and diameter d_{CNT} = 0.69 nm was cantilevered and immersed in a simulation domain of gaseous argon with a density of 1.8 kg m^{-3}. One end of the CNT, i.e. atoms within 0.1 nm of the clamped boundary, was fixed and the remainder of the CNT atoms were allowed to move freely according to the interaction forces on them following Newtonian mechanics. The simulation domain had the same dimensions to those of the study in *Part 1*, i.e., $L_x = L_y = 70$ nm in the transverse direction and L_z = 150 nm in the flow direction, as illustrated in Figure 7.1. The domain size was large enough to exclude inter-nanotube coupling interactions between periodic images. The simulations were conducted here with periodic boundary conditions on the side boundaries of the domain, representing an array of nanotubes with an area density of 0.0002 nm^{-2} and with an intertube spacing of 70 nm, which is similar to an experimental sample of CNT array shown in Chapter 3. A second generation REBO (Reactive Empirical Bond Order) (Brenner et al. 2002) potential was used to express the inter-atomic interactions between carbon atoms (carbon-carbon) in the CNT. The interactions between argon and carbon atoms (argon-carbon) were represented by a Lennard-Jones potential with parameters $\varepsilon_{\text{Ar-C}}$ (= 4.98 meV) and $\sigma_{\text{Ar-C}}$ (= 3.38 Å) (Carlborg et al. 2008). Details of the interaction parameters can be found in Chapter 4. Similar to the validation *Case 3* in Chapter 4 and the study in *Part 1* of the previous chapter, the oscillating wall and wave propagating media were modelled using solid and gaseous argon, respectively. The total number of molecules in the simulation domain $N_{\text{system}} = 60,127$ with $N_{\text{wall}} = 35,645$, $N_{\text{argon gas}} = 20,402$, $N_{\text{CNT}}^{\text{free}} = 3,990$, and

$N_{\text{CNT}}^{\text{fixed end}} = 90$, was constant during the simulations owing to the periodic boundary condition.

Simulations were initiated with a small timestep of 0.01 fs using a velocity-Verlet algorithm in order to relax the system and the timestep was gradually increased to 0.4 fs to speed up the process. Thereafter, simulations were continued with a time step of 0.5 fs. At the beginning of the relaxation of the system, the gas molecules and the CNT were at temperatures of 273 K and 0 K, respectively. The initial velocities of the gas molecules were chosen randomly from a Gaussian distribution. The initial temperature of the CNT was chosen to be 0 K as the solid atoms cannot be given a random velocity for a particular temperature similar to the gas atoms. Both the gas molecules and the CNT were equilibrated at 273 K and at a gas pressure of 1 atm. The temperature was maintained using two separate Langevin thermostats for both the argon gas and the CNT during the equilibration process. After the equilibration, the system was excited by an acoustic wave generated by a piston which was oscillated with a velocity amplitude of $v_0 = 0.15c = 49.69\,\text{m/s}$ and with a frequency of 1.5 GHz ($R = 1$). The simulation conditions during the acoustic wave propagation were then maintained by a Nosé-Hoover thermostat which was loosely coupled with the gas in the directions (x and y) perpendicular to the propagating wave. The CNT was not directly

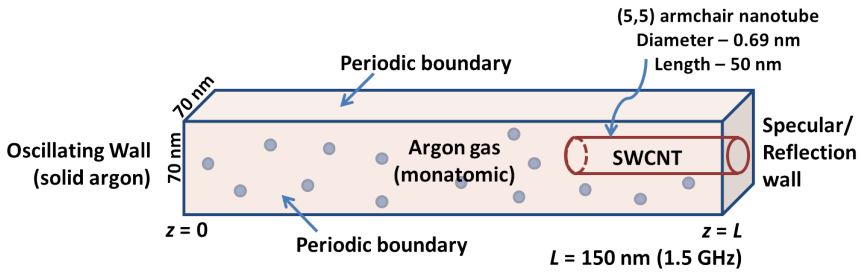

(a) Schematic of simulation geometry

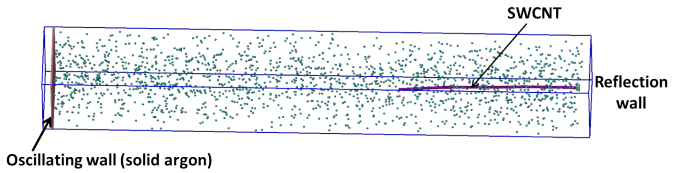

(b) Snapshot of the MD simulation domain

Figure 7.1: Simulation domain and sound source model for acoustic wave propagation in argon gas with the immersed CNT.

thermostatted during the acoustic wave propagation. As the flow reached the steady state, sampling was done for a total duration of 40 repeated wave cycle time periods. During the simulation, the temperature, pressure, velocity, density, kinetic and potential energies of the gas and the CNT were monitored and the data were collected at a rate of sampling time of 1 ps.

7.3 Attenuation due to the Presence of a CNT: Calculation Methods

7.3.1 Standing Wave Theory

Curve fitting of the waveform components over the entire domain (as discussed in 5.4) is no longer appropriate because there are two coupled domains: one between the source and the tip of the CNT which contains only argon atoms; and another for the remainder of the domain which contains both argon and the CNT. Hence standing wave equations based on classical acoustic wave theory, similar to Equations (5.10) - (5.12), were formulated by considering two separate domains between the source and receiver as illustrated in Figure 7.2.

Assume that a rectangular simulation domain of cross-sectional area S=($L_x \times L_y$) and length L_z, which is divided into two separate regions of length L_1 (Region 1) and L_2 (Region 2), is driven by a piston at $z = -L_2$. The

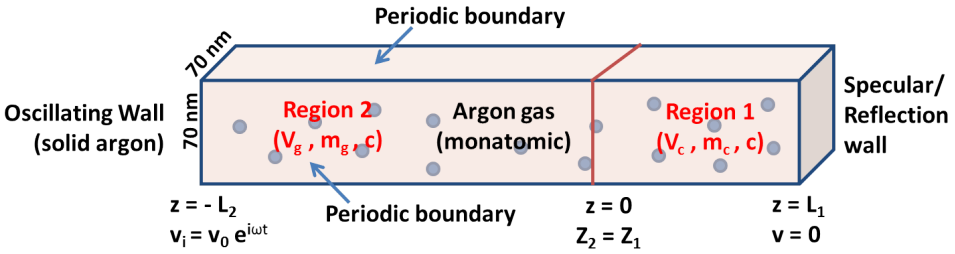

Figure 7.2: Schematic of the simulation domain showing two separate regions: one between the source and tip of the CNT which contains only argon atoms, namely gas region (Region 2); and another for the remainder of the domain which contains both argon and the CNT, namely CNT region (Region 1). Variables for particle velocity and attenuation constant in each region are represented by (v_g, m_g) for the gas region and by (v_c, m_c) for the CNT region. Sound speeds (c) are assumed to be constant in each region as required for the formulation of theoretical standing wave equations based on classical acoustic theory.

domain is terminated by a reflecting wall at $z = L_1$ and the two regions are separated at $z = 0$ as shown in Figure 7.2. If the piston oscillates harmonically at a frequency ω, then superposition of the incident and reflected waves on each side leads to a standing wave of the form

$$v_c(z,t) = A_1 \exp[i(\omega t - kz) - m_c z] - B_1 \exp[i(\omega t + kz) + m_c z], \quad (7.1)$$

and

$$v_g(z,t) = A_2 \exp[i(\omega t - kz) - m_g z] - B_2 \exp[i(\omega t + kz) + m_g z], \quad (7.2)$$

on the right and left sides of the domain, respectively. Subscripts c and g in Equations (7.1) and (7.2) denote the CNT and gaseous region representing the right (Region 1) and left (Region 2) sides, respectively, of the simulation domain separated at $z = 0$. *Region 2* is the domain between the source and tip of the CNT which contains only argon atoms, namely the gas region; and *Region 1* is for the remainder of the domain which contains both argon and a CNT, namely the CNT region. The terms A_1, A_2 and B_1, B_2 are the incident and reflected velocity amplitudes, respectively, of the generated standing waves in *Region 1* and *Region 2* of the simulation domain. Both A and B can be determined by the boundary conditions at $z = -L_2$, $z = L_1$ and $z = 0$. At $z = -L_2$, the incident wave would be equal to the velocity variation of the piston or oscillating wall, which can be realised as

$$A_2 \exp[i(\omega t + kL_2) + m_g L_2] = v_0 \exp[i\omega t]. \quad (7.3)$$

Similarly at the termination wall at $z = L_1$, $v_c = 0$, which can be expressed as

$$A_1 \exp[-ikL_1 - m_c L_1] = B_1 \exp[ikL_1 + m_c L_1]. \quad (7.4)$$

At the boundary between the regions, acoustic impedance (as a ratio of pressure and particle velocity) for both regions near to $z = 0$ would be equal, which can be expressed as

$$\frac{A_1 - B_1}{A_1 + B_1} = \frac{A_2 - B_2}{A_2 + B_2}. \quad (7.5)$$

These known boundary conditions can be used to derive a generalised standing wave equation of the developed wave forms in both regions of the simulation domain. By combining Equations (7.3), (7.4) and (7.5), the generalised form of the standing wave equation can be written as

$$v_{g/c}(z,t) = A_{g/c}(z) \sin\omega t + B_{g/c}(z) \cos\omega t. \quad (7.6)$$

In Equation (7.6), $A_{g/c}(z)$ and $B_{g/c}(z)$ are the components of the velocity amplitude of the standing wave on each side, where for the CNT region (*Region 1*),

$$A_c(z) = v_0 e^{-m_g L_2} \left[e^{-m_c z} \cos k(z + L_2) - e^{m_c(z-2L_1)} \cos k(z - L_2 - 2L_1)\right], \quad (7.7)$$

$$B_c(z) = -v_0 e^{-m_g L_2} \left[e^{-m_c z} \sin k(z + L_2) + e^{m_c(z-2L_1)} \sin k(z - L_2 - 2L_1)\right], \quad (7.8)$$

and for the gas region (*Region 2*),

$$A_g(z) = v_0 e^{-m_g L_2} \left[e^{-m_g z} \cos k(z + L_2) - e^{m_g z - 2m_c L_1} \cos k(z - L_2 - 2L_1)\right], \quad (7.9)$$

$$B_g(z) = -v_0 e^{-m_g L_2} \left[e^{-m_g z} \sin k(z + L_2) + e^{m_g z - 2m_c L_1} \sin k(z - L_2 - 2L_1)\right]. \quad (7.10)$$

These equations can be rearranged to form the standing wave equation for a single region between the source and receiver which contains only gas atoms similar to the case discussed in Section 5.4. By replacing $m_g = m_c = m$ for the case without CNT and by considering the same boundary coordinates illustrated in the schematic shown in Figure 5.9a, i.e. $L_2 = 0$ and $L_1 = L$, one may obtain the equations of velocity components. These are the same as Equations (5.11) and (5.12) and represent a standing wave for a single region of gas atoms between the source and receiver. The non-linear fitting of these equations to the components of the velocity amplitudes for a theoretical standing wave can be used to compare the acoustic variables predicted by the one-region (Equations (5.11)-(5.12)) and two-region (Equations (7.9)-(7.8)) approaches. The transmission matrix method was used to formulate a profile of the velocity components of a theoretical standing wave using acoustic variables such as the piston velocity amplitude $v_0 = 49.39\,\mathrm{m/s}$, sound speed $c = 500\,\mathrm{m/s}$ and attenuation coefficient $m = 1.34 \times 10^7\,\mathrm{m^{-1}}$. Figure 7.3 shows the fitting of the wave forms to the theoretical standing wave using both approaches. The predicted values of the acoustic variables such as the sound speed and attenuation are found to be the same as the values used to formulate the theoretical standing wave. It confirms that the two-region approach can predict the same value of the attenuation coefficients for two adjacent regions if both have the same medium.

The two-region approach was also used to predict the sound speed (c) and attenuation coefficient (m) from the simulation results of the case without the CNT for a wave frequency $f \approx 1.5\,\mathrm{GHz}$ for the velocity components shown in Figure 6.22. A comparison of the two approaches (one and two regions) for the non-linear fits of the waveforms is shown in Figure 7.4. The predicted values of c and m are $446\,\mathrm{m/s}$ and $0.967 \times 10^7\,\mathrm{m^{-1}}$, and $429\,\mathrm{m/s}$ and

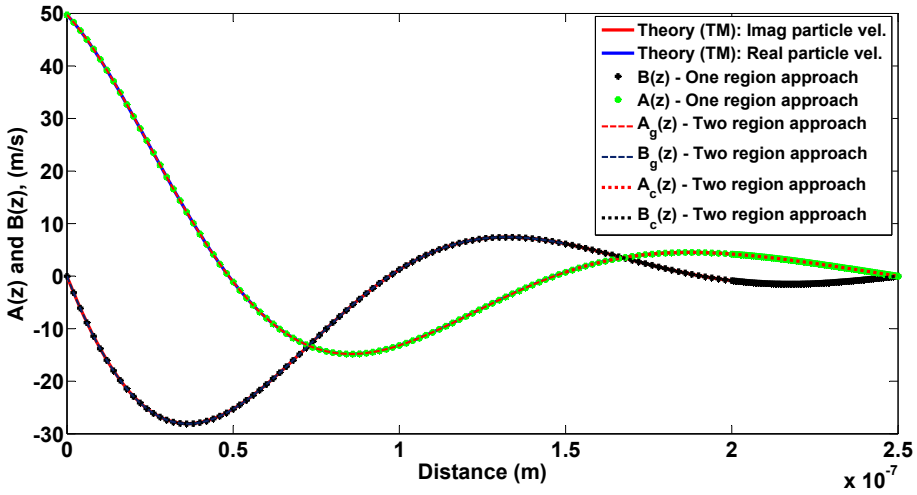

Figure 7.3: Comparison between one- and two-region approaches for non-linear fitting of the wave equations to the components of the velocity amplitude for a theoretical standing wave formulated using a transmission matrix for an acoustic wave of frequency $f \approx 2.5\,\text{GHz}$ ($R = 0.5$). The length of the domain $z < 1.5 \times 10^{-7}\,\text{m}$ represents the gas region (*Region 2*), and the domain length $z > 1.5 \times 10^{-7}\,\text{m}$ corresponds to the CNT region (*Region 1*). The waveforms fit perfectly to the velocity components for both approaches and predict the same value of the sound speed and attenuation coefficient as the value used to formulate the standing wave.

$0.952 \times 10^{7}\,\text{m}^{-1}$ by using the one- and two-region approaches, respectively. The difference in the attenuation coefficient is due to the variation in the sound speed between the two approaches, but if a constant value of c were used for the prediction in the two-region approach, then both attenuation coefficients would have been the same. It can be seen from Figure 7.4 that both approaches give a good fit to the waveforms for constant values of the sound speed and attenuation coefficient within the data fitting region outside one mean free path ($z > \lambda_{\text{mfp}}$).

Furthermore, it should be noted that the attenuation coefficient m_c represents sound attenuation in the CNT region, which has both gas and a CNT, hence the resultant attenuation by the CNT would only be $(m_c - m_g)$. If the CNT induces any acoustic absorption in the gas then m_c has to be larger than m_g. The acoustic absorption coefficient within the CNT region can be estimated from the calculated attenuation constant (m_c) using the relationship between the reflection coefficient (R_α) and attenuation constant as

$$R_\alpha = \exp[-(ik + m_c)\,2L_1]. \tag{7.11}$$

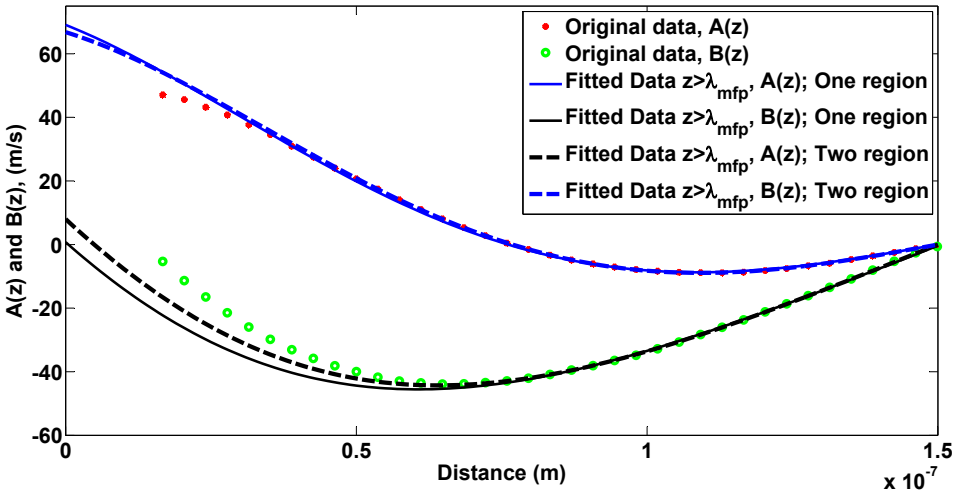

Figure 7.4: Comparison between one- and two-region approaches for non-linear fitting of the wave equations to the components of the velocity amplitude from the simulation results for a case without the CNT (with solid argon wall as acoustic source) for an acoustic wave of frequency $f \approx 1.5\,\mathrm{GHz}$ ($R = 1$). The length of the domain $z < \lambda_{\mathrm{mfp}}$ represents the gas region (*Region 2*), and the domain length $z > \lambda_{\mathrm{mfp}}$ corresponds to the CNT region (*Region 1*). Predicted values: one-region approach- $c = 446\,\mathrm{m/s}$, $m = 0.967 \times 10^7\,\mathrm{m}^{-1}$; two-region approach- $c = 429\,\mathrm{m/s}$, $m = 0.952 \times 10^7\,\mathrm{m}^{-1}$.

Similarly, the reflection coefficient for CNT only can be expressed as

$$R_\alpha^{\mathrm{CNT}} = \exp[-(ik + m_c - m_g)\,2L_{\mathrm{CNT}}]. \tag{7.12}$$

The resultant absorption coefficient is then calculated as

$$\alpha = 1 - |R_\alpha^{\mathrm{CNT}}|^2. \tag{7.13}$$

7.3.2 Exergy Concepts

The acoustic energy losses in the system can also be evaluated using the exergy concept. The concept of exergy was described in Section 6.3.2, in which the losses of acoustic energy in a system were considered as lost work and estimated as entropy generation which is responsible for the irreversibility in the system. A similar approach of energy balance was applied for the acoustic simulation domain in the presence of the CNT. A schematic of a generalised microscopic portion of an acoustic system in the presence of a CNT is shown in Figure 7.5. Following the method described in Section 6.3.2, the entropy generation for the generalised microscopic portion with a CNT

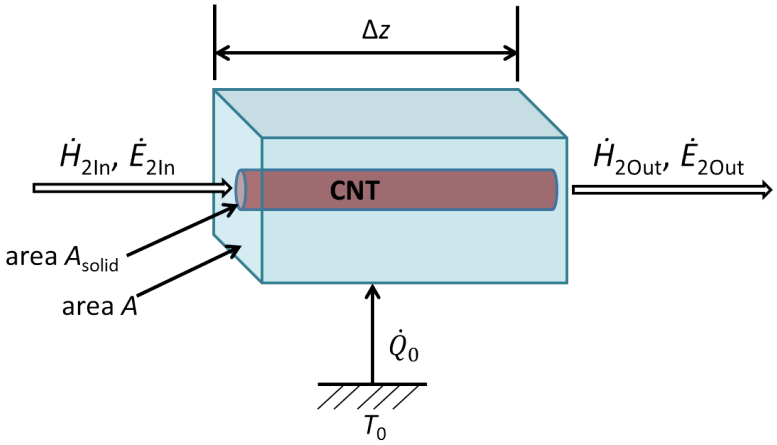

Figure 7.5: Schematic of generalised microscopic portion of the simulation domain in the presence of a CNT of the modelled acoustic system. The wave is propagating in the horizontal direction of the figure and corresponds to the z-direction in the simulation domain. The representative microscopic portion of the simulation domain with length Δz has acoustic power $\dot{E}_2$ and total power $\dot{H}_2$ flowing into and out of the left and right open end, respectively. In between the process, the system rejects (or absorbs) thermal power $\dot{Q}_0$ to ambient at T_0. The schematic is adapted from Swift (2002) (see Chapter 6, p154).

can be expressed in terms of exergy as

$$T_0 \sum \dot{S}_{\text{gen}} = \dot{X}_{2\text{In}} - \dot{X}_{2\text{Out}}. \tag{7.14}$$

For a simulation domain of a thermoacoustic system of plane wave propagation of a volume V and cross-sectional area A and length L_z consisting of a CNT with length $L_{\text{CNT}} = L_z$ and cross-sectional area A_{CNT}, the rate at which the energy per unit volume is being lost from the wave can be written as

$$\frac{\dot{W}_{\text{lost}}}{V} = -\frac{1}{V}\left[\int_0^{L_z} \nabla \,.\, \dot{X}_2 dz\right], \tag{7.15}$$

where $\dot{X}_2(z)$ is the time-averaged exergy flux in the z-direction in the simulation domain, which can be written as

$$\dot{X}_2 = \frac{T_0}{T_m}\dot{E}_2 + \left(1 - \frac{T_0}{T_m}\right)\dot{H}_2, \tag{7.16}$$

and the total power flux, $\dot{H}_2(z)$, in the z-direction can be written as (Swift 2002)

$$\dot{H}_2(z) = \frac{1}{2}\rho \int Re[h v^*] dA - (A\kappa + A_{\text{solid}}\kappa_{\text{solid}})\frac{\mathrm{d}T_{\text{m}}}{\mathrm{d}z}. \tag{7.17}$$

However, in the current simulation, the CNT was placed at the termination wall and the length of the tube L_{CNT} was smaller than the total length of the simulation domain L_z. Hence the heat conduction between the gas and the CNT can be considered limited to being within the region of the domain length equivalent to L_{CNT}. Therefore the simulation domain can be divided, similar to the schematic illustrated in Figure 7.2, into two adjacent regions: one with the gas atoms where heat conduction occurs only in the gas, another with the gas atoms and the CNT, where the conduction of heat occurs both in the gas and the CNT. These can be realised by separating the heat conduction terms during the calculation of total power flux using Equation (7.17). The total power flux can be expressed as

$$\dot{H}_2(z) = \dot{H}_{2g} - \dot{h}_{\mathrm{CNT}}, \tag{7.18}$$

where $\dot{H}_{2g}$ is the total power flux without the heat conduction term for the CNT and $\dot{h}_{\mathrm{CNT}}$ is the heat conduction term for the CNT. Both of these terms can be written as

$$\dot{H}_{2g}(z) = \frac{1}{2}\rho \int Re[hv^*]dA - A\kappa \frac{\mathrm{d}T_{\mathrm{m}}}{\mathrm{d}z}, \tag{7.19}$$

$$\dot{h}_{\mathrm{CNT}}(z) = A_{\mathrm{CNT}}\kappa_{\mathrm{CNT}} \frac{\mathrm{d}T_{\mathrm{m}}}{\mathrm{d}z}. \tag{7.20}$$

Combining Equations (7.18)-(7.20), the thermoacoustic approximation of exergy flux $\dot{X}_2$ presented in (7.16) can be rearranged for the gas in the absence of any solid in the system as

$$\dot{X}_2 = \frac{T_0}{T_m}\dot{E}_2 + \left(1 - \frac{T_0}{T_m}\right)\dot{H}_{2g}. \tag{7.21}$$

These can be inserted into Equation (7.15) to develop the generalised equation of entropy generation (lost work) for a simulation domain containing a CNT as shown in Figure 7.1. Equation (7.15) can then be written as

$$\frac{\dot{W}_{\mathrm{lost}}}{V} = -\frac{1}{V}\left[\int_0^{L_z} \nabla \,.\, \dot{X}_2 \mathrm{d}z - \left(1 - \frac{T_0}{T_{\mathrm{m}}}\right)\int_{L_z - L_{\mathrm{CNT}}}^{L_z} \nabla \,.\, \dot{h}_{\mathrm{CNT}} \mathrm{d}z\right], \tag{7.22}$$

where $(L_z - L_{\mathrm{CNT}})$ is the length of the domain with gas atoms only, which represents a domain similar to *Region 2* in Figure 7.2.

7.4 Observations

The simulation was initiated with a temperature difference of 273 K between the CNT and gas (see details in Section 7.2), and run for a total of 15 ns during

the equilibration process. Following initiation of the simulation, the CNT had reached a temperature of 273 K within 0.5 ns. Thereafter, the simulation was continued for a further 14.5 ns to relax both the gas and the CNT. The complete histories of the temperature of the CNT and temperature and pressure of the gas during the equilibration are shown in Figure 7.6. Both the CNT and the gas maintained a mean temperature of 273 K and the gas maintained a mean pressure of 1.05 bar at the end of the equilibration process. The velocity of the gas atoms was also monitored during the equilibration process at various monitoring points along the z-direction, yielding the profile shown in Figure 7.7.

After the equilibration of the flow, the simulations were run for 67.35 ns, which is equivalent to 100 periods of the propagating wave cycle. The variation of the mean spatial temperature of both the gas and the CNT during the wave propagation was closely monitored to observe the state of the flow. Figure 7.8 shows the change in the temperature of the gas and the CNT as a function of the integer period of the propagating acoustic wave cycle. It can be seen that the gas reached a steady temperature after 20 periods and maintained that steady temperature for further periods of the wave cycles. However, the temperature of the CNT steeply increased during the 20 periods of the wave cycle and reached a steady temperature after 40 periods from the start of the simulation. As the flow reached the steady state, i.e. after 40 periods, the simulations were run for a further 60 periods, a total of 100 periods to observe the interaction between the gas and the CNT. In addition, the variation of the mean spatial gas pressure and gas temperature were monitored to check the effect on the sound speed due to dissipation. The change of the gas pressure during the wave propagation as a function of the integer period of the propagating acoustic wave cycle is displayed in Figure 7.9. It can be observed that the maximum increase in the average temperature and pressure of the gas, which reached 284 K and 1.09 bar ($\approx$ 1 atm), was within 5% of the equilibrium temperature and pressure, which confirms that the change of sound speed was less than 2.5%.

7.4.1 Energy Balance and Thermostats

The system was checked for energy balance between the work done by the piston and the energy extracted by the thermostat. Figure 7.10 shows a complete history of the energy due to the work done by the piston and the energy extracted by the thermostat as a function of the oscillation period of the wave cycle. The plots are presented for the energy balance during the acoustic wave propagation, i.e. between $0 - 100$ periods of the simulated

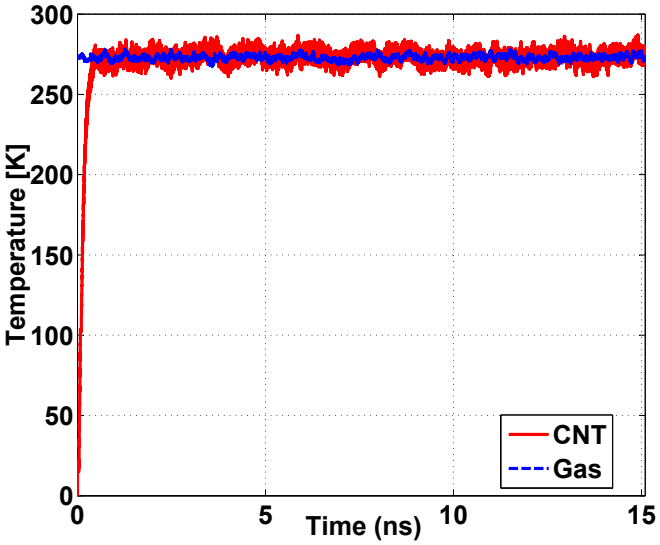

(a) Mean spatial temperature

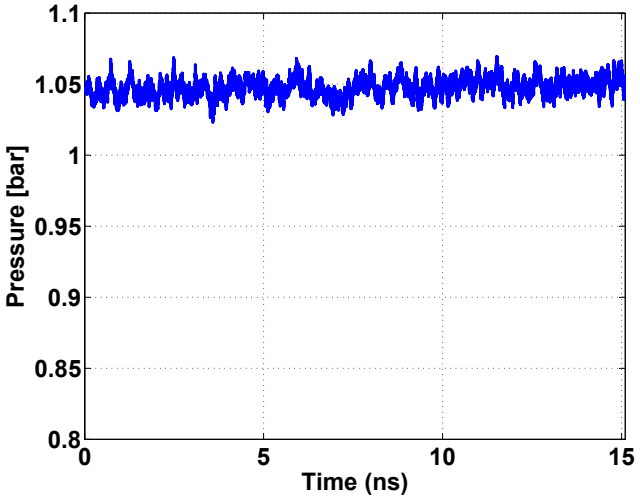

(b) Mean spatial pressure

Figure 7.6: Complete history of (a) mean spatial temperature of the gas and the CNT, and (b) mean spatial pressure of the gas during the equilibration of the system in preparation for subsequent acoustic excitation at frequency $f \approx 1.5\,\mathrm{GHz}$ ($R = 1$).

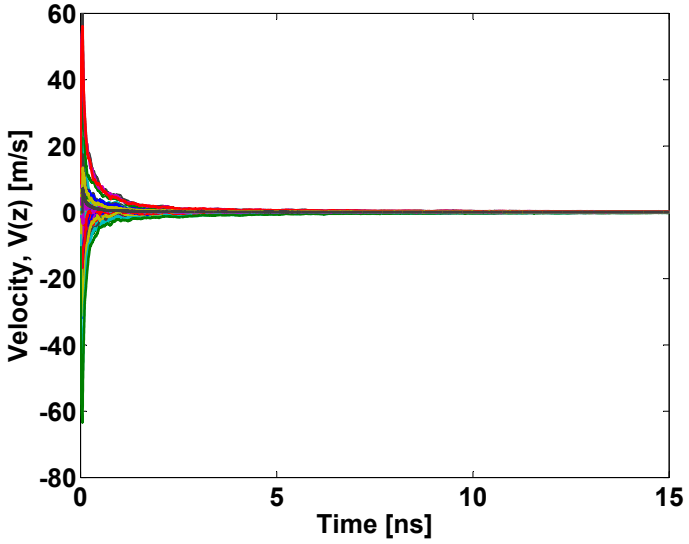

Figure 7.7: Cumulative average of velocity of the gas at each monitoring point along the z-direction of the simulation domain during the equilibrium process. Each colour represents the quantity for each particular monitoring point.

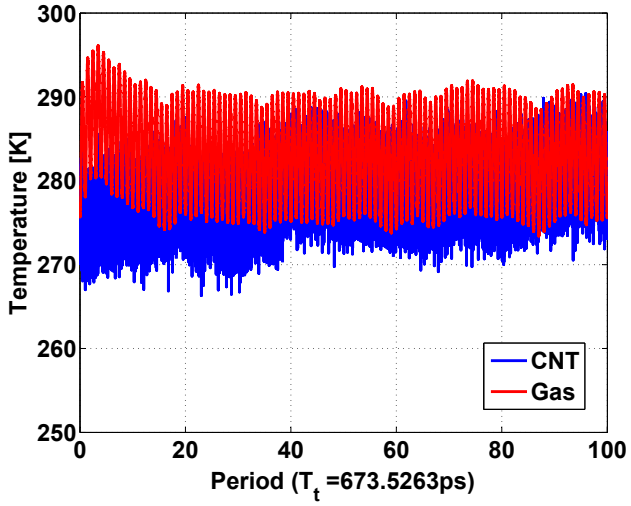

Figure 7.8: Mean spatial temperature of the gas and the CNT during the excitation of the system with an acoustic wave of frequency $f \approx 1.5\,\mathrm{GHz}$ ($R = 1$).

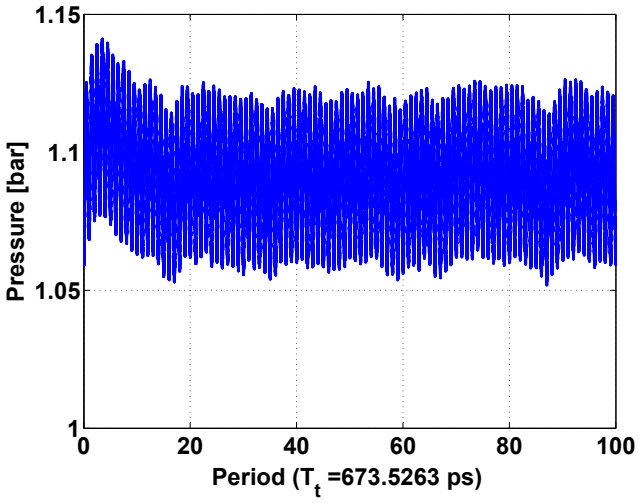

Figure 7.9: Mean spatial pressure of the gas during the excitation of the system with an acoustic wave of frequency $f \approx 1.5\,\text{GHz}$ ($R = 1$).

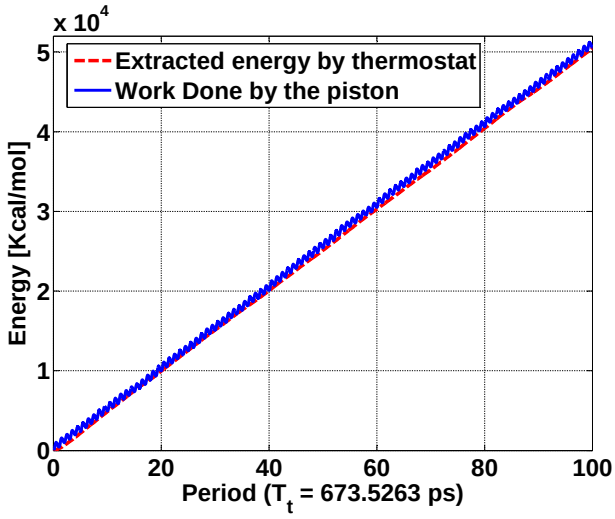

Figure 7.10: Comparison of the work done by the piston and the energy extracted by the thermostat as a function of the oscillation period of the wave cycle for a simulation domain incorporating a CNT for acoustic excitation at frequency $f \approx 1.5\,\text{GHz}$ ($R = 1$).

wave cycle. It can be seen that both curves show a similar trend for the slope of the energy input to and extracted from the system by the piston and the thermostat, respectively. A linear fit to these curves reveals that the work done by the piston and the energy extracted by the thermostat are approximately 509 kcal/mol and 507 kcal/mol per period, respectively. This indicates that an approximate energy balance per acoustic wave period is maintained between the energy input by oscillations of the piston for the repeated wave cycle and the extraction of the additional energy from the system by the thermostat. The small discrepancy can be attributed to the linear fitting of the curve for all wave periods, which includes the transition periods between the steady state condition and equilibration.

7.5 Simulation Results and Discussions

7.5.1 Sound Field

To observe the effect on acoustic parameters (such as the velocity profile, acoustic active and reactive intensity, and absorption coefficient) due to the interaction between the CNT and the gas, the acoustic sound field behaviour (simulation results) was compared between the cases with and without the CNT present for the same simulation conditions. The simulation results for the case without the CNT present were described previously in Section 6.5. Figure 7.11 shows a comparison of the velocity components, $A(z)$ and $B(z)$, of the particle velocity amplitudes $v(z)$ as a function of distance for both cases. It can be observed that the velocity components do not reveal any substantial changes compared with the case without the CNT present. Similarly no considerable changes are observed in the active and reactive intensities of the sound field shown in Figure 7.12.

The reason behind these insubstantial changes in the acoustic components between the domain with and without the CNT can be attributed to the small differences between the attenuation coefficients for these two domains. Both regions of the gas only (*Region 2*) and the gas with CNT (*Region 1*) have nearly the same attenuation coefficient, which is not significant enough to make any changes in any of the acoustic variable profiles. These can be verified by the predicted and estimated attenuation coefficient as discussed later in Section 7.5.2. So to observe any considerable changes in the acoustic variable profiles, the attenuation coefficient in the CNT region must be significant compared with that in the gas region. Indeed, the attenuation coefficient is affected by any substantial loss mechanisms involved in that region.

A similar comparison of the transfer function, $H_{p_0 p_z}$, between the acoustic

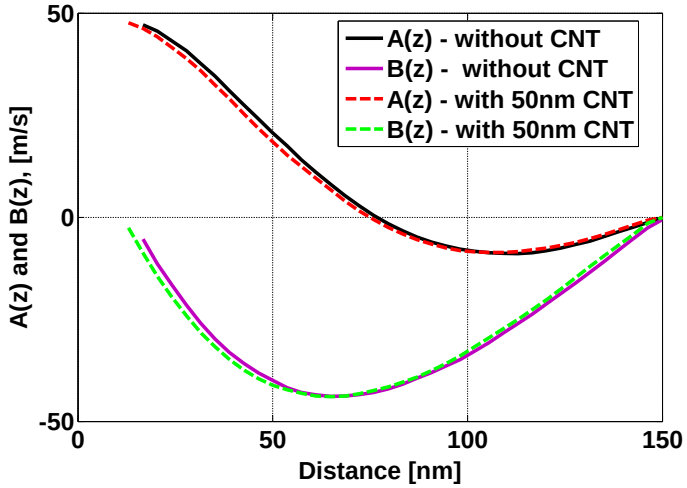

Figure 7.11: Components, $A(z)$ and $B(z)$, of particle velocity amplitude $v(z)$ as a function of distance in a simulation domain with and without the CNT present for the same simulation conditions for acoustic excitation at frequency $f \approx 1.5\,\text{GHz}$ ($R = 1$).

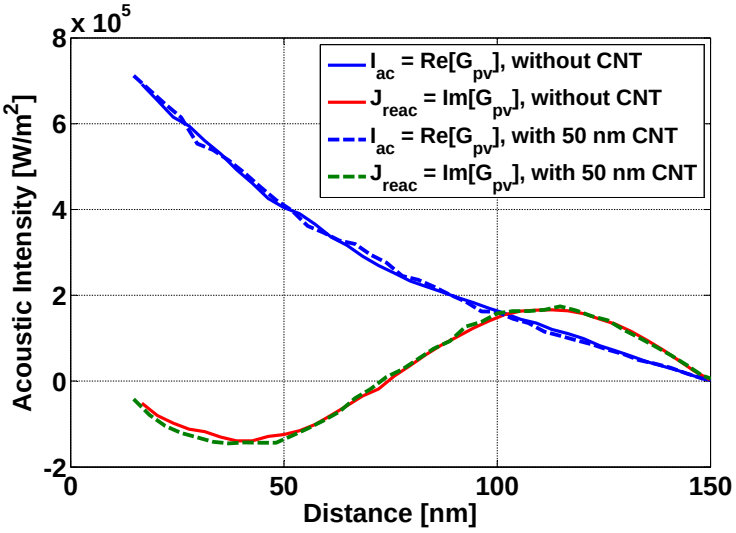

Figure 7.12: Active and reactive acoustic intensities as a function of distance in a simulation domain with and without the CNT present for the same simulation conditions for acoustic excitation at frequency $f \approx 1.5\,\text{GHz}$ ($R = 1$).

pressure at the sound source and that away from the source, for the two acoustic domains with and without the CNT is displayed in Figure 7.13.

Finally, the localised acoustic absorption coefficient between the acoustic domain with and without the CNT as a function of distance along the wave path is also compared and presented in Figure 7.14. Again, no considerable changes in the absorption coefficient are observed even near to the tip of the CNT or within the distance from the tip of the CNT to the termination wall.

The inconsistencies (distortions) near the reflection wall observed in some of the figures presented in this chapter (and in the previous chapter) is due to the mapping and averaging method of virtual (microscopic) bins (of a number of atoms) implemented for collecting the data from the simulation. Along the wave path in the z-direction, bins of a particular size were defined relative to a specified coordinate value or origin and the bins were created in both directions to cover the entire domain with respect to that specified position (LAMMPS-Manual 2013). During the simulation, atoms were mapped into one of the bins and any additional atoms beyond the lowermost/uppermost bin were counted in the first/last bin in that dimension (LAMMPS-Manual 2013). Hence, the first and last bins in the domain did not usually have sufficient atoms to perform a well-converged averaging of a macroscopic quantity (those sensitive to the number of particles such as pressure), which created inconsistencies in the quantities compared with those of the other microscopic bins in that dimension.

7.5.2 Sound Attenuation

Molecular simulations were performed for sound wave propagation with and without the CNT present in the acoustic domain with the same domain dimensions and simulation conditions. The simulation results of sound wave propagation without the CNT present in the domain were discussed in *Part 1* in the previous chapter. The results in the presence of the CNT were presented in the previous section (Section 7.5.1) of this chapter. These results were used to obtain a comparison of velocity components ($A(z)$ and $B(z)$) with and without the CNT present, as exhibited in Figure 7.11. This comparison was made in order to observe the acoustic damping due to the effect of fluid-structure interactions between the gas and the CNT, induced by the acoustic wave. It can be seen that the components of the velocity amplitude in the presence of the CNT show a small but discernible change in the velocity profile compared with those in the domain without the CNT, which may have been induced due to the interaction between the acoustic wave and the CNT. The results in Figure 7.11 reveal a subtle difference in the cosine and

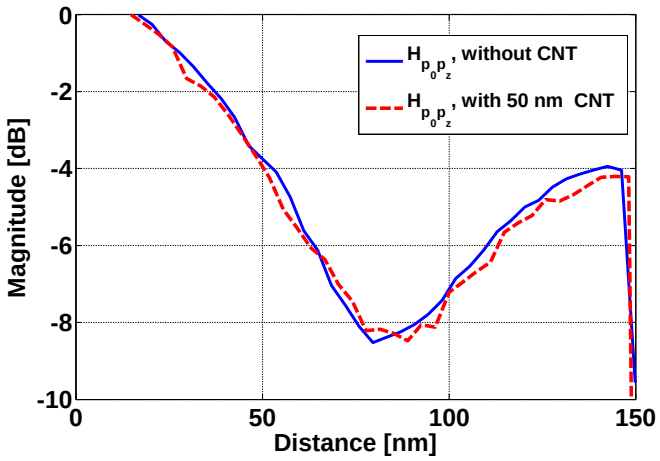

(a) Magnitude (dB)

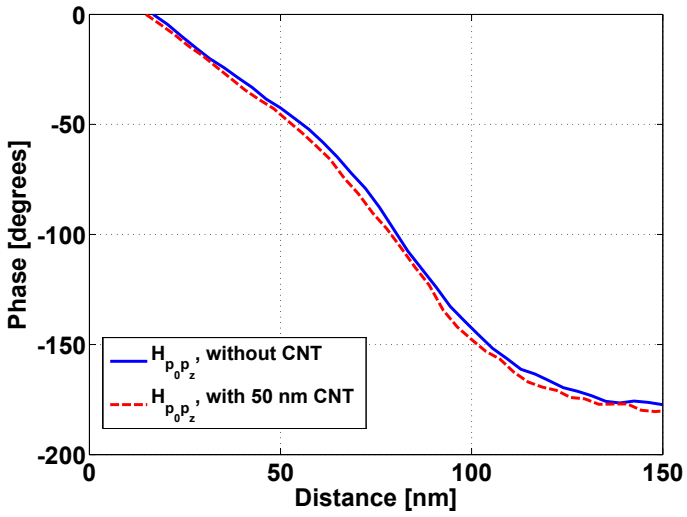

(b) Phase (degree)

Figure 7.13: (a) Magnitude and (b) phase of the transfer function, $H_{p_0 p_z}$, between the acoustic pressure at the sound source and that away from the source, as a function of distance for two acoustic domains with and without the CNT present for the same simulation conditions for acoustic excitation at frequency $f \approx 1.5\,\text{GHz}$ ($R = 1$).

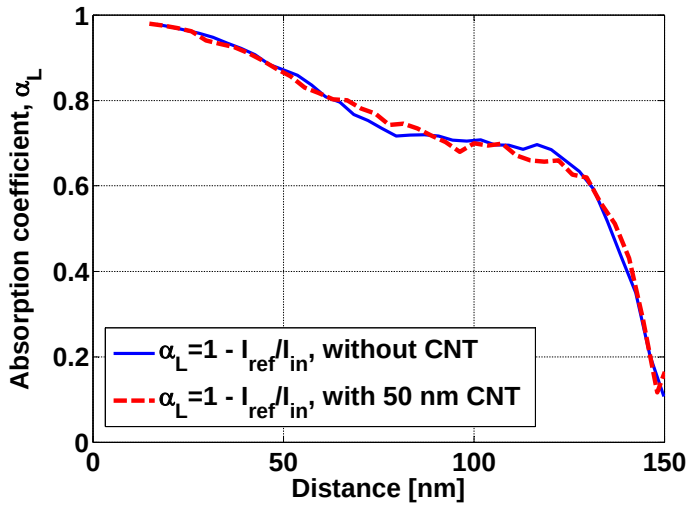

Figure 7.14: Localised acoustic absorption coefficient, α_{L}, as a function of distance along the wave path between the two acoustic domains with and without the CNT present for the same simulation conditions for acoustic excitation at frequency $f \approx 1.5\,\mathrm{GHz}$ ($R = 1$).

sine components and a shift of the curves relative to those obtained without the CNT present, although the differences are not substantial. The non-linear curve fitting, using the two-region approach described in Section 7.3.1, to the velocity components $A(z)$ and $B(z)$ of the acoustic domain with the CNT predict a value of $1.21 \times 10^7\,\mathrm{m}^{-1}$ for the attenuation coefficient m_c for the CNT region (*Region 1*) by considering a constant value of $m_g = 1.05 \times 10^7\,\mathrm{m}^{-1}$ and a sound speed of $c = 431\,\mathrm{m/s}$ for the gas. The constant values of $m_g = 1.05 \times 10^7\,\mathrm{m}^{-1}$ and $c = 431\,\mathrm{m/s}$ for the gas were predicted from the velocity curve obtained without the CNT present using the data fitting within a region of the gas equivalent to the CNT region from $z > 100\,\mathrm{nm}$. The fitting of the curve for the simulation results obtained both with and without the CNT present is illustrated in Figure 7.15. The value of $m_c > m_g$ indicates the occurrence of additional absorption of acoustic energy by the CNT in the CNT region. Hence, the value of $(m_c - m_g)$ represents the attenuation by the CNT only.

These predictions can be verified by the estimation of attenuation coefficients using a more rigorous approach for the energy balance: exergy, described in Section 7.3.2. Estimates of the acoustic power $\dot{E}_2$, total power $\dot{H}_2$ and exergy $\dot{X}_2$ for the simulation domain in the presence of the CNT are shown in Figure 7.16. The largest differences between the exergy and

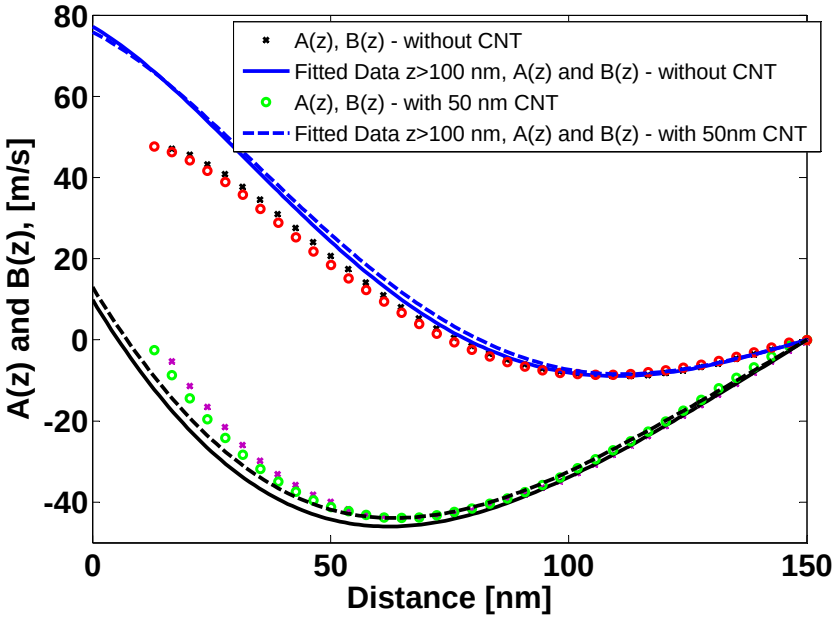

Figure 7.15: Curve fit, using two-region approach described in Section 7.3.1, to cosine and sine components, $A(z)$ and $B(z)$, of velocity amplitude from MD simulation as a function of wave propagation distance for acoustic excitation at frequency $f \approx 1.5\,\text{GHz}$ ($R = 1$). The curve fitting was performed for the simulation results obtained with and without the CNT present. The value of the attenuation constant $m_g = 1.05 \times 10^7\,\text{m}^{-1}$ and sound speed $c = 431\,\text{m/s}$ for the gas were predicted from the waveforms of the velocity components obtained without the CNT present by fitting the curve within the length of the domain $z > 100\,\text{nm}$, which is equivalent to the CNT region (*Region 1*).

acoustic power can be observed in the CNT region of the domain along the wave path of $z > 90\,\text{nm}$, indicating additional consumption of power by the CNT. These differences are more pronounced when these curves are compared with that of the domain with gas only as shown in Figure 7.17. As expected, only a subtle difference between the acoustic power curve (shown in Figure 7.12) can be observed between the domains with and without the CNT, considering that the calculation was performed based on the changes in the acoustic pressure and particle velocity. However, unlike the velocity components or acoustic power, substantial differences in the exergy and total power curves within the CNT region can be seen in Figure 7.17 between the two acoustic domains, whereas no substantial changes occur in the gas region $z < 90\,\text{nm}$. Using exergy concepts, the attenuation coefficient ($m_e^{\text{w/CNT}}$) for the whole system with the CNT present was calculated using Equation (7.22).

The value of $m_e^{w/CNT} = 2.17 \times 10^7\,m^{-1}$ obtained is approximately equal to the value of $(m_c + m_g) = 2.26 \times 10^7\,m^{-1}$ predicted from the curve fitting using the two-region approach. Note that the value of m_c represents only the CNT region, hence the value of $(m_c + m_g)$ represents the attenuation for the whole system combining both the gas and CNT regions in Figure 7.2. Indeed the value of $m_g = 1.05 \times 10^7\,m^{-1}$ was predicted from an equivalent region of gas atoms only. Hence by considering the original value of $m_g = 0.97 \times 10^7\,m^{-1}$ from Table 6.1, an estimate of the attenuation coefficient $(m_c + m_g)$ for the whole system would give nearly the same value of $m_e^{w/CNT}$.

An estimate of the acoustic absorption by the CNT only can be performed using the relations in Equations (7.12) and (7.13). A value of the attenuation by the CNT, $(m_c - m_g) = 1.5 \times 10^6\,m^{-1}$, calculated using the curve fitting method, gives an acoustic absorption coefficient of approximately 0.27 indicating 27% absorption by the 50 nm CNT only. This estimate seems reasonable considering that the experimental absorption coefficient (see Chapter 3) obtained for a 3 mm CNT forest, which includes millions of CNT per unit area, is 5% $\sim$ 10% for an audible frequency range of 125 Hz to 4 kHz. The value estimated here is for a CNT of 50 nm and an acoustic wave of a very high frequency at 1.5 GHz.

Furthermore, the transfer of acoustic energy from the gas atoms into the CNT during the wave propagation can also be confirmed by analysing the atomistic behaviour of the CNT. The atomistic behaviour of the CNT was monitored during the wave propagation and the results are discussed in the following section.

7.6 Effects on CNT

Several factors were analysed in terms of the molecular changes in the CNT to relate the attenuation (if any) of the acoustic wave energy during the interaction between the CNT and gas atoms. It was anticipated that two primary loss mechanisms (Kinsler et al. 2000; Seybert 2002) would be dominant for sound absorption by the CNT:

- Damping of the wave due to the induced structural vibrations of the material caused by the sound pressure and velocity fluctuations within the material. This effect was studied by analysing the vibrational behaviour of the CNT.
- Viscous and thermal losses caused by collisions of the oscillating gas atoms with the CNT atoms and heat conduction due to the differences

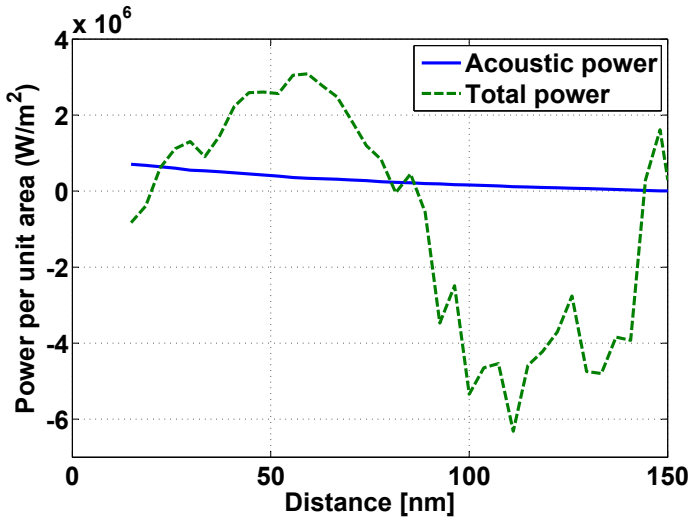

(a) Total power

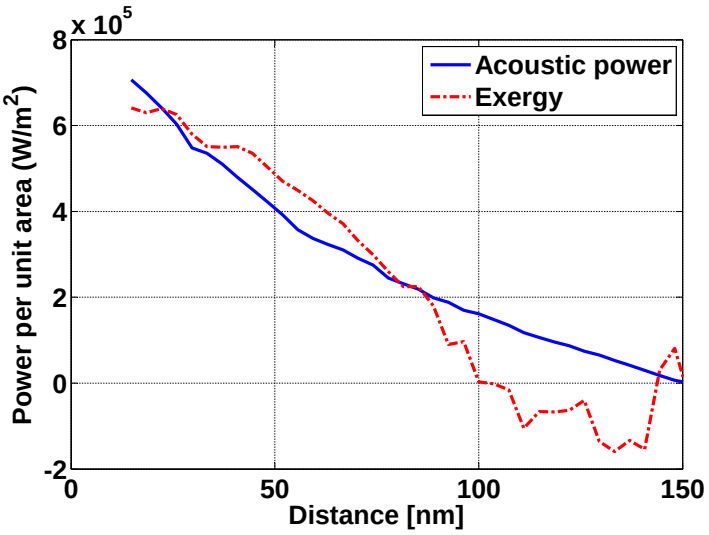

(b) Exergy

Figure 7.16: Comparison of acoustic power with (a) total power (Equation (7.18)) and (b) exergy (combination of Equations (7.20) and (7.21)) for an acoustic domain with the presence of the 50 nm CNT for acoustic excitation at frequency $f \approx 1.5\,\text{GHz}$ ($R = 1$).

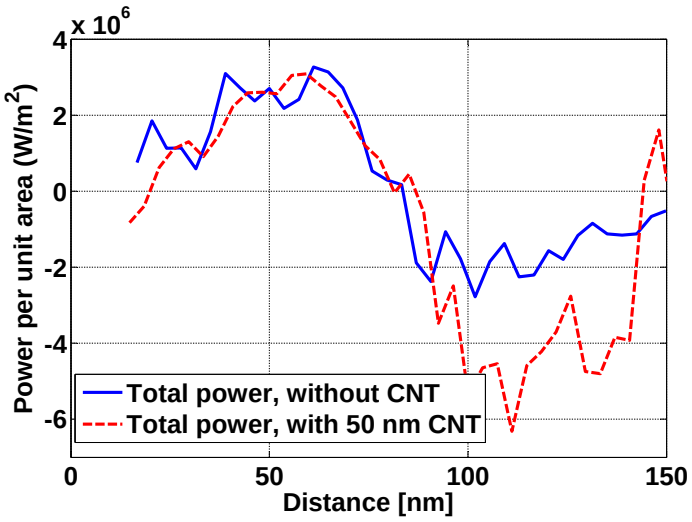

(a) Total power

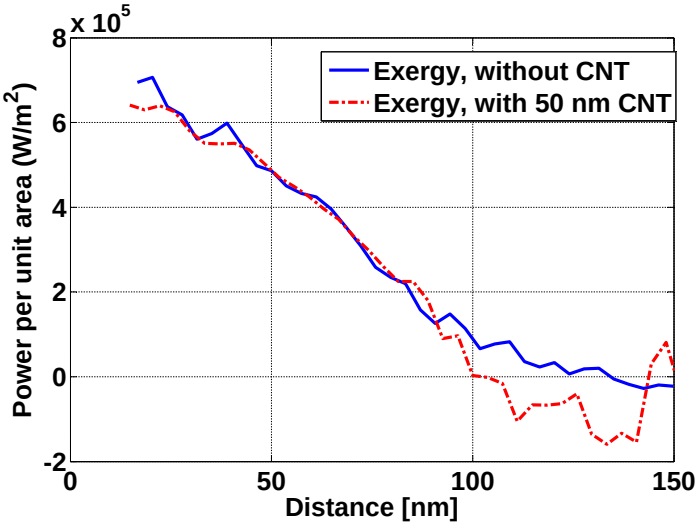

(b) Exergy

Figure 7.17: (a) Total power and (b) exergy in acoustic domains with and without the CNT present for acoustic excitation at frequency $f \approx 1.5\,\mathrm{GHz}$ ($R = 1$).

in the thermal conductivity between the wave medium and the CNT. This effect was studied by analysing the phonon spectrum behaviour of the CNT as any inelastic collisions between the gas atoms and the CNT would result in travelling of a phonon along the nanotube and the absorbed energy would be converted to heat by structural damping mechanisms. Hence the phonon behaviour would reveal any energy transfer mechanisms involved.

The atomic trajectory and velocity of each of the atoms in the nanotube were monitored to capture the atomistic behaviour of the CNT. In addition, the deflections and the stored potential energy of a tip atom and an atom in the middle of the nanotube were recorded to evaluate the evolution of vibrations of the CNT atoms at different positions and to confirm the transfer of energy.

7.6.1 Vibrational Behaviour of Carbon Nanotube

The vibrational behaviour of the CNT was analysed to investigate any significant changes in its structural modes. Although no considerable changes are observed in the velocity amplitude of the propagating wave, visualisation of the MD simulation using VMD (Visual Molecular Dynamics) shows several CNT structural modes of vibration. To gain further insight into the excitation of structural vibrations in the CNT, a principal component analysis (PCA) was performed for the last 40 periods of simulations without (equilibration) and with excitation (acoustic wave), for the atomic trajectory $z_i(t)$, where $i = 1, 2, ...3N$, where N is the total number of atoms (Chen et al. 2011). The results of the PCA are presented in the scree plot for CNT vibration modes shown in Figure 7.18. It can be seen from Figure 7.18 that for both cases with and without excitations, there are no considerable changes in the most dominant vibrational modes.

However, it was observed that the deflection frequency and energy of the CNT were amplified with acoustic excitation compared with the case without excitation, which can be verified from an examination of the recorded deflection of a tip atom and an atom at the middle of the CNT (as illustrated in Figure 7.19). The displacement of the CNT tip and its mid-atom, as well as the thermal fluctuation amplitude and potential energy were recorded during the simulations. Results both with and without acoustic wave excitation are plotted in Figures 7.20 and 7.21. As displayed in Figures 7.20a and 7.21a, when no acoustic wave is driving the system, i.e. when the system is in its equilibration state, the position of the CNT tip and middle atom oscillate around their original position $d_t(x, y, z) = d_0(t = 0)$ with a stan-

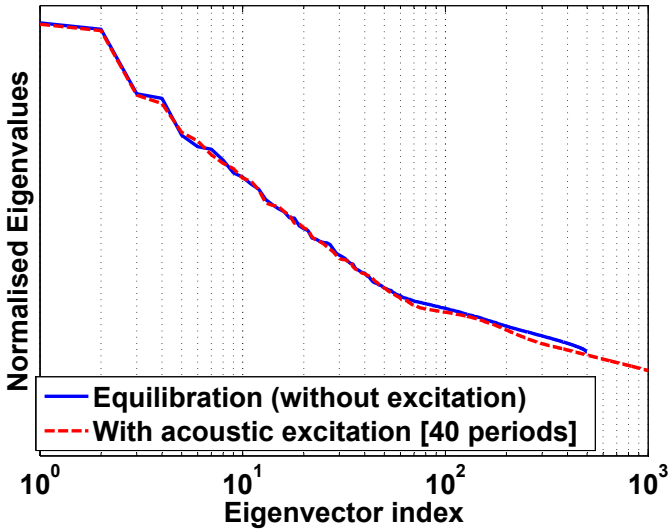

Figure 7.18: Deflection modes with and without excitation by the acoustic flow obtained from principal component analysis.

Figure 7.19: CNT atom positions used to observe the displacement of the tip and the middle of the CNT.

dard deviation of amplitude (a_x, a_y, a_z) = (1.858 nm, 1.961 nm, 0.102 nm) and (0.632 nm, 0.684 nm, 0.031 nm), respectively. This oscillation can be regarded as thermally induced motion attributed to both the excitation of phonon modes in the CNT and the contribution from random collisions with the surrounding argon molecules (Chen and Xu 2011). For the case with acoustic excitation, as shown in Figures 7.20b and 7.21b, the standard deviation of the deflections from their equilibrium position are (a_x, a_y, a_z) = (1.991 nm, 1.696 nm, 0.084 nm) and (0.683 nm, 0.577 nm, 0.028 nm) for tip and middle CNT atoms, respectively. This indicates that the deflection amplitudes for both atoms do not change considerably, which explains the absence of any dramatic changes in the vibrational modes of the nanotube structure during the interaction with the acoustic wave.

However, examining the recorded deflections of the CNT atoms at the tip position and middle of the tube shown in Figures 7.20 and 7.21, it can be noticed that the deflection frequencies of the CNT atoms with acoustic

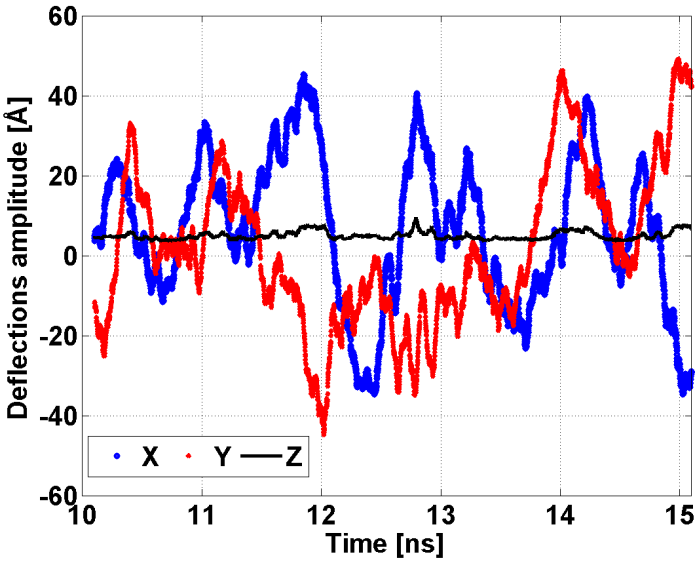

(a) Without excitation

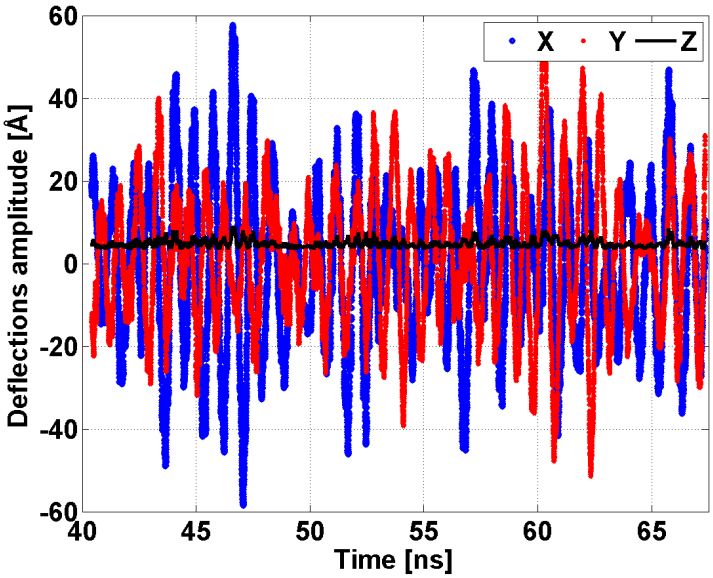

(b) With excitation

Figure 7.20: CNT tip displacement, $(dx, dy, dz) = d_t(x, y, z) - d_0(t = 0)$ with and without acoustic excitation. The atom positions of the tip and middle of the tube are shown in Figure 7.19. Acoustic excitation at frequency $f \approx 1.5\,\text{GHz}$ ($R = 1$), which is equivalent to a period of 0.67 ns.

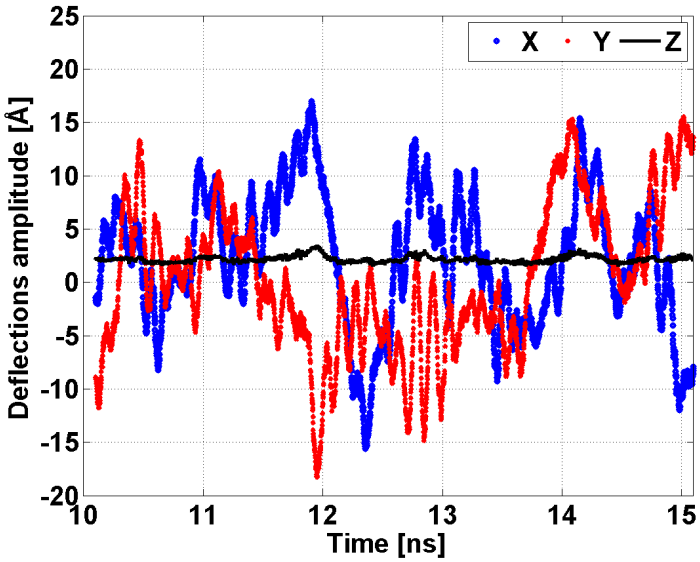

(a) Without excitation

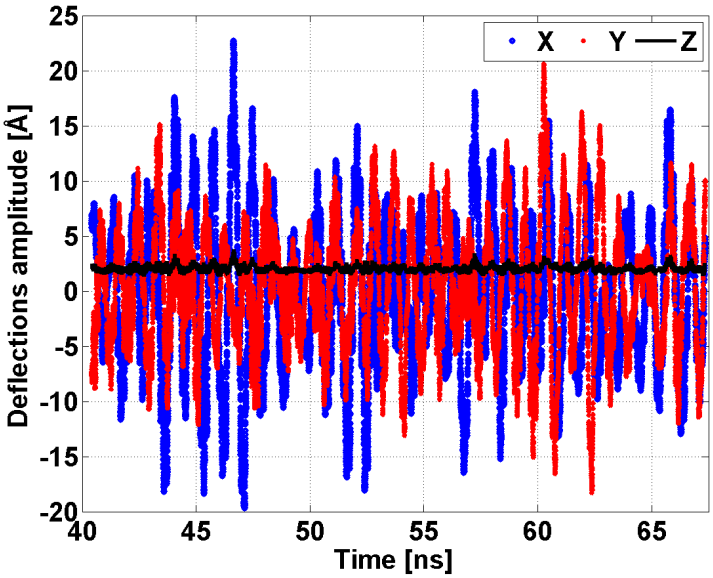

(b) With excitation

Figure 7.21: Displacement of atom in middle of CNT, $(dx, dy, dz) = d_t(x, y, z) - d_0(t = 0)$ with and without excitation. The atom positions of the tip and middle of the tube are shown in Figure 7.19. Acoustic excitation at frequency $f \approx 1.5\,\text{GHz}$ ($R = 1$), which is equivalent to a period of 0.67 ns.

excitation increase dramatically. The auto-spectral densities of the deflection amplitudes of the middle atom in the x-, y-, and z-directions reveals the presence of additional peaks at high frequency with the usual peaks at relatively lower frequencies. The single-sided spectra of the deflection amplitudes of the atom in the middle of the CNT are presented in Figure 7.22. It can be seen that, without acoustic excitation, the first three peaks of the deflection amplitude in the x-, y- and z-directions are at frequencies of approximately 1 GHz, 7 GHz and 40 GHz. These frequencies can be attributed to the random fluctuations of CNT atoms. With acoustic excitations, an additional peak can be observed at a frequency of approximately 20 GHz along with the peaks observed due to thermal fluctuations during the equilibration process of the CNT. In addition, the harmonics of the additional peak (20 GHz) excited by the acoustic wave can also be observed at higher frequencies in Figure 7.22. Additionally, it can be observed that the amplitudes of each of these peaks (including thermal fluctuations of CNT atoms) in the auto-spectral densities increased with acoustic excitation. This indicates that a portion of the acoustic energy contributes to amplifying the deflection frequencies of the atom in the middle of the CNT. This can also be verified by measuring the potential energy stored by the tip and middle atoms of the nanotube. It was found that, without excitation, the CNT tip and middle atom deflect with a standard deviation of potential energy $\epsilon = 0.0279$ eV and 0.0390 eV, respectively. On the other hand, with acoustic excitation, the standard deviation of the potential energy of the deflections of the tip and middle atoms were recorded as $\epsilon = 0.0281$ eV and 0.0392 eV, respectively. This means both the tip and middle atoms gained additional energy of $\epsilon = 0.0002$ eV during acoustic excitation, which is responsible for the higher deflection amplitudes compared with the thermal deflections. However, further atomistic analyses of the deflections of CNT atoms are required to elaborate the mechanisms involved with transferring energy from the acoustic waves to the CNT and how the deflection frequencies are related with the driving (acoustic) frequency.

These analyses suggest that the additional energy stored in the CNT atoms during acoustic excitation, which is facilitated by acoustic energy transfer from the gas atoms into the CNT structure, induces a dramatic increase of the atom deflections of the nantoube. This also indicates that the loss of acoustic energy may be attributed to viscous and heat conduction losses due to the collision of gas atoms with the nanotube, thus resulting in the travelling of a phonon down the nanotube. Analysis of the phonon spectrum behaviour of the CNT can confirm this hypothesis, and is explained in the following section.

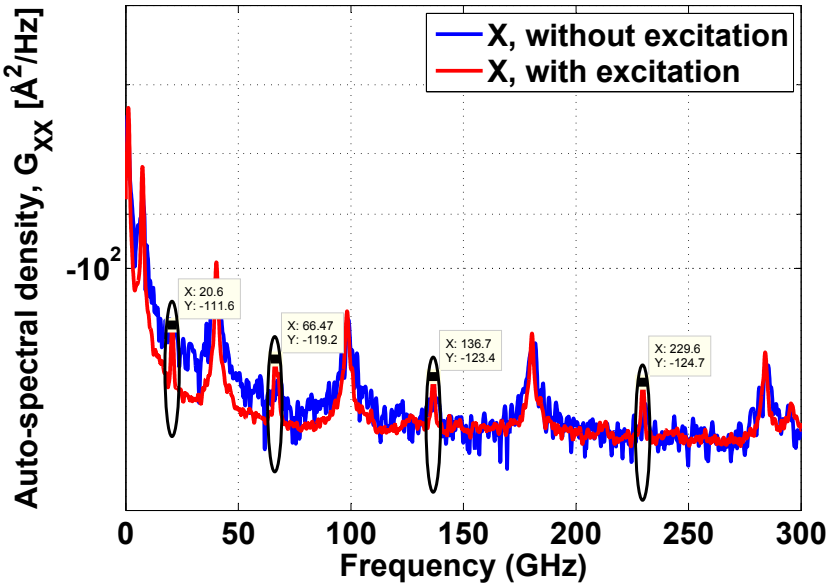

(a) Deflections in the x-direction

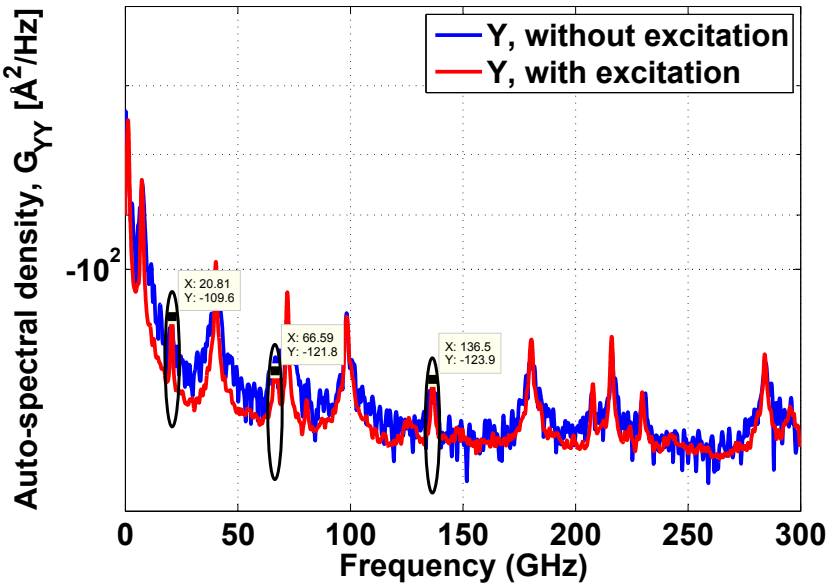

(b) Deflections in the y-direction

Figure 7.22: Single-sided spectrum of the auto-spectral density of the displacement amplitude of the atom in the middle of the CNT, $(dx, dy, dz) = d_t(x, y, z) - d_0(t = 0)$ with and without excitation. The atom positions of the tip and middle of the tube are shown in Figure 7.19. Acoustic excitation at frequency $f \approx 1.5\,\text{GHz}$ ($R = 1$), which is equivalent to a period of 0.67 ns. The circles in the figures indicate additional peaks of CNT atom deflections.

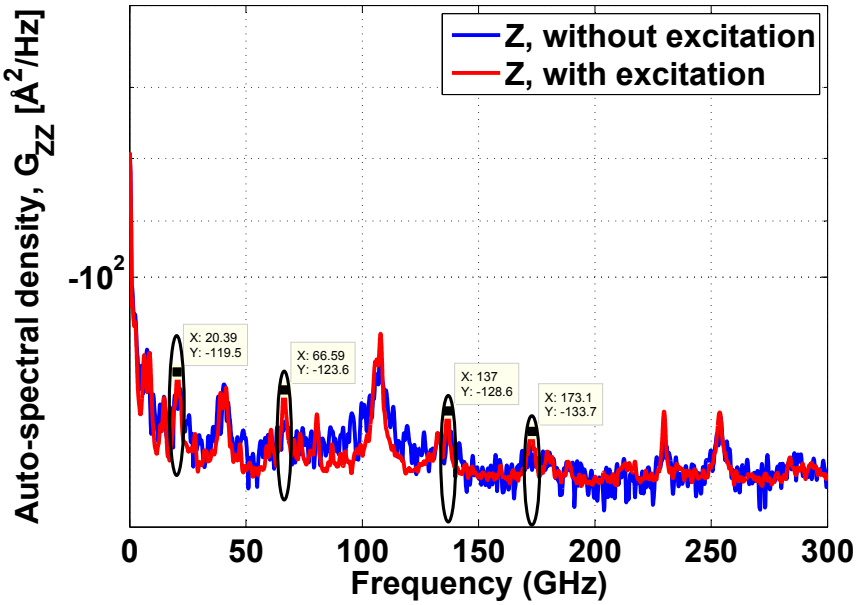

(c) Deflections in the z-direction

Figure 7.22: Single-sided spectrum of the auto-spectral density of the displacement amplitude of the atom in the middle of the CNT, $(dx, dy, dz) = d_t(x, y, z) - d_0(t = 0)$ with and without excitation. The atom positions of the tip and middle of the tube are shown in Figure 7.19. Acoustic excitation at frequency $f \approx 1.5\,\text{GHz}$ ($R = 1$), which is equivalent to a period of 0.67 ns. The circles in the figures indicate additional peaks of CNT atom deflections.

7.6.2 Phonon Spectrum Behaviour of Carbon Nanotube

The excitation of phonons by the acoustic wave can be observed from a comparison of the phonon spectra of the CNT for the cases with and without acoustic excitation. During the simulations, the velocities of the CNT atoms were recorded to estimate the phonon spectra of the CNT with and without acoustic excitation. The phonon spectrum was estimated from the power spectral density of the velocity fluctuations of the CNT atoms in the same way as the calculations performed for validation *Case 2* demonstrated in Section 5.3.2. The velocities were sampled at 133 THz for 66,667 trajectory snapshots during equilibrium (i.e. without acoustic excitation) and for 89,866 trajectory snapshots during acoustic wave propagation (i.e. with excitation) and ensemble averaged in 2048 sample windows for both cases. The phonon spectrum with acoustic excitations was calculated for only one wave period (between $100 - 101$ wave periods) as it was a memory-intensive process to

record the velocities of each of the 3990 CNT atoms for a repeated number of wave cycles. Figure 7.23 shows a comparison of the calculated phonon energy amplitude of the CNT as a function of excitation frequency between the cases with and without acoustic excitation. It can be observed that no significant differences are visible in the phonon modes over the broadband frequency spectrum of the CNT with and without acoustic excitation. However, a closeup of the phonon spectrum shown in Figure 7.23b reveals that low-frequency vibrations are excited at frequencies below 1 THz by the acoustic wave, indicating the transfer of energy due to the phonon excitations. Interestingly, significant changes in the phonon energy amplitude occur in the frequency range of $0 - 100$ GHz, which coincides with the earlier observations of the atom deflections for tip and middle CNT atoms at 20 GHz. Excitations of phonons during wave propagation can also be observed at a frequency of 2 THz.

Based on the above analysis and discussion, it can be identified that the current simulation setup with the CNT shows only a small amount of acoustic absorption and is not suitable for considering an analysis to investigate the absorption mechanisms. The analysis showed only subtle, not substantial, changes in acoustic properties of the gas between the simulation results obtained with and without the CNT present in the domain. However, the molecular analyses of the structural vibrational behaviour of the CNT, the deflections of the CNT atoms and the phonon behaviour of the CNT confirm that the interactions of the CNT with the acoustic wave have a significant effect on the molecular behaviour of the structure, which induce losses of acoustic energy. Listed below are the factors identified as the reasons responsible for not observing substantial losses induced by the CNT in the current setup of MD simulations:

- Length of the CNT: The absorption effect of an absorbent material for any acoustic frequency of interest is greatest when the material is placed at a distance a quarter of the wavelength from a wall, as this is where the particle velocity of the vibrating medium is its highest (Cox and Antonio 2009; Newell 2003). In the current simulation, the length of the CNT was $L_{\mathrm{CNT}} = 50$ nm (approximately the distance from the CNT tip to the termination wall). This distance was smaller than a quarter of a wavelength ($\lambda \approx 280$ nm) of the simulated acoustic frequency. Hence, a CNT either positioned at $\frac{\lambda}{4}$ away from the wall or with a length greater than a quarter of a wavelength of the acoustic frequency would potentially achieve greater acoustic absorption in the CNT.

- Cross-sectional area of the CNT: The diameter of the CNT simulated

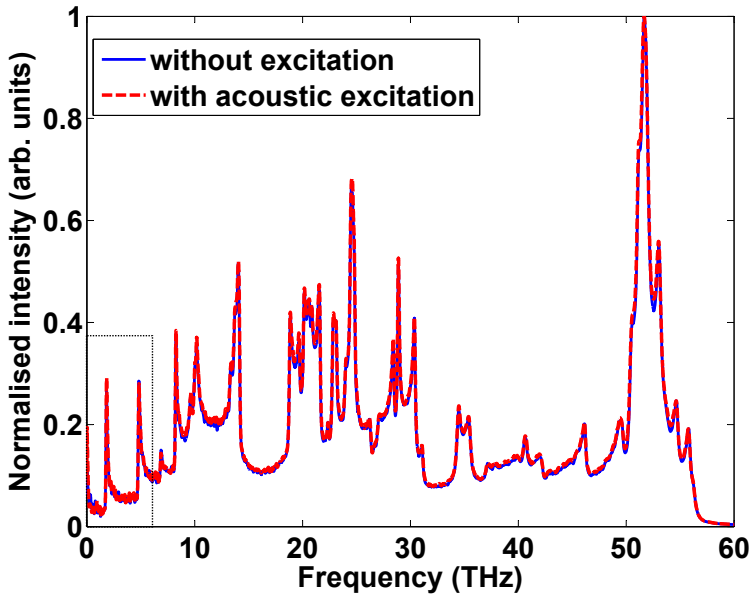

(a) Phonon energy spectrum

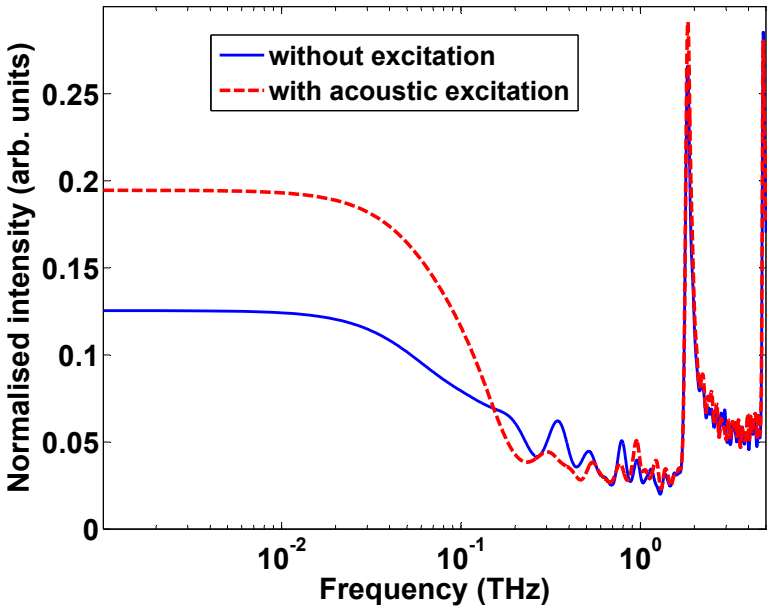

(b) Closeup of the first 5 THz

Figure 7.23: Phonon energy spectrum of the 50 nm-long SWCNT submerged in an acoustic medium of gaseous argon. The spectra are shown for cases with and without acoustic excitation. A frequency resolution of 0.001 THz was used for the spectrum.

in this study was d_{CNT} = 0.69 nm and the mean free path of the wave propagation medium (argon gas) was $\approx$ 72 nm. Since the simulation was performed for plane wave propagation with a normal incidence sound source, the wave strikes the cross-sectional area at the tip of the CNT. This means that the CNT would provide a cross-sectional area considerably smaller than a fraction of a mean free path required for a single collision to occur with gas atoms. Hence the interactions between the gas and CNT atoms were infrequent as observed from the atomic trajectory.

7.7 Summary

In summary, the modelled molecular system studied in Chapter 6 was extended in this chapter to investigate (high frequency) acoustic wave propagation in the presence of a CNT using the MD simulation. A standing wave model, namely a two-region approach, was developed based on plane-wave theory to separate the wave region consisting of the gas atoms only and that of the gas atoms and the CNT. The waves in these regions were expressed using the standing wave relation in terms of two different attenuation coefficients defined for each corresponding region. These wave equations were used to predict the sound speed and attenuation coefficients for the two adjacent regions of gas and CNT by performing nonlinear fits to the velocity components obtained from the MD simulation with and without the CNT present. The attenuation from the simulation results was also estimated using the exergy and compared against the standing wave model. It was observed that both estimates gave a good approximation of the attenuation coefficient for the region consisting of the gas and the CNT. Analysis of the simulation results indicated that a discernible amount of acoustic absorption by the CNT could be quantified and the occurrence of absorption was confirmed by the transfer of energy from the gas to the CNT. The molecular behaviour of a CNT in the presence of acoustic wave propagation in a monatomic gaseous medium was studied. It was observed that the acoustic energy contributes to the CNT atom deflections. The deflections of CNT atoms increased dramatically due to interactions with the acoustic wave, which is facilitated by the transfer of energy from the gas to the CNT atoms as confirmed by the increased potential energy of each atom. However, only weak coupling exists between the CNT structure and the propagating acoustic wave as no significant change in the vibrational modes could be observed in the CNT structure. The study presented in this chapter showed that the absorption effects of the CNT could be modelled using MD simulations even though the estimated

absorption was very small. This may be attributed to the length of the CNT used in these simulations being smaller than a quarter of a wavelength of the propagating acoustic wave, and the diameter of the CNT being too small to have frequent collisions with gas molecules.

The restrictions on the size of the CNT and the wave frequency for the MD simulations were due to the limited availability of computational resources. Based on the successful observation of the absorption effects of the CNT using the MD simulation of acoustic wave propagation in a simple gas, it can be concluded that a platform has been developed to conduct MD simulations to model and observe significant acoustic absorption by a nanomaterial, which can be used to investigate loss mechanisms in the audible frequency range. This would be beneficial to demonstrate the acoustic behaviour of CNT absorbers similar to those studied experimentally.

8 Conclusions and Future Work

8.1 Conclusions

The acoustic absorption behaviour of carbon nanotubes (CNTs) was investigated experimentally and numerically using the impedance tube method and a non-continuum method, respectively. The experimental investigation was conducted to explore the acoustic absorption capability of CNT absorbers and to identify possible deviations of the acoustic absorption behaviour of nanomaterials from continuum phenomena. The numerical investigation was performed to model the acoustic absorption of a CNT for the development of an understanding of the nanoscopic acoustic absorption mechanisms of absorption in nanomaterials. The basis for choosing a non-continuum method and the phenomena most likely to be incorporated in the methods to model the acoustic absorption were discussed in detail in Chapter 2. A detailed description of non-continuum particle based approaches, including LBM, DSMC, and MD, that have been implemented for various micro- and nanoscale analyses of relevance to the acoustics of nanotubes, was also presented in Chapter 2. MD was identified as the most suitable method to accurately simulate the acoustic absorption of carbon nanotubes. The selection of the method was justified by its incorporated features and capabilities to model the likely phenomena required for the molecular interaction of the CNT with acoustic wave propagation in a gas. This was demonstrated by a comparison among the suitable modelling approaches (LBM, DSMC and MD) based on their advantages, disadvantages and limitations. The two major advantages of the MD method over other methods are the ability to simulate large Knudsen number flows and compressible media, as well as the effective simulation of heat conduction through the material.

Chapter 3 presented the acoustic absorption characteristics of a CNT absorber based on an experimental investigation of the acoustic absorption of a forest of vertically aligned CNTs within the frequency range of 125 Hz to 4.2 kHz. The two-microphone impedance tube method was employed to mea-

sure the experimental absorption coefficient. Two additional corrections were implemented in addition to the traditional two-microphone measurement method to account for microphone phase mismatch error and tube attenuation. It was observed that a 3 mm-long forest of CNTs can provide as much as 10% acoustic absorption within the measured frequency range and can enhance the acoustic absorption of a combined panel of the CNT forest and a conventional porous material by 5% $\sim$ 10%. A comparison of absorption coefficients, between the experimental results and theoretical predictions using models based on classical absorption mechanisms, reveal that nanoscopic acoustic absorption is likely to deviate from the continuum behaviour. In addition, an independent investigation of the absorption coefficient of a relatively long CNT forest of 6 mm suggests that the absorption performance could be enhanced by having a greater length and lower forest density of the CNTs than that of the 3 mm forest. The experimental results presented in Chapter 3 suggest the need for acoustic modelling at the nanoscale to develop an understanding of nanoscopic absorption mechanisms of CNTs.

The requirement of the MD methods for successfully conducting molecular simulations to explore acoustic absorption mechanisms at the nanoscale was discussed in Chapter 4. A detailed review of the basics of the MD method and the application of MD simulations to the study of the relevant physics of acoustic absorption mechanisms at the nanoscale were also included in this chapter. From this review, it was identified that molecular simulations previously carried out, for either compressible or incompressible nanoscale flow, have not simultaneously accounted for all relevant aspects of the multi-physics phenomena relevant to acoustic absorption within CNTs in gas; namely fluid/structure interactions, bi-directional heat transfer, and acoustic wave propagation. Four potential cases of previous molecular simulation studies were identified as suitable for the validation study to assess whether MD can simulate acoustic absorption mechanisms. These cases were chosen so that each case captured a subset of the relevant phenomena and that collectively they would demonstrate the ability of MD to account for all of the required physics at the nanoscale. The current limitations of MD to perform simulations of acoustic wave propagation in the audible frequency range (0.02 - 20 kHz) are highlighted in Chapter 4. It was demonstrated that considerable computational resources would be required to extend the MD capabilities to the millisecond time scale in order to permit the study of acoustic wave propagation in the audible frequency range.

Chapter 5 presented the validation of MD simulation results against that of the reference case studies relevant to the phenomena of fluid/structure interactions, bi-directional heat transfer, and acoustic wave propagation.

The validation studies presented in this chapter demonstrated that a single approach (one force field - REBO, one method - MD), which was used to perform MD simulations in the current study, can be used to study all of the phenomena that were modelled using different approaches in the reference studies.

The study of wave propagation of high frequency sound in a simple gas using MD simulations, presented for validation *Case 3* in Chapter 5, was extended in Chapters 6 and 7 to investigate the acoustic characteristics and the absorption effects in the wave propagation medium without and with a CNT present, respectively. The sound field of the acoustic wave simulated in this study was thoroughly analysed and the wave characteristics of the high frequency sound are discussed in Chapter 6. The simulation results show that the reactive and non-progressive acoustic power is dominant (near the reflection wall) over the active and progressive acoustic power along the wave path for a high frequency wave in a domain of length smaller than that of a wavelength of the sound. The acoustic attenuation due to the classical losses in the fluid was quantified using exergy concepts and studied for three different frequencies of $f \approx 1.5\,\text{GHz}$, $2.0\,\text{GHz}$, and $2.5\,\text{GHz}$. Verifications of these estimates with standing wave theory and predictions using continuum mechanics confirm that the acoustic absorption effects of the fluid can be modelled effectively using the MD simulation method. Consequently, the demonstration of the attenuation as a factor of squared frequency and comparison against the relaxation frequency of viscous and thermal losses and the Greenspan's (1956) validity parameter, suggest that estimates of the attenuation coefficient for a high-frequency wave may deviate from the predictions of continuum theory. The modelled system studied in Chapter 6 was then extended in Chapter 7 to study wave propagation in the presence of a CNT and the induced absorption effects in the fluid by the CNT. A $50\,\text{nm}$-long CNT was included in the simulation domain aligned parallel to the direction of the acoustic flow at the wall at the opposite end of the domain to the acoustic source. A standing wave model based on plane wave theory was developed for wave propagation in the presence of the CNT by dividing the wave domain into two regions of gas atoms only and gas atoms with the CNT. Estimates of the attenuation coefficients using exergy concepts and comparisons against the predictions of the developed standing wave model indicate the additional attenuation of the acoustic power by the CNT. No substantial changes in the behaviour of the sound field were observed in the wave propagation between the two cases with and without the CNT present. However, molecular behaviour of the CNT confirm that the transfer of additional energy to the CNT during wave propagation resulted

in a change in the frequency of deflections and stored potential energy of the CNT atoms.

The conclusions of this investigation can be summarised as:

1. CNT acoustic absorbers made of CNT arrays have favourable acoustic absorption capabilities in the audible frequency range despite the fact that the absorption observed for the CNT forest samples available to this study was small and not sufficient to consider the thin CNT forest beneficial as a sound absorber. However, the absorption results of a CNT forest with a greater length and lower forest density indicate that the absorption performance can be enhanced with an optimised arrangement of the CNT structure.

2. The predictions of the absorption coefficient of the CNT forest using the classical theory of acoustic absorption do not agree well with the experimental results, indicating that the microscopic absorption mechanisms applicable for conventional materials are not applicable for nanoscopic fibres such as CNTs. Hence, to develop an understanding of the acoustic absorption mechanisms of the nanoscopic fibres, acoustic modelling at the nano-scale using non-continuum particle based methods such as MD simulations is essential.

3. Molecular dynamics (MD), a deterministic molecular simulation model, along with the REBO potential is amenable to the study of sound wave propagation in an environment where the effects of acoustic absorption, relaxation, nonlinearity, fluid/structure interactions, and bi-directional heat transfer with the CNT must be modelled simultaneously. The validation study of MD simulation for the phenomena required to investigating nanoscale acoustic absorption mechanisms, namely nanoscale fluid/structure interactions, bi-directional heat transfer effects, and acoustic wave propagation in a gas, confirms that MD can be used to study all the phenomena simultaneously and that the REBO potentials for CNTs can be used to model all these phenomena.

4. A platform for MD simulations of sound wave propagation in a simple gas was developed that can efficiently model the sound field characteristics and the acoustic absorption effects due to classical losses in the wave medium. The effects of changes in acoustic frequency on sound field characteristics and absorptions was also successfully simulated using the MD method.

5. The platform was successfully extended to simulate acoustic absorption of a CNT, although the absorption was too small to induce substantial changes in the acoustic characteristics of the fluid. However, the MD simulation method was able to capture the molecular interaction between the acoustic wave and the CNT and thereby confirm the transfer of energy into the CNT.

6. It was anticipated that the acoustic absorption of the CNT would be enhanced by the structural vibrations of the CNT excited by the acoustic wave. However, the simulations showed no substantial changes in the excitation of vibrational modes of the CNT structure during equilibration and wave propagation indicating weak coupling between the fluid/structure for the wave frequency of $f \approx 1.5\,\mathrm{GHz}$.

7. This is the first MD simulation to study acoustic absorption of a fluid and an absorber material in which the attenuations have been quantified in a conservative system using exergy concepts and studied using classical standing wave equations. The study also shows the usefulness of the MD method to model the acoustic absorption without concern for nonlinear effects in the absorption mechanisms, unlike for modelling nonlinearities using the continuum methods.

8. The study presented here was limited to MD simulations of high-frequency sound wave propagation in the range of GHz with a limited size of the CNT due to limitations in computational resources. Hence the MD simulations performed here were not able to model substantial absorption due to the CNT which could be analysed further to investigate the nanoscale absorption mechanisms and deviations from classical microscopic mechanisms.

8.2 Recommendations and Future Work

The acoustic absorption characteristics of an acoustic absorber made of CNTs and the use of the MD method to simulate the absorption effects of the wave medium and the CNT were explored in the present study. The results obtained from the experimental study conducted on a CNT forest of limited size indicate that further investigations of various non-acoustical parameters would be required to develop a fundamental understanding of the absorption characteristics of CNT forest and to determine their benefits for noise-control applications. Moreover, investigations could be made to observe the effect of different CNT structural arrangements on acoustic absorptions using CNT

samples with tube configurations specially optimised for acoustic absorption purposes. The orientation of the tubes with respect to the sound wave could also be investigated to observe the effect of structural vibrations on the acoustic absorption characteristics of the CNTs.

Similarly the results obtained from MD simulations of sound wave propagation with and without the CNT present are promising for studying the absorption effects of the gas and CNT. However, the current simulation setup with a complex force potential model (REBO) for the CNT, a piston made of solid argon, and small timestep of 0.5 fs uses considerable computational resources which makes it difficult to run simulations for relatively lower frequencies and larger CNT sizes. Hence, improvements could be made in terms of the simulation set up to speed up the computational process to reduce the computational time using existing resources. Several initiatives have already been undertaken in the AVC group at the University of Adelaide by Bennett et al. (2015). The following modifications in the simulation setup appear to speed up the computational process and reduce the computational time significantly.

- The piston made of solid argon and the termination (reflection) wall used in the results presented in this thesis can be replaced by an analytical potential function that interacts with atoms in the gas by generating a force on the atoms in a direction perpendicular to the wall (LAMMPS-Manual 2013).

- The complex REBO potential model can be replaced by the DREIDING force field (Mayo et al. 1990; Chen et al. 2011) for carbon-carbon interactions, which reduces the computational time significantly without changing sound wave propagation significantly. A list of the potential parameters for carbon-carbon interactions can also be found from Bennett et al. (2015).

- The velocity-Verlet integrator can be replaced by a multi-timestep integrator such as rRESPA (Tuckerman et al. 1992) to run the simulation with a large timestep of 10 fs for non-bonded interactions.

Moreover, a coarse-graining method such as DPD (dissipative particle dynamics) is not applicable for simulation of gaseous media since the diffuse nature of the gas precludes coarse-graining multiple gas molecules into a single coarse-grained particle. However, a coarse graining method may be employed for the simulation of carbon nanotubes in conjunction with the MD method for gaseous media to develop a hybrid model.

To observe enhanced absorption by the CNT using MD simulations (of improved computational time), the CNT could be placed at the centre of the simulation domain of 150 nm, which would allow the CNT to interact with the propagating wave at a quarter wavelength of the frequency of $f \approx 1.5$ GHz. In addition, the CNT could be chosen to be of larger size than the one studied here and oriented in the direction normal to the sound wave propagation. This will allow the CNT to have more frequent collision with the gas atoms and improve the fluid/structure interaction rates and hence the acoustic absorption.

Viscous and thermal boundary layers could be observed from the velocity and temperature profile of the gas around the CNT (if substantial changes in the sound field characteristics are observed). The length of the boundary layer could also be calculated from the velocity and temperature profiles, which could then be compared against the predictions of continuum mechanics to evaluate deviations in the absorption mechanisms.

Experimental measurements of acoustic absorption coefficients of a CNT in the gigahertz (GHz) frequency range to verify MD simulation results were not considered in this study. Performing experiments in this frequency (GHz) range are not feasible considering the setup required for the measurement. The experimental method using an impedance tube requires that only plane wave propagation occurs in the tube to conduct a standard measurement of acoustic impedance using two/four microphones (Katz 2000). Hence, the upper range of measurement frequency is limited by the cut-on frequency of the first cross mode of the tube, for which the diameter of the measurement tube should be less than $0.586c/f_{\max}$ (where c is the sound speed and $f_{\max}$ is the upper limit of the measurement frequency) as required by the ASTM standard (Katz 2000; ASTM E1050 1998). For a measurement frequency in the gigahertz (GHz) range will thus require a tube with a size smaller than a micrometre (µm), which is not feasible to conduct experiments with precision microphones. In addition, high frequency sound waves in the gigahertz (GHz) range attenuate very quickly which makes it difficult to maintain plane waves over a considerable length of the tube. Recently developed high frequency impedance tube can be used to measure acoustic absorption coefficients up to 12.8 kHz (Kimura et al. 2014). Hence, an alternative measurement method may need to be developed to estimate acoustic impedances and absorption coefficients in the gigahertz (GHz) range. In addition, performing experiments for a single nanotube with nanoscale dimensions are not viable as the exhibited acoustic absorption would be insignificant. It should be noted that the experiments in this study were performed for a CNT forest which contains millions of nanotubes. It should also be re-emphasized that

the simulations in this thesis represent a foundational study. Future work by other researchers will address lower frequencies and a greater number of nanotubes to mimic more closely the experimental systems studied.

Furthermore, the MD model of a region consisting of the CNT and gas atoms could be coupled with a CFD (computational fluid dynamics) model of a region consisting of gas only to simulate sound wave propagation at audible frequencies while simultaneously capturing the molecular interaction between the CNT and the acoustic wave. The CFD region would allow the savings of computational time while simulating a large system. With continued improvements in computational facilities, performing a large-scale MD simulation coupled with a CFD model at millisecond scale could realistically be achieved using supercomputers.

References

Aaltosalmi, U. (2005). "Fluid flow in porous media with the Lattice-Boltzmann method". PhD thesis. Jyväskylä, Finland: Faculty of Mathematics and Science, University of Jyväskylä (cit. on pp. 24, 25, 243–246).

Ackerman, D. M. et al. (2003). "Diffusivities of Ar and Ne in carbon nanotubes". In: *Molecular Simulation* 29.10 -11, pp. 677 –684 (cit. on pp. 92, 100).

Ajayan, P. et al. (2006). *Carbon nanotube foam and method of making and using thereof*. US Patent No. 11/005474, Rensselaer Polytechnic Institute. Patent Number US11/005474 (cit. on pp. 3, 4).

Alexiadis, A. and S. Kassinos (2008). "Molecular simulation of water in carbon nanotubes". In: *Chemical Review* 108, pp. 5014 –5034 (cit. on pp. 76–79).

Allard, J. F. and Y. Champoux (1992). "New empirical equations for sound propagation in rigid frame fibrous materials". In: *Journal of the Acoustical Society of America* 91, pp. 3346–3353 (cit. on p. 56).

Allard, J. (1993). *Propagation of Sound in Porous Media: Modelling Sound Absorbing Materials*. Elsevier Applied Science, London (cit. on pp. 56–58, 265).

Allen, M. P. (2004). "Introduction to molecular dynamics simulation". In: *Computational Soft Matter: From Synthetic Polymers to Proteins*. Ed. by Attig, N. et al. Vol. 23. NIC, pp. 1 –28 (cit. on pp. 7, 24, 31, 76–79, 81–85, 149).

Allinger, N. L. et al. (1989). "Molecular mechanics. The MM3 force field for hydrocarbons. 1". In: *Journal of the American Chemical Society* 111.23, pp. 8551 –8566 (cit. on p. 79).

Allinger, N. L. et al. (1996). "An improved force field (MM4) for saturated hydrocarbons". In: *Journal of Computational Chemistry* 17, pp. 642 –668 (cit. on p. 79).

Aminfar, H. and M. Mohammadpourfard (2008). "Lattice Boltzmann BGK model for gas flow in a microchannel". In: *Proceedings of the Institution of Mechanical Engineers, Part C: Journal of Mechanical Engineering Science* 222, pp. 1855 –1860 (cit. on p. 26).

Ansumali, S. and I. V. Karlin (2002). "Entropy function approach to the lattice Boltzmann method". In: *Journal of Statistical Physics* 107, pp. 291–308 (cit. on p. 26).

Ansumali, S. et al. (2006). "Entropic lattice Boltzmann method for microflows". In: *Physica A: Statistical Mechanics and its Applications* 359, pp. 289–305 (cit. on p. 5).

Arenas, J. P. and M. J. Crocker (2010). "Recent trends in porous sound-absorbing materials". In: *Sound & Vibration* Materials Reference Issue, pp. 12–17 (cit. on pp. 1, 2, 7).

Arora, G. and S. I. Sandler (2006). "Air separation by single wall carbon nanotubes: Mass transport and kinetic selectivity". In: *The Journal of Chemical Physics* 124, p. 084702 (cit. on pp. 92, 99).

Asdrubali, F. (2006). "Survey on the acoustical properties of new sustainable materials for noise control". In: *Proceedings of Euronoise*. Tampere, Finland (cit. on p. 2).

ASTM E1050 (1998). *Standard test method for impedance and absorption of acoustical materials using a tube, two microphones, and a digital frequency analysis system* (cit. on pp. 41, 44, 45, 219).

Attenborough, K. (1993). "Models for the acoustical characteristics of air filled granular materials". In: *Acta Acustica* 1, pp. 213–226 (cit. on p. 56).

Ballagh, K. (1996). "Acoustical properties of wool". In: *Applied Acoustics* 48.2, pp. 101–120. ISSN: 0003-682X (cit. on pp. 56, 58, 59).

Ban, S. and C. Huang (2012). "Molecular simulation of CO2/N2 separation using vertically-aligned carbon nanotube membranes". In: *Journal of Membrane Science* 417 - 418, pp. 113 –118 (cit. on pp. 92, 99).

Bandarian, M. et al. (2011). "Thermal, mechanical and acoustic damping properties of flexible open-cell polyurethane/multi-walled carbon nanotube foams: effect of surface functionality of nanotubes". In: *Polymer International* 60.3, pp. 475–482. ISSN: 1097-0126 (cit. on pp. 39, 40).

Banerjee, S. (2008). "Molecular simulation of nanoscale transport phenomena". PhD thesis. Blacksburg, Virginia, USA: Virginia Polytechnic Institute and State University (cit. on pp. 31–33, 36, 77, 94, 96).

Barisik, M. and A. Beskok (2011). "Molecular dynamics simulations of shear-driven gas flows in nano-channels". In: *Micro-fluidics and Nanofluidics* 11.5, pp. 611 –622 (cit. on p. 94).

Barisik, M. et al. (2010). "Molecular dynamics simulations of nanoscale gas flows". In: *Communication in Computational Physics* 7, pp. 977 –993 (cit. on pp. 24, 94).

Basirjafari, S. et al. (2012). "Low loading of carbon nanotubes to enhance acoustical properties of poly(ether)urethane foams". In: *Journal of Applied Physics* 112, 104312 (cit. on pp. 39, 40).

Beckman, W. (2007). *UC Researchers Shatter World Records with Length of Carbon Nanotube Arrays*. URL: https://www.uc.edu/News/NR.aspx?ID=5700 (cit. on p. 53).

Bejan, A. (1997). *Advanced Engineering Thermodynamics*. Second edition. Wiley, New York (cit. on p. 140).

Beltman, W. (1999). "Viscothermal wave propagation including acousto-elastic interaction, Part I: Theory". In: *Journal of Sound and Vibration* 227.3, pp. 555–586 (cit. on p. 6).

Bendat, J. S. and A. G. Piersol (1986). *Random Data: Analysis and Measurement Procedures*. Wiley-Interscience, p. 566 (cit. on p. 258).

Bennett, H. A. et al. (2015). "Speedup techniques for molecular dynamics simualtions of the interaction of acoustic waves and nanomaterials". In: *The 21st International Congress on Modelling and Simualtion (MODSIM2015)*. Queensland, Australia (cit. on p. 218).

Benzi, R. et al. (1992). "The lattice-Boltzmann equation: Theory and application". In: *Physics Report* 222.3, pp. 145–197 (cit. on p. 24).

Beranek, L. L. and I. L. Ver (1992). *Noise and Vibration Control Engineering: Principles and Applications*. New York, USA: John Wiley and Sons, p. 377 (cit. on pp. 56, 120, 129).

Berendsen, H. J. C. et al. (1984). "Molecular dynamics with coupling to an external bath". In: *The Journal of Chemical Physics* 81.8, pp. 3684 –3690 (cit. on pp. 108, 109).

Berendsen, H. J. C. et al. (1987). "The missing term in effective pair potentials". In: *The Journal of Physical Chemistry* 91.24, pp. 6269 –6271 (cit. on p. 108).

Berger, M. (2013). *Researchers grow half-meter long carbon nanotubes*. Nanowerk. URL: http://www.nanowerk.com/spotlight/spotid=31326.php (cit. on p. 53).

Bernsdorf, J. M. (2008). "Simulation of complex flows and multi-physics with the lattice-Boltzmann method". PhD Thesis. University of Amsterdam, Netherlands (cit. on pp. 21, 25, 243, 245).

Beskok, A. and G. E. Karniadakis (1999). "A model for flows in channels, pipes, and ducts at micro and nano scales". In: *Nanoscale and Microscale Thermophysical Engineering* 3.1, pp. 43–77 (cit. on p. 5).

Bhat, R. B. (2004). *Numerical Analysis in Engineering*. Alpha Science International, Oxford, UK (cit. on p. 45).

Bhatnagar, P. L. et al. (1954). "A model for collision processes in gases". In: *Physical Review E* 94.3, pp. 511–525 (cit. on p. 25).

Bies, D. and C. Hansen (2003). *Engineering Noise Control: Theory and Practice*. Third edition. Spon Press, London, UK (cit. on pp. 5, 17, 55–58).

Biot, M. (1962). "Generalized theory of acoustic propagation in porous media". In: *Journal of the Acoustical Society of America* 34.9, pp. 1254–1264 (cit. on pp. 57, 58).

Bird, G. (1994). *Molecular Gas Dynamics and the Direct Simulation of Gas Flows*. Second edition. Oxford University Press, Clarendon, Oxford (cit. on pp. 7, 24, 28, 33, 35).

Bodén, H. and M Åbom (1986). "Influence of errors on the two-microphone method for measuring acoustic properties in ducts". In: *Journal of the Acoustical Society of America* 79.2, pp. 541 –549 (cit. on pp. 247, 256, 257).

Boonen, R. et al. (2009). "Calibration of the two microphone transfer function method with hard wall impedance measurements at different reference sections". In: *Mechanical Systems and Signal Processing* 23, pp. 1662 –1671 (cit. on p. 45).

Bourzac, K. (2009). *Growing Nanotube Forests*. English. URL: `http://www.technologyreview.com/photoessay/412183/growing-nanotube-forests/` (cit. on pp. 65, 68).

Brenner, D. W. (1990). "Empirical potential for hydrocarbons for use in simulating the chemical vapor deposition of diamond films". In: *Physical Review B* 42.15, pp. 9458–9471 (cit. on p. 107).

Brenner, D. W. et al. (2002). "A second-generation reactive empirical bond order (REBO) potential energy expression for hydrocarbons". In: *Journal of Physics: Condensed Matter* 14.4, p. 783 (cit. on pp. 79–81, 106, 108, 180).

Brooks, B. R. et al. (1983). "CHARMM: A program for macromolecular energy, minimization, and dynamics calculations". In: *Journal of Computational Chemistry* 4.2, pp. 187 –217 (cit. on p. 79).

Brown, T. L. L. et al. (1999). *Chemistry: The Central Science*. 8th edition. Prentice-Hall (cit. on p. 14).

Buick, J. M. et al. (1998). "Lattice BGK simulation of sound waves". In: *Europhysics Letters* 43.3, pp. 235–240 (cit. on pp. 25, 245).

Buick, J. M. et al. (2000). "Lattice Boltzmann BGK simulation of nonlinear sound waves: The development of a shock front". In: *Journal of Physics A: Mathematical and General* 33, pp. 3917–3928 (cit. on pp. 25, 26, 101).

Cai, W. (2005). *Handout 1. An Overview of Molecular Simulation*. ME346-Introduction to Molecular Simulations, Stanford University (cit. on pp. 81, 83).

— (2007). *Handout 6. Periodic Boundary Conditions*. ME346-Introduction to Molecular Simulations, Stanford University (cit. on p. 83).

Cai, W. et al. (2010). "Comprehensive nuclear materials modelling section". In: ed. by Stoller, R. Chap. 128- Molecular Dynamics (cit. on pp. 83, 84, 89).

Carlborg, C. F. et al. (2008). "Thermal boundary resistance between single-walled carbon nano-tubes and surrounding matrices". In: *Physical Review B* 78.205406, pp. 1 –8 (cit. on pp. 80, 98, 100, 102, 105–107, 114, 115, 117, 118, 121, 132, 180).

Cercignani, C. (1988). *The Boltzmann Equation and its Applications*. New York, USA: Springer - Verlag (cit. on p. 29).

Chaudhri, A. (2005). *Molecular dynamics study of argon flow in a carbon nanotube*. Study report. URL: `http://anuj.chaudhris.com/files/IndStudyReport_AnujChaudhri.pdf?` (cit. on pp. 93, 99).

Chen, C. and Z. Xu (2011). "Flow-induced dynamics of carbon nanotube". In: *Nanoscale* 3, pp. 4383–4388 (cit. on p. 203).

Chen, C. et al. (2011). "Nanoscale fluid-structure interaction: Flow resistance and energy transfer between water and carbon nanotubes". In: *Physical Review E* 84, p. 046314 (cit. on pp. 95, 98, 100, 102, 105–112, 132, 202, 218).

Chen, S. and G. Doolan (1998). "Lattice Boltzmann method for fluid flows". In: *Annual Review of Fluid Mechanics* 30, pp. 329–364 (cit. on p. 24).

Cherng, J. (2006). *Smart acoustic materials for automotive applications*. Tech. rep. Henry W Patton Center for Engineering Education and Practice, The University of Michigan-Dearnborn (cit. on p. 40).

Cho, W. et al. (2014a). "Growth and characterization of vertically aligned centimeter long CNT arrays". In: *Carbon* 72, pp. 264–273 (cit. on pp. 4–6, 47, 53, 55, 57, 68).

— (2014b). "Growth termination mechanism of vertically aligned centimeter long carbon nanotube arrays". In: *Carbon* 69, pp. 609–620 (cit. on pp. 4, 5, 47, 53, 55, 57, 68).

Choy, Y. S. et al. (2009). "Sound propagation in and low frequency noise absorption by helium-filled porous material". In: *The Journal of the Acoustical Society of America* 126.6, pp. 3008–3019 (cit. on p. 52).

Chu, W. T. (1986). "Extension of the two-microphone transfer function method for impedance tube measurements". In: *The Journal of Acoustical Society of America* 80.1, pp. 347–348 (cit. on pp. 252, 253).

Chung, Y. J. and D. A. Blaser (1980a). "Transfer function method of measuring in-duct acoustic properties. I. Theory". In: *Journal of the Acoustical Society of America* 68.3, pp. 907–913 (cit. on pp. 41, 44).

— (1980b). "Transfer function method of measuring in-duct acoustic properties. II. Experiment". In: *Journal of the Acoustical Society of America* 68.3, pp. 914–921 (cit. on pp. 41, 43, 44, 247, 252).

Cieplak, M. et al. (2000). "Molecular dynamics of flows in the Knudsen regime". In: *Physica A-Statistical Mechanics and Its Applications* 287, pp. 153–160 (cit. on p. 24).

Cohen, M. L. and A. Zettl (2010). "The physics of boron nitride nanotubes". In: *Physics Today* 63.11, pp. 34–38 (cit. on p. 2).

Cox, T. J. and P. D. Antonio (2009). *Acoustic absorbers and diffusers - Theory, design and application*. Second edition. Taylor, Francis, London, and New York (cit. on p. 209).

Crawford, M. (2012). *Reducing airplane noise with nanofibers*. URL: `https://www.asme.org/engineering-topics/articles/aerospace-defense/reducing-airplane-noise-with-nanofibers` (cit. on p. 40).

Crocker, M. J. and J. P. Arenas (2007). *Use of Sound-Absorbing Materials, Chapter 57 in Handbook of Noise and Vibration Control*. Ed. by Crocker, M. J. John Wiley and Sons, New York. (cit. on pp. 1, 2).

CSIRO (2005). *Breakthrough for carbon nanotube materials*. Media release, Reference: 05/153. The Commonwealth Scientific and Industrial Research Organisation, Australia. URL: `http://www.csiro.au/csiro/content/standard/psh5.html` (cit. on pp. 3, 6).

Czerwinska, J. (2009). *Continuum and Non-Continuum Modelling of Nanofluidics*. Tech. rep. 8. pp. 1-22. NATO Research and Technology Organisation, pp. 1–22. URL: `<http://ftp.rta.nato.int/public//PubFullText/RTO/EN%5CRTO-EN-AVT-169///EN-AVT-169-08.pdf>` (cit. on pp. 7, 8, 20–23, 242).

Czichos, H. et al. (2011). "Springer Handbook of Metrology and Testing". In: ed. by Czichos, H. et al. 2nd. Springer Science and Business Media. Chap. 17 - Molecular Dynamics, pp. 975 –1012 (cit. on p. 82).

Dahl, M. D. et al. (1990). "Effects of fiber motion on the acoustic behaviour of an anisotropic, flexible fibrous material". In: *The Journal of the Acoustical Society of America* 87.1, pp. 54–66 (cit. on p. 70).

Danforth, A. L. and L. N. Long (2004a). "Nonlinear acoustic in diatomic gases using direct simulation Monte Carlo". In: *24th International Symposium on Rarefied Gas Dynamics*. Monopoli (Bari), Italy, pp. 553–558 (cit. on pp. 7, 28, 107).

— (2004b). "Nonlinear acoustic simulations using direct simulation Monte Carlo". In: *The Journal of the Acoustical Society of America* 116.4, pp. 1948 –1955 (cit. on pp. 28, 101, 245).

Danforth-Hanford, A. et al. (2006). "Molecular relaxation simulations in nonlinear acoustics using direct simulation monte carlo". In: *AIP Conference Proceedings* 838.1, pp. 556–559 (cit. on p. 28).

Darbandi, M. and E. Roohi (2011). "DSMC simulation of subsonic flow through nanochannels and micro/nano backward-facing steps". In: *International Communications in Heat and Mass Transfer* 38.10, pp. 1443 –1448. ISSN: 0735-1933 (cit. on p. 35).

Deladerriere, N. et al. (2008). "Effect of elastic collisions on acoustic wave propagation in simplified nuclear glass: Molecular dynamics simulation". In: *Nuclear Instruments and Methods in Physics Research B* 266, pp. 2687 –2690 (cit. on p. 94).

Delany, M. E. and E. N. Bazley (1970). "Acoustical properties of fibrous absorbent material". In: *Applied Acoustics* 3.2, pp. 105 –116 (cit. on pp. 57, 58).

Dendzik, Z. et al. (2004). "Vibrations of atoms in the argon cluster surrounding a single-walled carbon nanotube - MD study". In: *Journal of Molecular Structure* 704, pp. 203 –209 (cit. on pp. 93, 99).

Dresselhaus, M. S. et al. (1993). "Fullerenes". In: *Journal of Materials Research* 8, p. 2054 (cit. on p. 17).

Dresselhaus, M. S. et al. (1995). "Physics of carbon nanotube". In: *Carbon* 33.7, pp. 883 –891 (cit. on pp. 15, 16).

Dresselhaus, M. S. et al. (1996). *Science of Fullerenes and Carbon Nanotubes*. Academic Press, San Diego (cit. on p. 17).

Dünweg, B. and W. Paul (1991). "Brownian dynamics simulations without Gaussian random numbers". In: *International Journal of Modern Physics C* 2, pp. 817 –827 (cit. on p. 87).

Endo, M. et al. (2008). "Potential applications of carbon nanotubes". In: *Springer series on Topics in Applied Physics*. Ed. by A. Jorio, G. D. and Dresselhaus, M. Vol. 111. Berlin/Heidelberg: Springer-Verlag, pp. 13–61 (cit. on pp. 2, 3, 246).

Fahy, F. (2005). *Foundations of Engineering Acoustics, Chapter 7*. Elsevier Academic Press, London, UK (cit. on pp. 5, 17, 19, 20, 32).

Faller, L. D. (2010). *Relaxation Phenomenon*. Last Viewed: 16th November, 2011. Universalium academic dictionaries and encyclopedia. URL: `http://universalium.academic.ru/285081/relaxation_phenomenon` (cit. on p. 20).

Finnerty, J. (2011). *Molecular dynamics meets the physical world: Thermostats and barostats*. URL: `http://www.grs-sim.de/cms/upload/Carloni/Tutorials/FMCP/Thermostats_and_Barostats.pdf` (cit. on p. 88).

Frenkel, D. and B. Smit (2002). *Understanding Molecular Simulations: From algorithms to applications*. Chapter 4. Academic Press, San Diego, pp. 53–96 (cit. on pp. 7, 31, 81–84, 86, 88–90, 148, 149, 151).

Fujita, M. et al. (1992). "Formation of general fullerenes by their projection on a honeycomb lattice". In: *Physics Review B* 45.23, pp. 13834 –13836 (cit. on p. 17).

Gao, H. J. and Y. Kong (2004). "Simulations of DNA-nanotube interactions". In: *Annual Review of Materials Research* 34, pp. 123 –150 (cit. on p. 79).

Garai, M. and F. Pompoli (2005). "A simple empirical model of polyester fibre materials for acoustical applications". In: *Applied Acoustics* 66, pp. 1383 –1398 (cit. on pp. 55, 56, 58, 265).

Ghan, J. et al. (2004). "Statistical errors in the estimation of time-averaged acoustic energy density using the two-microphone method". In: *Journal of the Acoustical Society of America* 115.3, pp. 1179 –1184 (cit. on p. 256).

Greenspan, M. (1956). "Propagation of sound in five monatomic gases". In: *The Journal of the Acoustical Society of America* 28.4 (cit. on pp. 176, 177, 215).

Greenspan, M. and M. C. Thompson Jr. (1953). "An eleven megacycle interferometer for low pressure gases". In: *The Journal of the Acoustical Society of America* 25, p. 92 (cit. on p. 126).

Grossfield, A. and D. M. Zuckerman (2009). "Quantifying uncertainty and sampling quality in biomolecular simulations". In: *Annual Reports in Computational Chemistry* 5, pp. 23 –48 (cit. on p. 150).

Guhados, G. et al. (2007). "Simultaneous measurement of Young's and shear moduli of multiwalled carbon nanotubes using atomic force microscopy". In: *Journal of Applied Physics* 101.3, 033514, p. 033514 (cit. on p. 56).

Hadjiconstantinou, N. G. and O. Simek (2003). "Sound propagation at small scales under continuum and non-continuum transport". In: *Journal of Fluid Mechanics* 488, pp. 399 –408 (cit. on pp. 29, 101).

Hadjiconstantinou, N. G. (2002). "Sound wave propagation in transition-regime micro- and nanochannels". In: *Physics of Fluids* 14.2, pp. 802 –809 (cit. on pp. 7, 29, 101).

— (2006). "The limits of Navier-Stokes theory and kinetic extensions for describing small-scale gaseous hydrodynamics". In: *Physics of Fluids* 18.11, pp. 111301–19 (cit. on p. 30).

Hadjiconstantinou, N. G. and A. L. Garcia (2001). "Molecular simulations of sound wave propagation in simple gases". In: *Physics of Fluids* 13.4, pp. 1040 –1046 (cit. on pp. 7, 29, 98, 100, 101, 103, 105, 107, 120–124, 126, 128, 129, 132).

Halgren, T. A. (1996). "Merck molecular force field. I. Basis, form, scope, parameterization and performance of MMFF94". In: *Journal of Computational Chemistry* 17, pp. 490 –519 (cit. on p. 79).

Hall, L. J. et al. (2008). "Sign change of Poisson's ratio for carbon nanotube sheets". In: *Science* 320.5875, pp. 504–507 (cit. on p. 56).

Han, J. et al. (2007). *Accurate measurement of small absorption coefficients*. Tech. rep. SAE Technical Paper 2007-01-2224. DOI: 10.4271/2007-01-2224 (cit. on pp. 41, 44, 45, 51, 252, 254).

Hanford, A. D. and L. N. Long (2007). "Investigation of amplitude dependence on nonlinear acoustics using the Direct Simulation Monte Carlo method". In: *19th International Congress on Acoustics*. Madrid, Spain (cit. on p. 7).

Hanford, A. D. (2008). "Numerical simulations of acoustics problems using the direct simulation Monte Carlo method". PhD Thesis. Pennsylvania, USA: The Pennsylvania State University (cit. on pp. 7, 8, 20–25, 27–29, 32, 35, 243–245).

Hockney, R. W. and J. W. Eastwood (1989). *Computer Simulation Using Particles*. Adam Hilger, NY (cit. on p. 84).

Hofmann, T. (2003). *Molecular dynamics simulation of shock formation and reflection at a solid wall*. Diploma Thesis, ETH Zurich, Switzerland (cit. on pp. 76, 95, 101).

Hong, Z. et al. (2007). "A novel composite sound absorber with recycled rubber particles". In: *Journal of Sound and Vibration* 304.1-2, pp. 400–406 (cit. on p. 2).

Hooijdonk, E. V. et al. (2013). "Functionalization of vertically aligned carbon nanotubes". In: *Beilstein Journal of Nanotechnology* 4, pp. 129–152. ISSN: 2190-4286 (cit. on p. 53).

Hosseini Fouladi, M. et al. (2011). "Analysis of coir fiber acoustical characteristics". In: *Applied Acoustics* 72.1, pp. 35–42. ISSN: 0003-682X (cit. on pp. 2, 57, 265).

Hou, K. and J. S. Bolton (2009). *A Transfer Matrix Method for Estimating the Dispersion and Attenuation of Plane Waves in a Standing Wave Tube*. Tech. rep. Publications of the Ray W. Herrick Laboratories. Paper 54 (Abstract published in the J. Acout. Soc. Am., 125, 2596) (cit. on p. 252).

Howard, C. Q. and B. S. Cazzolato (2014). *Acoustic analysis using Matlab and Ansys*. CRC press (cit. on p. 145).

Hu, M. et al. (2007). "Air flow through carbon nanotube arrays". In: *Applied Physics Letters* 91.131905, pp. 1–3 (cit. on pp. 93, 99).

Huang, D. M. (2013). "Statistical mechanics and computer simulation of liquids". In: Honours Chemistry Lecture notes, University of Adelaide (cit. on p. 79).

Huang, S. et al. (2000). "Patterned growth of well-aligned carbon nanotubes: A soft-lithographic approach". In: *The Journal of Physical Chemistry B* 104.10, pp. 2193 –2196 (cit. on p. 3).

Hünenberger, P. H. (2005). "Thermostat algorithms for molecular dynamics simulations". In: *Advances in Polymer Science* 173, pp. 105 –149 (cit. on pp. 86, 87).

Iijima, S. (1991). "Helical microtubules of graphitic carbon". In: *Nature (London)* 354, pp. 56–58 (cit. on pp. 2, 14).

Ingard, K. (1994). *Notes on Sound Absorption Technology*. Poughkeepsie, NY, USA.: Noise Control Foundation (cit. on pp. 5, 17, 32).

Ingard, U. (2009). *Noise Reduction Analysis, Chapter 2*. Jones and Bartlett Publishers, Science Press, LLC, USA (cit. on pp. 17, 18, 32).

Insepov, Z. et al. (2006). "Nanopumping using carbon nanotubes". In: *Nano Letters* 6.9, pp. 1893 –1895 (cit. on pp. 96, 99).

ISO 10534-1 (2001). *Acoustics - Determination of sound absorption coefficient and impedance in impedance tubes, Part 1: Standing Wave Method* (cit. on p. 43).

ISO 10534-2 (2001). *Acoustics - Determination of sound absorption coefficient and impedance in impedance tubes, Part 2: Transfer-function method* (cit. on pp. 43, 45).

Ivanov, M. S. et al. (2007). "Recent achievements in the DSMC method and its applications to studying jets in vacuum chamber". In: *51st IUVSTA Workshop on Modern Problems & Capability of Vacuum Gas Dynamics. Djurönäset, Värmdö, Sweden* (cit. on p. 8).

Jacobsen, F. (1989). "Active and reactive, coherent and incoherent sound fields". In: *Journal of Sound and Vibration* 130.3, pp. 493–507 (cit. on pp. 137, 157, 159, 161, 163–165).

— (1991). "A note on instantaneous and time-averaged active and reactive sound intensity". In: *Journal of Sound and Vibration* 147.3, pp. 489–496 (cit. on p. 157).

— (2011). *Sound intensity and its measurement and applications*. Acoustic Technology, Department of Electrical Engineering. Note no 31262. Technical University of Denmark, Building 352, Ørsteds Plads, DK-2800 Lyngby, Denmark (cit. on pp. 157, 159).

Jalili, S. and R. Majidi (2007). "Study of Xe and Kr adsorption on open single-walled carbon nanotubes using molecular dynamics simulations". In: *Physica E* 39, pp. 166 –170 (cit. on p. 99).

Jha, A. (2009). *Carbon nanotubes may suppress human immunity*. URL: <http://www.guardian.co.uk/science/2009/jun/15/carbon-nanotubes-immune-system-nanotechnology> (cit. on p. 3).

Johnson, A. et al. (2012). *Thermostats in Molecular Dynamics Simulations*. University of Massachusetts Amherst. URL: people.math.umass.edu/~markos/697SC/ThermostatMD_Final.pdf (cit. on pp. 86, 87).

Jorgensen, W. L. et al. (1996). "Development and testing of the OPLS all-atom force field on conformational energetics and properties of organic liquids". In: *Journal of American Chemical Society* 118, pp. 11225 –11236 (cit. on p. 79).

Jover, J. et al. (2012). "Pseudo hard-sphere potential for use in continuous molecular dynamics simulation of spherical and chain molecules". In: *The Journal of Chemical Physics* 137.144505, pp. 1 –13 (cit. on pp. 101, 102).

Kandemir, I. and A. M. Kaya (2012). "Molecular dynamics simulation of compressible hot/cold moving lid-driven micro-cavity flow". In: *Microfluid Nanofluid* 12, pp. 509 –520 (cit. on p. 93).

Kandemir, I. and F. E. Sevilgen (2008). "Molecular dynamics simulation of helium-argon gas mixture under various wall conditions". In: *Molecular Simulation* 34, pp. 795 –808 (cit. on pp. 24, 31).

Karniadakis, G et al. (2005). *Microflows and Nanoflows: Fundamentals and Simulation*. Indisciplinary Applied Mathmatics. New York: Springer (cit. on pp. 5, 7–9, 24, 30, 31, 84–87, 242, 244).

Katz, B. F. G. (2000). "Method to resolve microphone and sample location errors in the two-microphone duct measurement method". In: *Journal of the Acoustical Society of America* 108.5, pp. 2231–2237 (cit. on pp. 44, 51, 219, 247, 252, 253, 255).

Kawasima, Y. (1960). "Sound propagation in a fibre block as a composite medium". In: *Acoustica* 10, pp. 208–217 (cit. on p. 70).

Kim, B. H. (2009). "Molecular dynamics simulations of heat transfer in nanoscale liquid films". PhD thesis. Mechanical Engineering, Texas A & M University (cit. on pp. 31–33, 36, 77, 94, 96, 97).

Kimura, M. et al. (2014). "A new high-frequency impedance tube for measuring sound absorption coefficient and sound transmission loss". In: *Inter-noise 2014, Melbourne, Australia*, p. 10 (cit. on p. 219).

Kino, N. and T. Ueno (2008). "Comparisons between characteristic lengths and fibre equivalent diameters in glass fibre and melamine foam materials of similar flow resistivity". In: *Applied Acoustics* 69, pp. 325–331 (cit. on pp. 56, 57, 59, 261, 265).

Kinsler, L. et al. (2000). *Fundamentals of Acoustics*. 4th. John Wiley & Sons, Inc., New York (cit. on pp. 45, 46, 143–145, 169, 171–173, 176, 177, 199).

Kohlmeyer, A. (2013). *TopoTools Plugin*. Theoretical and Computational Biophysics Group, University of Illinois at Urbana-Champaign. URL: http://www.ks.uiuc.edu/Research/vmd/plugins/topotools/ (cit. on p. 91).

Kosmider, M. et al. (2004). "Computer simulation of argon cluster inside a single-walled carbon nanotube". In: *Journal of Molecular Structure* 704, pp. 197 –201 (cit. on p. 99).

Koziol, K. et al. (2007). "High-Performance Carbon Nanotube Fiber". In: *Science* 318.5858, pp. 1892–1895 (cit. on p. 2).

Kroto, H. W. et al. (1985). "C60: Buckminsterfullerene". In: *Nature* 318.6402, pp. 162–163 (cit. on p. 13).

Kuipers, E. (2013). "Measuring sound absorption using local field assumptions". PhD thesis. University of Twente, Enschede, The Netherlands (cit. on pp. 137, 138).

LAMMPS-Manual (2013). *LAMMPS Users Manual*. Sandia National Laboratories. URL: `http://lammps.sandia.gov` (cit. on pp. 91, 142, 148, 155, 195, 218).

LDS Group (2013). *LDS-Dactron RT Pro Dynamic Signal Analysis, User Guide, Rev. 7.10* (cit. on p. 43).

Le, T. C. (2010). "Computational simulation of hyperbranched polymer melts under shear". PhD thesis. Faculty of Information and Communication Technologies, Swinburne University of Technology: Centre for Molecular Simulation (cit. on pp. 77, 83).

Lee K, H. and S. B. Sinnott (2003). "Computational study of the non-equilibrium flow of gases through carbon nanotubes". In: *Nanotechnology, IEEE-NANO* 2 (cit. on pp. 4, 99).

Lee, K. H. and S. B. Sinnott (2004). "Computational studies of non-equilibrium molecular transport through carbon nanotubes". In: *Journal of Physical Chemistry B* 108, pp. 9861 –9870 (cit. on pp. 93, 99).

Leissa, A. W. (1969). *Vibration of Plates*. Scientific, Technical Information Division, National Aeronautics, and Space Administration, Washington (cit. on p. 69).

Leroy, P. et al. (2008). "'Smart foams' for enhancing acoustic absorption". In: *Acoustics'08*. Paris, France (cit. on p. 2).

Li, J. (2005). "Handbook of Materials Modeling". In: ed. by Yip, S. Netherlands: Springer. Chap. 2.8 Basic Molecular Dynamics, pp. 565 –588 (cit. on p. 76).

Li, Z. and Z. Hong (2007). "On the Knudsen transport of gases in nanochannels". In: *The Journal of Chemical Physics* 127.074706, pp. 1–5 (cit. on pp. 96, 99).

Lindsay, L. and D. A. Broido (2010). "Optimized Tersoff and Brenner empirical potential parameters for lattice dynamics and phonon thermal transport in carbon nanotubes and graphene". In: *Physical Review B* 81, p. 205441 (cit. on pp. 80, 81).

Liu, Q. X. et al. (2012). "Experimental and molecular dynamics study of gas flow characteristics in nanopores". In: *Chinese Science Bulletin* 57, pp. 1488 –1493 (cit. on pp. 93, 99).

Liu, Y. C. et al. (2010). "Dual diffusion mechanism of argon confined in single-walled carbon nanotube bundles". In: *Physical Chemistry Chemical Physics* 12, pp. 6632 –6640 (cit. on pp. 92, 99).

Longhurst, M. J. and N. Quirke (2007). "Temperature-driven pumping of fluid through single-walled carbon nanotubes". In: *Nano Letters* 7.7, pp. 3324 –3328 (cit. on p. 93).

Makeev, M. A. et al. (2009). "Shock-wave propagation through pristine a-SiC and carbon-nanotube-reinforced a-SiC matrix composites". In: *Journal of Applied Physics* 106, p. 014311 (cit. on pp. 94, 101).

Mantzalis, D. et al. (2011). "Filtering carbon dioxide through carbon nanotubes". In: *Chemical Physics Letters* 506, pp. 81 –85 (cit. on pp. 93, 99).

Mao, Z. and S. B. Sinnott (2000). "A computational study of molecular diffusion and dynamic flow through carbon nanotubes". In: *The Journal of Physical Chemistry B* 104, pp. 4618 –4624 (cit. on pp. 92, 93, 100).

Maruyama, S. (2002). "Molecular dynamics methods in microscale heat transfer". In: Begell house, Inc. Chap. 2.13 Heat Transfer and Fluid Flow in Microchannels (cit. on pp. 24, 106).

Maruyama, S. (2003). "A molecular dynamics simulation of heat conduction of a finite length single-walled carbon nanotube". In: *Microscale Thermophysical Engineering* 7.1, pp. 41–50 (cit. on p. 106).

Mayo, S. L. et al. (1990). "DREIDING: A generic force field for molecular simulations". In: *Journal of Physical Chemistry* 94, pp. 8897 –8909 (cit. on pp. 76, 77, 79, 107, 108, 218).

Mechel, F. P. and I. L. Ver (1992). "Sound absorbing materials and sound absorbers". In: *Chapter 8 of Noise and Vibration Control Engineering: Principles and Applications*. Ed. by Beranek, L. L. and Ver, I. L. John Wiley & Sons, Inc. (cit. on pp. 5, 17).

Meller, J. (2001). *Molecular Dynamics, Encyclopedia of life sciences*. Nature Publishing Group, pp. 1–8. URL: `www.els.net` (cit. on pp. 31, 243, 245).

Mohan, R. and Y. Liang (2008). "Molecular dynamics simulations of flexural deformation of nickel nanowires". In: *8th IEEE Conference on Nanotechnology (NANO '08)*, pp. 366 –369 (cit. on pp. 24, 36).

Morse, P. M. and K. U. Ingard (1968). *Theoretical Acoustics*. McGraw-Hill, New York (cit. on pp. 143–145, 173).

Mutat, T. et al. (2012). "Single species transport and self diffusion in wide single-walled carbon nanotubes". In: *The Journal of Chemical Physics* 136, p. 234902 (cit. on pp. 92, 99).

Nakano, A. (2014). *Molecular Dynamics Basics*. Lecture Note- Methods of Computational Physics, University of South Carolina. URL: http://cacs.usc.edu/education/phys516/02MD.pdf (cit. on p. 83).

Natsuki, T. et al. (2004). "Effects of carbon nanotube structures on mechanical properties". In: *Applied Physics A: Materials Science & Processing* 79.1, pp. 117–124 (cit. on pp. 14–16).

Newell, P. R. (2003). *Recording Studio Design*. Focal Press, UK (cit. on p. 209).

Ni, C. et al. (2008). "Optical determination of the flexural rigidity of carbon nanotube ensembles". In: *Applied Physics Letters* 92.173106, pp. 1–3 (cit. on p. 69).

Nick, A. et al. (2002). "Improved acoustic behavior of interior parts of renewable resources in the automotive industry". In: *Journal of Polymers and the Environment* 10.3, pp. 115–118 (cit. on p. 2).

Niu, X. D. et al. (2004). "A lattice Boltzmann BGK model for simulation of micro flows". In: *Europhysics Letters* 67.4, pp. 600–606 (cit. on pp. 5, 26).

Niu, X.-D. et al. (2007). "Kinetic lattice Boltzmann method for microscale gas flows: Issues on boundary condition, relaxation time, and regularization". In: *Physical Review E* 76.036711, pp. 1 –8 (cit. on p. 26).

Nor, M. J. M. et al. (2010). "Effect of different factors on the acoustic absorption of coir fiber". In: *Journal of Applied Sciences* 10.22, pp. 2887 –2892 (cit. on p. 4).

Oldfield, R. and F. Bechwati (2008). "Accurate low frequency impedance tube measurements". In: *Proceedings of the Institute of Acoustics*. Vol. 30. 4. Institute of Acoustics, pp. 1–11 (cit. on p. 43).

Olofsson, N. et al. (2009). "Determination of the effective Young's modulus of vertically aligned carbon nanotube arrays: a simple nanotube-based varactor". In: *Nanotechnology* 20.38, 385710 (6pp) (cit. on p. 69).

Oran, E. et al. (1998). "Direct Simulation Monte Carlo: Recent advances and applications". In: *Annual Review of Fluid Mechanics* 30.1, pp. 403–441 (cit. on pp. 24, 27, 28, 243, 244).

Osman, M. A. and D. Srivastava (2005). "Molecular dynamics simulation of heat pulse propagation in single-wall carbon nanotubes". In: *Physical Review B* 72.125413, pp. 1 –7 (cit. on pp. 97, 98, 100).

Pearlman, D. et al. (1995). "AMBER, a package of computer programs for applying molecular mechanics, normal mode analysis, molecular dynamics and free energy calculations to simulate the structural and energetic properties of molecules." In: *Computer Physics Communications* 91, pp. 1 –41 (cit. on p. 79).

Peng, H. et al. (2005). "Synthesis of bundle-like structure of titania nanotubes". In: *Materials Letters* 59.10, pp. 1142–1145 (cit. on p. 2).

Pierce, A. D. (1989). *Acoustics: An introduction to its physical principles and applications*. Acoustical Society of America, New York (cit. on pp. 145, 146, 176).

Pilon, D. et al. (2004). "Behavioral criterion quantifying the effects of circumferential air gaps on porous materials in the standing wave tube". In: *The Journal of the Acoustical Society of America* 116.1, pp. 344–356 (cit. on pp. 63–65).

Piquemal, J. P. et al. (2006). "Towards accurate solvation dynamics of divalent cations in water using the polarizable Amoeba force field: from energetics to structure". In: *Journal of Computational Chemistry* 125, p. 054511 (cit. on p. 79).

Plimpton, S. J. et al. (1997). "Particle-Mesh Ewald and rRESPA for Parallel Molecular Dynamics Simulations". In: *The Eighth SIAM Conference on Parallel Processing for Scientific Computing*. Minneapolis, MN (cit. on p. 84).

Plimpton, S. (1995). "Fast parallel algorithms for short-range molecular dynamics". In: *J. Comput. Phys.* 117.1, pp. 1 –19. ISSN: 0021-9991 (cit. on p. 91).

Ponder, J. W. and D. A. Case (2003). "Force fields for protein simulations". In: *Advances in Protein Chemistry* 66, pp. 27 –85 (cit. on p. 79).

Prasanth, P. and J. K. Kakkassery (2006). "Direct Simulation Monte Carlo (DSMC): A numerical method for transition-regime flows - A review". In: *Journal of the Indian Institute of Science* 86, pp. 169–192 (cit. on pp. 8, 27, 244–246).

Press, W. H. et al. (1992). *Numerical Recipes in C*. Second edition. Cambridge University Press, Cambridge (cit. on p. 122).

Qian, Y. J. et al. (2014). "Improvement of sound absorption characteristics under low frequency for micro-perforated panel absorbers using super-aligned carbon nanotube arrays". In: *Applied Acoustics* 82, pp. 23 –27 (cit. on pp. 39, 40, 55).

Robinson, R. (2008). *Micro-Honeycomb Material Wears Out Engine Noise*. Georgia Tech Research Institue- Case study. URL: `http://gtri.gatech.edu/casestudy/reducing-noise-micr-honeycomb` (cit. on p. 2).

Rühle, V. (2007). *Berendsen and Nose-Hoover thermostats*. URL: `http://www2.mpip-mainz.mpg.de/~andrienk/journal_club/thermostats.pdf` (cit. on pp. 85, 86).

Ruoff, R. S. et al. (2003). "Mechanical properties of carbon nanotubes: theoretical predictions and experimental measurements". In: *Comptes Rendus Physique* 4.9, pp. 993–1008 (cit. on pp. 14–17).

Saito, Y. et al. (1993). "Interlayer spacings in carbon nanotubes". In: *Physics Review B* 49.3, pp. 1907 –1909 (cit. on p. 16).

Sakurai, S. et al. (2013). "A fundamental limitation of small diameter single-walled carbon nanotube synthesis - A scaling rule of the carbon nanotube yield with catalyst volume". In: *Materials* 6, pp. 2633 –2641 (cit. on p. 55).

Salomons, E. and M. Mareschal (1992). "Usefulness of the Burnett description of strong shock waves". In: *Physics Review Letters* 69.2, pp. 269 –272 (cit. on p. 101).

Satoh, T. et al. (2014). "An impedance tube measurement technique for controlling elastic behavior of test samples". In: *Inter-noise 2014*. Melbourne, Australia (cit. on pp. 65, 66).

Schneider, T. and E. Stoll (1978). "Molecular-dynamics study of a three-dimensional one-component model for distortive phase transitions". In: *Physical Review B* 17, pp. 1302 –1322 (cit. on p. 87).

Seetharamappa, J. et al. (2006). "Carbon nanotubes: Next generation of electronic materials". In: *The Electrochemical Society Interface* 15.2, pp. 23 –25 (cit. on pp. 3, 14, 16, 56).

Seybert, A. F. (1988). "Two-sensor methods for the measurement of sound intensity and acoustic properties in ducts". In: *The Journal of the Acoustical Society of America* 83.6, pp. 2233–2239 (cit. on pp. 250, 251).

— (2002). *Sound absoprtion by porous materials*. Lecture sildes ME 599/699, Department of Mechanical Engineering, University of Kentucky (cit. on p. 199).

Seybert, A. F. and B. Soenarko (1981). "Error analysis of spectral estimates with application to the measurement of acoustic parameters using random sound field in ducts". In: *Journal of the Acoustical Society of America* 69.4, pp. 1190 –1199 (cit. on pp. 256, 258).

Sgard, F. C. et al. (2005). "On the use of perforations to improve the sound absorption of porous materials". In: *Applied Acoustics* 66, pp. 625–651 (cit. on pp. 65, 66).

Shaw, D. E. et al. (2010). "Atomic-level characterization of the structural dynamics of proteins". In: *Science* 330, pp. 341 –346 (cit. on p. 102).

Shell, M. S. (2012). *Advanced molecular dynamics techniques*. URL: `http://www.engr.ucsb.edu/~shell/che210d/Advanced_molecular_dynamics.pdf` (cit. on p. 88).

Shenai, P. M. et al. (2012). "Principal Component Analysis - Engineering Applications". In: ed. by Sanguansat, D. P. InTech. Chap. 2: Applications of Principal Component Analysis (PCA) in Materials Science (cit. on p. 111).

Shenogin, S. et al. (2004). "Role of thermal boundary resistance on the heat flow in carbon-nanotube composites". In: *Journal of Applied Physics* 95, pp. 8136–8144 (cit. on pp. 117, 118).

Shiomi, J. and S. Maruyama (2006). "Non-Fourier heat conduction in a single-walled carbon nanotube: Classical molecular dynamics simulations". In: *Physical Review B* 73, 205420–(1–7) (cit. on p. 106).

Sirovich, L. and J. K. Thurber (1965). "Propagation of forced sound waves in rarefied gas dynamics". In: *The Journal of the Acoustical Society of America* 37, p. 329 (cit. on p. 126).

Sokhan, V. P. et al. (2002). "Fluid flow in nanopores: Accurate boundary conditions for carbon nanotubes". In: *Journal of Chemical Physics* 117.18 (cit. on pp. 93, 98, 100, 103, 105, 106).

— (2004). "Transport properties of nitrogen in single walled carbon nanotubes". In: *Journal of Chemical Physics* 120.8, pp. 3855 –3863 (cit. on pp. 92, 100).

Stansell, P. and C. A. Greated (1997). "Lattice Gas Automaton Simulation of. Acoustic Streaming in a Two-Dimensional Pipe". In: *Physics of Fluids* 9.11, pp. 3288–3299 (cit. on p. 245).

Stone, J. (2012). *Using VMD- A Tutorial*. University of Illinois at Urbana-Champaign. Theoretical, Computational Biophysics Group, Beckman Institute for Advanced Science, and Technology. URL: `http://www.ks.uiuc.edu/Training/Tutorials/` (cit. on p. 91).

Stote, R. et al. (1999). *Theory of Molecular Dynamics Simulations*. URL: `http://www.ch.embnet.org/MD_tutorial/pages/MD.Part1.html` (cit. on pp. 81, 83, 88, 89).

Strodel, B. (2014). *Simulation of biomolecules - Molecular dynamics*. Lecture Notes. Last viewed: 3 October 2014. URL: `http://www.grssim.de/cms/` (cit. on p. 245).

Stuart, S. J. et al. (2000). "A reactive potential for hydrocarbons with intermolecular interactions". In: *The Journal of Chemical Physics* 112.14, pp. 6472–6486 (cit. on p. 108).

Succi, S. (2001). *The lattice Boltzmann equation for fluid dynamics and beyond*. Numerical Mathmatics and Scientific Computation, Clarendon Press, Oxford (cit. on pp. 24, 245).

Suga, K. et al. (2010). "Lattice Boltzmann Flow Simulation in a Combined Nanochannel". In: *Advances in Applied Mathematics and Mechanics (Adv. Appl. Math. Mech.)* 2.5, pp. 609–625 (cit. on pp. 26, 27).

Sun, C. et al. (2014). "Mechanisms of molecular permeation through nanoporous graphene membranes". In: *Langmuir* 30.2, pp. 675 –682 (cit. on p. 106).

Sun, F. et al. (1993). "Sound absorption in an anisotropic periodically layered fluid-saturated porous medium". In: *Applied Acoustics* 39.1-2, pp. 65 –76 (cit. on p. 4).

Swift, G. W. (2002). *Thermoacoustics: A unifying perspective for some engines and refrigerators*. Acoustical Society of America, New York (cit. on pp. 33, 139–142, 173, 187).

Swift, M. J. et al. (2000). "On the effect of the bending vibration on the acoustic properties of thin poroelastic plates". In: *The Journal of the Acoustical Society of America* 107.3, pp. 1786–1789 (cit. on p. 70).

Tang, G.-H. et al. (2008). "Lattice Boltzmann models for nonequilibrium gas flows". In: *Physical Review E* 77.046701, pp. 1 –6 (cit. on p. 26).

Thomas, J. A. et al. (2010). "Thermal conductivity and phonon transport in empty and waterfilled carbon nanotubes". In: *Physical Review B* 81.045413, pp. 1 –7 (cit. on pp. 97, 100).

Toon, J. (2004). *New Class of Fibres: Composites Made with Carbon Nanotubes Offer Improved Mechanical and Electrical Properties*. Georgia Tech research news. URL: <http://gtresearchnews.gatech.edu/newsrelease/nanofibers.htm> (cit. on p. 3).

Tuckerman, M. et al. (1992). "Reversible mulitple time scale molecular dynamics". In: *The Journal of Chemical Physics* 97.3, pp. 1990–2001 (cit. on p. 218).

Tuckerman, M. E. (2010). *Statistical Mechanics: Theory and Molecular Simulation*. Oxford Graduate Texts (cit. on pp. 86, 87).

Tuzun, R. E. et al. (1996). "Dynamics of fluid flow inside carbon nanotubes". In: *Nanotechnology* 7, pp. 241 –246 (cit. on pp. 92, 93, 99).

Valentini, P. and T. E. Schwartzentruber (2009). "Large-scale molecular dynamics simulations of normal shock waves in dilute argon". In: *Physics of Fluids* 21.066101, pp. 1 –9 (cit. on pp. 95, 101, 102).

Valentini, P. et al. (2013). "Molecular dynamics simulations of shock waves in mixtures of noble gas". In: *Journal of Thermophysics and Heat Transfer* 27.2, pp. 226 –234 (cit. on pp. 95, 101).

Van Der Spoel, D. et al. (2005). "GROMACS: fast, flexible, and free". In: *Journal of Computational Chemistry* 26.16, pp. 1071 –18 (cit. on p. 79).

Verdejo, R. et al. (2009). "Enhanced acoustic damping in flexible polyurethane foams filled with carbon nanotubes". In: *Composites Science and Technology* 69.10, pp. 1564 –1569. ISSN: 0266-3538 (cit. on pp. 39, 40).

Viggen, E. M. (2009). "The Lattice Boltzmann Method with Applications in Acoustics". MA thesis. Norway: Department of Physics, NTNU (cit. on p. 25).

VMD-Guide (2012). *VMD User's Guide*. Version 1.9.1. NIH Resource for Macromolecular Modeling and Bioinformatics, Theoretical, Computational Biophysics Group, Beckman Institute for Advanced Science, and

Technology, University of Illinois at Urbana-Champaign. URL: http://www.ks.uiuc.edu/Research/vmd/ (cit. on p. 91).

Voter, A. F. et al. (2002). "Extending the time scale in atomistic simulation of materials". In: *Annual Review of Materials Research* 32, pp. 321 –346 (cit. on p. 30).

Wahnström, G. (2013). *Molecular Dynamics*. Lecture Notes (cit. on pp. 76, 84, 88–90).

Wang, R. J. and K. Xu (2012). "The study of sound wave propagation in rarefied gases using unified gas-kinetic scheme". In: *Acta Mechanica Sinica* 28.4, pp. 1022–1029 (cit. on pp. 121, 123).

Wayman, J. L. (1984). *New methods of measuring normal acoustic impedance*. Tech. rep. Naval Postgraduate School, Monterey, California (cit. on p. 247).

Weeks, J. D. et al. (1971). "Role of repulsive forces in determining the equilibrium structure of simple liquids". In: *Journal of Chemical Physics* 54.12, pp. 5237–5247 (cit. on pp. 77, 121).

Werder, T. U. (2005). "Multiscale simulations of carbon nanotubes in aqueous environments". PhD thesis. Switzerland: Doctor of Technical Sciences, Swiss Federal Institute of Technology Zurich (ETH) (cit. on p. 31).

WHO (2010). *Deafness and hearing impairment - Fact sheet*. WHO, Media release. URL: <http://www.who.int/mediacentre/factsheets/fs300/en/> (cit. on p. 5).

WHO-Europe (2011). *Environment and Health Noise: Facts and Figures*. World Health Organisation (WHO), Europe. URL: http://www.euro.who.int/en/what-we-do/health-topics/environment-and-health/noise/facts-and-figure (cit. on p. 5).

Xiang, H. F et al. (2013). "Investigation of sound absorption properties of Kapok fibres". In: *Chinese Journal of Polymer Science* 31.3, pp. 521 –529 (cit. on p. 59).

Yang, Y. et al. (1999). "Patterned growth of well-aligned carbon nanotubes: A photolithographic approach". In: *Journal of the American Chemical Society* 121.46, pp. 10832–10833 (cit. on p. 3).

Yano, T. (2012). "Molecular dynamics study of sound propagation in a gas". In: *AIP Conference Proceedings*. Vol. 1474, pp. 75–78 (cit. on pp. 94, 100, 101, 128, 129).

Yuan, C. (2010). "A molecular dynamics study of the spreading of nanodroplets". Scientific Computing International Master Program. Stockholm, Sweden: KTH Computer Science and Communication (cit. on p. 87).

Zhang, J. (2011). "Lattice Boltzmann method for microfluidics: models and applications". In: *Microfluidics and Nanofluidics* 10.1, pp. 1–28 (cit. on p. 5).

Zhang, R. et al. (2013). “Growth of half-meter long carbon nanotubes based on Schulz-Flory distribution”. In: *ACS Nano* 7.7, pp. 6156–61 (cit. on p. 53).

Zhang, X. et al. (2012). “A low-frequency wave motion mechanism enables efficient energy transport in carbon nanotubes at high heat fluxes”. In: *Nano Letters* 12, pp. 3410–3416 (cit. on p. 118).

Zhou, O. et al. (1994). “Defects in carbon nanostructures”. In: *Science* 263.5154, pp. 1744 –1747 (cit. on p. 16).

Zou, Q. and A. E. Hay (2003). “The vertical structure of the wave bottom boundary layer over a sloping bed: theory and field measurements”. In: *Journal of Physical Oceanography* 33, pp. 1380–1400 (cit. on p. 258).

Appendices

A Comparison of LBM, DSMC and MD

Table A.1: Comparison on the advantages, disadvantages, limitations, and applicability range of LBM, DSMC and MD reported in the literature.

Simulation Method	**LBM**	**DSMC**	**MD**
Collision Grid:	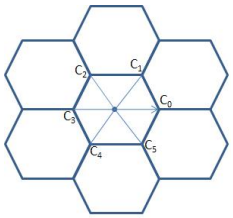 The collision grid for LBM (Czerwinska 2009)	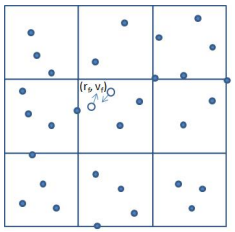 The collision space for DSMC (Czerwinska 2009)	No collision grid is specified for MD
Approach:	• Lattice gas based model. • Particles interact and move on the fixed lattice (Czerwinska 2009). • Kinetic Gas theory equations satisfied (Czerwinska 2009).	• Purely stochastic (DSMC) object oriented model. • Translation of particle position (Czerwinska 2009). • Calculation of collision rate; select collision pairs; adjust trajectories in the imposed mesh (Czerwinska 2009).	• Purely deterministic (MD) for collision modelling. • Particle moves according to the Newton's equation of motion. • Initialisation of the particle positions and velocities; calculate interaction forces; integrate the equations of motion; generate trajectories at each time step (Karniadakis et al. 2005).

Advantages:

- Simple collusion rules for the conservation of mass and momentum (Hanford 2008).
- Simplification and discretisation of physical and velocity space (Hanford 2008).
- Simple implementation of boundary condition and uniform grid (Aaltosalmi 2005).
- Specific way of handling large computational meshes regardless of the complexity of the geometry of the structure (Bernsdorf 2008).
- Computations can be performed on smaller grids with fewer iterations and the final values can be directly obtained without any time and space averaging process (Bernsdorf 2008).
- Very high performance and nearly ideal scalability on high performance vector-parallel computers (Bernsdorf 2008).
- Very efficient handling of equidistant Cartesian meshes generated by the semi-automatic discretisation of complex geometries (Bernsdorf 2008).
- Bypass continuum limitations (Hanford 2008).
- Applicable for whole range of Knudsen Number (Hanford 2008).
- Minimised numerical complexity (Hanford 2008).
- Computational flexibility for all Kn in a wide range of systems (Hanford 2008).
- Not plagued by the boundary condition problems of kinetic theory predictions (Hanford 2008).
- Sound propagation properties such as nonlinear phenomena and absorption are inherent in the algorithm, which make DSMC more applicable for sound wave propagation (Hanford 2008).
- Unlike LBM, conservation laws are required to apply for individual molecules for molecule-surface interactions instead of using velocity distribution functions, which allows DSMC to be extended to include physical effects without major modifications in the basic procedure (Oran et al. 1998).
- Suitable for the simulation of complex physics in gas, liquid and solid states.
- Provides better accuracy than DSMC.
- Efficient for the simulation of coupled fluid-solid interactions, structural vibrations, and bi-directional heat transfer.
- Generalisations of MD can be used to sample statistical ensembles such as cannonical ensemble (Meller 2001).

Table A.1: Comparison on the advantages, disadvantages, limitations, and applicability range of LBM, DSMC and MD reported in the literature.

Simulation Method	LBM	DSMC	MD
Disadvantages:	• Solution of Boltzmann equation is improbable in the case of non-trivial gases or multidimensional flows, even using standard numerical methods (Hanford 2008). • Standard numerical method solutions only exist for simplified geometries or approximations to the Boltzmann collision integral (Hanford 2008). • Given information of boundary conditions has to be translated from macroscopic variable to distribution function (Aaltosalmi 2005).	• Time consuming computation. To minimise the computation costs, simulated domain length has to keep in the range of a few wavelengths (Hanford 2008). • For much lower values of Knudsen number, DSMC extremely expensive to use (Oran et al. 1998). • A priori knowledge of the accommodation coefficients is required (Karniadakis et al. 2005). • Produces unsteady flow simulation; hence, an ensemble of many computations is usually assembled and averaged to obtain acceptable statistical accuracy, which results in large computational time marching process (Prasanth and Kakkassery 2006).	• Requires extensive computational resources leading to high computational cost. • For much lower values of Knudsen number, MD is more expensive than DSMC. • Simulation is needed to run for a longer time to obtain meaningful results.

Limitations:

- Inability to simulate heat transfer effect on transport properties (Hanford 2008).
- Strong compressibility and substantial heat transfer cannot be simulated (Succi 2001; Aaltosalmi 2005; Bernsdorf 2008).
- Particle motion restricted to a lattice grid (Hanford 2008).
- Difficulty in simulating flows at high Reynolds number (Aaltosalmi 2005).
- Only applicable in the low Mach number limit to flows where there is a density variation which is much smaller compared to the mean density (Stansell and Greated 1997; Buick et al. 1998).
- The cell size must be proportional to the local mean free path (Prasanth and Kakkassery 2006).
- The number of particles per cell must be roughly constant in order to preserve collision statistics (Prasanth and Kakkassery 2006).
- Simulation time-step must be chosen so that particles only transverse a fraction of the average cell length per time-step (Prasanth and Kakkassery 2006).
- Limited to binary collisions (Danforth and Long 2004b).
- Extension of the model for multidimensional flows may create a memory intensive program, which could result in large computational time (Hanford 2008).
- The results of a MD simulation can only be as good as the underlying force field (Strodel 2014).
- Classical MD is unsuitable for low temperatures where quantum effects are more pronounced (Strodel 2014).
- The quality of sampling and the accuracy of the interatomic potentials used in simulations are always limited (Meller 2001).
- The presence of significant fast atomic motions limits the time step in numerical integration to about one femtosecond (Meller 2001).
- The desired length of simulations also places limits on increasing the size of the problem (Meller 2001).

Table A.1: Comparison on the advantages, disadvantages, limitations, and applicability range of LBM, DSMC and MD reported in the literature.

Simulation Method	LBM	DSMC	MD
Potential Sources of Error:	• Error mainly occurs due to the finite-size effects, compressibility effect and boundary effects (Aaltosalmi 2005). • Error due to finite-size effect caused by the limited number of grid points in the calculation lattice (Aaltosalmi 2005). • Compressibility errors can occur for the simulation in the case of both incompressible fluid and/or strongly compressible fluid. They are caused by the dependence of pressure on density and varying nature of the density in LBM assumptions (Aaltosalmi 2005).	• Statistical error corresponding to the stochastic nature of the method, which is induced by the use of a simulated molecule to represent a large number of actual molecules (Endo et al. 2008; Prasanth and Kakkassery 2006). • Deterministic error depends on the selection of numerical parameters such as the time-step, cell volume, and the total number of cell particles (Endo et al. 2008; Prasanth and Kakkassery 2006).	• Statistical error arises from the use of finite time length for the simulation. • Deterministic error depends on the system size, selection of the sampling rate and sampling bin size.

B Verification Procedure for the Experimental Results

B.1 Repeatability Tests

The repeatability and accuracy of the experimental measurements were checked by conducting repeated tests and varying parameters such as the amplitude and phase compensation of the microphones (Wayman 1984); tests were also repeated with the samples moved in and out of the apparatus a number of times. The results exhibited similar absorption trends over the measured operating frequency range for the variation of different parameters. For instance, Figure B.1a shows the repeatability of test results for the same CNT forest sample. These results were obtained by repeating the same test four times, each time calibrating the microphone pairs, taking the sample in and out, and rotating the sample to different surface positions each at approximately 90 ° to the previous one. As illustrated in Figure B.1a, the test results indicate that the mean variation of the results is within 1% for measurement frequencies above 125 Hz. It also confirms that the results are repeatable, even though the measured acoustic absorption coefficient is very small. The discrepancy and variation in the absorption curve at certain frequencies are due to irregularities in the tests and slight variations in the mounting conditions of the sample (Chung and Blaser 1980b), as low absorption (high reflection coefficient) materials are very sensitive to the consistency in the mounting conditions (Katz 2000; Bodén and Åbom 1986). In addition, difficulty in maintaining a uniform wall contact with the rigid termination in the case of single layer samples did not help to create consistent mounting conditions of the sample inside the impedance tube. The sample mounting configuration as shown in Figure 3.4b is a somewhat manual setup with a flange-like system for the tube-end termination assembled using a number of nuts and bolts. Hence it is difficult to maintain consistency among repeated tests for the mounting conditions and perfect positioning of the

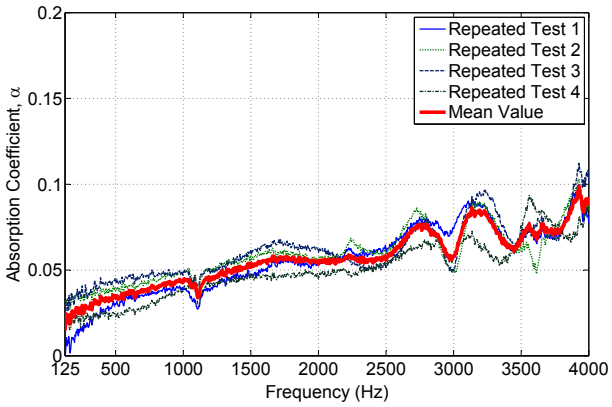

(a) Absorption of CNT for repeated test data

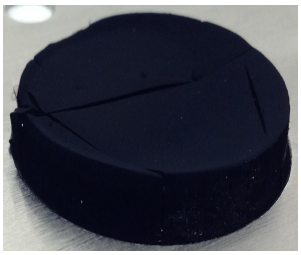

(b) Zoomed CNT sample surface

Figure B.1: Comparison of absorption coefficients of a CNT forest for four repeated tests with the same sample.

annular plates aligned with the tube. This type of setup was required to accommodate the method by which the CNT sample was prepared. Hence a simpler and more convenient method for mounting sample configurations and the CNT sample arrangement will be the subject of work for future test samples.

B.2 Reproducibility Tests

A reproducibility test was performed using a separate 3 mm CNT sample in an impedance tube of diameter 25.4 mm. This test result offers systematic experimental data on the reproducibility of the impedance tube measurements on a similar material with different circular size[1], which would also provide a general idea of the variance in the measured absorption coefficient data obtained for two different samples (in regard to the circular dimension) of approximately equal thicknesses. Figure B.2 shows the absorption coefficient results for repeated tests of a 3 mm CNT forest of 25.4 mm circular diameter. The tests were conducted following the procedure described earlier in Section B.1. As shown in Figure B.2 the test results exhibit a consistent absorption trend among the repeated tests for the 3 mm CNT forest and show a 5-10% absorption. Similar to the previous test results presented in Figure B.1a, the

[1]Previous acoustic absorption results of 3 mm CNT forest, presented in Section 3.4, were for a sample of diameter 22.1 mm and the tests were conducted in an impedance tube of diameter 22.1 mm.

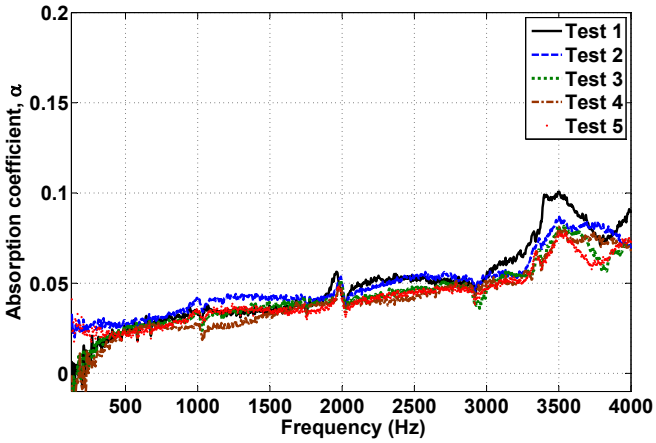

Figure B.2: Comparison of absorption coefficients of a 3 mm long CNT forest of circular diameter 25.4 mm for five repeated tests with the same sample.

variation in the results of the 3 mm CNT forest of 25.4 mm circular diameter is attributable to inconsistencies in the mounting conditions.

An additional comparison of the test results obtained from the two impedance tubes (of diameters 25.4 mm and 22.1 mm) is presented in Figure B.3. It can be seen that both results show a similar trend in terms of the absorption coefficient. The variance in the absorption results for the two different tests are due to the non-uniformities of the materials.

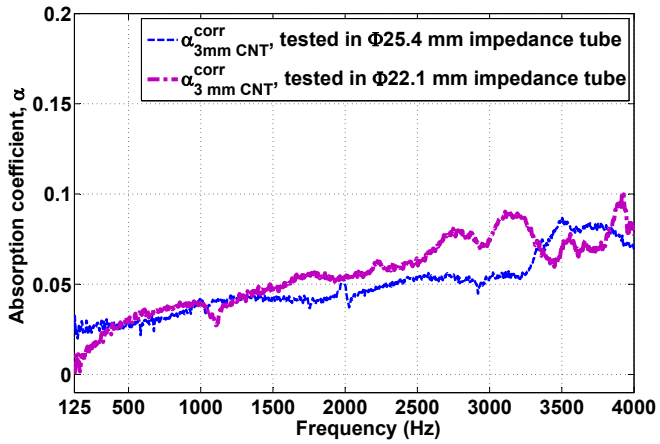

Figure B.3: Comparison of absorption coefficients of 3 mm long CNT forest samples of circular diameters 25.4 mm and 22.1 mm with a similar sample arrangement.

The dips in the absorption curve shown in Figure B.2 at frequencies around 1100 Hz, 2000 Hz, 2900 Hz, and 3400 Hz are due to the tube resonance, which occurs at frequencies corresponding to $kL = m\frac{\pi}{2}$, $m = 1, 3, 5, \cdots$. They can also be observed in the absorption curve of the blank impedance tube of diameter 25.4 mm, as displayed in Figure B.4. The extent of the ill-conditioning in the measured results due to the tube resonance can be explained using the wave spectra in the tube. The wave spectra can be evaluated using the decomposition theory of Seybert (1988). Any small measurement errors occurring in the neighbourhood of the tube resonance frequencies will cause large errors in the decomposition and hence in the evaluation of acoustic properties using this theory (Seybert 1988). Figure B.5 shows the estimates of the decomposed incident and reflected wave spectra, S_{AA} and S_{BB}, respectively, in the tube for the rigid termination. It can be seen that the spectra of the waves are strongly influenced by the resonances of the tube at the corresponding frequencies where the dips appear in the absorption curve shown in Figure B.2 (Seybert 1988). The effect of this ill-conditioning is extended on either side of the frequency region near the resonance peaks in the measured reflection coefficient of the rigid termination, as shown in Figure B.6, which was evaluated using the decomposed wave spectra.

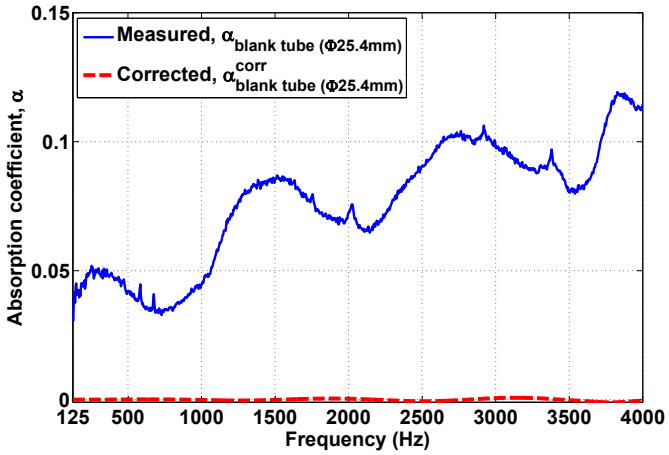

Figure B.4: Absorption coefficient of an empty impedance tube of diameter 25.4 mm with rigid termination. Corrected absorption coefficient (α^{corr}) in the figure indicates the result were obtained with the implementation of the correction for tube attenuation.

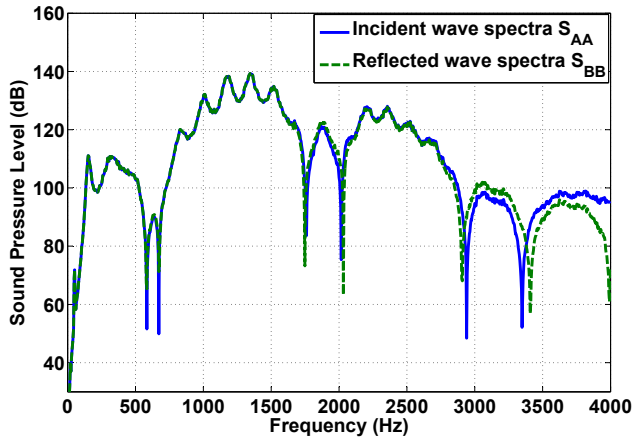

Figure B.5: Decomposed wave spectra of the two microphones in the tube, showing the effect of tube resonances.

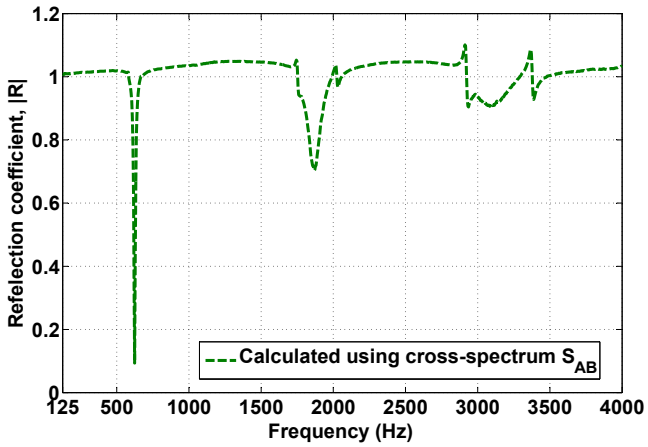

Figure B.6: Measured reflection coefficient in the tube for the rigid termination using the decomposition theory of Seybert (1988).

B.3 Error Analysis

For the accurate estimation of the optimum results over the measurement frequency range using the impedance tube method, several standard verification procedures were performed to eliminate the effect of errors associated with the following factors:

- sensor mismatch;
- waveguide damping;
- uncertainty in the separation distance between the microphones, and the distance of the furthest microphone from the termination; and
- bias and random errors.

These are explained in the following sections.

B.3.1 Sensor Mismatch

As discussed earlier in Section 3.3.2, the effect of phase and magnitude mismatch of the measured transfer function between two microphones was eliminated using the standard sensor-switching technique (Chung and Blaser 1980b; Katz 2000). Prior to each measurement session, a separate calibrated transfer function H_{cal} was calculated for each data set, which was used to calculate the corrected transfer function $H_{\text{corrected}}$ from the measured data. Figure B.7 displays the overlay of the magnitude and phase of the measured (H_{12}) and corrected ($H_{\text{corrected}}$) transfer function. It can be observed that the magnitude and phase mismatch of the transfer function at low frequencies below 500 Hz were eliminated in the corrected transfer function. However, the overall deviation between the magnitude and phase of the two transfer functions remained very small.

B.3.2 Waveguide Damping

The standards for the impedance tube method recommend correcting for tube attenuation when the distance from the specimen to the nearest microphone exceeds three tube diameters (Han et al. 2007; Hou and Bolton 2009). For all experiments conducted in this study, the nearest microphone was placed at a distance greater than 130 mm from the test specimen, which is approximately six tube diameters (22.10 mm) of the impedance tube. In addition, as determined by Chu (1986), the effect of tube attenuation can be significant for a material of high reflection coefficient (similar to the case

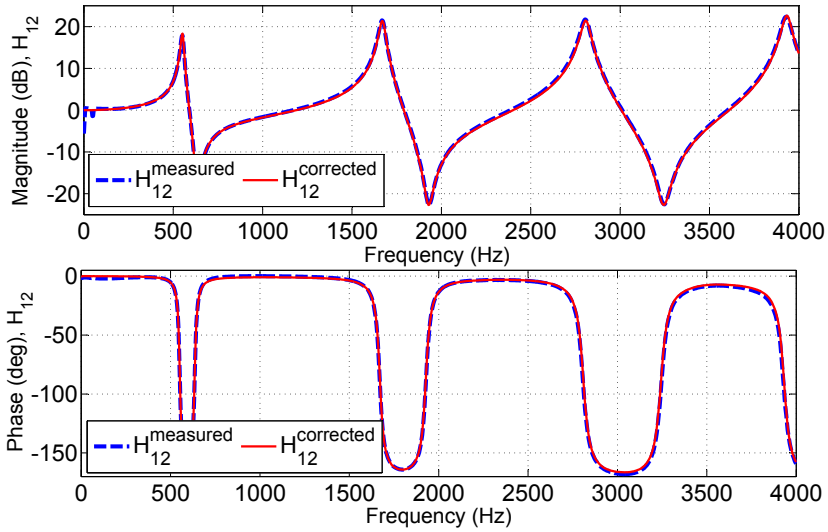

Figure B.7: Magnitude (top) and phase (bottom) of the transfer function measured between two microphones (dashed line) and the transfer function corrected using microphone switching technique (solid line).

studied here), even though the tube attenuation appears to be small (Equation (3.7)). For instance, as estimated by Chu (1986), 1% error in the measured reflection coefficient ($|R|$) can result in an error of 8.5% in the absorption coefficient (α) for $|R| = 0.9$. Therefore, the correction for tube attenuation was applied as described earlier in Section 3.3.2. The experimental estimates and the theoretical prediction using Equation (3.7) of the attenuation constant are presented in Figure B.8. It may be observed that the difference between these two estimates of the attenuation constant is small. The estimates of the attenuation constant indicates that the tube attenuation is very significant and that the effect is observed in the measured absorption coefficient of the impedance tube with a rigid termination. Figures 3.6 and 3.7 show the effect of the correction for tube attenuation in the estimation of acoustic absorption coefficient. It can be seen that the measured value of the absorption coefficient without the implementation of the correction for tube attenuation leads to an overestimate in the calculated absorption coefficient by a factor of two.

B.3.3 Microphone Separation Distance

The measurement accuracy of the microphone separation distance d was verified with the frequency null method presented in Katz (2000). The distance from the acoustic centre of the diaphragm of the microphone closest to the fixed termination can be determined from the frequency null of the transfer

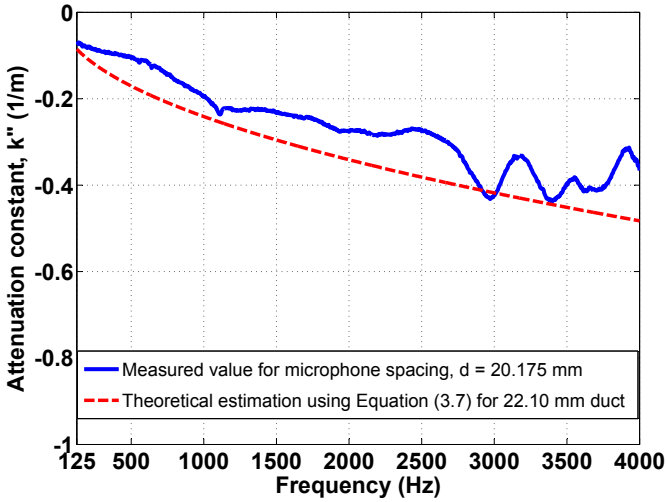

Figure B.8: Comparison of the theoretical and measured attenuation constant for a 22.10 mm diameter tube. The theoretical value is calculated from Equation (3.7) using the value of the constant $A = 0.0194$ (Han et al. 2007).

function measured between the measurement microphones (microphone 1 or microphone 2) and the microphone embedded in the rigid termination using the setup shown in Figure B.9a. A separate set of measurements was conducted to obtain the transfer function for the measurement microphone (microphone 1 or microphone 2) and the termination microphone, an example of which is shown in Figure B.9b. It can be observed that several frequency nulls existed over the selected measurement frequency range. A second-order polynomial fit was used to determine the null positions accurately from the termination transfer function. Resulting null positions of the frequency and the calculated distance of the microphones to the termination are given in Table B.1. The null at low frequencies below 1000 Hz is not considered for the calculation of the distance to avoid the influence of the error at low

Table B.1: Microphone distance to termination calculations for each null in measurement (Ch1: 3 nulls, Ch2: 2 nulls) using rigid termination with embedded microphone (Ch4).

Trial	**Ch1 (mm)**			**Ch2 (mm)**	
$\sim$ null frequency (Hz)	1660	2780	3887	1909	3195
T1	155.9	155.2	155.4	135.6	135.0
T2	156.0	155.2	155.3	135.5	135.2
Average		**155.50**		**135.25**	

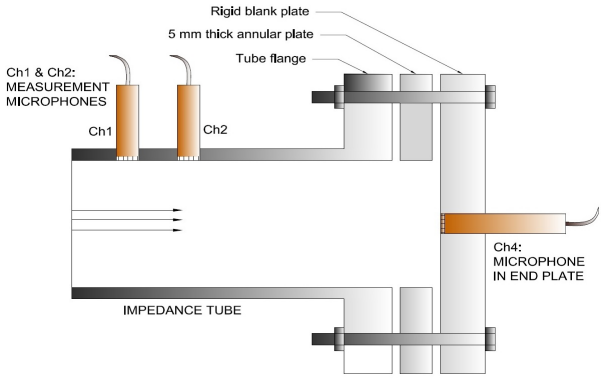

(a) Schematic of the setup of the microphone in the end plate.

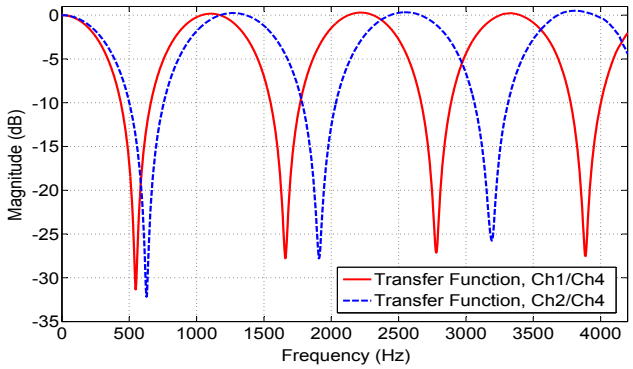

(b) Measured transfer function using sensor-switching technique

Figure B.9: Schematic of (a) the modified impedance tube setup with the additional termination microphone used to measure (b) the transfer function between the measurement microphones (Ch1: microphone 1, Ch2: microphone 2) and the embedded termination microphone (Ch4: microphone 4). Details of the setup and calculation procedure can be found in (Katz 2000).

frequencies from the sensor mismatch shown in Figure B.7, even though the sensor-switching technique was applied for this measurement. Taking an average of the distances determined from each null yielded the separation distance between two microphones as 20.18 mm, which was originally measured using the vernier scale as 20.43 mm. Hence, the resulting microphone separation distance of 20.18 mm was used in the estimation of the sound absorption coefficient for all measurements.

B.3.4 Bias and Random Error

In previous investigations (Seybert and Soenarko 1981; Bodén and Åbom 1986; Ghan et al. 2004) of systematic errors in measurements using impedance tubes, it was shown that the influence of bias and random errors in the estimates of the transfer function can be significant when the measurements are performed using the two-microphone method. Their effect on the calculated acoustic quantities can be important and they need to be taken into consideration and treated accordingly. Hence, considerations were given to minimise the bias error by employing a small frequency resolution of 4 Hz. Bodén and Åbom (1986) have discussed the influence of bias error caused by inadequate spectral resolution, even though several sources of bias errors are possible. Two types of bias error were demonstrated, which are dominated by variations associated with the auto-spectral density function. These two types of bias error can be evaluated as follows:

1. If the distance of the furthest microphone from the termination/surface of the sample is much smaller than the tube length L, i.e. $z_1 \ll L$, and the normalised acoustic impedance of the source z_i (= $Z_i/\rho c$) is not too close to unity, the normalised bias error (ε_b^T) in the transfer function estimate can be calculated as (Bodén and Åbom 1986)

$$\varepsilon_b^T = 2|\varepsilon_b^S|, \tag{B.1}$$

$$\varepsilon_b^S = \frac{\pi^2 L^2 \Delta f^2}{6c^2} H(z_i, z_s), \tag{B.2}$$

where

$$H(z_i, z_s) = \frac{2(|\beta|^2 - |\alpha|^2)\cos 2\varphi + 4\delta \sin 2\varphi}{|\alpha|^2 \sin^2 \varphi + |\beta|^2 \cos^2 \varphi + \delta \sin 2\varphi}, \tag{B.3}$$

$$\tan 2\varphi = \frac{2\delta}{|\beta|^2 - |\alpha|^2}, \tag{B.4}$$

and $\alpha = z_s + \frac{1}{z_i}$, $\beta = 1 + \frac{z_s}{z_i}$, $\delta = \mathrm{Im}[\alpha^* \beta]$, Δf is the frequency resolution, c is the sound speed and z_s (= $Z_s/\rho c$) is the normalised surface acoustic

impedance of the load at the termination, i.e. at a distance z_1 from the microphone 1. Here superscripts S and T represents the bias error in the spectral density and transfer function estimate, Im[] denotes the imaginary part and asterisk (*) denotes complex conjugation.

2. If the reflection coefficient or the acoustic impedance for the source is close to unity, i.e. $|R|$ or $\xi_i \approx 1$, then the normalised bias error (ε_b^T) in the transfer function estimate can be calculated as (Bodén and Åbom 1986)

$$\varepsilon_b^T = 2|\varepsilon_b^S|, \tag{B.5}$$

$$\varepsilon_b^S = \frac{4\pi^2 z_1^2 \Delta f^2 |R|^2}{3c^2(1-|R|^2)}. \tag{B.6}$$

Figure B.10 shows the estimated bias error of both types for a single test case of the CNT forest for the results presented in Figure 3.7. As shown in Figure B.10, the bias error of type 1 (given by Equation (B.1)) dominates the type 2 error (given by Equation (B.5)). It may be observed that the average error in the transfer function estimate is around or less than 1% for the magnitude and 0.6 ° for the phase over the frequency range $1-4$ kHz. However, the bias error of type 1 is slightly higher (about 3%) in the frequencies below 1 kHz, which might be due to the limited measurement response of the low cut-off frequency range set by the microphone separation distance d = 20.18 mm as indicated in Table 3.1.

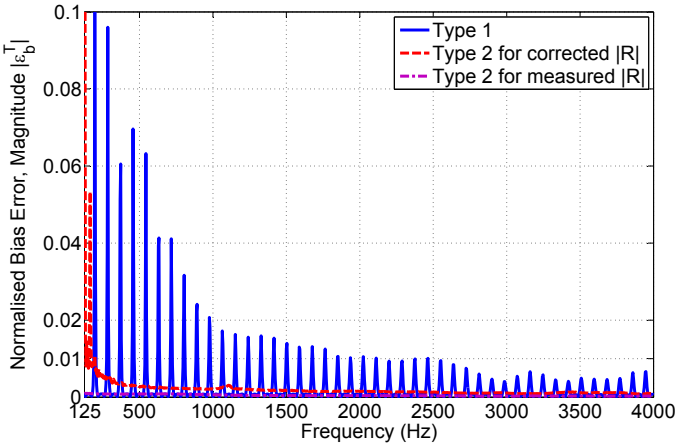

Figure B.10: Estimated normalised bias error in the transfer function measured between the two microphones. Bias error type 1 is given by Equation (B.1), and bias error type 2 is given by Equation (B.5).

The normalised random error (ε_r) of the measured transfer function is estimated as (Bendat and Piersol 1986)

$$\varepsilon_r = \frac{[1-\gamma^2(\omega)]^{\frac{1}{2}}}{|\gamma(\omega)|\sqrt{2n_d}}, \tag{B.7}$$

where n_d is the number of averages and $\gamma^2(\omega)$ is the corresponding estimated coherence between two signals. As the standard deviation of the phase (in radians) and normalised random error of the magnitude (in dB) of the measured transfer function is approximately equal (Zou and Hay 2003; Bendat and Piersol 1986), only the error for the magnitude was estimated as shown in Figure B.11. The normalised error presented in Figure B.11 is for a single test case of the CNT forest, but all other cases showed a similar trend. It can be seen that the random error in the measured transfer function is less than 1% in this case. This error results from the dips in the coherence function (low in magnitude) shown in Figure B.11a associated with the frequencies where either microphone position coincides with a node and the magnitude of the transfer function becomes zero or infinite with a 90 ° phase difference between the microphones (Seybert and Soenarko 1981).

As discussed in this section, the overall error in the entire measurement range can be divided into two ranges of frequencies: 125−1 kHz, and above 1 kHz. In the frequency range above 1 kHz, the total error is significantly lower than 1%. On the other hand, the overall error is slightly higher than 1% in the low frequency range below 1 kHz, which is induced mainly by limitations in the measurement response below the operating frequency range of the impedance tube. This is added to the phase difference between the microphones. The phase at low frequency is small, so any error in the phase leads to large errors.

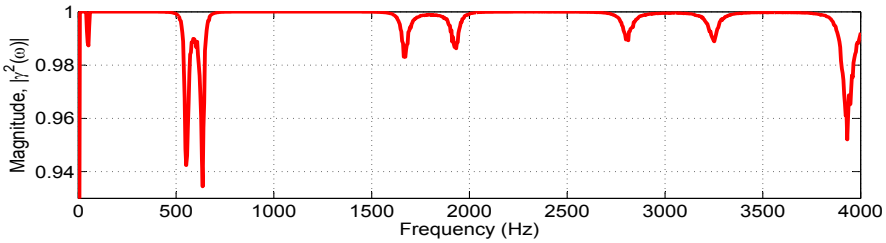

(a) Magnitude of the coherence function

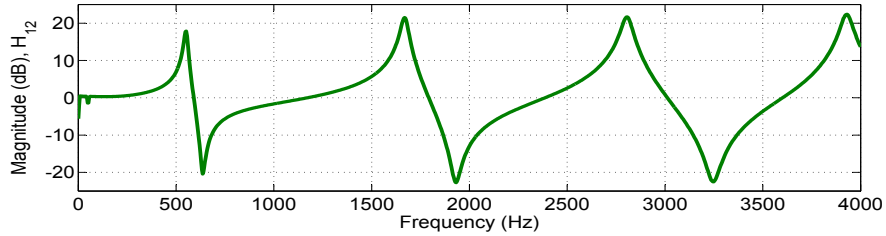

(b) Amplitude of the measured transfer function

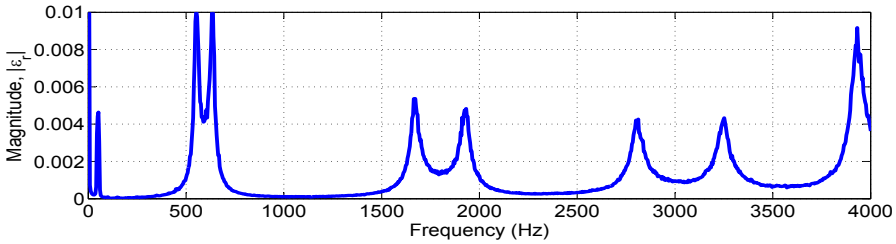

(c) Magnitude of the normalised random error

Figure B.11: Estimated normalised random error in the transfer function measured between the two microphones.

C Comparison with Conventional Materials

The significance of the acoustic absorption performance of CNT forests can be demonstrated by considering the absorption characteristics of conventional materials such as melamine foam and glass wool for an equivalent thickness or mass of the material. The analytical framework applied here was adapted from Kino and Ueno (2008) to predict the normal incidence acoustic absorption coefficient of a reference thickness of 25.5 mm melamine foam and 25 mm of glass wool using the relevant non-acoustical parameters. Thereafter, the model was used to predict the acoustic absorption coefficient of both materials by reducing the material thickness to 3 mm, equivalent to that of the CNT forest. Comparison of the absorption coefficient of the 3 mm CNT forest and conventional porous materials of equivalent thickness is displayed in Figure C.1, which shows that both conventional materials exhibit lower absorption than the CNT forest for an equivalent thickness. A similar comparison of the acoustic absorption coefficient of the CNT forest and porous materials is presented in Figure C.2 for an equivalent mass to the CNT sample (0.0499 g). It can be observed that 4.09 mm of glass wool of equivalent mass (0.0499 g) may provide similar absorption to a 3 mm CNT forest. On the other hand, 12.63 mm of melamine foam of equivalent mass may yield a maximum absorption of 50% over the measured frequency range, which is significantly higher than the CNT forest. As shown in Figure C.2, even though an equivalent mass of melamine foam may produce significantly higher sound absorption than that of a CNT forest, it is four times as thick as the CNT forest. These results highlight the significance of the absorption ability of CNTs and their potential for implementation in compact CNT acoustic absorbers.

High flow resistivity porous materials may exhibit a similar or even higher absorption than a CNT forest. For instance, the sound absorption coefficient of a 3.5 mm Refrasil sample (0.224 g and 166.8 kgm^{-3}) was measured and the

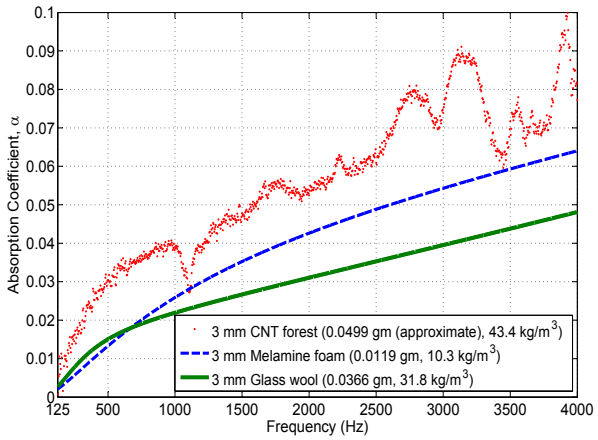

Figure C.1: Comparison of the experimentally measured acoustic absorption coefficient of the CNT forest with theoretical estimates for two conventional porous materials of equivalent thickness: melamine foam and glass wool. It should be noted that the mass of CNTs (without the substrate) presented here is an estimate from the sample configuration shown in Figure 3.3a, in which the CNTs were attached to the substrate. A more accurate estimate of the mass, which should be made separately after extracting the CNTs from the substrate, may differ from the approximate value. However, the difference is anticipated to not be significant.

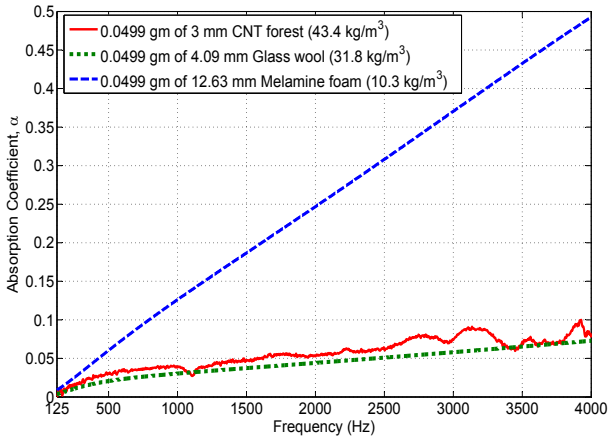

Figure C.2: Comparison of the experimentally measured acoustic absorption coefficient of the CNT forest with theoretical estimates for two conventional porous materials of equivalent mass: melamine foam and glass wool.

result is presented in Figure C.3. As shown in the figure, this conventional porous material with a high flow resistivity shows higher absorption (by almost a factor of two) than the CNT forest.

(a) Refrasil sample

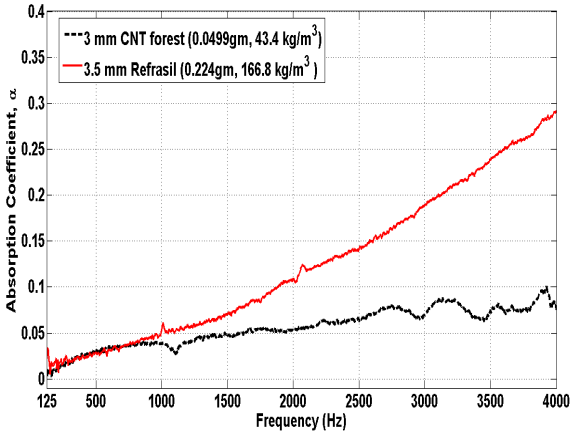

(b) Measured absorption coefficients of 3.5 mm Refrasil and the 3 mm CNT forest

Figure C.3: Comparison of the sound absorption coefficient of the CNT forest with a high absorption coefficient specimen, Refrasil (3.5 mm), measured using the impedance tube.

D Effects of CNT Length and Bulk Density

The effects of CNT length and bulk density of the CNT forest on the acoustic absorption performance of CNT absorbers were explored using the theoretical estimates of absorption coefficients based on the Biot-Allard model (Hosseini Fouladi et al. 2011; Allard 1993) and the flow resistivity model of Garai-Pompoli (Garai and Pompoli 2005). The acoustic absorption performance of a 3 mm CNT forest was compared with that of CNT forests of varying thickness in the range of $3 - 50$ mm and varying density in the range of $5 - 43.4\,\mathrm{kgm}^{-3}$ (which are in the range of densities of melamine foam and glass wool (Kino and Ueno 2008)) to determine the effects on the absorption of CNT absorbers. Figure D.1 shows the estimates of acoustic absorption coefficients for varying bulk density of the 3 mm CNT forest in the frequency range of $0 - 4.0$ kHz. It can be seen that absorption increases significantly as the bulk density of the CNT forest decreases. A 50 % reduction in the bulk density of the 3 mm CNT forest from its measured bulk density of $43.4\,\mathrm{kgm}^{-3}$ exhibits a 50 % increase in the absorption coefficient. Similarly, a 90 % reduction in the bulk density increases the absorption coefficient by as much as a factor of 4. This suggests that the absorption performance of CNT absorbers can be improved significantly with a lower CNT forest density and that the density may be optimised to tailor a CNT absorber with absorption capabilities suitable for commercial applications of noise control. The result also implies that the bulk density of the 3 mm CNT sample used for the experiments was excessively high, which created a congested internal structure of the CNT forest and reduced the effect of the torturous path that allows the sound travelling inside the absorber to be absorbed. Thus, most of the incident sound waves were reflected back from the CNT surface instead of being absorbed, resulting in the low absorption of the sample investigated in this study.

The acoustic absorption performance of the CNT forest with a bulk

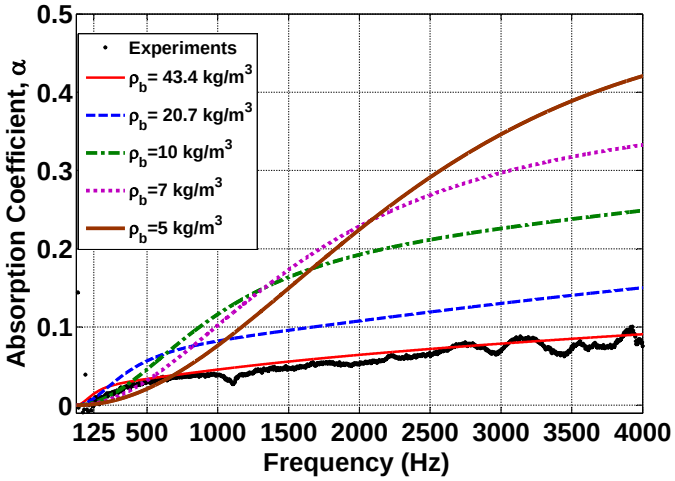

Figure D.1: Comparison of theoretical estimates of acoustic absorption coefficient of the 3 mm CNT forest with varying bulk density in the range of $5 - 43.4\,\mathrm{kgm}^{-3}$.

density of $43.4\,\mathrm{kgm}^{-3}$ was calculated for varying thickness of CNTs and the results are presented in Figure D.2. It can be observed that the length of the CNTs has a very small and subtle effect (at low frequency) on the absorption performance of the CNT forest, which is in contrast to conventional materials, for which the thickness is a dominating factor for enhancing the absorption. This can be attributed to the high bulk density of the sample, as mentioned earlier. Hence, the absorption performance of CNT forests with varying thickness were also estimated for a much lower bulk density of the sample. For instance, the acoustic absorption of a 3 mm CNT forest with a bulk density of $10\,\mathrm{kgm}^{-3}$ shown in Figure D.3 indicates that the absorption of the CNT forest increases at low frequency as the thickness increases from 3 to 50 mm. However, the effect of the thickness is not as significant as that of the bulk density.

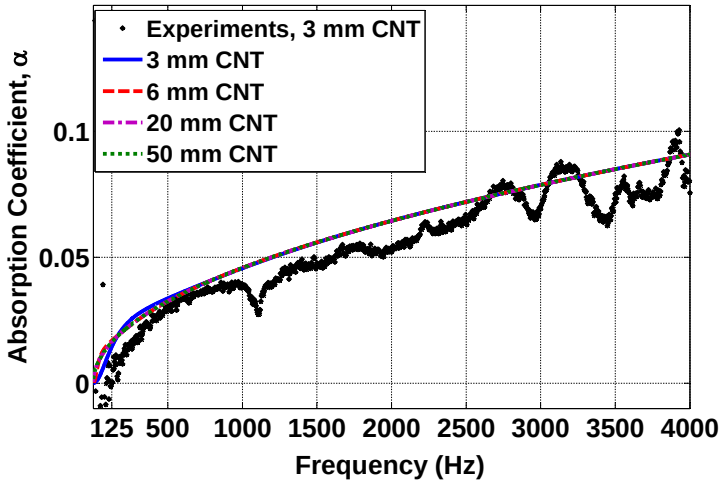

Figure D.2: Comparison of theoretical estimates of the acoustic absorption coefficient of a CNT forest with a bulk density of $43.4\,\mathrm{kgm}^{-3}$ for varying thickness in the range of $3 - 50\,\mathrm{mm}$.

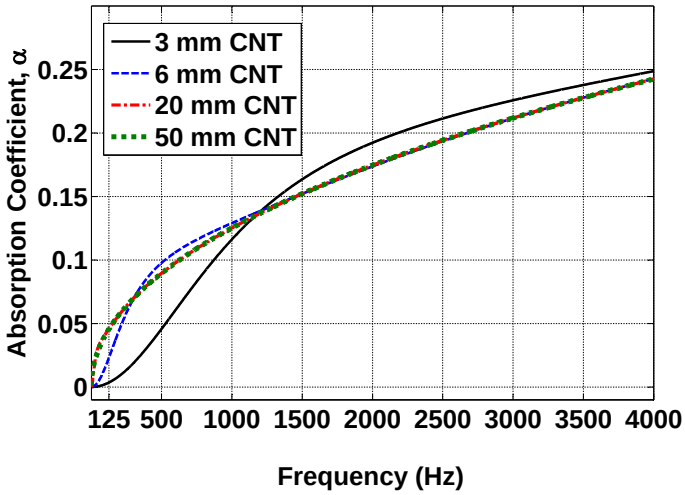

Figure D.3: Comparison of theoretical estimates of acoustic absorption coefficient of a CNT forest with a bulk density of $10\,\mathrm{kgm}^{-3}$ for varying thickness in the range of $3 - 50\,\mathrm{mm}$.

E Typical Input Script of LAMMPS and Tcl

E.1 Sound Wave Propagation in Argon Gas

```
# ====================================
# Molecular simulations of sound wave propagation in simple gases
# ====================================
# Typical input script used to investigate the dynamics of
# acoustic effect in argon gas contained in a rectangular domain,
# as detailed in Chapter 6 of this thesis.
# Additional reference:
# Hadjiconstantinuo & Garcia (2001), Physics of Fluids, 13(4),
# http://pof.aip.org/resource/1/phfle6/v13/i4/p1040_s1

units           real
dimension       3
boundary        p p f

variable        t equal 273                     #[K] temperature of the gas
variable        P equal 1                       #[atm] pressure of the gas
variable        gamma equal 5/3                 #ratio of heat capacities for Ar
variable        kb equal 0.0019872041           #[Kcal/mol.K] Boltzmann constant
variable        r equal 8.3145                  #[J/mol/K] universal gas constant
variable        M equal 39.948                  #[gm/mol] molecular mass of argon
variable        m equal $M*1e-3/6.023e23        #[kg]mass of each argon atom
variable        c equal 331.3                   #[m/s] speed of sound at 't' temperature
```

```
#variable       c equal sqrt((${gamma}*(${kb}*4.2*1e3)*$t)/($M*1e-3))
variable        R equal 1       #[] acoustic Reynold's number
variable        rho equal 1.784 #[kg/m^3] density of argon gas at '273 K & 1 atm (1.013 bar)'

## Dynamic viscosity of argon gas at '273 K & 1 atm (1.013 bar)'
variable        miu equal 2.099e-5      #[pa.s]

## Mean free path
variable        lm equal ($m/(sqrt(2)*PI*((3.4e-10)^2)*${rho}))*1e10    #[Angstrom(A)]

variable        l equal (2*PI*${miu}*$R*1e10)/($c*${rho})       #[A] acoustic wave length
variable        L equal (7/4)*$l        #[A] length of the wave propagating domain
variable        k equal 2*PI/$l         #[1/A] wave number
variable        angFr equal (2*PI*$c*1e-5)/$l   #[rad/fs] angular frequency of the wave
#variable       angFr equal 1.61592249787000430 73e-05
variable        T equal 2*PI/${angFr}   #[fs] wave periods
variable        Therm equal 1*$T        #[fs] thermostat damping time
variable        Vo equal (0.15*$c)/1e5  #[A/fs] velocity amplitude of sinusoidal wave
variable        A equal ${Vo}/${angFr}  #[A] displacement amplitude for x

## The wall was placed with an offset from its zero coordinates to position it inside
## the domain so that all wall atoms can be considered inside the boundary of the domain.
variable        Xo equal 6.0    #[A] initial position of the piston
```

```
variable        Ls equal 1500.0 #[A] length of simulation domain for wave propagation
variable        Lm equal ${Ls}

## Bin size to monitor velocity of the propagating wave
variable        dx1 equal round($l/60)          #[A]

variable        dx2 equal round(0.025*${lm})
variable        Lx equal 700.0  #[A] Simulation box width
variable        Ly equal 700.0  #[A] Simulation box height
atom_style      atomic

#-----------------------------------------------------------------------------
# Create geometry
#-----------------------------------------------------------------------------
region          box block 0 ${Lx} 0 ${Ly} 0 ${Ls} units box
create_box      2 box

lattice         fcc 5.26        #Lattice for wall
region          1 block 0 ${Lx} 0 ${Ly} 3.0 ${Xo} units box
create_atoms    1 region 1 units box

lattice         fcc 53          #Lattice for gaseous region
region          2 block 0 ${Lx} 0 ${Ly} 6.0 ${Lm}  units box
create_atoms    2 region 2 units box
```

```
#Define groups
group           wall region 1
group           media region 2

mass            1 39.948  #mass of solid wall
mass            2 39.948  #mass of gaseous argon (media)

set             group wall type 1
set             group media type 2

# LJ potentials
pair_style      lj/cut 10.0
pair_modify     shift yes
pair_coeff      2 2 0.238 3.40  #atoms in the media interacting with each other
pair_coeff      1 1 0.238 3.40  #wall atoms interacting with each other

## Wall atoms interacting with the atoms from media using WCA potential
## with cut-off=2^(1/6)*sigma.
pair_coeff      1 2 0.238 3.40 3.815

neighbor        0.3 bin
neigh_modify    delay 5
neigh_modify    exclude group wall wall
```

```
velocity        media create 273.0 485738 dist gaussian units box
fix             Tlang media langevin 273.0 273.0 1000.0 693483
fix             NVE media nve

fix             freeze wall setforce 0.0 0.0 0.0
fix             spec_wall all wall/reflect zhi EDGE units box

compute         Tgas media temp
compute         Twall wall temp
compute         KEg media ke
compute         KEw wall ke

compute         PEg1 media pe/atom
compute         PEg media reduce sum c_PEg1

compute         PEw1 wall pe/atom
compute         PEw wall reduce sum c_PEw1

variable        Press equal press

compute         Gperatom media stress/atom
compute         Pgas media reduce sum c_Gperatom[1] c_Gperatom[2] c_Gperatom[3]
variable        Gpress equal -(c_Pgas[1]+c_Pgas[2]+c_Pgas[3])/(3*vol)
```

```
dump            1 all atom 100000 acoustic_R1_f.lammpstrj
dump_modify     1 flush yes sort id scale no
dump            2 wall atom 100000 wall_R1.lammpstrj
dump_modify     2 flush yes sort id scale no

compute         vx media property/atom vx
variable        Vx atom c_vx-vcm(media,x)
compute         vy media property/atom vy
variable        Vy atom c_vy-vcm(media,y)
compute         vz media property/atom vz
variable        Vz atom c_vz-vcm(media,z)

## Converting KE from 'gm/mol.A^2/fs^2' units to 'kcal/mol' units,
## so 1e4 for converting 'gm/mol.A^2/fs^2' to 'kg/mol.m^2/s^2' or kJ/mol
## and 0.24 for kcal/mol
variable        KE atom 0.5*mass*((v_Vx^2)+(v_Vy^2)+(v_Vz^2))*1e4*0.24
variable        Tatom atom v_KE/(1.5*${kb})     #Temp per atom in K

## Alternative method [Temp]
compute         KEatom media ke/atom
variable        Ta atom c_KEatom/(1.5*${kb})    #per-atom Temp in K

##Here 'stress/atom' is in 'pressure*volume' unit i.e 'atm*A^3' unit
compute         peratom media stress/atom
```

```
## To get pressure per bin (atm)= ([collected 'patom' from ave/spatial]*Ncount);
## Volume 'V' should be in 'A' unit
variable        patom atom -(c_peratom[1]+c_peratom[2]+c_peratom[3])/(3*(${dx1}*${Lx}*${Ly}))

## Alternative method [Pressure]
variable        Patom atom -(c_peratom[1]+c_peratom[2]+c_peratom[3])/3

fix             flowvelEqm media ave/spatial 10 100 1000 z 0.0 ${dx1} vz v_Vz vy vx ...
                density/mass v_Tatom v_Patom units box ave running ...
                file velEqm_R1_dx1_f.profile
fix             flowEqm media ave/time 1 1000 1000 c_Tgas v_Gpress c_KEg c_PEg ...
                ave running file FlowEqm_R1_f.profile

thermo_style    custom step cpu c_Tgas c_Twall temp v_Gpress press vol c_KEg c_KEw c_PEg ...
                      c_PEw ke pe etotal enthalpy f_freeze[1] f_freeze[2] f_freeze[3]
timestep        0.5
thermo          1000
thermo_modify   flush yes
run             4000000
write_restart   restart.eqm1

unfix           Tlang
unfix           NVE
```

```
fix             NVT media nvt temp 273.0 273.0 100.0

run             1500000
write_restart   restart.eqm2
reset_timestep  0
##-------------------------------------------------------------------
unfix           flowvelEqm
unfix           flowEqm
unfix           NVT

###Applying thermostat in the direction perpendicular to the acoustic flow
compute         tempXY media temp/partial 1 1 0
fix             thmfix media nvt temp 273.0 273.0 ${Therm}
fix_modify      thmfix temp tempXY energy yes

##Amount of energy transferred by thermostat
variable        thmfixE equal f_thmfix[7]+f_thmfix[8]+f_thmfix[9]+f_thmfix[10]+ ...
                f_thmfix[11]+f_thmfix[12]

compute         PEthermost all pe
compute_modify  PEthermost thermo no

variable        z equal cwiggle(0.0,$A,$T)
variable        v equal swiggle(0.0,${Vo},$T)
```

```
fix             4 wall move variable NULL NULL v_z NULL NULL v_v

fix             SHMgiven wall ave/time 1000 1 1000 v_z v_v file SHMmotion.given
compute         SHMrec1 wall property/atom z vz
compute         SHMrec2 wall reduce ave c_SHMrec1[1] c_SHMrec1[2]
variable        SHMrecZ equal c_SHMrec2[1]
variable        SHMrecVz equal c_SHMrec2[2]

variable        PistonFx equal f_freeze[1]
variable        PistonFy equal f_freeze[2]
variable        PistonFz equal f_freeze[3]

fix             PistonForce wall ave/time 1 1000 1000 v_PistonFx v_PistonFy v_PistonFz ...
                file PistonForce.wall
fix             flowvel1 media ave/spatial 10 100 1000 z 0.0 ${dx1} vz v_Vz vx vy v_Tatom ...
                density/mass c_KEatom c_PEg1 v_Patom units box file vel_R1_dx1_f.profile
fix             flowvelYZ media ave/spatial 10 100 1000 y 0.0 ${dx1} z 0.0 ${dx1} vy vz ...
                v_Ta v_Patom units box file vel_R1_YZ_f.profile

thermo_style    custom step cpu c_Tgas c_Twall temp v_Gpress press vol c_KEg c_KEw c_PEg ...
                c_PEw ke pe etotal enthalpy v_SHMrecZ v_SHMrecVz f_freeze[1] ...
                f_freeze[2] f_freeze[3] c_tempXY v_thmfixE  c_PEthermost
thermo          1000
thermo_modify   flush yes
```

```
timestep        1.0
run             67353000    #Running for 100 periods
write_restart   restart_67353000.AC1
```

E.2 Sound Wave Propagation in the Presence of a CNT

E.2.1 Simulation for Equilibration Process

```
# ====================================
# Molecular simulations of sound wave propagation in simple gases
# ====================================
# Typical input script used to investigate the dynamics
# of acoustic effect in argon gas contained in a rectangular
# domain with the presence of a CNT, as detailed in Chapter 7
# of this thesis.

units           metal  #Changes in units: Time [ps]; Energy [eV]
dimension       3
boundary        p p f
communicate     single vel yes
newton          on

variable        t equal 273
variable        P equal 1
variable        gamma equal 5/3
variable        kb equal 0.0019872041
variable        r equal 8.3145
variable        M equal 39.948
variable        m equal $M*1e-3/6.023e23
#variable       c equal sqrt((${gamma}*(${kb}*4.2*1e3)*$t)/($M*1e-3))
variable        c equal 331.3
variable        R equal 1
variable        rho equal 1.784
variable        miu equal 2.099e-5
variable        lm equal ($m/(sqrt(2)*PI*((3.4e-10)^2)*${rho}))*1e10
variable        l equal (2*PI*${miu}*$R*1e10)/($c*${rho})
variable        L equal (7/4)*$l
variable        k equal 2*PI/$l
variable        angFr equal (2*PI*$c*1e-2)/$l    #[rad/ps]
#variable       angFr equal 1.6159224978700043073e-02
variable        T equal 2*PI/${angFr}            #[ps] wave periods
#variable       Therm equal 5*$T
variable        Therm equal 1*$T
```

```
variable        Vo equal (0.15*$c)/1e2  #[A/ps] velocity amplitude
variable        A equal (${Vo}/${angFr})
variable        Xo equal 6.0
variable        Ls equal 1500.0
variable        Lm equal ${Ls}
variable        dx1 equal round($l/60)
variable        dx2 equal round(0.01*${lm})
#variable       dx2 equal round(0.5*${lm})
#variable       dx3 equal round(${lm})
variable        Lx equal 700.0
variable        Ly equal 700.0

#-----------------------------------------------------------------
# Create geometry
#-----------------------------------------------------------------
atom_style      molecular

## Data file: 70nm x 70nm simulation domain, 50nm CNT
read_data       data.ArCNT_AC

#Define groups
group           wall type 2
group           media type 1
group           fixend type 3
group           tube type 4
group           ArCNT type 1 4
group           CNT type 3 4
group           Tip1 id 56048
group           Tip2 id 58088

# LJ and REBO potentials
pair_style      hybrid rebo lj/cut 11.9  #cutoff distance as 3.5*3.40
pair_modify     shift yes

pair_coeff      * * rebo CH.airebo NULL NULL C C #Carbon & Carbon
pair_coeff      1 3*4 lj/cut 4.98e-3 3.38       #Carbon & Argon

## Atoms in the media interacting with each other
pair_coeff      1 1 lj/cut 10.33e-3 3.40 10.0   #Argon & Argon
```

```
## Wall atoms interacting with each other
pair_coeff      2 2 lj/cut 10.33e-3 3.40 10.0    #Argon & Argon

## Wall atoms interacting with the atoms from media using
## WCA potential with cut-off=2^(1/6)*sigma
pair_coeff      1 2 lj/cut 10.33e-3 3.40 3.816   #Argon & Argon

## Wall atoms interacting with the CNT atoms using
## WCA potential with cut-off=2^(1/6)*sigma
pair_coeff      2 3*4 lj/cut 4.98e-3 3.38 3.794 #Argon & Carbon

neighbor        2.0 bin
neigh_modify    delay 5
neigh_modify    exclude group wall wall
neigh_modify    exclude group fixend fixend

fix             spec_wall all wall/reflect zhi EDGE units box
fix             freezeF fixend setforce 0.0 0.0 0.0
fix             freezeW wall setforce 0.0 0.0 0.0

compute         Tgas media temp
compute         Twall wall temp
compute         Ttube tube temp
compute         Tfixend fixend temp
compute         KEg media ke
compute         KEtip1 Tip1 ke
compute         KEtip2 Tip2 ke
compute         KEt tube ke
compute         KEf fixend ke
compute         KEw wall ke

compute         PEg1 media pe/atom
compute         PEg media reduce sum c_PEg1

compute         PEw1 wall pe/atom
compute         PEw wall reduce sum c_PEw1

compute         PEt1 tube pe/atom
compute         PEt tube reduce sum c_PEt1
```

```
compute         PEf1 fixend pe/atom
compute         PEf fixend reduce sum c_PEf1

compute         fcnt tube property/atom fx fy fz
compute         FxyzCNT tube reduce sum c_fcnt[1] c_fcnt[2] c_fcnt[3]

compute         Gperatom media stress/atom
compute         Pgas media reduce sum c_Gperatom[1] ...
                        c_Gperatom[2] c_Gperatom[3]
variable        Gpress equal -(c_Pgas[1]+c_Pgas[2]+c_Pgas[3])/(3*vol)

###
dump            1 all atom 100000 acoustic_R1.lammpstrj
dump_modify     1 flush yes sort id scale no
dump            2 wall atom 100000 wall_R1.lammpstrj
dump_modify     2 flush yes sort id scale no
dump            3 CNT atom 100000 cnt_R1_1.lammpstrj
dump_modify     3 flush yes sort id scale no

compute         vx media property/atom vx
variable        Vx atom c_vx-vcm(media,x)
compute         vy media property/atom vy
variable        Vy atom c_vy-vcm(media,y)
compute         vz media property/atom vz
variable        Vz atom c_vz-vcm(media,z)

##Converting KE in 'gm/mol.A^2/ps^2' to 'Kcal/mol' units,
## so 1e-2 for converting 'gm/mol.A^2/ps^2' to
## 'Kilo x Kg/mol.m^2/s^2' or 'kJ/mol'
## and 0.24 for kcal/mol
variable        KE atom 0.5*mass*((v_Vx^2)+(v_Vy^2)+(v_Vz^2))*1e-2*0.24
variable        Tatom atom v_KE/(1.5*${kb}) #Temp in K

##Here 'stress/atom' in 'pressure*volume' unit i.e 'bars*A^3' unit
compute         peratom media stress/atom
variable        Patom atom -(c_peratom[1]+c_peratom[2]+c_peratom[3])/3

fix             flowvelEqm media ave/spatial 20 100 2000 z 0.0 ...
                ${dx1} vz v_Vz vy vx density/mass v_Tatom v_Patom ...
                units box ave running file velEqm_R1_dx1_f.profile
```

```
fix             flowEqm media ave/time 2 1000 2000 c_Tgas v_Gpress ...
                c_KEg c_PEg ave running file FlowEqm_R1_f.profile

fix             TlangA media langevin 273.0 273.0 100.0 686473
fix             TlangT tube langevin 273.0 273.0 100.0 654373
fix             NVEA media nve
fix             NVET tube nve

velocity        media create 273.0 488639 mom yes ...
                dist gaussian units box

thermo_style    custom step cpu c_Tgas c_Ttube c_Twall temp v_Gpress ...
                press vol c_KEg c_KEw c_KEt c_KEf c_PEg c_PEw c_PEt ...
                c_PEf ke pe etotal enthalpy f_freezeF[1] f_freezeF[2] ...
                f_freezeF[3] f_freezeW[1] f_freezeW[2] f_freezeW[3] ...
                c_FxyzCNT[1] c_FxyzCNT[2] c_FxyzCNT[3] c_KEtip1 c_KEtip2
thermo          1000
thermo_modify   flush yes

timestep        0.00001
run             100000

timestep        0.0004
run             100000

timestep        0.0005
run             20000000
write_restart   restart.eqm1

velocity        media create 273.0 488639 mom yes ...
                dist gaussian units box

undump          3
dump            4 CNT atom 20000 cnt_R0.5_2.lammpstrj
dump_modify     4 flush yes sort id scale no

compute         PEtip1 Tip1 pe/atom
compute         PEtip2 Tip2 pe/atom

dump            DeflTip1 Tip1 custom 2000 DeflectionEqm.Tip1 ...
```

```
                                x y z c_PEtip1
dump            DeflTip2 Tip2 custom 2000 DeflectionEqm.Tip2 ...
                                x y z c_PEtip2
dump_modify     DeflTip1 sort id
dump_modify     DeflTip2 sort id

timestep        0.0005
run             10000000
write_restart   restart.eqm2
##-----------------------------------------------------------------------
```

E.2.2 Restarting Simulation for Wave Propagation

```
#====================================
# Molecular simulations of sound wave propagation in simple gases
# ====================================
# Typical input script used to investigate the dynamics
# of acoustic effect in argon gas contained in a rectangular
# domain with the presence of a CNT, as detailed in Chapter 7
# of this thesis.

units           metal
dimension       3
boundary        p p f
communicate     single vel yes
newton          on

variable        t equal 273
variable        P equal 1
variable        gamma equal 5/3
variable        kb equal 0.0019872041
variable        r equal 8.3145
variable        M equal 39.948
variable        m equal $M*1e-3/6.023e23
#variable       c equal sqrt((${gamma}*(${kb}*4.2*1e3)*$t)/($M*1e-3))
variable        c equal 331.3
variable        R equal 1
variable        rho equal 1.784
variable        miu equal 2.099e-5
variable        lm equal ($m/(sqrt(2)*PI*((3.4e-10)^2)*${rho}))*1e10
variable        l equal (2*PI*${miu}*$R*1e10)/($c*${rho})
variable        L equal (7/4)*$l
variable        k equal 2*PI/$l
variable        angFr equal (2*PI*$c*1e-2)/$l
variable        T equal 2*PI/${angFr}
variable        Therm equal 1*$T
variable        Vo equal (0.15*$c)/1e2
variable        A equal (${Vo}/${angFr})
variable        Xo equal 6.0
variable        Ls equal 1500.0
variable        Lm equal ${Ls}
```

```
variable        dx1 equal round($l/60)
variable        dx2 equal round(0.01*${lm})
variable        Lx equal 700.0
variable        Ly equal 700.0

#-----------------------------------------------------------
# Create geometry
#-----------------------------------------------------------
atom_style      molecular

## Restarting simulation after equilibrium
## Structure: 70nm x 70nm simulation domain, 50nm CNT
read_restart    restart.eqm2

#Define groups
group           wall type 2
group           media type 1
group           fixend type 3
group           tube type 4
group           ArCNT type 1 4
group           CNT type 3 4
group           Tip1 id 56048
group           Tip2 id 58088

# LJ and REBO potentials
pair_style      hybrid rebo lj/cut 11.9  #cutoff distance as 3.5*3.40
pair_modify     shift yes

pair_coeff      * * rebo CH.airebo NULL NULL C C #Carbon & Carbon
pair_coeff      1 3*4 lj/cut 4.98e-3 3.38       #Carbon & Argon
pair_coeff      1 1 lj/cut 10.33e-3 3.40 10.0   #Argon & Argon
pair_coeff      2 2 lj/cut 10.33e-3 3.40 10.0   #Argon & Argon
pair_coeff      1 2 lj/cut 10.33e-3 3.40 3.816  #Argon & Argon
pair_coeff      2 3*4 lj/cut 4.98e-3 3.38 3.794 #Argon & Carbon

neighbor        2.0 bin
neigh_modify    delay 5
neigh_modify    exclude group wall wall
neigh_modify    exclude group fixend fixend
```

```
fix             spec_wall all wall/reflect zhi EDGE units box
fix             freezeF fixend setforce 0.0 0.0 0.0
fix             freezeW wall setforce 0.0 0.0 0.0

compute         Tgas media temp
compute         Twall wall temp
compute         Ttube tube temp
compute         Tfixend fixend temp
compute         KEg media ke
compute         KEtip1 Tip1 ke
compute         KEtip2 Tip2 ke
compute         KEt tube ke
compute         KEf fixend ke
compute         KEw wall ke

compute         PEg1 media pe/atom
compute         PEg media reduce sum c_PEg1

compute         PEw1 wall pe/atom
compute         PEw wall reduce sum c_PEw1

compute         PEt1 tube pe/atom
compute         PEt tube reduce sum c_PEt1

compute         PEf1 fixend pe/atom
compute         PEf fixend reduce sum c_PEf1

compute         fcnt tube property/atom fx fy fz
compute         FxyzCNT tube reduce sum c_fcnt[1] c_fcnt[2] c_fcnt[3]

compute         Gperatom media stress/atom
compute         Pgas media reduce sum c_Gperatom[1] ...
                        c_Gperatom[2] c_Gperatom[3]
variable        Gpress equal -(c_Pgas[1]+c_Pgas[2]+c_Pgas[3])/(3*vol)

###
dump            1 all atom 100000 acoustic_R0.5.lammpstrj
dump_modify     1 flush yes sort id scale no
dump            2 wall atom 100000 wall_R0.5.lammpstrj
dump_modify     2 flush yes sort id scale no
```

```
compute         vx media property/atom vx
variable        Vx atom c_vx-vcm(media,x)
compute         vy media property/atom vy
variable        Vy atom c_vy-vcm(media,y)
compute         vz media property/atom vz
variable        vz2 atom c_vz^2
variable        Vz atom c_vz-vcm(media,z)
variable        KE atom 0.5*mass*((v_Vx^2)+(v_Vy^2)+(v_Vz^2))*1e-2*0.24
variable        Tatom atom v_KE/(1.5*${kb})
compute         KEatom media ke/atom

compute         peratom media stress/atom
variable        Patom atom -(c_peratom[1]+c_peratom[2]+c_peratom[3])/3

fix             TlangA media langevin 273.0 273.0 100.0 686473
fix             TlangT tube langevin 273.0 273.0 100.0 654373
fix             NVEA media nve
fix             NVET tube nve

velocity        media create 273.0 488639 mom yes dist gaussian units box

thermo_style    custom step cpu c_Tgas c_Ttube c_Twall temp v_Gpress ...
                press vol c_KEg c_KEw c_KEt c_KEf c_PEg c_PEw c_PEt ...
                c_PEf ke pe etotal enthalpy f_freezeW[1] f_freezeW[2] ...
                f_freezeW[3] c_FxyzCNT[1] c_FxyzCNT[2] c_FxyzCNT[3] ...
                c_KEtip1 c_KEtip2
thermo          1000
thermo_modify   flush yes

timestep        0.0005
run             200000
write_restart   restart.eqm3
reset_timestep  0
##-----------------------------------------------------------------------
unfix           TlangA
unfix           TlangT
unfix           NVEA
unfix           NVET
fix             NVET tube nve
```

```
dump            3 CNT atom 20000 cnt_R0.5.lammpstrj
dump_modify     3 flush yes sort id scale no

compute         PEtip1 Tip1 pe/atom
compute         PEtip2 Tip2 pe/atom
dump            DeflTip1 Tip1 custom 2000 DeflectionAC.Tip1 ...
                                x y z c_PEtip1
dump            DeflTip2 Tip2 custom 2000 DeflectionAC.Tip2 ...
                                x y z c_PEtip2
dump_modify     DeflTip1 sort id
dump_modify     DeflTip2 sort id

## Applying thermostat in the direction perpendicular
## to the acoustic flow
compute         tempXY media temp/partial 1 1 0
fix             thmfix media nvt temp 273.0 273.0 ${Therm}
fix_modify      thmfix temp tempXY energy yes

variable        thmfixE equal f_thmfix[7]+f_thmfix[8]+f_thmfix[9]+ ...
                f_thmfix[10]+f_thmfix[11]+f_thmfix[12]

compute         PEthermost all pe
compute_modify  PEthermost thermo no

## sinusoidal motion of the piston
variable        z equal cwiggle(0.0,$A,$T)
variable        v equal swiggle(0.0,${Vo},$T)
fix             4 wall move variable NULL NULL v_z NULL NULL v_v

variable        PistonFx equal f_freezeW[1]
variable        PistonFy equal f_freezeW[2]
variable        PistonFz equal f_freezeW[3]

fix             PistonForce wall ave/time 2 1000 2000 v_PistonFx ...
                v_PistonFy v_PistonFz file PistonForce.wall

## These are just for verifications
fix             SHMgiven wall ave/time 2000 1 2000 v_z v_v ...
                file SHMmotion.given
```

```
compute         SHMrec1 wall property/atom z vz
compute         SHMrec2 wall reduce ave c_SHMrec1[1] c_SHMrec1[2]
variable        SHMrecZ equal c_SHMrec2[1]
variable        SHMrecVz equal c_SHMrec2[2]

fix             flowvel1ave media ave/spatial 20 100 2000 z 0.0 ${dx1} ...
                vz v_Vz vx vy v_Tatom density/mass c_KEatom c_PEg1 ...
                v_Patom units box ave running file velave_R1_dx1_f.profile
fix             flowvel1 media ave/spatial 20 100 2000 z 0.0 ${dx1} ...
                vz v_Vz vx vy v_Tatom density/mass c_KEatom c_PEg1 ...
                v_Patom units box file vel_R0.5_dx1_f.profile
fix             flowvelYZ media ave/spatial 20 100 2000 y 0.0 ${dx1}
                z 0.0 ${dx1} vy vz v_Tatom v_Patom units box ...
                file vel_R1_YZ_f.profile

thermo_style    custom step cpu c_Tgas c_Ttube c_Twall temp v_Gpress ...
                press vol c_KEg c_KEw c_KEt c_KEf c_PEg c_PEw c_PEt ...
                c_PEf ke pe etotal enthalpy v_SHMrecZ v_SHMrecVz ...
                f_freezeF[1] f_freezeF[2] f_freezeF[3] f_freezeW[1] ...
                f_freezeW[2] f_freezeW[3] c_FxyzCNT[1] c_FxyzCNT[2] ...
                c_FxyzCNT[3] c_KEtip1 c_KEtip2  c_tempXY v_thmfixE ...
                c_PEthermost
thermo          2000
thermo_modify   flush yes
timestep        0.0005
run             40411800        #Running for 0-30 wave periods
write_restart   restart_40411800.AC1
```

E.2.3 Tcl Script to Create Data Input File for Molecular Structure

```
## ------------------------------------------------------------
# Generate topology data from coordinate data
## ------------------------------------------------------------
# This is a modified version of the template provided
# by Axel Kohlmeyer in the following link:
#
# Reference:
# Kohlmeyer, A. (2013). TopoTools Plugin
# http://www.ks.uiuc.edu/Research/vmd/plugins/topotools/
##############################################
# explicitly load topotools and pbctools packages since
# they are not automatically required in text mode and
# abort if their version numbers are insufficient.

if {[catch {package require topotools 1.1} ver]} {
   vmdcon -error "$ver.
   This script requires at least TopoTools v1.1. Exiting..."
   quit
}

if {[catch {package require pbctools 2.3} ver]} {
   vmdcon -error "$ver.
   This script requires at least pbctools v2.3. Exiting..."
   quit
}
#-------------------------------------------------------------
set fname acoustic_R1_f.lammpstrj
# The LAMMPS trajectory file 'acoustic_R1_f.lammpstrj' is
# for argon gas and argon wall, which can be generated
# using a script similar to Section E.1

# check for presence of coordinate file
if {! [file exists $fname]} {
    vmdcon -error "Required file '$fname' not available. Exiting..."
   quit
}

# load coordinates and use automatically computed bonds
```

```
mol new $fname autobonds no waitfor all

set sel [atomselect top all frame first]
$sel writexyz ArgonAC.xyz
#$sel writepdb ArgonAC.pdb
#topo writelammpsdata data.ArgonAC atomic $sel

#-------------------------------------------------------------------
set fname ArgonAC.xyz

# check for presence of coordinate file
if {! [file exists $fname]} {
    vmdcon -error "Required file '$fname' not available. Exiting..."
   quit
}

# load coordinates and use automatically computed bonds
mol new $fname autobonds no waitfor all
#topo readlammpsdata $fname atomic autobonds no waitefor all

set sel [atomselect top all]
set center [measure center $sel weight none]
$sel moveby [vecscale -1.0 $center]
vmdcon -info "moved center from $center to
                        [measure center $sel weight none]"


set center [measure center $sel weight none]; #Center of geometry
set cx [lindex $center 0]
set cy [lindex $center 1]
set cz [lindex $center 2]

set sel [atomselect top all]
set minmax [measure minmax $sel -withradii]


set lz 500.0;     #Nanotube length lz=50nm

##Length of rectangular domain of argon
set L [lindex [lindex $minmax 1] 2];
```

```
$sel delete
set selA [atomselect top "not (sqrt(sqr(x-$cx)+sqr(y-$cy))<10 and ...
                (z-$cz)>=($L-$lz))"]; #CNT diameter=6.9 Angstrom
#$selA writepdb ArboxAC.pdb
#$selA writepsf ArboxAC.psf
$selA writexyz ArboxAC.xyz
#topo writelammpsdata data.ArboxAC atomic $selA
$selA delete

mol delete top

#-------------------------------------------------------------------
set fname ArboxAC.xyz
# check for presence of coordinate file
if {! [file exists $fname]} {
   vmdcon -error "Required file '$fname' not available. Exiting..."
   quit
}

# load coordinates and use automatically computed bonds
mol new $fname autobonds no waitfor all

set sel [atomselect top all]
set center [measure center $sel weight none]
$sel moveby [vecinvert [measure center $sel weight none]]
#$sel moveby [vecscale -1.0 $center]
vmdcon -info "moved center from $center to
                        [measure center $sel weight mass]"

set sel1 [atomselect top {type 1}]
$sel1 set type Aw
$sel1 set resname AR1
$sel1 set mass 39.948
$sel1 set charge 0.0; #Argon is an inert gas, so no charge


#set residue ID to a 1-based index for Argon.
set resid {}
foreach r [$sel1 get residue] { incr r; lappend resid $r }
```

```
$sel1 set resid $resid

set sel2 [atomselect top {type 2}]
$sel2 set type Am
$sel2 set resname AR2
$sel2 set mass 39.948
$sel2 set charge 0.0; #Argon is an inert gas, so no charge


#set residue ID to a 1-based index for Argon.
set resid {}
foreach r [$sel2 get residue] { incr r; lappend resid $r }
$sel2 set resid $resid


set sel [atomselect top all]
set minmax [measure minmax $sel -withradii]

#The distance required to move the wall to the left side of the media
set mzw [lindex [lindex $minmax 0] 2];

# the distance required to move the CNT to the right side of the media
set mzc [lindex [lindex $minmax 1] 2];

# remember this molecule
set mol1 [molinfo top]

#-------------------------------------------------------------------------
#Building nanotube with bonds and angles using Nanotube Builder
nanotube -l [expr $lz/10] -n 5 -m 5 -b 0 -a 0 -d 0 -i 0
;
# For Tersoff-Brenner potential, bond/angle of CNT will be
# calculated automatically, no need to define it in the data file.

$sel delete
set sel [atomselect top all]
set center [measure center $sel weight none]
$sel moveby [vecinvert [measure center $sel weight none]]
$sel moveby [vecscale -1.0 $center]
vmdcon -info "moved center from $center to
```

```
                        [measure center $sel weight mass]"

## setting the distance required to move the box in -ve Z direction
set sel [atomselect top all]
set center [measure center $sel weight none]
set b [list [lindex $center 0] [lindex $center 1] [expr ($mzc)+10]];
## Here, Nanotube fixend length, L_{fix}=10A
$sel moveby [vecscale 1.0 $b]


set selc [atomselect top "z>=$mzc"];
$selc set type C1
$selc set resname CNT
$selc set mass 12.0110
$selc set charge 0.0

set selC [atomselect top "not(z>=$mzc)"];
$selC set type C2
$selC set resname CNT
$selC set mass 12.0110
$selC set charge 0.0

# remember this molecule
set mol2 [molinfo top]

#-------------------------------------------------------------------------------
# now combine the two molecules into one
set molcom [::TopoTools::mergemols [list $mol1 $mol2]]

topo clearimpropers

set sel [atomselect top all]
set minmax [measure minmax $sel -withradii]
#set box [vecscale 1.0 [vecsub [lindex $minmax 1] [lindex $minmax 0]]]
set box [list 700.0 700.0 1500.0]
pbc set $box
vmdcon -info "box size: $box"


# and write out the result as a lammps data file.
```

```
topo writelammpsdata data.ArCNT_AC molecular

#animate write pdb ArCNT_AC.pdb
#animate write psf ArCNT_AC.psf

# final sanity check the whole system has to be neutral.
$sel delete
set sel [atomselect top all]
$sel writexyz ArCNT_AC.xyz
set totq [measure sumweights $sel weight charge]
if {[expr {abs($totq)}] > 0.0005} {
    vmdcon -warning "Total system not neutral: $totq"
}
```

List of Publications

Conference Papers

- Ayub, M., Zander, A. C., Howard, C. Q., Cazzolato, B. S., Shanov, V. N., Alvarez, N. T., and Huang, D. M. (2014), "Acoustic absorption behaviour of carbon nanotube arrays", *Inter-noise and Noise-Con congress and conference proceedings*, 249(7), 929-938 (Peer reviewed).

- Ayub, M., Zander, A.C., Howard, C.Q., Huang, D.M. and Cazzolato, B.S. (2014). "Molecular dynamics simulations of sound wave propagation in a gas and thermo-acoustic effects on a carbon nanotube", *11th International Conference on Theoretical and Computational Acoustics* (ICTCA),10-14 March, Texas A&M University, USA (Full-length paper is under review for publication in *Journal of Computational Acoustics*).

- Ayub, M., Zander, A.C., Howard, C.Q., Cazzolato, B.S. and Huang, D.M. (2013). "A review of MD simulations of acoustic absorption mechanisms at the nanoscale", *Proceedings of Acoustics 2013*, 17-20 November, Victor Harbor, SA, Australia (Peer reviewed).

- Ayub, M., Zander, A.C., Howard, C.Q. and Cazzolato, B.S. (2011). "A review of acoustic absorption mechanisms of nanoscopic fibres", *Proceedings of Acoustics 2011*, 2-4 November, Gold Coast, Australia (Peer reviewed).

Poster Presentation

- Ayub, M., Zander, A.C., Howard, C.Q., Cazzolato (2012). "Investigation of a carbon nanotube acoustic absorber", *MechExpo 2012*, 24-25 October,

Adelaide Showground, Goyder pavilion, SA, Australia.

Journal Articles in Preparation

- Ayub, M., Zander, A.C., Howard, C.Q., Cazzolato, B.S., Shanov, V. N., Alvarez, N. T., and Huang, D. M. (2015). ”Normal incidence acoustic absorption characteristics of a carbon nanotube forest", *Nanotechnology*.

- Ayub, M., Zander, A.C., Howard, C.Q., Cazzolato, B.S., and Huang, D. M. (2015). ”Molecular dynamics simulation of sound wave propagation in a monatomic gas", *Physics of Fluids*.

- Ayub, M., Zander, A.C., Howard, C.Q., Cazzolato, B.S., and Huang, D. M. (2015). ”Molecular dynamics simulation of classical sound absorption in a monatomic gas", *Physics of Fluids*.

- Ayub, M., Zander, A.C., Howard, C.Q., Cazzolato, B.S., and Huang, D. M. (2015). ”Molecular dynamics simulation of acoustic absorption in a carbon nanotube", *Physics of Fluids*.